

A novel approach to precision measurements of the top quark-antiquark pair production cross section with the ATLAS experiment

DISSERTATION

zur Erlangung des akademischen Grades

doctor rerum naturalium

(Dr. rer. nat.)

im Fach Physik

eingereicht an der
Mathematisch-Naturwissenschaftlichen Fakultät I
der Humboldt-Universität zu Berlin

von

Dipl.-Phys. Clemens Gregor Lange

Präsident der Humboldt-Universität zu Berlin:

Prof. Dr. Jan-Hendrik Olbertz

Dekan der Mathematisch-Naturwissenschaftlichen Fakultät I:

Prof. Stefan Hecht, PhD

Gutachter/-innen:

1. Prof. Dr. Ulrich Husemann

2. Prof. Dr. Heiko Lacker

3. Jun.-Prof. Dr. Lucia Masetti

Tag der mündlichen Prüfung: 12. Juli 2013

Für meinen Opa, der sicher auch gerne damit angegeben hätte.



To my grandfather who surely would have liked showing off with this as well.

Abstract

This doctoral thesis presents three measurements of the top quark-antiquark pair production cross section in proton-proton collisions at a centre-of-mass energy of $\sqrt{s} = 7$ TeV recorded in 2010 and 2011 with the ATLAS Experiment at the Large Hadron Collider. Events are selected in the single lepton topology by requiring an electron or muon, large missing transverse momentum and at least three jets. While one analysis relies on kinematic information only to discriminate the $t\bar{t}$ signal from the background processes, the other two also make use of b -tagging information. With the help of multivariate methods the most precise measurements in this topology are obtained. This is for two of the measurements in particular possible due to the use of a profile likelihood method which is studied in detail. For the first time a fiducial inclusive cross section measurement for top quark events is performed allowing a measurement almost independent of theoretical uncertainties. All measurements are in agreement with theory predictions performed in perturbation theory at approximate NNLO.

Zusammenfassung

In dieser Dissertation werden drei Messungen des Produktionswirkungsquerschnitts von Top-Quark-Antiquark-Paaren in Proton-Proton-Kollisionen bei einer Schwerpunktsenergie von 7 TeV vorgestellt. Die Daten wurden mit dem ATLAS-Experiment am Large Hadron Collider in den Jahren 2010 und 2011 aufgezeichnet. Für die Analyse werden Endzustände mit genau einem Myon oder Elektron, mindestens drei Jets sowie großem fehlenden Transversalimpuls selektiert. Während eine Analyse ausschließlich kinematische Informationen für die Trennung von Signal- und Untergrundprozessen verwendet, nutzen die anderen beiden zusätzlich Informationen zur Identifizierung von Bottom-Quark-Jets. Mit Hilfe von multivariaten Methoden werden die präzisesten Messungen in dieser Ereignistopologie erreicht. Dies ist für zwei der Analysen insbesondere dank der Profile-Likelihood-Methode möglich, welche sorgfältig untersucht wird. Desweiteren wird zum ersten Mal ein sogenannter sichtbarer Wirkungsquerschnitt in Top-Quark-Ereignissen gemessen. Alle Ergebnisse sind in Übereinstimmung mit den theoretischen Vorhersagen in angenäherter nächstnächstführender Ordnung der Störungstheorie (approx. NNLO).

Contents

1. Introduction	1
2. Top Quark Physics at Hadron Colliders	3
2.1. The top quark in the Standard Model	3
2.1.1. Electroweak theory	3
2.1.2. Quantum Chromodynamics	8
2.1.3. Model predictions of top quark properties	10
2.2. Top quark production in pp collisions	14
2.2.1. Cross sections	14
2.2.2. Factorisation ansatz	15
2.2.3. Parametrisations of parton distribution functions	16
2.2.4. $t\bar{t}$ production and cross section prediction	18
2.2.5. Single top production	23
2.2.6. Top quark decay	24
3. The LHC and the ATLAS detector	29
3.1. The Large Hadron Collider	29
3.2. The ATLAS detector	31
3.2.1. Geometry and coordinate system	33
3.2.2. Magnet system	33
3.2.3. Inner Detector	34
3.2.4. Calorimetry	37
3.2.5. Muon System	40
3.2.6. Forward and Luminosity Detectors	41
3.2.7. Trigger and Data Acquisition	42
3.3. Performance of the LHC and ATLAS	43
4. Object and event reconstruction	47
4.1. Tracks and vertices	47
4.1.1. Track reconstruction	47
4.1.2. Vertex reconstruction	48
4.2. Electrons	49
4.2.1. Electron identification and reconstruction	50
4.2.2. Electron energy calibration and resolution	52
4.2.3. Electron trigger	52
4.2.4. Electron isolation	55

Contents

4.3.	Muons	56
4.3.1.	Muon identification and reconstruction	56
4.3.2.	Muon momentum calibration and resolution	57
4.3.3.	Muon trigger	58
4.3.4.	Muon isolation	60
4.4.	Jets	60
4.4.1.	The anti- k_T algorithm	61
4.4.2.	Jet reconstruction	62
4.4.3.	Jet calibration	62
4.4.4.	Jet energy resolution	63
4.4.5.	Jet quality and pileup rejection	64
4.4.6.	Jet reconstruction efficiency	64
4.5.	Identification of b -jets	65
4.5.1.	2010 analysis b -jet identification and calibration	65
4.5.2.	2011 analysis (b) b -jet identification and calibration	68
4.6.	Missing transverse energy	70
4.6.1.	Reconstruction and calibration of missing transverse energy	72
4.6.2.	Missing transverse energy performance	72
4.7.	Overlap removal	73
4.7.1.	Electron muon overlap removal	73
4.7.2.	Muon jet overlap removal	73
4.7.3.	Jet electron overlap removal	74
5.	Dataset and event generation	75
5.1.	Dataset	75
5.1.1.	Data Quality and Good Runs Lists	75
5.2.	Event generation using Monte Carlo generators	76
5.2.1.	Simulation of hard processes and physics events	77
5.2.2.	Parton shower and hadronisation	77
5.3.	Detector simulation and event reconstruction	78
5.4.	Monte Carlo data samples	79
5.4.1.	Simulation of top quark pair events	80
5.4.2.	Simulation of W/Z + jets events	81
5.4.3.	Simulation of other electroweak processes	83
5.4.4.	Summary of Monte Carlo samples	84
6.	Basic event selection and data-driven background estimation	87
6.1.	Selection cuts	87
6.2.	QCD multi-jet background estimation	89
6.2.1.	Template fitting methods	90
6.2.2.	Matrix methods	95
6.2.3.	Discussion of QCD multi-jet estimation methods	97

6.3.	Data-driven estimation of the $W + \text{jets}$ background	98
6.3.1.	Data-driven estimation of the heavy flavour content in the $W + \text{jets}$ background	100
7.	Measurement and signal extraction method	101
7.1.	Discriminating variables	102
7.1.1.	Projective likelihood discriminant	108
7.2.	Systematic uncertainties	109
7.2.1.	Experimental uncertainties	109
7.2.2.	Model uncertainties	116
7.3.	Likelihood fit method	121
7.3.1.	Likelihood function	121
7.3.2.	Minimisation and profiling	123
7.4.	Performance and uncertainty evaluation using pseudo experiments	124
7.4.1.	Use of pseudo experiments in the 2010 and 2011 analysis (a)	124
7.4.2.	Use of pseudo experiments in the 2011 analysis (b)	125
7.5.	Summary of uncertainties	125
8.	Cross section measurement using b-tagging	127
8.1.	Results of event selection and multivariate signal and background separation	127
8.2.	Cross section extraction	133
8.2.1.	Expected uncertainties	133
8.2.2.	Fit results	136
8.2.3.	Observed uncertainties	141
8.3.	Method and stability tests	143
8.3.1.	Use of envelope of uncertainties	145
8.3.2.	Uncertainty absorption	145
8.3.3.	Effect of acceptance corrections	147
8.3.4.	Correlation effects in jet energy scale uncertainties	147
8.4.	Discussion of results	149
8.4.1.	Lepton + jets cross section measurement	149
8.4.2.	Combination of cross section measurements	150
8.4.3.	Indirect top quark mass determination	151
9.	Cross section measurement using kinematic information only	155
9.1.	Results of event selection and multivariate signal and background separation	155
9.2.	Cross section extraction	159
9.2.1.	Expected uncertainties	159
9.2.2.	Fit results	161
9.2.3.	Observed uncertainties	167
9.3.	Method and stability tests	169
9.4.	Discussion of results	172
9.4.1.	Lepton + jets cross section measurement	172
9.4.2.	Combination of cross section measurements	172

9.4.3. Parametrisation of the cross section as a function of the top quark mass	174
10. Fiducial cross section measurement	177
10.1. Event selection and measurement approach	178
10.1.1. Fit procedure	186
10.1.2. Multivariate signal and background separation	186
10.2. Cross section extraction	187
10.2.1. Evaluation of systematic uncertainties	187
10.2.2. Fit results	196
10.3. Discussion of results	196
10.3.1. Lepton + jets fiducial cross section measurement	196
10.3.2. Interpretation in full phase space	200
10.3.3. Comparison to previous measurements	202
10.3.4. Prospects of the measurement method	205
11. Conclusions	207
A. Monte Carlo samples used in the analyses	209
B. QCD multi-jet background estimation using the anti-electron model	213
B.1. Fit procedure	213
B.2. Evaluation of systematic uncertainties	213
B.2.1. Statistical uncertainties	214
B.2.2. Systematic uncertainties	214
B.3. Further benchmark distributions	216
C. Investigation of the W + heavy flavour contribution uncertainty	223
D. Additional details of the cross section measurement using b-tagging	231
D.1. Behaviour of the normalisation and nuisance parameters in profiling procedure	231
E. Additional details of the cross section measurement using kinematic information only	235
E.1. Behaviour of the normalisation and nuisance parameters in profiling procedure	235
E.2. Detailed listing of estimated systematic uncertainties	239
F. Additional details of the fiducial cross section measurement in 2011 data	241
F.1. Signal Monte Carlo event normalisation	241
F.2. Cross section extraction and error propagation	241
F.3. Additional control plots	242
F.4. Results of the minimum log-likelihood fit to data	242

1. Introduction

Elementary particle physics aims to describe the constituents of matter and the interactions between them. The current theoretical understanding is summarised by the Standard Model of Particle Physics (SM). Matter as known from everyday life consists only of electrons, neutrons and protons (the latter two consisting of up and down quarks). The SM, however, contains twelve different types of fermions, six leptons and six quarks, one of them being the top quark, which have been confirmed in experiment. Their interactions are described by gauge bosons of the electroweak force [1–3] and the strong force [4]. In addition, a scalar particle, the Higgs boson, is needed for theoretical consistency and to explain the masses of the elementary particles [5–9].

Until today, the Standard Model has passed all experimental tests successfully. It is, however, expected that it is only an approximation to a more complete theory since the SM has some shortcomings. For example, the inclusion of gravity into the model has not been accomplished. Furthermore, it is not yet understood why gravitation is sixteen orders of magnitudes weaker than electroweak interaction. Additionally, there are indications from astrophysics that the universe consists only to about four percent of matter as described by the SM, whereas 73% are made of dark energy and 23% of dark matter [10–14].

The top quark is the heaviest known elementary particle and has only been discovered in 1995. Its large mass suggests that the properties of the top quark are not simply those predicted by theory. Furthermore, any deviation from the theoretical expectations give hints to yet unknown physics that might answer open questions. In order to obtain conditions in which production of elementary particles can be studied, particle accelerators are used. The Large Hadron Collider (LHC) at CERN is the highest energy collider ever built. It produces millions of top quarks per year, allowing detailed scrutiny of the top quark's properties.

This thesis describes three measurements of the top quark pair production cross section, i.e. the likelihood of top quark pairs to be produced in the LHC's proton-proton collisions. In Chapter 2, the reader is introduced to the role of the top quark within the Standard Model. The second part of the chapter describes the theoretical predictions for the production of top quarks in proton-proton collisions. Chapter 3 summarises the experimental setup, focussing on the Large Hadron Collider and the ATLAS detector. The event reconstruction, the physics objects used and the corrections applied to match simulation and data are reviewed in Chapter 4. Chapter 5 describes the generation and simulation of collision data. The different Monte Carlo generators and samples used as well as the data sets analysed are detailed. Other processes that look very similar to top quark decays and therefore pose backgrounds to the measurement are discussed. Chapter 6 describes the estimation of QCD multi-jet and $W + \text{jets}$ events from data and the

1. Introduction

selection cuts applied for the analyses. The likelihood method employed to perform the measurements is detailed in Chapter 7. The three cross section measurements use three different data sets and will for the sake of clarity be referred to as *2010 measurement* for the measurement using 35 pb^{-1} of 2010 data, and *2011 measurement (a)* and *(b)* for the measurement using 0.7 fb^{-1} of 2011 data and the full 2011 data set, respectively. They are found in this order in Chapters 8, 9, and 10. Throughout the whole thesis the convention $\hbar = c = 1$ is used.

2. Top Quark Physics at Hadron Colliders

The measurements described in this thesis analyse top quark production within the context of the Standard Model of Particle Physics (SM). The SM summarises the current theoretical understanding of particle physics. It describes three of the four fundamental interactions — electromagnetic, weak and strong interaction in the form of quantum field theories with local gauge invariance. This theory is supported by numerous experimental results in the last forty years. The theory of strong interactions, quantum chromodynamics, and the unified theory of electroweak interaction constitute the cornerstones of the SM and are essential for the understanding of the production and decay of top quarks.

In the first part of this chapter a brief introduction to the Standard Model is given, explaining the importance of the top quark within the theoretical framework. The second part of this chapter is concerned with the production mechanisms of top quarks in hadron collisions and its subsequent decay, which is important for the identification of top quark events. Furthermore, processes that mimic top quark events in their final state are discussed. During the last years, several reviews on top quark physics have been written. This chapter is partly based on References [15–20]. The latest review on top quark physics can be found in Ref. [21].

2.1. The top quark in the Standard Model

The Standard Model is a quantum field theory describing the interactions of elementary particles based on a set of fields that are described later and the gauge symmetries $SU(3)_C \times SU(2)_L \times U(1)_Y$ [22]. Matter particles are grouped into two categories: quarks and leptons, both of them are fermions carrying spin 1/2. These are again arranged in generations ordered by mass: charged leptons together with their corresponding neutrino and up-type quarks with a down-type quark. The forces acting between the particles are described by fields, whose quanta are called gauge bosons carrying spin 1. The electromagnetic force is mediated by the massless photon (γ), the (electro)weak force by the W^\pm and the Z^0 bosons and the strong force by eight massless gluons (g). All particles participate in weak interactions, charged particles also in electromagnetic interactions and the quarks additionally in strong interactions.

2.1.1. Electroweak theory

The theory of electroweak interactions is based on the $SU(2)_L \times U(1)_Y$ gauge group with the quantum numbers weak isospin I and hypercharge Y [1–3]. Quarks and leptons are represented by spinor fields ψ , which are functions of continuous space-time

2. Top Quark Physics at Hadron Colliders

Table 2.1.: *The fields of the Standard Model and their gauge quantum numbers. I and I_3 demoninate the weak isospin and its third component, respectively, and Q is the electric charge.*

	SU(3) _C	SU(2) _L	U(1) _Y	I	I_3	Q		
$Q_L^i = \begin{pmatrix} u \\ d \end{pmatrix}_L$	$\begin{pmatrix} c \\ s \end{pmatrix}_L$	$\begin{pmatrix} t \\ b \end{pmatrix}_L$	3	2	1/3	1/2	+1/2	+2/3
$u_R^i = u_R$	c_R	t_R	3	1	4/3	0	0	+2/3
$d_R^i = d_R$	s_R	b_R	3	1	-2/3	0	0	-1/3
$L_L^i = \begin{pmatrix} \nu_e \\ e \end{pmatrix}_L$	$\begin{pmatrix} \nu_\mu \\ \mu \end{pmatrix}_L$	$\begin{pmatrix} \nu_\tau \\ \tau \end{pmatrix}_L$	1	2	-1	1/2	+1/2	0
$e_R^i = e_R$	μ_R	τ_R	1	1	-2	0	0	-1
$\nu_R^i = \nu_R^e$	ν_R^μ	ν_R^τ	0	0	0	0	0	0
$\phi = \begin{pmatrix} \phi^+ \\ \phi^0 \end{pmatrix}$			1	2	1	1/2	+1/2	+1
							-1/2	0

coordinates x^μ . Since the weak interaction in the form of vector minus axial current ($V - A$) couples only to left-handed chirality states, left- and right-handed spinor fields are introduced:

$$\psi_L = \frac{1}{2}(1 - \gamma_5)\psi \quad \text{and} \quad \psi_R = \frac{1}{2}(1 + \gamma_5)\psi. \quad (2.1)$$

Left-handed states of one generation are grouped into weak-isospin doublets with $I = \frac{1}{2}$ whereas right-handed states form singlets with $I = 0$ as summarised in Tab. 2.1.

For up-type quarks and neutrinos the third component of the weak isospin is assigned as $I_3 = +1/2$. For down-type quarks and charged leptons the component is $I_3 = -1/2$. The weak hypercharge Y mentioned afore is then defined via electric charge Q and weak isospin to be $Y = 2Q - 2I_3$. Hence, members within a doublet carry the same hypercharge: $Y = -1$ for leptons and $Y = 1/3$ for quarks. Historically, right-handed neutrino states are omitted in the Standard Model, i.e. neutrinos are assumed to be massless based on earlier experimental results [23, 24]. However, from the measurement of neutrino oscillations it has been found that this is not the case, see e.g. [10, 25, 26]. An extension of the SM is possible and discussed in Sec. 2.1.1.1, but usually ignored in top quark physics, since the effect is negligible for this field.

The dynamics of interactions described by theory can be understood by starting from the free particle Lagrangian:

$$\mathcal{L}_0 = i\bar{\psi}\gamma^\mu\partial_\mu\psi, \quad (2.2)$$

where γ^μ are the Dirac γ matrices. To successfully explain the dynamics of elementary particles, it has been found that gauge invariance of the Lagrangian under local phase transformations is required. In general, for an arbitrary phase, $\alpha(x)$, depending on space

2.1. The top quark in the Standard Model

and time, one demands invariance under the transformation:

$$\psi(x) \rightarrow e^{i\alpha(x)}\psi(x). \quad (2.3)$$

Consequently, for the Lagrangian \mathcal{L}_0 to be invariant under the gauge transformations given in Equation 2.3, a covariant derivative, D_μ , is introduced:

$$D_\mu = \partial_\mu - igA_\mu. \quad (2.4)$$

This brings along a vector field, A_μ , that transforms as $A_\mu \rightarrow A_\mu + \frac{1}{e}\partial_\mu\alpha$. Additionally, the coupling, g , is introduced quantifying the strength of the interaction.

Before applying the phase transformation to the special case of electroweak theory, a few more details need to be clarified: The $SU(2)_L$ group has three symmetry transformation generators, T_i , which are combined to the weak isospin operator $\mathbf{T} = (T_1, T_2, T_3)$. The Lie group is defined by the commutator relation $[T_i, T_j] = i\epsilon_{ijk}T_k$. As the T_i do not commute, the $SU(2)_L$ group is called non-Abelian. Due to the generator structure, the phase $\alpha(x)$ has to be extended to a three-component vector with the same dependencies as above. For the $U(1)_Y$ group, a one-dimensional function $\beta(x)$ with a similar role as α is introduced. The generator of the symmetry group $U(1)_Y$ is the weak hypercharge Y . As mentioned above, it satisfies the relation $Q = I_3 + Y/2$, where Q is the electromagnetic charge and I_3 the eigenvalue of T_3 . With this knowledge, the phase transformation yields:

$$\psi_L \rightarrow e^{ig\alpha(x)\cdot\mathbf{T}+ig'\beta(x)Y}\psi_L \quad \text{and} \quad \psi_R \rightarrow e^{ig'\beta(x)Y}\psi_R. \quad (2.5)$$

Since the electroweak theory combines two Lie groups, two different couplings g and g' are needed. One also finds that the phase transformations of the $SU(2)_L$ group act only on left-handed states denoted with index L .

For gauge invariance to hold, terms have to be added to the free Lagrangian involving four additional vector fields of spin 1: the isotriplet $\mathbf{W}_\mu = (W_{1\mu}, W_{2\mu}, W_{3\mu})$ for the $SU(2)_L$ and the singlet B_μ for the $U(1)_Y$. These replace the general vector field A_μ in Equation 2.4:

$$D_\mu = \partial_\mu + ig\mathbf{W}_\mu \cdot \mathbf{T} + ig'\frac{1}{2}B_\mu Y. \quad (2.6)$$

The kinetic energy terms of these gauge fields, $-\frac{1}{4}\mathbf{W}_{\mu\nu} \cdot \mathbf{W}^{\mu\nu}$ and $-\frac{1}{4}B_{\mu\nu} \cdot B^{\mu\nu}$, also have to be added to the Lagrangian. The field tensors $\mathbf{W}_{\mu\nu}$ and $B_{\mu\nu}$ are given by $\mathbf{W}_{\mu\nu} = \partial_\mu\mathbf{W}_\nu - \partial_\nu\mathbf{W}_\mu - g \cdot \mathbf{W}_\mu \times \mathbf{W}_\nu$ and $B_{\mu\nu} = \partial_\mu B_\nu - \partial_\nu B_\mu$. The quanta of these fields are called gauge bosons. The resulting Lagrangian for the fermion fields is then:

$$\begin{aligned} \mathcal{L}_F = & i \sum_j \bar{\psi}_L^j \gamma^\mu \left[\partial_\mu + ig\mathbf{W}_\mu \cdot \mathbf{T} + ig'Y_L \frac{1}{2}B_\mu \right] \psi_L^j + \\ & i \sum_j \bar{\psi}_R^j \left[\partial_\mu - g'Y_R B_\mu \right] \psi_R^j - \frac{1}{4}\mathbf{W}_{\mu\nu} \cdot \mathbf{W}^{\mu\nu} - \frac{1}{4}B_{\mu\nu} \cdot B^{\mu\nu}, \end{aligned} \quad (2.7)$$

where repeated indices are summed over. This model is called the unified electroweak theory, developed by Glashow [1], Weinberg [2] and Salam [3].

2. Top Quark Physics at Hadron Colliders

2.1.1.1. Higgs mechanism

Introducing mass terms to the $SU(2)_L \times U(1)_Y$ gauge group violates gauge invariance. However, for the electroweak theory the W^\pm and Z bosons need to be massive. To achieve this, the Higgs mechanism [5–9] is used by adding four scalar fields to the theory in form of an isospin doublet with hypercharge $Y = 1$:

$$\Phi = \begin{bmatrix} \Phi^+ \\ \Phi^0 \end{bmatrix} = \frac{1}{\sqrt{2}} \begin{bmatrix} \Phi_1 + i\Phi_2 \\ \Phi_3 + i\Phi_4 \end{bmatrix}. \quad (2.8)$$

Considering the (required) coupling to the doublets and the degrees of freedom this is the minimal choice for this theory. The scalar Higgs potential has the form

$$V(\Phi^\dagger\Phi) = \mu^2\Phi^\dagger\Phi + \lambda(\Phi^\dagger\Phi)^2, \quad (2.9)$$

where the first term contains the mass $m = \sqrt{-\mu^2}$ and the second term corresponds to a self-interaction. To the Lagrangian \mathcal{L}_1 in Eq. 2.7 the term $\mathcal{L}_H = |D_\mu\Phi|^2 - V(\Phi^\dagger\Phi)$ is added. The parameters of the potential can be chosen such that its vacuum expectation value is different from zero:

$$|\Phi_{\text{vac}}| = \sqrt{-\frac{1}{2}\mu^2/\lambda}, \quad (2.10)$$

where $\mu^2 < 0$ and $\lambda > 0$. Hence, a possible choice for the components is:

$$\Phi_1 = \Phi_2 = \Phi_4 = 0, \quad \Phi_3 = -\frac{\mu^2}{\lambda} \equiv v^2. \quad (2.11)$$

The complex scalar field Φ is now expanded around this minimum such that $v \rightarrow v + h(x)$. The vacuum fluctuations are parametrised by three real scalar fields and the real scalar field $h(x)$. Substituting these into the Lagrangian and enforcing local gauge invariance, results in breaking the symmetry of the Lagrangian. According to the Goldstone theorem [27], with four scalar fields and three broken symmetries one obtains three Goldstone bosons and one massive Higgs boson. The Goldstone bosons can be identified with the longitudinal polarisation components of the $SU(2)_L$, W^i . Usually, one rewrites the fields in terms of the three massive vector bosons W^\pm and Z and a massless vector boson, the photon A . One finds that they are mixtures of the original fields \mathbf{W}_μ and B_μ :

$$W_\mu^\pm = (W_\mu^1 \mp iW_\mu^2)/\sqrt{2}, \quad (2.12)$$

$$\begin{pmatrix} A_\mu \\ Z_\mu \end{pmatrix} = \begin{pmatrix} \cos\theta_W & \sin\theta_W \\ -\sin\theta_W & \cos\theta_W \end{pmatrix} \begin{pmatrix} B_\mu \\ W_\mu^3 \end{pmatrix}. \quad (2.13)$$

The Weinberg angle θ_W is defined as the ratio of coupling constants

$$\tan\theta_W := \frac{g'}{g}. \quad (2.14)$$

2.1. The top quark in the Standard Model

After this rewriting the theory remains $SU(3) \times U(1)$ invariant. The $U(1)$ symmetry now corresponds to the electrical charge. For the $SU(3)$ symmetry see the discussion of Quantum Chromodynamics (QCD) in Sec. 2.1.2.

By adding Yukawa interaction terms [28] of the lepton and Higgs field to the Lagrangian, lepton masses can also be generated by spontaneous symmetry breaking. Similarly, this applies for quarks. However, for these and for massive neutrinos both, the members of the lower and the upper weak isospin doublet, have to acquire mass. Therefore an additional conjugate Higgs multiplet has to be constructed, which transforms in the same way as Φ , but has hypercharge $Y = -1$. After spontaneous symmetry breaking, the Yukawa terms produce mass terms for the quarks, which can be described by mass matrices in generation space, each depending on nine complex parameters:

$$\begin{aligned} \overline{(u_1, u_2, u_3)_R} \mathcal{M}^u \begin{pmatrix} u_1 \\ u_2 \\ u_3 \end{pmatrix}_L + \text{hermitian conjugate,} \\ \overline{(d_1, d_2, d_3)_R} \mathcal{M}^d \begin{pmatrix} d_1 \\ d_2 \\ d_3 \end{pmatrix}_L + \text{hermitian conjugate,} \end{aligned} \quad (2.15)$$

where the u_i and the d_i are the weak eigenstates of the i -th generation. The mass matrices, \mathcal{M}^i , are non-diagonal but can be diagonalised by unitary transformations. This changes the basis from weak eigenstates to mass eigenstates, which are identical to the flavour eigenstates u, c, t and d, s, b . In charged current interactions, this leads to transitions between mass eigenstates of different generations. By setting the weak and mass eigenstates equal for the up-type quarks, one can assign the mixing entirely to the down-type quarks such that:

$$\begin{pmatrix} d' \\ s' \\ b' \end{pmatrix} = \mathbf{V} \begin{pmatrix} d \\ s \\ b \end{pmatrix}_L = \begin{pmatrix} V_{ud} & V_{us} & V_{ub} \\ V_{cd} & V_{cs} & V_{cb} \\ V_{td} & V_{ts} & V_{tb} \end{pmatrix} \begin{pmatrix} d \\ s \\ b \end{pmatrix}_L, \quad (2.16)$$

where d', s' and b' are the weak eigenstates. The mixing matrix \mathbf{V} is called the Cabibbo-Kobayashi-Maskawa (CKM) matrix [29]. The absolute values of its entries can be measured independently, but most precisely determined by a global fit that uses all available measurements. Requiring three generations of quarks and unitarity of the matrix yields the following absolute values [10, 30, 31]:

$$\mathbf{V}_{\text{CKM}} = \begin{pmatrix} 0.97428 \pm 0.00015 & 0.2253 \pm 0.0007 & 0.00347 \begin{smallmatrix} + 0.00016 \\ - 0.00012 \end{smallmatrix} \\ 0.2252 \pm 0.0007 & 0.97345 \begin{smallmatrix} + 0.00015 \\ - 0.00016 \end{smallmatrix} & 0.0410 \begin{smallmatrix} + 0.0011 \\ - 0.0007 \end{smallmatrix} \\ 0.00862 \begin{smallmatrix} + 0.00026 \\ - 0.00020 \end{smallmatrix} & 0.0403 \begin{smallmatrix} + 0.0011 \\ - 0.0007 \end{smallmatrix} & 0.999152 \begin{smallmatrix} + 0.000030 \\ - 0.000045 \end{smallmatrix} \end{pmatrix}. \quad (2.17)$$

One observes large couplings close to 1 within the same generation (diagonal entries) whereas the off-diagonal entries are significantly smaller. With three quark generations,

2. Top Quark Physics at Hadron Colliders

the unitarity requirement and taking into account that the quark phases cannot be measured the number of independent parameters of the matrix is reduced to four: three mixing angles between the quark generations and one complex phase that accounts for CP violation. Analogously, there exists a matrix describing the leptonic mixing, the Pontecorvo-Maki-Nakagawa-Sakata (PMNS) matrix [32, 33]. It also contains four independent parameters if one assumes that neutrinos are not Majorana particles.

2.1.1.2. Observation of a particle compatible with the production and decay of the Standard Model Higgs boson

The search for the massive Higgs boson as a result of the spontaneous symmetry breaking as described above has been long and tedious. In summer 2012, however, both the ATLAS and the CMS experiment announced the observation of a particle compatible with the production and decay of the Standard Model Higgs boson [34, 35] in data taken in 2011 and 2012. The combination of the search channels $H \rightarrow ZZ^{(*)}$, $H \rightarrow \gamma\gamma$, $H \rightarrow WW^{(*)}$, $H \rightarrow b\bar{b}$ and $H \rightarrow \tau\tau$, the latter two exploited by CMS only in the first publication, led to an excess of events above the expected background around a mass of 125 GeV. The CMS result yields a local significance of 5.0σ with a global significance of 4.6σ using a Higgs mass search range of $115 \text{ GeV} < m_H < 130 \text{ GeV}$. For ATLAS, the local significance is found to be 5.9σ with a global significance of 5.1σ ($100 \text{ GeV} < m_H < 600 \text{ GeV}$). A fit to the signal in the decay modes with the highest mass resolution, $H \rightarrow ZZ^{(*)}$ and $H \rightarrow \gamma\gamma$, gives a mass of $125.3 \pm 0.4 \text{ (stat.)} \pm 0.5 \text{ (syst.) GeV}$ (CMS) and $126.0 \pm 0.4 \text{ (stat.)} \pm 0.4 \text{ (syst.) GeV}$ (ATLAS). The observed decay into two photons indicates that the new particle is a boson with spin different from one. Although the results are compatible with a SM Higgs boson, more data is needed for conclusive evidence. The local p -values and corresponding significances as a function of the Higgs mass are shown in Fig. 2.1 for both experiments.

2.1.2. Quantum Chromodynamics

Quantum Chromodynamics (QCD) describes the strong interactions of coloured quarks and gluons and is the $SU(3)_C$ component of the Standard Model, where C denotes the colour. The Lagrangian is given by

$$\mathcal{L}_{\text{QCD}} = \sum_q \bar{\psi}_{q,a} (i\gamma^\mu \partial_\mu \delta_{ab} - g_s \gamma^\mu t_{ab}^C \mathcal{A}_\mu^C - m_q \delta_{ab}) \psi_{q,b} - \frac{1}{4} F_{\mu\nu}^A F^{A\mu\nu}. \quad (2.18)$$

As before, repeated indices are summed over. Since quarks come in three colours, the quarks spinor fields $\psi_{q,a}$ for a quark of flavour q and mass m_q have an additional colour-index a that runs from 1 to 3 (usually identified with red, green, blue). One can observe similarities to the Lagrangian of electroweak theory before symmetry breaking as given in Eq. 2.7, but due to the different Lie group the gauge field \mathcal{A}_μ^C corresponds to the eight gluons fields, since C runs from 1 to $N_c^2 - 1 = 8$. Each gluon carries one unit of colour and one unit of anticolour. The generators, t_{ab}^C , of the $SU(3)$ colour group are eight 3×3 matrices that rotate the quark's colour in a quark-gluon interaction, i.e. colour is

2.1. The top quark in the Standard Model

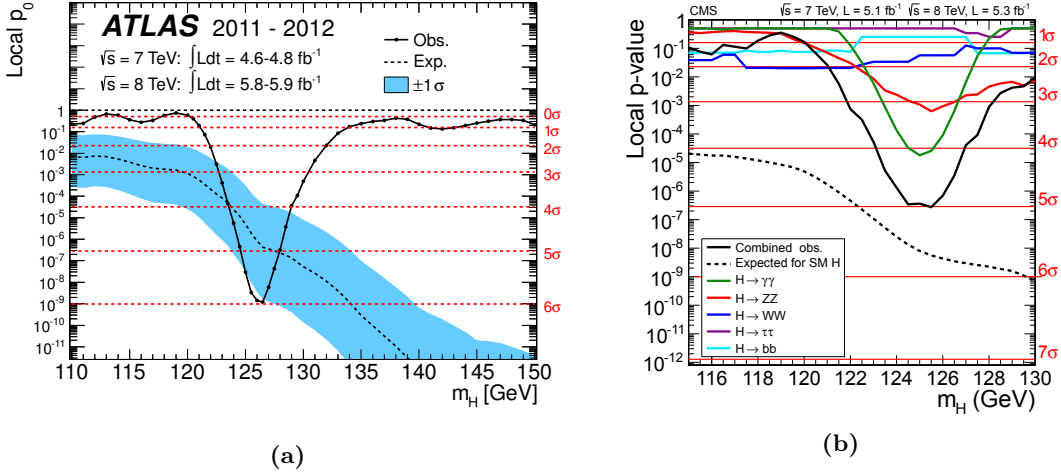


Figure 2.1.: Observed local p -value (solid line) for data as a function of the SM Higgs boson mass for (a) the ATLAS experiment, and (b) the CMS experiment, also showing the individual channels. The dashed line shows the expected local p -values for a SM Higgs boson with a mass m_H . The horizontal red lines indicate the significances corresponding to the p -values. [34, 35]

conserved. The strong coupling constant is g_s and the field tensor is given by

$$F_{\mu\nu}^A = \partial_\mu A_\nu^C - \partial_\nu A_\mu^C - g_s f_{ABC} A_\mu^B A_\nu^C, \quad (2.19)$$

where f_{ABC} are the structure constants of the $SU(3)$ group. As $[t^A, t^B] = if_{ABC} t^C$ the group is non-Abelian. The fundamental parameters of QCD are the coupling g_s , often written in terms of $\alpha_s = \frac{g_s^2}{4\pi}$, and the quark masses m_q .

2.1.2.1. Running coupling

If one wants to describe high energy reactions within the Standard Model, one can read off the allowed interactions from the Lagrangian and represent them in Feynman diagrams. Using Feynman rules, one can compute the transition amplitudes for a given process from a set of initial state particles to a set of final state particles. More details can be found in the literature, e.g. Refs. [36, 37], and in Sec. 2.2.2.

Diagrams with few interactions usually yield the largest contributions whereas so-called higher order contributions are suppressed by additional factors of the respective coupling constants (for couplings less than 1). Sorting the diagrams by the factors of the coupling constants and calculating them to a certain order is called perturbation theory. However, higher order diagrams generally contain loops. Integration over all possible momenta of these internal lines naively causes divergences. In order to obtain finite predictions, the theory is renormalised which cancels the divergent terms. In the framework of perturbative QCD, predictions for observables are expressed in terms of

2. Top Quark Physics at Hadron Colliders

the renormalised coupling $\alpha_s(\mu_R^2)$, a function of an (unphysical) renormalisation scale μ_R . Choosing μ_R close to the scale of the momentum transfer Q in a given process gives an indication of the effective strength of the strong interaction in that process. The coupling satisfies the renormalisation group equation:

$$\mu_R^2 \frac{d\alpha_s}{d\mu_R^2} = \beta(\alpha_s) = -(b_1\alpha_s^2 + b_2\alpha_s^3 + b_3\alpha_s^4 + \dots), \quad (2.20)$$

where the b_i are the i -loop β -function coefficients. The b_i depend on the number of quark flavours and for sixteen or less flavours the strong coupling gets smaller for processes that involve large momentum transfer (hard processes), see Sec. 2.2.4, the so-called asymptotic freedom [38, 39]. Furthermore, for energies approaching zero, the coupling tends to infinity. This means that the further away a quark is pulled from another one, the stronger the force gets. As a consequence, quarks cannot exist as free particles. This is generally referred to as colour-confinement [40]. Instead, they form bound colour-singlet states called hadrons, consisting of either a quark and an antiquark (mesons) or three quarks or antiquarks (baryons).

The exact leading order solution for Eq. 2.20 can be obtained by neglecting all but the b_0 term giving $\alpha_s(Q^2) = b_0 \ln(Q^2/\Lambda_{\text{QCD}}^2)$. Here Q is the momentum transfer of the process and Λ_{QCD} is a constant of integration corresponding to the scale where the perturbatively-defined coupling would diverge, i.e. it is the non-perturbative scale of QCD.

2.1.3. Model predictions of top quark properties

In total, the Standard Model comprises 25 a priori unknown parameters that need to be determined by experiment. These are eight parameters for CKM and PMNS mixing matrices discussed in Sec. 2.1.1.1, twelve Yukawa couplings for the fermion masses and two parameters from electroweak symmetry breaking (see also Sec. 2.1.1.1). Three further parameters are the coupling constants α_s , g and g' of $SU(3)_C$, $SU(2)_L$ and $U(1)_Y$, respectively. All physical observables can be expressed in terms of these parameters and therefore predictions can be made.

Historically, the SM contained fewer than three generations of quarks and leptons. The quark model consisting only of up, down and strange quarks was only proposed in 1964 [41, 42]. However, experimentally it has been found that flavour changing neutral currents are strongly suppressed. To explain this circumstance, the GIM mechanism [43] was introduced, which at the same time postulated the existence of a charm quark completing the second quark generation.

The discovery of the τ -lepton [44] initiated a third generation of particles. Shortly after, the heavy Υ meson was discovered [45]. When it was realised that it consisted of a new quark-antiquark pair ($b\bar{b}$) the doublet structure of the Standard Model (see Sec. 2.1.1) and the GIM mechanism strongly suggested the existence of a third neutrino and the existence of a sixth quark, called top quark.

A further argument supporting the need for a complete third quark generation comes from perturbation theory and the desire to obtain a renormalisable gauge theory of weak

interactions. This part of the Standard Model can be shown to be renormalisable, if the sum of the weak hypercharges, Y_i , of all left-handed fermions vanishes [46–48]. Since lepton multiplets contribute a value of -2 and quark multiplets of $+2/3$ (see Tab. 2.1) the sum only adds up to zero if every quark exists in three colour versions and the number of quarks and leptons are the same (see also further discussion in [18]).

The most compelling experimental arguments for the existence of the top quark come from the measurements of the properties of the b quark and the b hadrons. By relating the leptonic width of the Υ meson to the charge of the constituent b quark at the electron-positron storage ring DORIS at DESY [49–51], the electric charge of the b quark has been found to be close to $-1/3$. Knowing its charge, the isospin can be measured by studying the $Zb\bar{b}$ vertex near the Z resonance [52] and determining the weak vector and axial-vector coupling of the b quark to the Z boson. The LEP measurement of the partial decay width of the Z boson to $b\bar{b}$ to the total hadronic decay width rules out the hypothesis of an isosinglet b quark. Additionally, the weak isospin has been obtained via the forward-backward asymmetry of muon production in the process $e^+e^- \rightarrow b\bar{b} \rightarrow \mu^\pm + \text{hadrons}$ with the JADE detector at PETRA [53]. This asymmetry would vanish for a weak isospin singlet, but takes up sizeable values for a $I_3 = -\frac{1}{2}$ and $Q = -\frac{1}{3}$ b quark. The measurement is in good agreement with the doublet prediction. This therefore implies that the b quark must have a weak isospin partner, i.e. the top quark with $I_3 = +\frac{1}{2}$.

2.1.3.1. Top quark mass

As discussed in the previous Sec. 2.1.3, one can employ some Standard Model parameters to determine or restrict others. The top quark mass, however, is not predicted. First indications of a very high top quark mass compared to the other quarks (see e.g. [54]) have been found in the analysis of $B^0\bar{B}^0$ oscillations by the ARGUS experiment [55]. Nevertheless, the strongest constraints on the top quark mass can be inferred from the calculation of radiative corrections to electroweak processes [56, 57] where m_t enters as a parameter. Radiative corrections denote higher order contributions to a perturbation series, for instance for the W mass:

$$m_W = \frac{\pi\alpha}{\sqrt{2}G_F} \cdot \frac{1}{\sin^2\theta_W(1-\Delta r)}, \quad (2.21)$$

where G_F is the Fermi constant, Δr are electroweak corrections and θ_W is the Weinberg or electroweak mixing angle (see also Sec. 2.1.1.1) defined via the vector boson masses:

$$\sin^2\theta_W = 1 - \frac{m_W^2}{m_Z^2}. \quad (2.22)$$

The corrections to the W mass from single-loop insertions containing the top quark as depicted in Fig. 2.2 are:

$$\Delta r^{\text{top}} = -\frac{3\sqrt{2}G_F \cot^2\theta_W}{16\pi^2} \cdot m_t^2 \quad (\text{for } m_t \gg m_b). \quad (2.23)$$

2. Top Quark Physics at Hadron Colliders

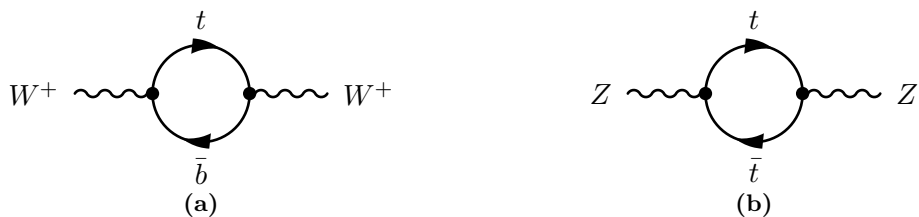


Figure 2.2.: Radiative corrections to the (a) W and (b) Z propagator with top quark contribution.

Also, the Higgs boson contributes to Δr via the one-loop diagrams shown in Fig. 2.3 in the form of:

$$\Delta r^{\text{Higgs}} = \frac{3\sqrt{2}G_F m_W^2}{16\pi^2} \cdot \left(\ln \frac{m_H^2}{m_Z^2} - \frac{5}{6} \right). \quad (2.24)$$

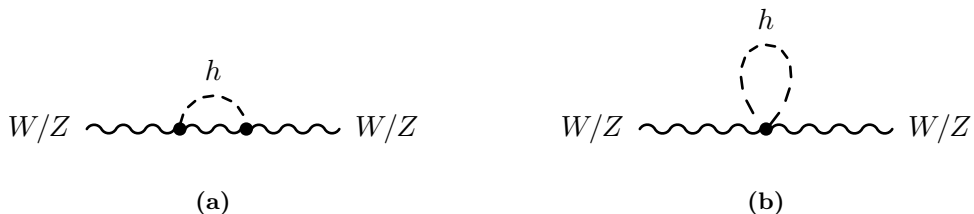


Figure 2.3.: Radiative corrections to the W and Z propagator with Higgs boson contribution.

Compared to the quadratic dependence on m_t , one observes a much weaker logarithmic m_H dependence. With the other parameters being measured to high precision, one can indirectly predict the top quark mass. One year before the discovery of the top quark by the Tevatron experiments CDF and D0 [58, 59] the prediction for the top quark mass combined from data of several experiments by the LEP Electroweak Working Group had been $178 \pm 11^{+18}_{-19}$ GeV [60], illustrated in Fig. 2.4a. The latest mass prediction from electroweak precision data, yielding 179^{+12}_{-9} GeV without using constraints on the Higgs Boson mass [61], is in good agreement with the current Tevatron average mass of 173.2 ± 0.9 GeV [62]. A graphical representation of this is shown in Fig. 2.4b.

It has to be noted that the top quark mass is like all parameters of the SM a convention dependent parameter. As the top quark does not hadronise (see Sec. 2.2.6), it is usually considered as a highly unstable bare fermion. Therefore one usually uses the on-shell or pole mass, which is the real part of the complex-valued pole of the quark propagator (see e.g. discussion in [19]). This concept can only be treated in perturbation theory, since a quark cannot be observed freely (see 2.1.2.1), i.e. its propagator has no pole. In finite-order perturbation theory there is a pole at $(m_t - i\Gamma_t/2)$, where m_t is the pole mass and Γ_t the decay width of the top quark. There is, however, an ambiguity of $\mathcal{O}(\Lambda_{\text{QCD}})$ associated with this definition. Therefore, it is theoretically often preferred to use so-called short-distance masses that are non-ambiguously defined, for instance the

2.1. The top quark in the Standard Model

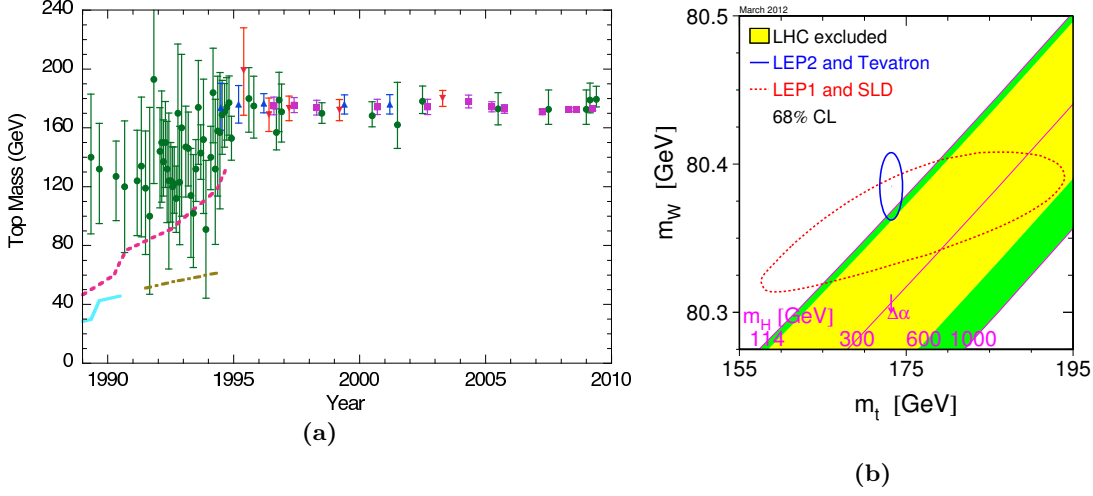


Figure 2.4.: (a) Comparison of the indirect top mass measurements via radiative corrections (green circles) and 95% confidence-level lower bounds on the top-quark mass inferred from direct searches in e^+e^- annihilations (solid line) and in $p\bar{p}$ collisions (broken and dot-dashed line) with direct measurements (triangles) from $D0$ (red) and CDF (blue) and the Tevatron average (magenta squares) from direct observations vs. time [63]. (b) Contour curves of 68% probability in the (m_t, m_W) plane. The dotted line encloses the area preferred by the Standard Model fit to data from $LEP1$ and SLD . The full line indicates the result of the $LEP2$, $UA2$ and Tevatron m_W measurements and the direct m_t mass measurement. The plot also shows the Standard Model relationship of the masses as a function of the Higgs boson [64].

quark mass $\bar{m}_q(\mu_R)$ defined in the $\overline{\text{MS}}$ renormalisation scheme, where μ_R denotes the renormalisation scale. The relation between pole and the $\overline{\text{MS}}$ is known from QCD to $\mathcal{O}(\alpha_s^3)$. At $\mu_R = \bar{m}_t$ it yields [19]:

$$\bar{m}_t(\bar{m}_t) = m_t \left(1 + \frac{4}{3} \frac{\alpha_s}{\pi} + 8.2364 \left(\frac{\alpha_s}{\pi} \right)^2 + 73.638 \left(\frac{\alpha_s}{\pi} \right)^3 + \mathcal{O}(\alpha_s^4) \right), \quad (2.25)$$

where $\alpha_s(\mu_R = \bar{m}_t)$ is the $\overline{\text{MS}}$ coupling of six-flavour QCD. Using $\alpha_s = 0.109$ one obtains

$$\frac{m_t}{\bar{m}_t} = 1.06, \quad (2.26)$$

i.e. the $\overline{\text{MS}}$ mass for $m_t = 172.5$ GeV is about 10 GeV lower. The interpretation of experimental results and their comparison to theory is still under discussion. In the following, m_t always refers to the pole mass.

2.2. Top quark production in pp collisions

The production of top quarks requires a very high centre of mass energy, \sqrt{s} , which is set by the mass of the top quark. In this section the calculation of production cross sections is discussed. The two basic production modes of top quarks at the Large Hadron Collider (LHC) are detailed. These are top quark pair production through strong interactions and the production of single top quarks. Furthermore, their decay topology is described.

2.2.1. Cross sections

The production of top quarks at the LHC occurs in particle collisions, i.e. scattering processes. The incoming particles collide, interact with each other, and the resulting outgoing particles are measured. The theoretical description of scattering and decay processes is given by quantum mechanical transition probabilities. The probability of an initial state $|i\rangle$ with four-momenta p_k transforming into an final state $|f\rangle$ with four-momenta p'_k is mediated by the absolute square of the elements of the so-called S -matrix (scattering matrix). These are written in terms of an invariant amplitude $-i\mathcal{M}$ that is process-dependent. Using the notation of [10], the S -matrix e.g. for a $2 \rightarrow 2$ scattering process is related to \mathcal{M} by:

$$\langle p'_1 p'_2 | S | p_1 p_2 \rangle = \mathbb{1} - i(2\pi)^2 \delta^4(p_1 + p_2 - p'_1 - p'_2) \cdot \frac{\mathcal{M}(p_1, p_2; p'_1, p'_2)}{(2E_1)^{1/2} (2E_2)^{1/2} (2E'_1)^{1/2} (2E'_2)^{1/2}}, \quad (2.27)$$

where $\mathbb{1}$ is the unit matrix and the E_k denote the energies of the particles. The state normalisation is such that:

$$\langle p' | p \rangle = (2\pi)^3 \delta^3(\mathbf{p} - \mathbf{p}'). \quad (2.28)$$

Several different particles can be created in a scattering process. Depending on their properties, these can decay further into other particles. Using Fermi's Golden Rule, the partial decay rate of a particle of four-momentum p_1 and mass m into n bodies in its rest frame is given by:

$$d\Gamma = \frac{(2\pi)^4}{2m} |\mathcal{M}|^2 d\Phi_n(p_1; p_2, \dots, p_{n+1}), \quad (2.29)$$

where $d\Phi_n$ is an element of n -body phase space given by:

$$d\Phi_n(p_1; p_2, \dots, p_{n+1}) = \delta^4\left(p_1 - \sum_{k=2}^{n+1} p_k\right) \prod_{k=1}^{n+1} \frac{d^3 p_k}{(2\pi)^3 2E_k}. \quad (2.30)$$

With these definitions the differential cross section can be written as:

$$d\hat{\sigma} = \frac{(2\pi)^4 |\mathcal{M}|^2}{4\sqrt{(p_1 \cdot p_2)^2 - m_1^2 m_2^2}} \cdot d\Phi_n(p_1 + p_2; p_3, \dots, p_{n+2}). \quad (2.31)$$

The total cross section is obtained by integrating over phase space. The cross section contains information about the form of the interaction potential and the coupling strength. One can therefore directly relate reaction rates and energy and angular distributions to the cross section and compare theory and experiment. Further details can e.g. be found in [36, 65].

2.2.2. Factorisation ansatz

The cross section ansatz described in the previous section cannot directly be applied to the LHC since the LHC collides hadrons, which are composite particles. In order to calculate cross sections for these processes the so-called parton model is used. Hadrons are regarded as a composition of quarks and gluons, which share the longitudinal hadron momentum. According to the factorisation theorem [66, 67], the hadron itself is described by the whole particle composition interacting on a soft binding energy scale, whereas the collisions occur between the partons on a hard energy scale with large transverse momenta. The differential cross section for a process (e.g. for $t\bar{t}$ production) is then given by the convolution of parton distribution functions (PDF), $f_i(x, Q^2)$, for the colliding hadrons (A, B) at an energy scale Q^2 and the hard parton-parton cross sections $d\hat{\sigma}_{ij}$ (refer to Sec. 2.2.1) of all combinations of two partons i and j :

$$d\sigma(AB \rightarrow t\bar{t}) = \sum_{i,j} \int dx_i dx_j f_{i,A}(x_i, \mu_F^2) f_{j,B}(x_j, \mu_F^2) d\hat{\sigma}_{ij}(ij \rightarrow t\bar{t}; \hat{s}, \mu_F, \mu_R, \alpha_s(\mu_R)), \quad (2.32)$$

where x_i denotes the longitudinal momentum fraction of the parton and

$$\hat{s} = (x_i p_A + x_j p_B)^2 \stackrel{(m=0)}{\approx} 2x_i x_j p_A \cdot p_B = x_i x_j s \quad (2.33)$$

is the square of the centre of mass energy of the colliding partons. The parton distribution function $f_{i,A}(x_i, \mu_F^2)$ yields the probability to find a given parton i inside a hadron A with momentum fraction x_i when probed at an energy scale μ_F^2 , where μ_F^2 is the momentum transfer squared for the process (see also Sec. 2.2.3). The factorisation scale μ_F and the renormalisation scale μ_R (see Sec. 2.1.2.1) are usually set equal to the typical momentum scale of the hard scattering process, e.g. for top $\mu = \mu_F = \mu_R = m_t$. To test the μ -dependence of the cross section, the scale is by convention typically varied independently for μ_F and μ_R between $\mu_{\min} = \mu/2$ and $\mu_{\max} = 2\mu$ and the largest deviations are quoted excluding the points where μ_F and μ_R are both at the minimum and maximum values.

The partonic cross sections can be expanded in a fixed-order series in the strong coupling constant $\alpha_s(\mu_R)$ as

$$d\hat{\sigma}_{ij} = \alpha_s^2 \left(d\hat{\sigma}_{ij}^{(0)} + \frac{\alpha_s}{\pi} d\hat{\sigma}_{ij}^{(1)} + \frac{\alpha_s^2}{\pi^2} d\hat{\sigma}_{ij}^{(2)} \dots \right), \quad (2.34)$$

where the first term in brackets is referred to as leading order (LO), the second term as next-to-leading order (NLO), the third term as next-to-next-to-leading order (NNLO),

and so on.

2.2.3. Parametrisations of parton distribution functions

Parton distribution functions (PDFs) are used to describe the soft part of the interaction, i.e. the particle composition inside the hadron. As this interaction corresponds to small momentum transfer and therefore to large α_s values, it cannot be described by perturbative QCD, but is described differently as follows.

The PDFs are extracted from measurements in deep-inelastic scattering experiments where elementary leptons collide with composite nucleons and related hard scattering data using parameterisations at a low energy scale Q_0^2 ($\approx 1\text{--}7 \text{ GeV}^2$). Most of the parameterisations of proton PDFs now used for the LHC have been extracted from the ZEUS [68] and H1 [69] experiments in electron-proton collisions at the HERA collider and fixed target experiments. The more recent parameterisations also take into account vector boson production and single-inclusive jet production from the Tevatron experiments. Once measured for a certain momentum fraction x_i at an energy scale Q^2 , they can be extrapolated to another scale using the DGLAP (Dokshitzer-Gribov-Lipatov-Altarelli-Parisi) evolution equation [70–72]. Furthermore, assuming based on the factorisation theorem that the PDFs do not depend on the process they have been derived from, they can be used for the calculation of any other hard scattering process.

The PDF sets used for signal simulation samples in these analyses (see Sec. 5.4.1) are provided by the CTEQ/CT group [73, 74] derived at NLO using the \overline{MS} renormalisation scheme [54]. This set especially incorporates the effects of Tevatron Run I jet production data on the gluon distribution and is therefore expected to describe the mainly gluon based LHC processes realistically. The CT sets additionally include combined data set of HERA-1 data and new data on the asymmetry in the rapidity distribution of the charged lepton from W boson decay from CDF and rapidity distributions of Z bosons from both CDF and D0 (see [74] for more details). An example of the most important parton distributions inside the proton is shown in Fig. 2.5. From this figure one can extract that the gluons start to dominate the x -region below 0.11. The central values for the CT10 set only differ at very large x and are therefore not shown.

To produce a top quark, the squared centre of mass energy at parton level as given in Equation 2.33 therefore has to be at least equal to m_t^2 , for top pair production equal to $(2m_t)^2$. Assuming $x_i \approx x_j =: x_{\text{threshold}}$ yields the threshold for production at the LHC ($\sqrt{s} = 7 \text{ TeV}$, see Sec. 3.1):

$$x_{\text{threshold}} = \sqrt{\frac{\hat{s}}{s}} = \frac{m_t}{\sqrt{s}} \approx 0.025. \quad (2.35)$$

The production threshold is at an x -value where the gluon density dominates over the quark density.

2.2. Top quark production in pp collisions

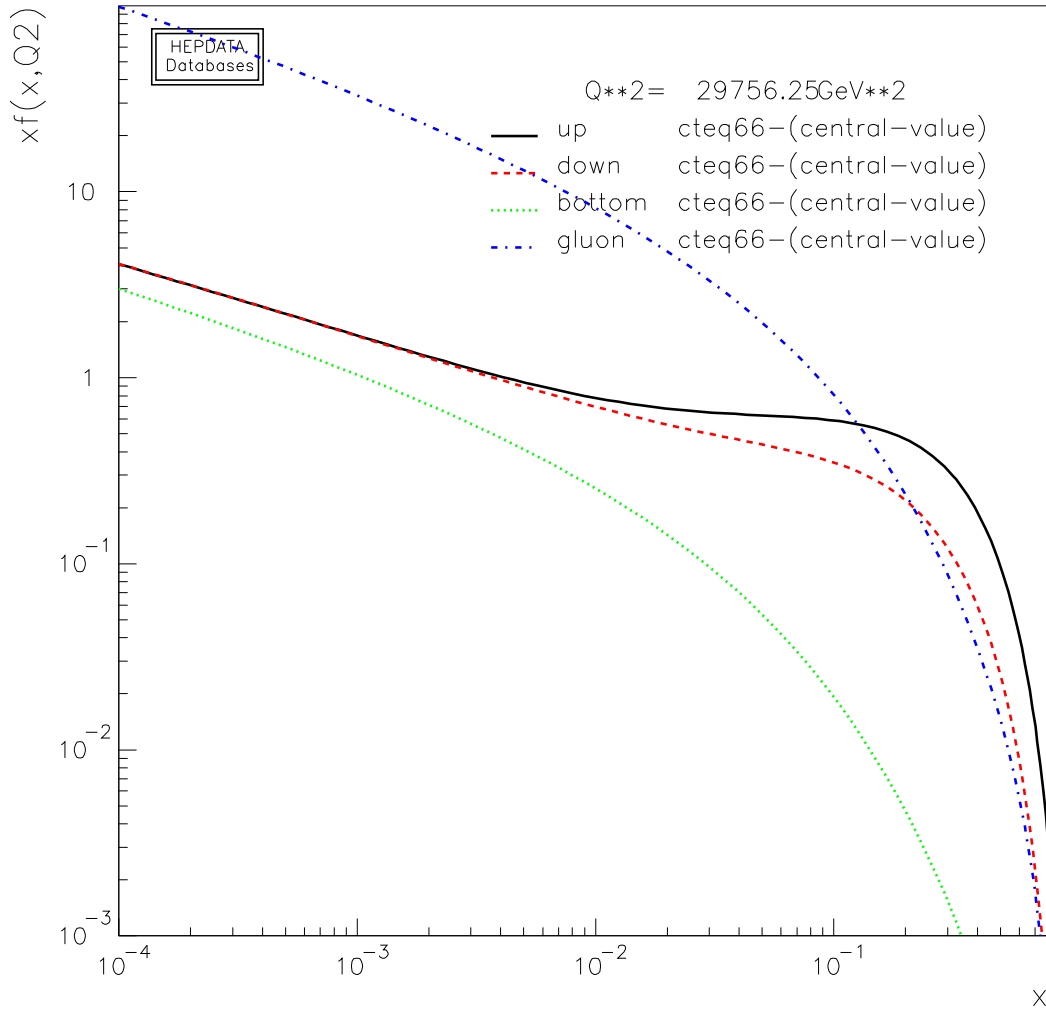


Figure 2.5.: CTEQ6.6 [73] central value parton distribution functions at the top quark mass scale ($Q^2 = (172.5 \text{ GeV})^2$) for up, down and bottom quarks and gluons in the proton in double-logarithmic scale. [75]

2.2.4. $t\bar{t}$ production and cross section prediction

Top quark antiquark pair, $t\bar{t}$, production is the dominant production process for top quarks at the LHC since it happens in strong interactions. The leading order Feynman diagrams are shown in Fig. 2.6. Using the knowledge from the previous section it becomes clear that gluon-gluon fusion dominates over quark-antiquark production with a share of about 80% at a centre of mass energy of 7 TeV [76]. Gluon-quark initial states are possible at next-to-leading order (NLO).

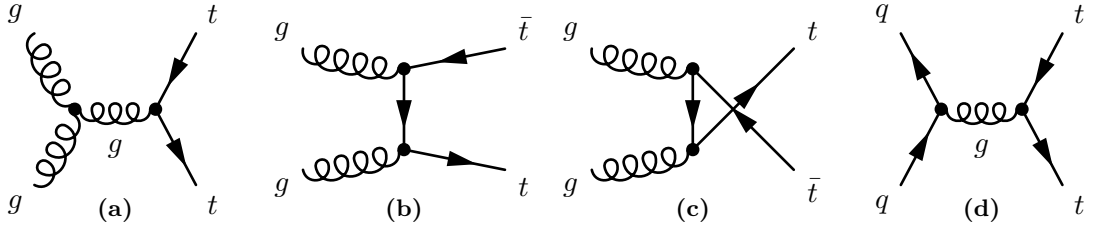


Figure 2.6.: Feynman diagrams of the leading order processes for $t\bar{t}$ production: (a)-(c) gluon-gluon fusion and (d) quark-antiquark annihilation.

The leading order cross section calculations at Born level for heavy quark production exist since the late 1970s [77], mostly concerning charm quark production. The differential cross section for the gluon-gluon fusion process is given by [78]:

$$\begin{aligned}
 \frac{d\hat{\sigma}}{d\hat{t}}(g_1 g_2 \rightarrow t\bar{t}) = & \frac{\pi \alpha_s^2}{8 \hat{s}^2} \cdot \left[\frac{6(m_t^2 - \hat{t})(m_t^2 - \hat{u})}{\hat{s}^2} - \frac{m_t^2(\hat{s} - 4m_t^2)}{3(m_t^2 - \hat{t})(m_t^2 - \hat{u})} \right. \\
 & + \frac{4}{3} \cdot \frac{(m_t^2 - \hat{t})(m_t^2 - \hat{u}) - 2m_t^2(m_t^2 + \hat{t})}{(m_t^2 - \hat{t})^2} \\
 & + \frac{4}{3} \cdot \frac{(m_t^2 - \hat{t})(m_t^2 - \hat{u}) - 2m_t^2(m_t^2 + \hat{u})}{(m_t^2 - \hat{u})^2} \\
 & - 3 \cdot \frac{(m_t^2 - \hat{t})(m_t^2 - \hat{u}) - m_t^2(\hat{u} - \hat{t})}{\hat{s}(m_t^2 - \hat{t})} \\
 & \left. - 3 \cdot \frac{(m_t^2 - \hat{t})(m_t^2 - \hat{u}) - m_t^2(\hat{t} - \hat{u})}{\hat{s}(m_t^2 - \hat{u})} \right]. \tag{2.36}
 \end{aligned}$$

The variables \hat{s} , \hat{t} and \hat{u} are the Lorentz-invariant Mandelstam variables. They are defined as $\hat{s} = (p_{g1} + p_{g2})^2$, $\hat{t} = (p_{g1} - p_t)^2$ and $\hat{u} = (p_{g1} - p_{\bar{t}})^2$, where p_{g_i} denotes the corresponding four-vector of the gluon i and m_t is the top quark mass. Using the same notation, the Born level differential cross section for quark-antiquark annihilation is given by:

$$\frac{d\hat{\sigma}}{d\hat{t}}(q\bar{q} \rightarrow t\bar{t}) = \frac{4\pi \alpha_s^2}{9 \hat{s}^4} \cdot \left[(m_t^2 - \hat{t})^2 + (m_t^2 - \hat{u})^2 + 2m_t^2 \hat{s} \right]. \tag{2.37}$$

2.2. Top quark production in pp collisions

Following the convention of [79], the total cross section can then be written as:

$$\sigma(s, m_t) = \frac{\alpha_s^2(\mu_R)}{m_t^2} \sum_{i,j} \int_{4m_t^2}^s \frac{d\hat{s}}{s} f_{ij} \left(\frac{\hat{s}}{s}, \mu_F \right) \hat{\sigma}_{ij} \left(\frac{4m_t^2}{\hat{s}}, \mu_F, \mu_R \right), \quad (2.38)$$

with the parton luminosities defined as

$$f_{ij}(y, \mu_F) = \int_y^1 \frac{dx}{x} f_{i,A}(x, \mu_F) f_{j,B}(y/x, \mu_F). \quad (2.39)$$

The perturbative calculation at NLO has been performed around 1990 [80, 81]. Since then several groups have developed and used techniques to predict the top quark pair cross section at approximate next-to-next-to-leading order (NNLO) using soft gluon resummation. The idea is to use properties of real radiation in the soft limit to calculate either an infinite set of logarithmic corrections to the partonic cross section or to determine only the logarithmic corrections to a certain accuracy in the fixed-order expansion. Soft limit in this context means that the variable of interest (e.g. the invariant mass of the $t\bar{t}$ system) in the differential cross section approaches the partonic centre of mass energy. At that threshold there is just enough energy to produce the top quark pair so that all other additionally radiated partons have to be soft. In the calculation of those large logarithms appear that need to be taken into account via resummation. Evaluating these terms far away from the threshold at NLO one has found that the leading terms in the soft limit give the largest contributions to the full result. Assuming that this is the case beyond NLO, the predictions using soft gluon resummation are a major improvement on the fixed-order expansion giving results close to NNLO precision, thus called approximate NNLO. The advantages and disadvantages of the different methods are reviewed in [79]. Only very recently a full calculation at NNLO has been made public for $q\bar{q} \rightarrow t\bar{t} + X$ [82] with an uncertainty of 2.7% and for $q\bar{q} \rightarrow t\bar{t}q\bar{q}$ [83] also reducing the uncertainties significantly. Since the dominant gluon-gluon fusion process is not yet available, these results are not used in this thesis. However, uncertainties are expected to be at most 6% [84]. The currently most precise predictions for pp collisions at a centre of mass energy of $\sqrt{s} = 7$ TeV are outlined in the following and summarised in Tab. 2.2.

2.2.4.1. Langenfeld, Moch and Uwer

The result of Langenfeld, Moch and Uwer [86, 87] is used as theoretical reference for the measurements presented in this work. As for all cross section predictions discussed in the following the group performs calculations at approximate NNLO. They include several different terms, such as next-to-next-to-leading-logarithm (NNLL) enhancements at production threshold, corrections from Coulomb terms in two-loops and scale dependent terms at NNLO. As a convenience, the calculations are provided as a function of the top quark mass and a parametrisation of the centre of mass energy \sqrt{s} valid from $3 \text{ TeV} \leq \sqrt{s} \leq 14 \text{ TeV}$. Using a top quark mass of $m_t = 172.5 \text{ GeV}$ and renormalisation and factorisation scales of $\mu = m_t$ and the PDF set CTEQ6.6 at 90% confidence level [85]

2. Top Quark Physics at Hadron Colliders

Table 2.2.: Cross sections for $t\bar{t}$ production at the LHC ($\sqrt{s} = 7$ TeV) as discussed in the text. The first uncertainty is related to scale uncertainties, and the second is the PDF error.

Cross-section [pb]	PDF set	Group
$166.8^{+4.7+5.1}_{-9.3-4.9}$	CTEQ6.6 [85]	Moch et al. [86, 87]
$166.6^{+4.3+7.2}_{-9.3-6.5}$	MSTW2008NNLO [88]	Moch et al. [86, 87]
$163.0^{+7}_{-5} \pm 9$	MSTW2008NNLO [88]	Kidonakis [89]
$155.0^{+8.0+8.0}_{-9.0-9.0}$	MSTW2008NNLO [88]	Ahrens et al. [90]
$162.6^{+7.4+15.4}_{-7.6-14.7}$	MSTW2008NNLO [88]	Beneke et al. [91]
$158.7^{+12.2+4.3}_{-13.5-4.4}$	MSTW2008NNLO [88]	Cacciari et al. [92]
$174.9^{+10.3+4.7}_{-13.2-4.8}$	MSTW2008NLO [88]	Moch et al. [93]
160^{+20+8}_{-21-9}	MSTW2008NLO [88]	NLO [79]

one obtains

$$166.8^{+4.7}_{-9.3}(\text{scale})^{+5.1}_{-4.9}(\text{PDF}) \text{ pb.} \quad (2.40)$$

The value has been calculated using `Hathor` 1.2 [94] and cross checked with the calculation of Cacciari et al. [92] mentioned later as implemented in `Top++` 1.0 [95]. This value is used for the first two measurements presented in this thesis since the signal Monte Carlo samples used employ the same PDF sets and top mass as outlined in Chapter 5. For the scale uncertainty the renormalisation and factorisation scales are varied by factors of two.

For the 2011 analysis (b) that uses the CT10 NLO set [74] a calculation using the MSTW2008 90% NNLO PDF sets [88] incorporating PDF+ α_s uncertainties is performed and cross checked as before. It yields

$$166.6^{+4.3}_{-9.3}(\text{scale})^{+7.2}_{-6.5}(\text{PDF}) \text{ pb.} \quad (2.41)$$

To obtain the full uncertainty, the PDF uncertainty is added in quadrature to the scale uncertainty following the MSTW prescription [96]. However, it is under discussion whether one should be more conservative and instead add the PDF and α_s uncertainties linearly, since the relation of these uncertainties to the scale uncertainties are unknown.

2.2.4.2. Kidonakis

Nikolaos Kidonakis resums soft-gluon corrections to the differential cross section at next-to-next-to-leading-logarithm (NNLL) accuracy via the two-loop soft anomalous dimension matrices [89]. A top quark mass of $m_t = 173$ GeV and the MSTW2008 90% NNLO PDF sets are used. The enhancement of the NLO cross section from the NNLO soft-gluon corrections is 7.6%, and leads to a reduction of the uncertainties of 15%. Thus,

the total cross section at approximate NNLO yields

$$163.0^{+7}_{-5}(\text{scale}) \pm 9(\text{PDF}) \text{ pb.} \quad (2.42)$$

2.2.4.3. Ahrens et al.

Ahrens and collaborators [90] also use higher-order corrections from soft gluon resummation at NNLL accuracy. They base their results on previous publications that apply threshold resummation using soft-collinear effective theory to $t\bar{t}$ production. Even though the approaches using single-particle inclusive and pair invariant-mass kinematics are used to describe different differential cross sections (see [79] for details) one can use them both to obtain the total hadronic cross section. By doing this one can estimate uncertainties that are due to power corrections to the soft limit. The total cross section is quoted as the average of the two and yields

$$155^{+8}_{-9}(\text{scale})^{+8}_{-9}(\text{PDF}) \text{ pb} \quad (2.43)$$

for a top quark mass of $m_t = 173.1$ GeV and the MSTW2008 PDFs.

2.2.4.4. Beneke, Falgari, Klein and Schwinn

Beneke et al. [91] combine the resummation of soft threshold logarithms and Coulomb corrections for the NNLL resummation. Their calculation accounts for bound-state corrections and higher-order Coulomb corrections not included in previous calculations based on summing threshold logarithms at fixed invariant mass. In contrast to the other calculations mentioned, Cacciari et al. resum the total cross section whereas the other groups perform resummation at differential level. For a pole mass of $m_t = 173.3$ GeV, the MSTW2008 90% PDFs and five sets of α_s variations [96] also entering the PDF uncertainty they obtain a total $t\bar{t}$ production cross section of

$$162.6^{+7.4}_{-7.6}(\text{scale})^{+15.4}_{-14.7}(\text{PDF}) \text{ pb.} \quad (2.44)$$

The inclusion of α_s variations leads to a higher PDF uncertainty with respect to the other predictions.

2.2.4.5. Cacciari et al.

Cacciari et al. [92] resum soft-gluon corrections to the total $t\bar{t}$ cross section at NNLL using Mellin N -space resummation. The resummation approach is very similar to Ref. [91] with the exception that Beneke et al. use momentum space resummation instead of N -space resummation the latter having some advantages (see also [79] for a discussion). With respect to the NLL approximation only a small decrease in the perturbative uncertainty is found. Using $m_t = 173.3$ GeV and the MSTW2008 PDF set with 68% C.L. variations the total cross section yields

$$158.7^{+12.2}_{-13.5}(\text{scale})^{+4.3}_{-4.4}(\text{PDF}) \text{ pb.} \quad (2.45)$$

2. Top Quark Physics at Hadron Colliders

In their paper the authors pay particular attention to the systematic uncertainties and critically review the other approaches criticising with regards to stability and the evaluation of scale uncertainties. For instance, they criticise that Moch et al. [86] pursue an too optimistic approach regarding the evaluation of scale uncertainties by not varying finite terms of $\mathcal{O}(\alpha_s^4)$, refer to the discussion later.

2.2.4.6. Moch, Uwer and Vogt

Very recently, Moch, Uwer and Vogt [93] published the most complete NNLO predictions (with the exception of the numerically determined complete NNLO result for the $q\bar{q}$ channel mentioned above [82]) with uncertainties of about $\mathcal{O}(5\%)$. They consider the constraints on hadronic heavy-flavour production imposed by the high-energy factorisation of the cross section, i.e. including results where the centre of mass energy is much higher than the quark's mass. They, however, do not account for uncertainties that arise from electro-weak radiative corrections at NLO as well as from bound state effects and the resummation of Coulomb type corrections. The total cross section yields

$$174.9^{+10.3}_{-13.2} (\text{scale})^{+4.7}_{-4.8} (\text{PDF}) \text{ pb} \quad (2.46)$$

for $m_t = 173$ GeV and the MSTW2008 PDFs.

2.2.4.7. Discussion

The calculations for inclusive top quark pair production at approximate NNLO have made a lot of progress during the last years. Compared to NLO predictions, these calculations show smaller dependence on the factorisation and renormalisation scales. Their dependence on the PDF set as discussed in detail in Reference [97], which is also an important point of investigation, is not discussed here since most samples use the same PDF sets. Regarding the scale variations it has to be noted that a smaller scale uncertainty does not necessarily hint at a more correct calculation. The different resummation techniques yield very different results with up to 9% difference between the central values summarised in Tab. 2.2, which is larger than the single scale uncertainty. As described above, the most important discriminator between the different approaches is the soft limit in which the resummation is performed. Discussion in Reference [79] shows that one can argue in favour of any of the approaches presented above. In this work it has been decided to use the production threshold results obtained by **Hathor** [94]. It can be shown that the production threshold results $\beta \rightarrow 0$, where at Born level $\beta = \sqrt{1 - 4m_T^2/s}$, are actually a special case of the single-particle inclusive (1PI) and pair invariant-mass kinematics (PIM) calculations as used e.g. by References [89, 90]. In cases when the production threshold limit differs significantly from the 1PI and PIM approaches subleading terms in β have a sizable effect and one might argue that **Hathor** must not ignore these. However, for $t\bar{t}$ production at the LHC it is found that the total cross section saturates to 95% at parton energies at about 1 TeV [86]. Therefore soft gluon emission near threshold still contributes a numerically sizable fraction to the total

cross section and does not neglect large effects. Another advantage of **Hathor** is that it includes the complete tower of Sudakov logarithms, all Coulomb-type corrections at NNLO [98] and the full NNLO scale dependence allowing variation thereof. Furthermore, one can calculate the $t\bar{t}$ cross section for any given pole or $\overline{\text{MS}}$ mass (see Sec. 2.1.3.1).

2.2.5. Single top production

In contrast to the strong top pair production, top quarks can also be produced singly via the electroweak interaction through a W boson. There are three production modes which are distinguished by the virtuality, Q^2 , of the W boson, where $Q^2 = -q^2$ and q is the four-momentum of the W boson: the t -channel, the s -channel and the so-called associated production, which are described in the following. Some example Feynman diagrams for single top production are shown in Fig. 2.7.

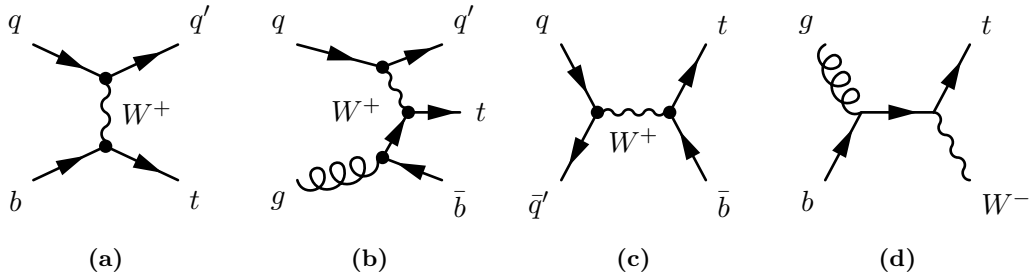


Figure 2.7.: Example Feynman diagrams of the leading order processes for single top production: t -channel production as (a) flavour excitation and (b) W -gluon fusion, (c) s -channel production and (d) associated tW production. Charge conjugate production modes are implied.

The cross section for single top production in hadron collisions at NLO is known since about ten years [99, 100]. The most recent cross section predictions incorporate NNLL resummation [101–104]. The cross section predictions used here are summarised in Tab. 2.3. It should be noted that with the exception of tW production the cross sections for top production at the LHC are larger than for top antiquark production due to the proton PDF.

The t -channel production mode is dominant at the LHC. A virtual W ($q^2 < 0$) strikes a b quark from the quark sea inside the proton to produce a top quark: $qb \rightarrow tq'$. In the reactions depicted in Figs. 2.7a and 2.7b q and q' indicate light-flavour quarks (u, d, s, c). The process containing up and down quarks is dominating in proton-proton collisions. Contributions from the second weak isospin doublet only have an effect of about 6% [105]. If one assumes the CKM matrix to be unitary and to only include three generations of quarks, a global fit to the Standard Model yields $|V_{tb}| \approx 1$ and $|V_{ts}|, |V_{td}| = \mathcal{O}(10^{-3})$ at 95% confidence level [31] (see also Sec. 2.1.1.1). Thus single top production occurs mainly via the Wtb vertex. The contribution of Wtd and Wts is small with about $\sim 0.1\%$ and $\sim 1\%$ respectively [106]. Measurements by CDF, D0 and

2. Top Quark Physics at Hadron Colliders

Table 2.3.: Cross sections for single top production at the LHC ($\sqrt{s} = 7$ TeV) for $m_t = 172.5$ GeV and the MSTW2008 90% NNLO PDF sets. The first uncertainty is related to scale uncertainties, and the second is the PDF error. Uncertainties are added linearly.

Production mode	σ_t [pb]	$\sigma_{\bar{t}}$ [pb]	σ_{tot} [pb]
t -channel ([101])	$41.92 \pm 0.83^{+1.59}_{-0.21}$	$22.65 \pm 0.50^{+0.68}_{-0.91}$	$64.57 \pm 1.33^{+1.38}_{-0.68}$
s -channel ([102])	$3.19 \pm 0.06^{+0.13}_{-0.10}$	$1.44 \pm 0.01^{+0.06}_{-0.07}$	$4.63 \pm 0.07^{+0.12}_{-0.10}$
tW production ([104])	$7.87 \pm 0.20^{+0.55}_{-0.57}$	same as t	$15.74 \pm 0.40^{+0.66}_{-0.68}$

CMS using the assumption of a three generation CKM matrix and using events with top quark pairs are in agreement with the theoretical models yielding $|V_{tb}| > 0.78$ at 95% C.L., $|V_{tb}| = 0.95 \pm 0.02$ and $|V_{tb}| = 0.98 \pm 0.04$ respectively [107–109]. Measurements of $|V_{tb}|$ using single top events have also been performed, but yield lower precision so far, see e.g. References [110, 111].

The Drell-Yan-type s -channel production (Fig. 2.7c) occurs via quark-antiquark annihilation into a time-like virtual W boson ($q^2 \geq (m_t + m_b)^2 > 0$). The s -channel production cross section at the LHC is strongly suppressed compared to the Tevatron because of the proton structure.

The so-called associated single top production is characterised by an on-shell W boson ($q^2 = m_W^2$) created together with a top quark from a b quark and a gluon, see Fig. 2.7d. It makes up about 19% of the single top production at the LHC.

Single top production has first been observed at the Tevatron in 2009 in the t -channel production mode [112, 113] combining several measurements and using powerful statistical methods. At the LHC, the single top cross section has also been measured [111, 114]. The measurements have rather large uncertainties since they suffer from the low cross sections of the processes and large backgrounds. The other production channels have not yet been discovered in experiment.

2.2.6. Top quark decay

The top quark mass is above the threshold for (top) decays to a W boson and a down-like quark, which is therefore the dominant decay. The contribution of each quark flavour q is proportional to the square of the respective CKM matrix element, V_{tq} . As discussed in the previous Sec. 2.2.5 the CKM matrix element for the top quark decaying to a b quark is $|V_{tb}| \approx 1$ if one demands matrix unitarity and three quark generations only. Therefore, the top quark would almost exclusively decay into a W boson and b quark. This is assumed for the analyses performed here, forcing the top quark to decay into a b quark in all cases at event generation level, i.e. $t \rightarrow Wb$.

If, however, one assumed more than three quark generations, the limits on the CKM matrix elements change dramatically. Although $|V_{td}|$ and $|V_{ts}|$ still vary only between 0–0.08 and 0–0.11, respectively, $|V_{tb}|$ can lie between 0.07 and 0.9993 at 90% confidence

2.2. Top quark production in pp collisions

level [115]. Since not only the decay of the top quark but also the electroweak production process is directly proportional to $|V_{tb}|^2$, a different value of $|V_{tb}|$, e.g. in the case of a fourth generation, would directly be reflected in the cross section. If the unitarity of the CKM matrix is relaxed, further possibilities come into play, which is discussed for example in Ref. [116]. However, the recent Higgs boson results strongly disfavour those.

The fact that the top quark is 35 times heavier than the next-heaviest quark brings along further features, which make studies of the top quark even more interesting. The decay width of the top quark is proportional to the cube of its mass and, including first order QCD corrections, is given by (see e.g. References [117, 118]):

$$\Gamma_t = \frac{G_F m_t^3}{8\pi\sqrt{2}} \left(1 - \frac{m_W^2}{m_t^2}\right)^2 \left(1 + 2\frac{m_W^2}{m_t^2}\right) \left[1 - \frac{3\alpha_s}{3\pi} \left(\frac{2\pi^2}{3} - \frac{5}{2}\right)\right]. \quad (2.47)$$

Corrections of $\mathcal{O}(\frac{\alpha_s m_W^2}{\pi m_t^2})$ and $\mathcal{O}(\alpha_s^2)$ are neglected, and one assumes $m_b^2/m_t^2 \rightarrow 0$ and $m_t^2 \gg m_W^2$. If further corrections are applied, the decay width is predicted in the Standard Model framework with a precision of 1%. The decays of the top quark to d and s quarks give only negligible contributions as they are proportional to the absolute square of the according CKM matrix elements. Plugging in values as given in [10] for a top quark mass of 172.5 GeV yields:

$$\Gamma_t \approx 1.40 \text{ GeV}. \quad (2.48)$$

This corresponds to an average lifetime of:

$$\tau_t = \frac{1}{\Gamma_t} \approx 5 \cdot 10^{-25} \text{ s}, \quad (2.49)$$

which is one order of magnitude smaller than the hadronisation time of $\tau_{\text{had}} = \Lambda_{\text{QCD}}^{-1} \approx 3 \cdot 10^{-24}$ s. Thus the top quark decays before hadronisation and one does not expect toponium states [119–121]. Although one might consider the top quark as a free particle, one has to take into account that it still is a quark and therefore has a colour quantum number assigned to it from the hard interaction. This might be reflected in the fragmentation and hadronisation process. For example, colour reconnections with beam remnants before hadronisation might lead to a different final state in some cases. This is discussed in more detail in [122, 123].

As the top quark decay is a weak decay it follows a vector minus axial vector (V–A) structure according to the Standard Model. This can be observed in the helicity states of the W boson, which can be used to test the coupling at the Wtb vertex [124–126]. A well defined angular distribution is expected for the decay products due to their spins allowing to measure the helicity of the W boson. A deviation from the theoretical expectations would signal physics beyond the Standard Model. Recent experimental results such as the combination of the measurements of the CDF and the D0 collaborations and the latest ATLAS and CMS measurements, however, show no deviation from the Standard Model [127–129].

2.2.6.1. Top quark pair decay topology

Top quark decays are classified by the decay of the W bosons. The W boson can decay into a lepton and a neutrino $W \rightarrow l\nu$, i.e. leptonically, and into two quarks $W \rightarrow q\bar{q}'$ that form hadrons, i.e. hadronically. Each possible decay occurs at the same frequency. The leptonic decays are into $(e\nu_e)$, $(\mu\nu_\mu)$ and $(\tau\nu_\tau)$. The possible hadronic decays are into quarks of the first and second generation, i.e. $(u\bar{d})$ and $(c\bar{s})$. Since quarks carry colour but have to form colour neutral hadrons, the possible colour configurations for the quark pairs are colour-anticolour, i.e. $(r\bar{r})$, $(b\bar{b})$ and $(g\bar{g})$. Therefore, six hadronic final and three leptonic states are possible and the W boson decays into each about 11% of the time.

When looking at top quark pair events one can arrange them into three groups depending on the decay of the two W bosons. If both W bosons decay hadronically, the final state is called all-hadronic channel. Hadrons within a certain distance measure are bundled into a so-called jet, see Sec. 4.4 for more details. The experimental signature shown in Fig. 2.8a consists of two jets from the b quarks and four jets from the W bosons. In the case of both W bosons decaying leptonically one speaks of a dileptonic final state as depicted in Fig. 2.8c. In the detector one observes two jets from the b quarks, two leptons of opposite charge and an energy imbalance due to the two neutrinos that escape the detector undetected. The final state investigated in this thesis considers the case where one W boson decays leptonically and the other one hadronically. This final state is called lepton + jets or semi-leptonic channel and displayed in Fig. 2.8b. The experimental signature consists of four jets two of which stem from the b quarks, a lepton with high momentum as well as missing energy due to the escaping neutrino.

The rate at which the top quark pairs decay into each channel can be calculated from the branching ratio of the W boson and is shown in Fig. 2.9. Each final state has its advantages and disadvantages. The all-hadronic channel has the highest statistics, but is prone to large background from multi-jet events. The dileptonic channel allows a very clean signal selection. However, in the data set recorded in 2010 and 2011 at $\sqrt{s} = 7$ TeV it suffers from low statistics. Furthermore, the top quark reconstruction is ambiguous due to the two unmeasured neutrinos. The lepton + jets channel shows the best trade-off between signal purity and manageable background, and statistics. It also allows full reconstruction of at least one of the top quarks and is used for this work.

2.2. Top quark production in pp collisions

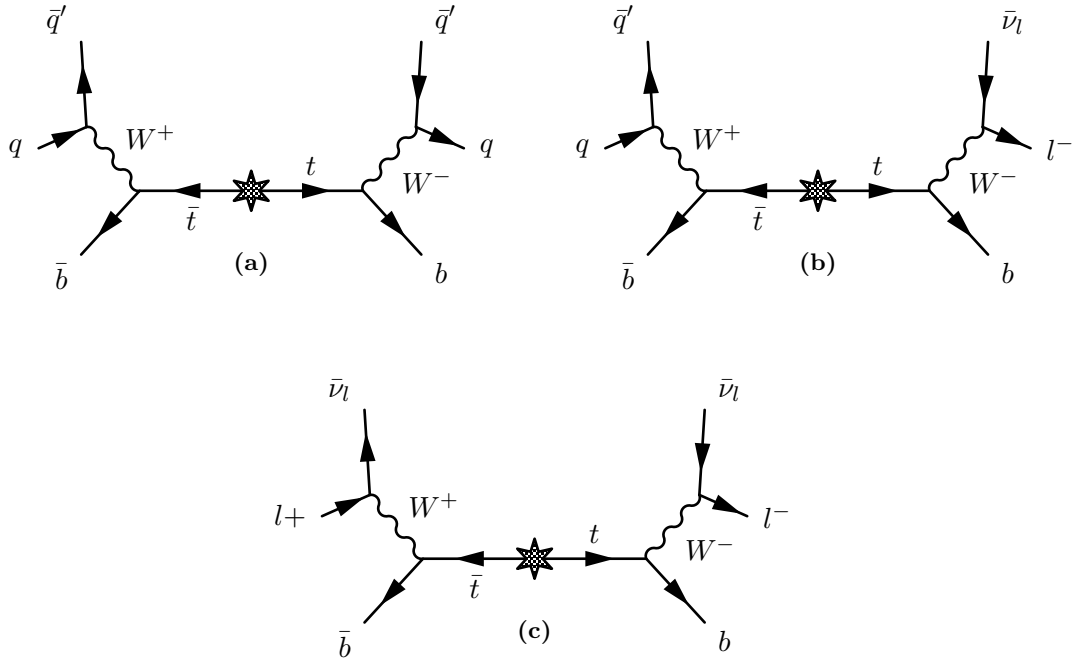


Figure 2.8.: Top quark pair decay in the (a) all-hadronic, (b) lepton + jets or semi-leptonic, and (c) dilepton channel. Charge conjugate production modes are implied.

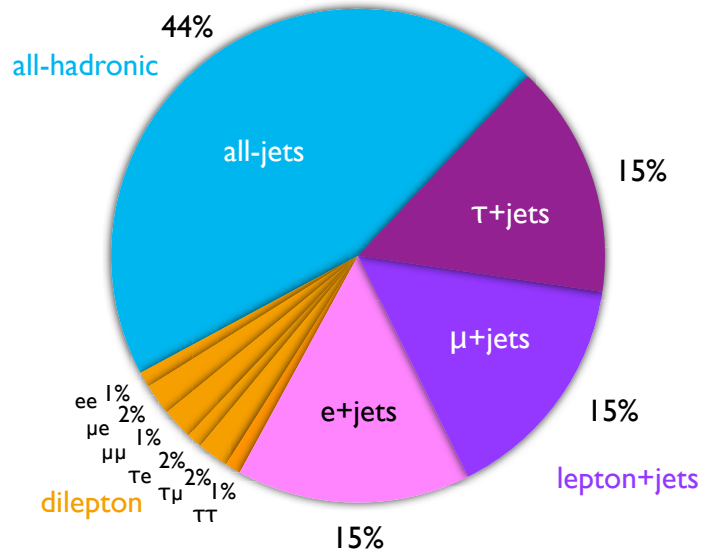


Figure 2.9.: Top quark pair branching fractions into decay channels and their rate.

3. The LHC and the ATLAS detector

The data used for the analyses presented in this thesis have been recorded by the ATLAS experiment in proton-proton collisions created by the Large Hadron Collider (LHC) at a centre of mass energy of $\sqrt{s} = 7$ TeV in the years 2010 and 2011. In this chapter the experimental setup and design of the LHC and ATLAS are described in Secs. 3.1 and 3.2 respectively. Section 3.3 summarises the performance of both ATLAS and the LHC.

3.1. The Large Hadron Collider

The Large Hadron Collider (LHC) [130, 131] is a proton-proton (pp) collider based at the European Particle Physics Laboratory CERN near Geneva, Switzerland. It is situated in the former LEP [132] tunnel with a circumference of 26.659 km about 100 m under ground crossing the border between France and Switzerland. A hadron collider has been chosen to allow higher centre of mass energies compared to electron-positron (e^-e^+) colliders, the latter limited by synchrotron radiation due to the mass of the particles to be accelerated. High centre of mass energies are required for the production of heavy particles such as the top quark and the Higgs boson. A large kinematic range is covered since due to the substructure of the protons, partons with different momentum fractions collide (see Sec. 2.2.2). In addition to colliding protons, the LHC is also capable of accelerating and colliding heavy nuclei, which is, however, not considered in this work.

The hadron beams are preaccelerated by the existing acceleration facilities shown in Fig. 3.1 increasing the energy step by step. Protons are obtained using a duoplasmatron in which hydrogen gas is ionised by an electron beam. The hydrogen ions, i.e. the protons are then attracted by an extraction electrode and lead to the first linear accelerator, the Radio Frequency Quadrupole (RFQ). In the RFQ they are focussed, separated into bunches and accelerated to 750 keV towards the next linear accelerator LINAC 2 where they reach an energy of 50 MeV. The first ring accelerator is then the Proton Synchrotron Booster (PSB) with a diameter of 50 m, where the energy is increased to 1.4 GeV [133]. Hereafter, the protons are transferred to the Proton Synchrotron (PS) which divides the six bunches from the PSB into 72 bunches with a spacing of 25 ns by varying voltage and frequency [134]. Having obtained an energy of 25 GeV, the bunches are passed on to the Super Proton Synchrotron (SPS) with the help of kicker magnets where they are accelerated to 450 GeV [135]. Using two transfer lines the protons are eventually injected into the two beam pipes of the LHC ring, where they circulate in opposite directions. In the Large Hadron Collider both beams are accelerated simultaneously to the maximum energy of 3.5 TeV per beam in 2010 and 2011 and 4 TeV in 2012 resulting in a centre of mass energy of 7 TeV and 8 TeV, respectively.

3. The LHC and the ATLAS detector

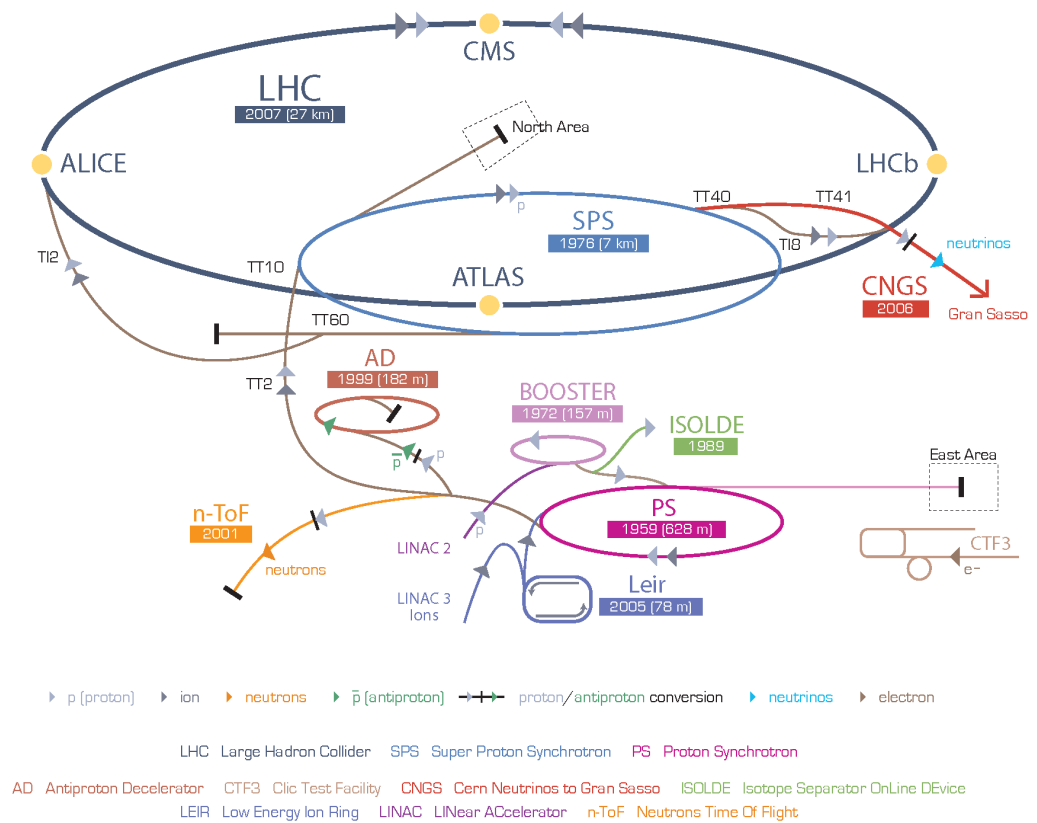


Figure 3.1.: The CERN accelerator complex showing the Large Hadron Collider, the experiments and the existing accelerator facilities. Protons are preaccelerated in the LINAC 2, the Booster, the PS and the SPS before being injected into the LHC. [136]

The energy of the protons is limited by the strength of the magnetic field required for keeping the protons inside the ring. The design energy of the LHC is 7 TeV per beam, which is planned to be reached in 2014. For 7 TeV-protons a magnetic field of 8.33 T has to be produced, which can only be reasonably obtained by superconducting magnets. 1232 dipole magnets for bending and 392 quadrupole magnets for focussing made of niobium-titanium (NbTi) are therefore cooled down to a temperature of 1.9 K with the help of super-fluid helium. To obtain two usable proton beams, the protons are bundled into a maximum of 2808 bunches with a spacing of 25 ns, containing $1.15 \cdot 10^{11}$ particles each. The beams are accelerated from injection energy to the maximum energy within 20 minutes using radio-frequency (RF) cavities. After further beam optimisation the beams are brought into collision at four points, where the experiments are located. As each bunch contains such a large number of protons in a small area, which have to be focussed for collisions, more than one collision can take place simultaneously and

overlap, which is referred to as “pileup” of events (see also Chapter 5).

Besides the high centre of mass energy required for the production of heavy particles, a high event rate has to be obtained to allow the discovery of processes with low production cross sections. The event rate R is proportional to the interaction cross section σ_{int} and the proportionality is called the instantaneous luminosity:

$$R = L\sigma_{\text{int}}. \quad (3.1)$$

If two bunches containing N_p particles each collide with frequency f_{rev} , the instantaneous luminosity is:

$$L = \frac{N_p^2 n_b f_{\text{rev}} \gamma_r}{4\pi\sigma_x\sigma_y}, \quad (3.2)$$

where σ_x and σ_y characterise the widths of the transverse beam profiles in the horizontal and vertical direction, respectively. The luminosity furthermore depends on the number of bunches n_b in the beam, and the relativistic gamma factor γ_r . At the interaction points, the beam has a width of about 16 μm and a length of about 8 cm. With the above parameters an instantaneous luminosity of $L = 10^{34} \text{ cm}^{-2}\text{s}^{-1}$ can be reached. Instead of referring to the total number of events for a process, the integrated luminosity:

$$\mathcal{L} = \int dtL, \quad (3.3)$$

is used. One year of data taking at low design luminosity corresponds to an integrated luminosity of approximately $\mathcal{L} = 10 \text{ fb}^{-1}$ and at high luminosity $\mathcal{L} = 100 \text{ fb}^{-1}$. See Sec. 3.3 for the luminosity delivered so far.

The four large experiments at the LHC are built for different purposes. The ALICE (A Large Ion Collider Experiment [137]) and the LHCb (Large Hadron Collider beauty experiment [138]) detectors are designed for the study of the quark-gluon plasma created in heavy ion collisions and the study of CP-violation in the b quark system, respectively. ATLAS (A Toroidal LHC ApparatuS [139]) and CMS (Compact Muon Solenoid [140]) are so-called general purpose detectors that are designed for a broad study of Standard Model and unknown physics.

3.2. The ATLAS detector

The ATLAS detector is about 44 m long, 25 m high as shown in Fig. 3.2 and weighs about 7000 tonnes. Its overall task as a general purpose detector is to reconstruct the primary interaction entirely. Therefore, one needs to collect all possible information on the particles passing through the detector. Since these have different properties, a mixture of subdetectors is required for a complete event reconstruction. The design and performance of the sub-systems of ATLAS have been driven by the search for the Standard Model Higgs boson using the expected event topologies as a benchmark. However, ATLAS should also be able to perform precision measurements of known Standard Model parameters. In order not to lose any information, a large geometrical acceptance

3. The LHC and the ATLAS detector

has been aimed for. Hence, the detector is designed in a radial and forward-backward symmetry, consisting of a barrel and two end-cap parts. Furthermore, due to the high interaction rate, radiation-hard electronics and sensor elements are required. A fine detector granularity is needed to handle particle fluxes and to reduce the influence of overlapping events.

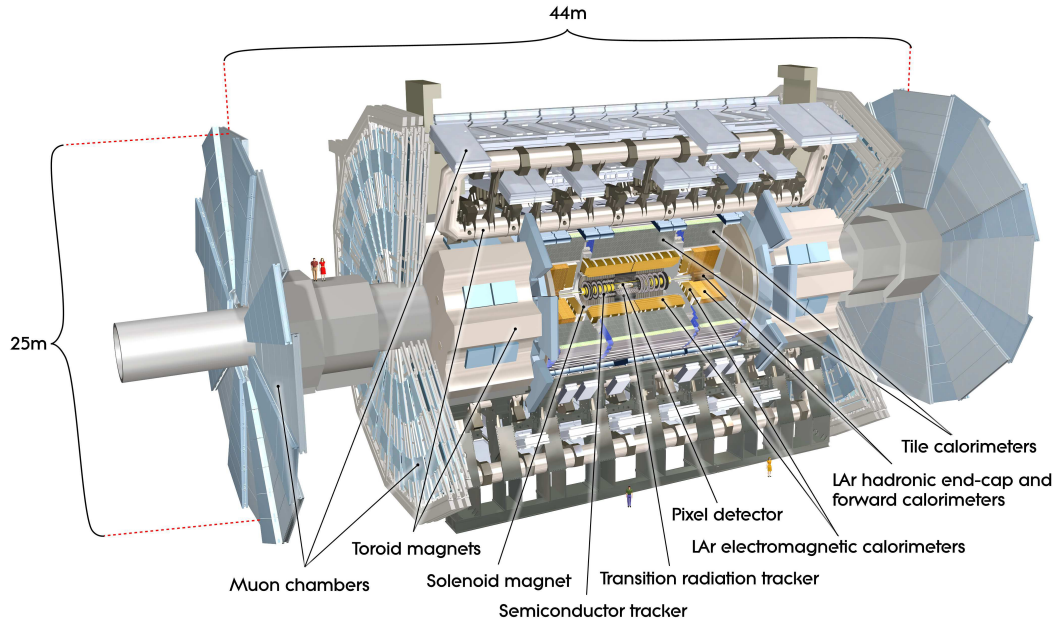


Figure 3.2.: *Cut-away view of the ATLAS detector. The dimensions of the detector are 25 m in height and 44 m in length. The overall weight of the detector is approximately 7000 tonnes. [139]*

The subdetectors in ATLAS can be categorised into two general types: Either they measure the tracks of charged particles allowing momentum reconstruction and charge identification with the help of a magnetic field or they measure the energy of particles by absorbing them in a calorimeter, see Chapter 4. The ATLAS detector is designed in an onion shell structure: High resolution tracking detectors described in Sec. 3.2.3 are placed around the interaction point in order to measure momenta, charges and direction of all charged particles. Additionally, the secondary vertices of jets containing instable b and c quark hadrons and also of τ -leptons can be reconstructed. Behind the tracking detectors, two calorimeter systems outlined in Sec. 3.2.4 try to stop the particles created in the collision and subsequent decays measuring their energy. The outermost layer of the ATLAS detector are further tracking detectors specifically designed for the measurement of the momenta of muons (see Sec. 3.2.5), which are the most penetrating of all particles and thus not absorbed by the calorimeters. In the following, the detector is described in more detail starting with the geometry in Sec. 3.2.1 followed by the magnet system in Sec. 3.2.2 that is essential for the tracking systems. The additional forward detector systems used for luminosity measurements are described in Sec. 3.2.6 and details about

the data acquisition and trigger system are found in Sec. 3.2.7.

3.2.1. Geometry and coordinate system

The ATLAS geometry is defined by a coordinate system whose origin is the nominal interaction point in the centre of the detector. The anti-clockwise beam direction defines the z -axis while the x - y plane is transverse to the beam. The positive x -axis is defined as pointing from the interaction point to the centre of the LHC ring. The positive y -axis points upwards. The azimuthal angle ϕ is measured around the beam axis. The polar angle θ is measured from the beam axis and defines the pseudorapidity:

$$\eta = -\ln \left(\tan \frac{\theta}{2} \right). \quad (3.4)$$

The distance between two objects in the η - ϕ plane is given as:

$$\Delta R = \sqrt{\Delta\eta^2 + \Delta\phi^2}. \quad (3.5)$$

The transverse distance r from the beam pipe or z -axis is defined as:

$$r = \sqrt{x^2 + y^2}. \quad (3.6)$$

Energy and momentum measured orthogonally with respect to the beam axis are denoted as transverse momentum $p_T = p_x^2 + p_y^2$ and transverse energy $E_T = E \cdot \sin \theta$.

3.2.2. Magnet system

A strong magnetic field is needed in order to bend the tracks of charged particles which allows for momentum measurement and charge identification. Two different fields are generated by a hybrid system of four superconducting Al-stabilised NbTi magnets. The system consists of one solenoid magnet encapsulating the ID and three toroid magnets for the muon spectrometer and can store an energy of 1.6 GJ with a total diameter of 22 m and 26 m length. The solenoid magnet generates a 2 T axial field with an inner bore of 2.46 m and an axial length of 5.8 m immersing the ID. At nominal current, a total energy of 40 MJ is stored within the magnet. Since the solenoid magnet itself is encapsulated by the calorimeter system, one has aimed to minimise the amount of additional material in front of the calorimeter totalling only approximately 0.66 radiation lengths. The steel of the hadronic calorimeter serves as return yoke.

The large toroid system provides the magnetic field for the muon spectrometer. The barrel part consists of eight racetrack-shaped coils with a total length of 25.3 m. The inner and outer diameters are 9.4 m and 20.1 m, respectively. At the nominal current of 20.5 kA 1.1 GJ are stored in the system. The end-caps of the muon spectrometer are additionally equipped with smaller toroid magnets. The magnetic field of the toroid system is highly non-uniform with field strengths ranging from 0.5 T to 1 T. However, an accuracy of 1 mT of the B -field strength and 3 mrad in direction is necessary for

3. The LHC and the ATLAS detector

the required momentum resolution in the muon spectrometer. Thus, the toroid field is monitored by 1840 B -field sensors. Further details can be found in References [139, 141].

3.2.3. Inner Detector

The Inner Detector (ID) extends over a length of 5.3 m with a diameter of 2.5 m as shown in Fig. 3.3 covering a pseudorapidity range of $|\eta| < 2.5$. The ID is built out of three parts in cylindrical layers: the Silicon Pixel Detector, the Semiconductor Tracker (SCT) and the Transition Radiation Tracker (TRT). Surrounded by the previously described solenoid generating a magnetic field of 2 T, the ID is used for measuring the momenta of charged particles, primary and secondary vertices and the sign of the electric charge. The TRT can also be used for particle identification.

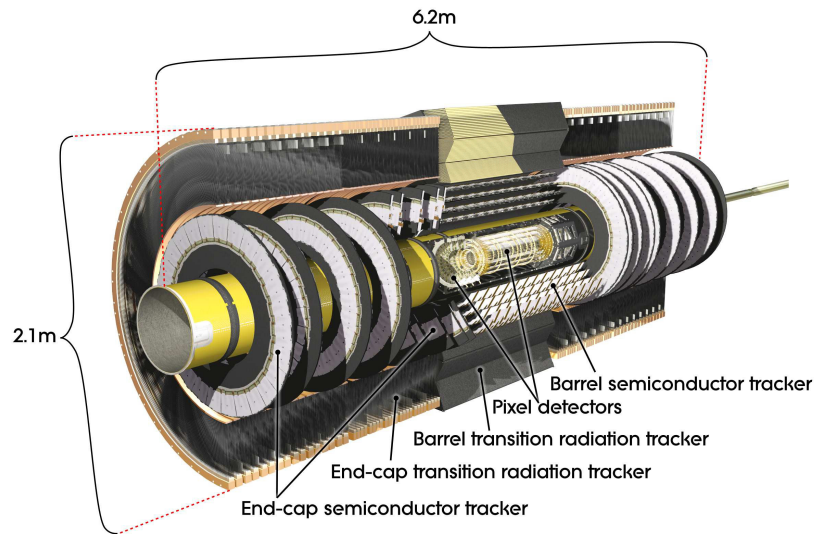


Figure 3.3.: *Cut-away view of the ATLAS Inner Detector. [139]*

3.2.3.1. Pixel Detector¹

Designed to operate in the high particle multiplicity of LHC, the ATLAS Pixel Detector [139, 143] has a position resolution in the $r - \phi$ plane of $< 15 \mu\text{m}$, as well as a time resolution of less than the 25 ns collision rate of the LHC. Built as a three-hit system for the central region of the ATLAS detector (pseudo-rapidity $|\eta| < 2.5$), it consists of three cylindrical barrel layers with 1456 modules and two end-caps with three disks each having a total of 288 modules as depicted in Fig. 3.4. The barrel layers have radii of 50.5 mm, 88.5 mm and 122.5 mm and are 800 mm long.

The modules need to be cooled to prevent overheating and reverse annealing of the silicon sensors. Therefore, a cooling system that is shared with the SCT (see following

¹The following text is an excerpt taken from Ref. [142].

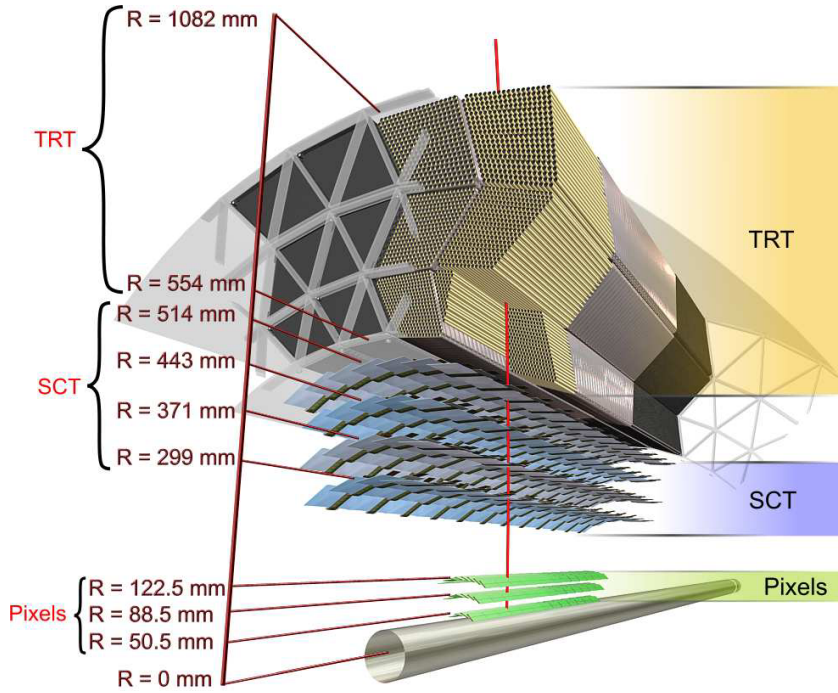


Figure 3.4.: Barrel region of the ATLAS Inner Detector. Shown are the beryllium beampipe, the three cylindrical silicon-pixel layers, the four cylindrical double layers of barrel silicon-microstrip sensors (SCT), and approximately 36 axial straws of 4 mm diameter contained in the barrel transition-radiation tracker modules within their support structure. [139]

Sec. 3.2.3.2) using evaporative C_3F_8 cooling is integrated into the support structure. The target temperature for the silicon sensors after irradiation is 0°C for the Pixel Detector and -7°C for the SCT.

A pixel module as shown in Fig. 3.5 consists of a $250\ \mu\text{m}$ thick silicon sensor with n^+ pixels implanted on the n -doped bulk with a p^+ backplane, 16 Front-End chips (FE-I3) and a module controller chip (MCC) [144]. The FE-I3 chips [145] were manufactured in radiation tolerant $0.25\ \mu\text{m}$ CMOS technology and have 2880 readout channels. Each module has an active area of $16.4 \times 60.8\ \text{mm}^2$ consisting of 47232 (328×144) pixels. The typical pixel size is $50 \times 400\ \mu\text{m}^2$. To enable full coverage in the regions between front-end chips, approximately 10% of the sensor pixels have a size of $600 \times 50\ \mu\text{m}^2$ (long pixels). In order to fully deplete the semi-conductor a bias voltage 150 to 600 V can be applied. The modules are designed to cope with a lifetime dose of 500 kGy.

The data connection to the Pixel Detector is realised using optical links. They connect the off-detector Read-Out Drivers (RODs) to the modules over a distance of 80 m. Each module has one downlink (TTC) providing clock, trigger signals, detector calibration data and commands. These are encoded into a Bi-Phase Mark (BPM) signal which is transmitted at 40 MHz. The BPM signals are decoded using a Digital Opti-

3. The LHC and the ATLAS detector

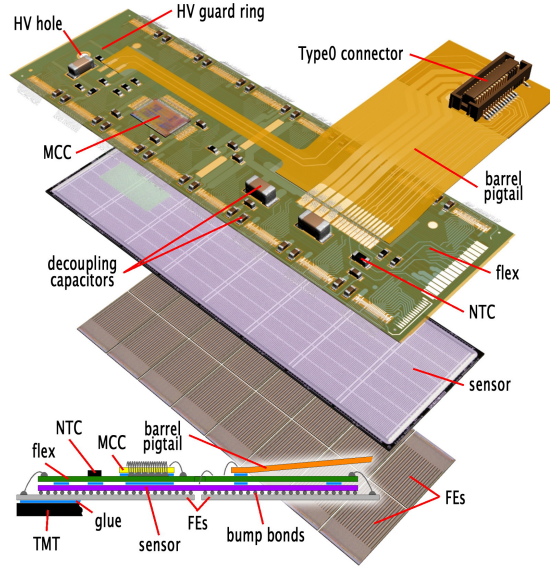


Figure 3.5.: *The ATLAS Pixel Detector module [143].*

cal Receiver Integrated Circuit (DORIC) located on an Opto-Board [146] before being transmitted via Low Voltage Differential Signals (LVDS) to the modules. The Module Control Chip (MCC) sends data from collision events to the data acquisition system outside the detector utilising Opto-Boards, where the signal is converted to an optical signal by vertical-cavity surface-emitting lasers (VCSEL) arrays, so-called Tx-plugins. Data is then transferred off-detector from the modules to the RODs via a data-link whose speed and modularity depend on the location of the modules in the detector. Barrel Layer-2 modules have one data-link transmitting at 40 MHz while the modules in the Disks and Barrel Layer-1 have one link which can run at either 40 or 80 MHz. The innermost barrel layer (B-layer) has, due to the high expected hit rate, two data-links per module which can each be read out at 80 MHz for an equivalent readout speed of 160 MHz. The layout of the pixel readout system from the signal generation in the sensor to the off-detector RODs can be found in Fig. 3.6. In total there are approximately 80 million electronic channels to be read out. For more details see also Reference [142]. The typical resolution achieved is approximately $10 \mu\text{m}$ in the $r - \phi$ plane and $115 \mu\text{m}$ in the z -direction [147].

3.2.3.2. Semiconductor Tracker

The Semiconductor Tracker (SCT) is positioned in the intermediate radial range of the Inner Detector. It is built out of four double layers of silicon microstrip detectors with radii between 299 mm and 514 mm and a full length of 1492 mm. Two of the 6.4 cm long sensors are daisy-chained together, each of these rotated by an angle of 40 mrad to another pair to allow measurement of both coordinates with one pair parallel to the beam direction, measuring $r - \phi$. The detector consists of 4088 modules typically providing a total of eight strip measurements (four space-points) for particles originating in the

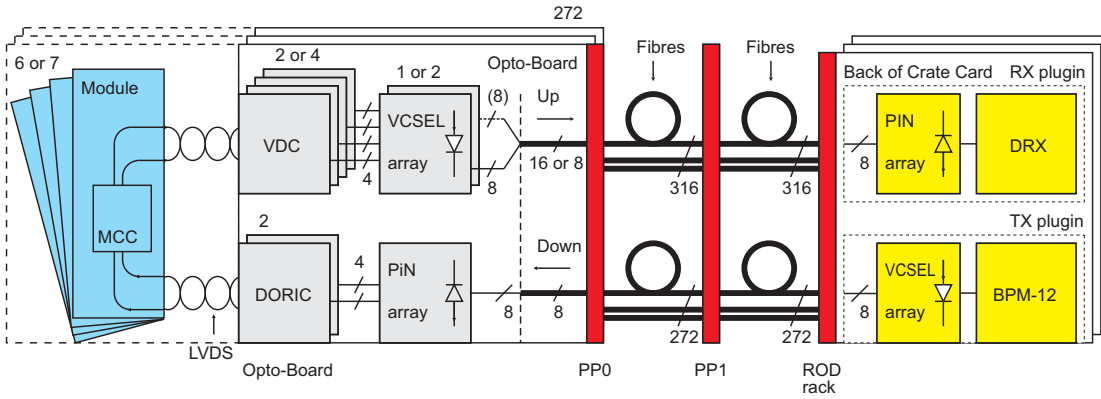


Figure 3.6.: *Layout of pixel readout system [143].*

beam-interaction region. In the end-cap region, the modules are arranged in 9 disks with one set of modules running radially and another one at an angle of 40 mrad. A hit resolution per module of $17 \mu\text{m}$ in $r - \phi$ and $580 \mu\text{m}$ in z in the barrel and of $17 \mu\text{m}$ in $r - \phi$ and $580 \mu\text{m}$ in r in the disks is reached. The total number of read-out channels in the SCT is approximately 6.3 million.

3.2.3.3. Transition Radiation Tracker

The outermost part of the Inner Detector is the Transition Radiation Tracker (TRT) covering radial distances from 563 mm to 1066 mm. It is a multi-wire proportional counting detector, using 298,304 independent drift tubes, so-called straws, also capable of transition radiation detection for electron identification. The straw tubes of 4 mm diameter containing a tungsten wire enable track-following up to $|\eta| = 2.0$ with a hit resolution of $130 \mu\text{m}$ per straw in $r - \phi$ yielding a combined resolution of approximately $30 \mu\text{m}$. In the barrel region, the straws of length 144 cm are parallel to the beam axis divided in two at the centre to reduce occupancy and read-out at each end. They are contained in carbon and polypropylene fibres, the spaced filled with foam-like material to provide transition radiation. In the end-cap regions, the 37 cm long straws are arranged radially in nine wheels each and interleaved with foils. An average of 36 hits per track is expected. The number of readout channels amounts to approximately 351,000.

The gas mixture of Xe (70%), CO_2 (27%) and O_2 (3%) is a compromise between transition radiation and drift properties. An electron crossing the radiator foils or foam will emit X-ray photons, which are absorbed by the gas mixture, leading to a significantly higher signal for electrons than for other particles traversing the gas.

3.2.4. Calorimetry

In ATLAS, an electromagnetic and a hadronic sampling calorimeter are used as shown in Fig. 3.7. They enclose the solenoid magnet around the Inner Detector and cover a range of $|\eta| < 4.9$.

3. The LHC and the ATLAS detector

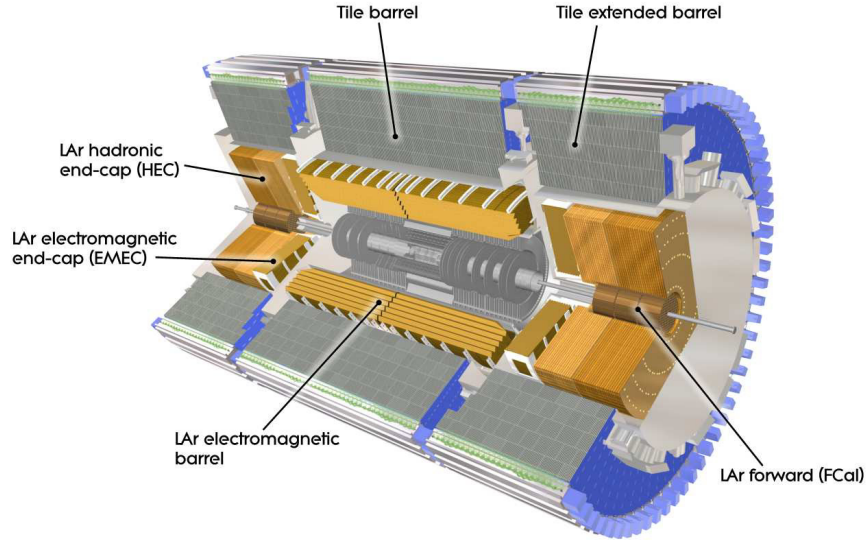


Figure 3.7.: *Cut-away view of the ATLAS calorimeter system. [139]*

3.2.4.1. Electromagnetic Calorimeter

The Electromagnetic (EM) Calorimeter is a lead-liquid argon (LAr) sampling calorimeter built in an accordion-shaped geometry providing full ϕ symmetry. It is divided into a barrel part ($|\eta| < 1.475$) and two end-cap components ($1.375 < |\eta| < 3.2$), each one with its own cryostat. The Barrel calorimeter consists of two identical half-barrels that are separated by a small gap of 4 mm at $z = 0$. The end-cap is mechanically divided into two coaxial wheels: the outer wheel covers the region $1.375 < |\eta| < 2.5$ whereas the inner wheel covers the region $2.5 < |\eta| < 3.2$. The total thickness of the calorimeter amounts to more than 22 radiation lengths in the barrel and more than 24 radiation lengths in the end-caps. The region that matches with the Inner Detector is segmented into three sections in depth getting coarser with larger distance to the interaction point. The first layer is used as a preshower detector for photon separation. The smallest granularity is available in the second calorimeter layer with a depth of about 16 radiation lengths. In this region, where most of the energy is deposited, the granularity yields $\Delta\eta \times \Delta\phi = 0.025 \times 0.025$ up to $|\eta| = 2.5$. The third layer has half the resolution in η . Since most of the central calorimetry is located behind the cryostat, the solenoid and the Inner Detector of 1–4 hadronic interaction lengths thickness, electromagnetic showers develop well before the calorimeter. To account for that, a presampler is added in front of the calorimeter up to $|\eta| = 1.8$ allowing the measurement of energy losses of the incident particles before reaching the calorimeter. Since the presampler does not have an absorber layer, it behaves almost like a single-layer LAr tracker. A sketch of a calorimeter barrel module is shown in Fig. 3.8. The energy resolution is $\sigma_E/E = 10\%/\sqrt{E} [\text{GeV}] \oplus 0.7\%$ (see e.g. [148]).

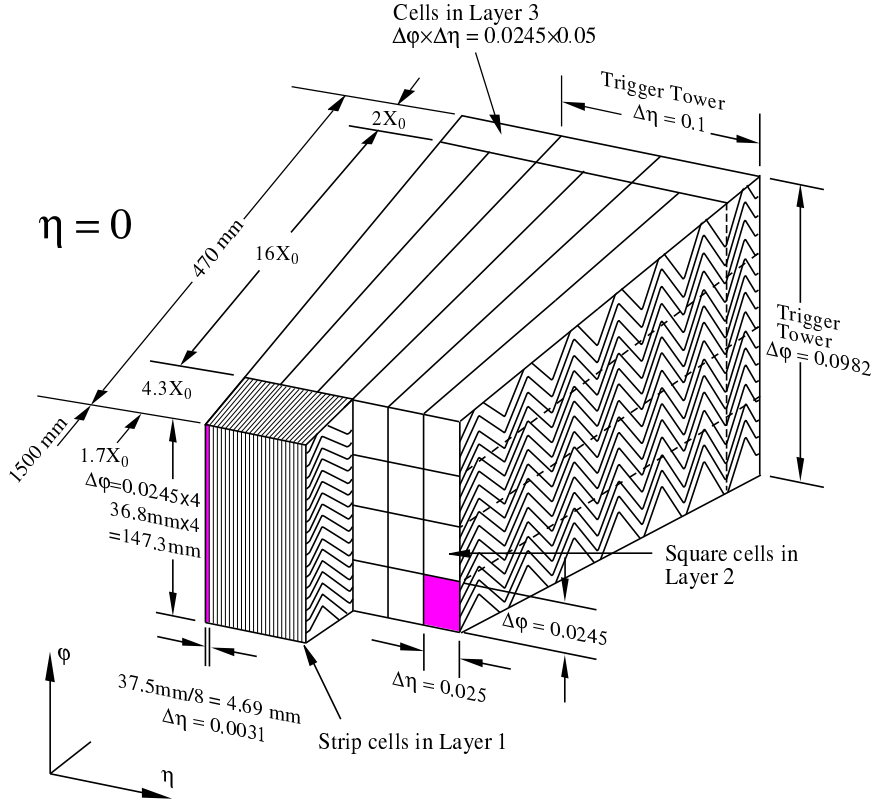


Figure 3.8.: Sketch of a barrel module of the electromagnetic calorimeter, where the different layers are clearly visible. The granularity in η and ϕ of the cells of each of the three layers and of the trigger towers is also shown. [139]

3.2.4.2. Hadronic Calorimeter

The ATLAS Hadronic Calorimeter has an approximate depth of 9.7 hadronic interaction lengths to provide good resolution for high- p_T jets reaching from an inner radius of 2.28 m to 4.25 m. It is split into three subsystems using two different calorimeter techniques. The Tile Calorimeter is placed directly outside the EM calorimeter. Its barrel covers the region $|\eta| < 1.0$ and its two extended barrels range from $0.8 < |\eta| < 1.7$. Scintillating plastic plates, so-called tiles, are used as the active material of 3 mm thickness alternating with steel of 4–5 mm thickness for absorption. The tiles are read out at two sides using wavelength shifting fibres into separate photomultiplier tubes.

The Hadronic End-Cap Calorimeter covers a region of $1.5 < |\eta| < 3.2$ overlapping with parts of the Tile Calorimeter and the LAr Forward Calorimeter described in the next paragraph. It consists of two independent wheels per end-cap located directly behind the EM calorimeter end-caps. Each wheel is built from 32 identical wedge-shaped modules. The wheels closest to the interaction point have 25 mm thick copper plates alternating with 8.5 mm LAr gaps as active material, while those further away have 50 mm copper plates. The energy resolution for the Barrel and End-Cap Calorimeter is

3. The LHC and the ATLAS detector

$$\sigma_E/E = 50\%/\sqrt{E} [\text{GeV}] \oplus 3\% [147].$$

The LAr Forward Calorimeter (FCal) ranges from $|\eta| = 3.1$ up to 1° to the beam axis ($|\eta| = 4.9$) and is therefore exposed to a very high level of radiation. Thus, the FCal is recessed by about 1.2 m with respect to the EM calorimeter front face to reduce neutron albedo to the Inner Detector. It consists of three modules in each end-cap: the copper module is optimised for electromagnetic measurements while the other outer two are made of tungsten, measuring predominantly the hadronic products. The modules each consist of a metal matrix filled with concentric rods and tubes parallel to the beam axis. The gap between the rod and the tube is filled with LAr. The FCal has an energy resolution of $\sigma_E/E = 100\%/\sqrt{E} [\text{GeV}] \oplus 10\% [147]$.

3.2.5. Muon System

The Muon System shown in Fig. 3.9 constitutes the outermost part of the ATLAS detector and therefore covers the largest surface area. Only the muons are expected to fly unhindered through the calorimeters to reach the Muon System. Their momenta are reconstructed by measuring the tracks of the muons deflected by a magnetic field generated by a system of three large air-core toroids as described previously in Sec. 3.2.2. The barrel toroid provides the magnetic field in the region $0 < |\eta| < 1.4$ and the end-cap toroids in the range of $1.6 < |\eta| < 2.7$. In the region where the systems overlap, the so-called transition region, a lower bending power is reached.

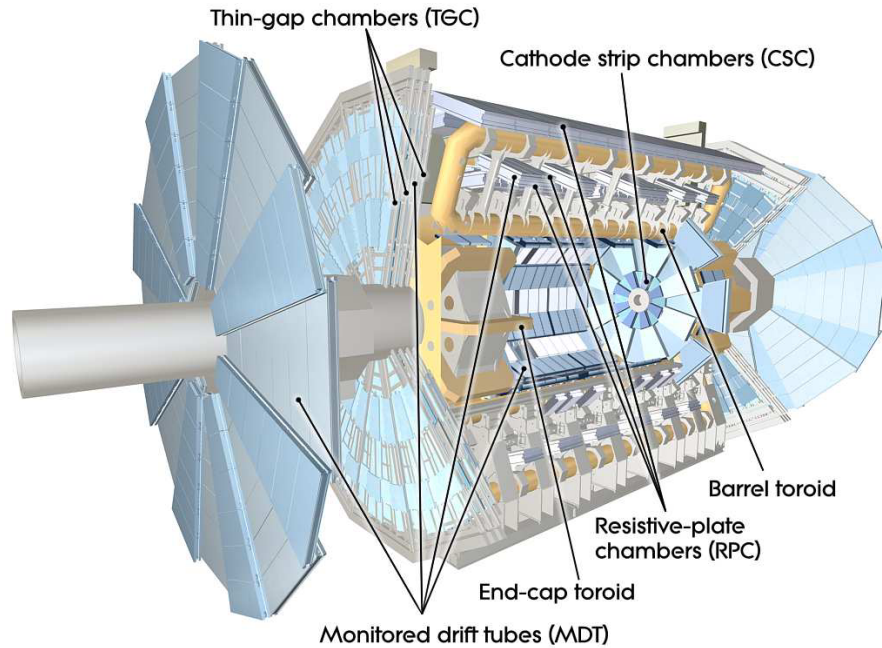


Figure 3.9.: *Cut-away view of the ATLAS muon system. [139]*

The Muon Spectrometer consists of four different detector types. Over most of the

pseudorapidity range the track measurement is performed by the Monitored Drift Tubes (MDT). These are aluminium drift tubes each containing a tungsten-rhenium wire of $30\ \mu\text{m}$ diameter and filled with a gas mixture of Ar (93%) and CO_2 (7%). Between $2 < |\eta| < 2.7$, multiwire proportional chambers with cathodes segmented into strips, called Cathode Strip Chambers (CSC) are used with a higher granularity due to higher radiation exposure. There are holes in the acceptance at $|\eta| < 0.1$ and $|\eta| \approx 1.3$ due to support structures and cabling for the other detectors.

The Muon System also has a dedicated trigger system covering a region up to $|\eta| = 2.4$, because the MDT and CSC have too large drift times to be used in the trigger. Up to $|\eta| = 1.05$ so-called Resistive Plate Chambers (RPC) are used. These are gaseous parallel electrode plate detectors forming three concentric cylindrical layers around the beam axis at radii of about 5, 7.5, and 10 m. The large distance between the inner and outer RPC allow for selection of high momentum tracks of 9–35 GeV based on detector hits, while the two inner chambers provide low- p_T values of 6–9 GeV. The Thin Gap Chambers (TGC) covering a range of $1.05 < |\eta| < 2.7$ (trigger $|\eta| < 2.4$) are multi-wire proportional chambers. They are arranged in four disks at distances of 7, 10, 14, and 21–23 m from the interaction point, concentric with the beam axis. In addition to the trigger capability, the trigger system also provides a measurement of the muon coordinate in the direction orthogonal to the one determined by the MDT and CSC.

The MS reconstruction efficiency and resolution were obtained using cosmic ray events in 2008 and 2009 [149]. Integrating over the full detector acceptance the reconstruction efficiency is found to be about 94%. When excluding the gap region around $\eta = 0$, the reconstruction efficiency is increased to 97%. Using this data the transverse momentum resolution yields:

$$\frac{\sigma_{p_T}}{p_T} = \frac{0.29\ \text{GeV}}{p_T} \oplus 0.043 \oplus 4.1 \times 10^{-4}\ \text{GeV}^{-1} \times p_T, \quad (3.7)$$

for $5\ \text{GeV} < p_T < 400\ \text{GeV}$. Specific details for the muons used in the analyses are given in Sec. 4.3.

3.2.6. Forward and Luminosity Detectors

In addition to the main ATLAS detector systems described in the previous sections, three smaller systems are used as special purpose detectors in the forward direction. Located at a distance of ± 17 m from the interaction point, the LUCID (LUminosity measurement using Cherenkov Integrating Detector [150]) detector is used as the main relative luminosity monitor in ATLAS. This is done by detecting inelastic pp scattering in the forward direction using the number of particles passing as a measure of the luminosity. The detector consists of 20 aluminium tubes of length 1.5 m and 15 mm diameter surrounding the beam pipe and pointing towards the interaction point. These are filled with C_4F_{10} under constant pressure causing particles to emit Cherenkov radiation, which is then directed to photomultiplier tubes.

Designed to monitor the beam background level to issue a beam abort in case of beam losses, the Beam Conditions Monitor (BCM) [151] can also be used to obtain the bunch-

3. The LHC and the ATLAS detector

by-bunch luminosity by measuring the hit rates. The BCM consists of four diamond sensors placed as horizontal and vertical pairs at each side of the interaction point at a position of $|\eta| = 4.2$ around the beam pipe.

Another luminosity measurement system is the Zero-Degree Calorimeter located at a distance of ± 140 m mainly used for detecting forward neutrons in heavy ion collisions and therefore not described in detail here.

The absolute luminosity measurement is performed ± 240 m away from the interaction point with the ALFA (Absolute Luminosity For ATLAS [150]) detector. It measures elastic scattering at small scattering angles of $3 \mu\text{rad}$, which is only possible with special beam conditions not available during physics runs. For the measurement the Roman-pot technique is used, which is based upon a detector volume, the pot, that is separated from the vacuum of the accelerator by a thin window. For ALFA, a scintillating fibre tracker is used inside the pot. Using the optical theorem, one can relate the elastic scattering amplitude in forward direction to the total inelastic cross section at the interaction point. ALFA, however, has not yet been fully commissioned.

The luminosity is calibrated by so-called van-der-Meer scans [152]. By moving the beams horizontally and vertically against each other one can measure the beam profile, which is an input to the luminosity calculation as shown in Eq. 3.2 in Sec. 3.1. The uncertainty on the integrated luminosity yields 3.4% in 2010 [153, 154]. For the results presented in this thesis using data from 2011 the uncertainty yields 3.7% for the cross section measurement using 1 fb^{-1} [155] and only 1.8% for the analysis using the full data set after further studies in particular to improve the understanding of the van-der-Meer scans have been conducted [156].

3.2.7. Trigger and Data Acquisition

The high bunch-crossing rate of 40 MHz at the Large Hadron Collider is required to obtain substantial event numbers for processes with a low production cross section. Reading out the millions of channels, however, can only be done at a rate of 75 kHz and saving the events to hard disk can only be done at a rate of 200–400 Hz. In order to reduce the rate of events to this level while selecting the physically “interesting” events, a trigger system is used. The trigger system has three levels, Level 1 (L1), Level 2 (L2) and the Event Filter (EF), the latter two collectively called High Level Trigger (HLT). Each level refines the decisions made at the previous level and applies additional selection criteria where necessary. The Data Acquisition System (DAQ) is responsible for buffering the event data from the detector-specific read-out electronics at the L1 trigger accept rate.

The L1 trigger [157] searches for signatures from high- p_T muons, electrons, photons, jets, and τ -leptons decaying into hadrons. It also selects events with large missing transverse energy (E_T^{miss} , see Sec. 4.6) and large total transverse energy. The L1 trigger uses reduced-granularity information from a subset of detectors: the Resistive Plate Chambers (RPC) and Thin-Gap Chambers (TGC) for high- p_T muons, and all the calorimeter sub-systems for the other measurements. The L1 decision must reach the front-end electronics within $2.5 \mu\text{s}$ after the bunch-crossing with which it is associated. If the event is

accepted by L1, the data are moved through the Readout Drivers to the 1574 Readout Buffers. There, they are contained in Readout System units, where they are temporarily stored and on request provided to the subsequent stages of the DAQ/HLT system. The functionality of the trigger and data acquisition systems is shown in Fig. 3.10.

The L2 trigger [158] is seeded by regions of the detector in which the L1 trigger has identified possible trigger objects. These are called Regions of Interest (RoI). To limit the amount of data, the coordinates, energy, and type of signatures of each RoI are used to transfer only the corresponding information from the Readout System. The full granularity and precision of calorimeter and muon chamber data, as well as the data from the inner detector is used, which due to the RoI only constitutes 2% of the full detector data. The L2 trigger reduces the event rate to below 3.5 kHz, with an average event processing time of approximately 40 ms.

If the L2 selection criteria are fulfilled, the events are built and moved to the Event Filter. The Event Filter uses as many post data-taking algorithms (see Chapter 4) as possible to further select events down to a rate that can be recorded for subsequent offline analysis. It reduces the event rate to approximately 200 Hz, with an average event processing time of $\mathcal{O}(4\text{ s})$.

In addition to controlling transmission of data down the trigger selection chain, the Data Acquisition System also provides for the configuration, control and monitoring of the ATLAS detector during data-taking. Supervision of the detector hardware (gas systems, power-supply voltages, etc.) is provided by the Detector Control System.

3.3. Performance of the LHC and ATLAS

The kick-off of the LHC project was a workshop in Lausanne in March 1984 where particle and accelerator physicists came together to discuss the possibility of building a large hadron collider in the LEP tunnel [159]. Eventually, in 1994 the CERN member states decided to build the Large Hadron Collider after the shutdown of LEP in 2000. Parallel to the machine planning the detectors were designed. The ATLAS Letter of Intent [160] came out in 1992 and the Technical Proposal two years later [161] with several subdetector technical design reports following from 1995 onwards. In 1996 it was decided to operate the LHC at a centre of mass energy of 14 TeV. During construction, however, it became clear that one initially would have to run at lower energies around 7–10 GeV to reduce the risk of magnet quenches.

First proton beams were successfully steered around the LHC on 10th September 2008. Only nine days later, however, a faulty electrical connection between two of the accelerator's magnets led to a resistive zone that in return caused an electrical arc puncturing the helium enclosure. This led to a release of helium into the tunnel and additionally damage to several magnets, since the relief discs were unable to contain the pressure rise. Repairs and installation of additional protection systems took more than a year. Eventually, on 23rd September 2009 first proton-proton collisions took place in the LHC at the injection energy of 900 GeV. Six days later the LHC became the most powerful particle accelerator in the world overcoming the Tevatron by reaching proton

3. The LHC and the ATLAS detector

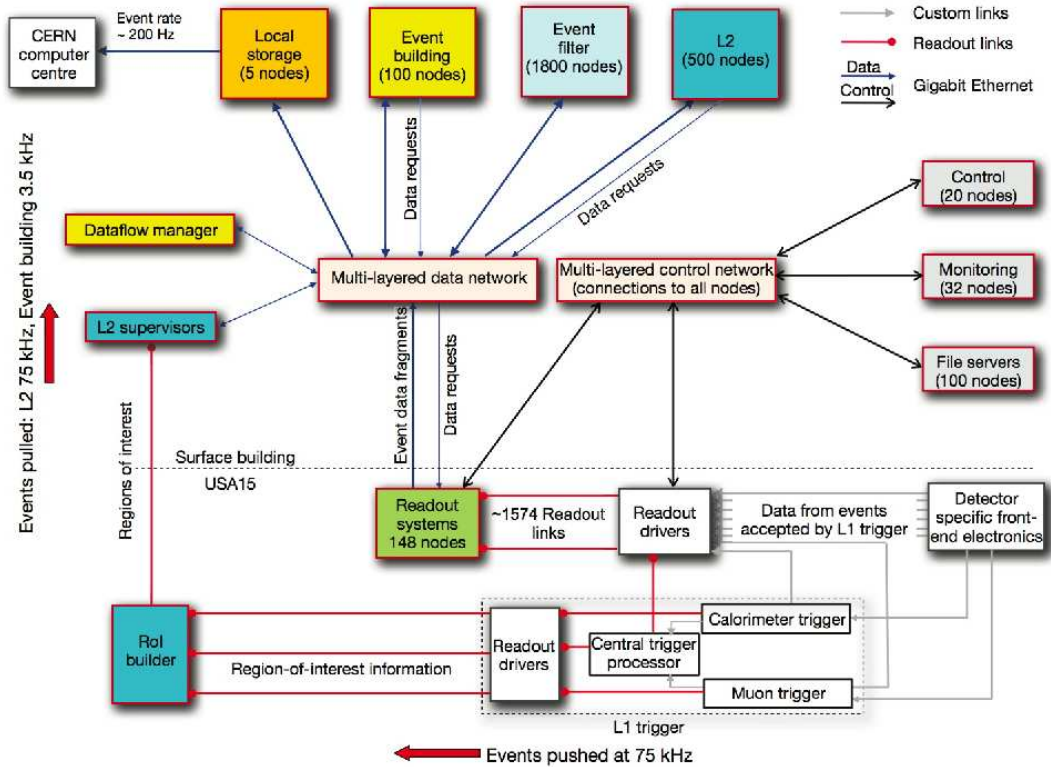


Figure 3.10.: Block diagram of the ATLAS trigger and data acquisition systems. [139]

beams with energies of 1.05 TeV each that were increased to 1.18 TeV during the night. On 30th March 2010, after some more magnet training had taken place during the winter of 2009/2010 the LHC reached a centre of mass energy of 7 TeV in a setup that was considered as a good compromise between machine safety and ensuring that there will be enough data across all the potential discovery areas for the detection experiments.

The LHC continued running at $\sqrt{s} = 7$ TeV throughout the year 2010 delivering a total integrated luminosity of $\mathcal{L} = 48 \text{ pb}^{-1}$ at the interaction point where the ATLAS experiment resides of which $\mathcal{L} = 45 \text{ pb}^{-1}$ were recorded as shown in Fig. 3.11a [153, 154]. At the end of the year 4 weeks were devoted to running with heavy ions.

Over the course of the year 2011 the beam parameters were further improved to reach higher instantaneous luminosities. A significant improvement was the reduction of the beam size in the interaction points by lowering the β^* , which is a measure of the distance from the interaction point at which the beam is twice the size of that at the interaction point, from 3.5 to 1.5. At the same time the beam emittance was decreased to $40 \mu\text{m}$ and a crossing angle of $240 \mu\text{rad}$ was used. A maximum of 1380 bunch pairs was collided in ATLAS and CMS with a bunch spacing of 50 ns. The maximum peak luminosity reached was $3.65 \cdot 10^{33} \text{ cm}^{-2}\text{s}^{-1}$ as shown in Fig. 3.11c. At the end of 2011 a total of $\mathcal{L} = 5.25 \text{ fb}^{-1}$ were on ATLAS tapes (see Fig. 3.11b), which corresponds to a data

taking efficiency of 95% of the detector [155]. After the 2011 proton-proton collisions there were again heavy ion collisions taking place. In 2012, the centre of mass energy was increased to $\sqrt{s} = 8$ TeV adding another 22 fb^{-1} to the pp data set. From mid-January 2013 proton-lead collisions were produced for month, after which the accelerator and detectors were shut down in order to upgrade them for operation at the design centre of mass energy of $\sqrt{s} = 14$ TeV or at least 13 TeV.

The data sets used for final analysis are a subset of the full data set recorded since strict data quality requirements are applied as described in Sec. 5.1.1. In general, the data taken by the ATLAS experiment are divided up into run periods that represent data with a coherent configuration of the detector and the trigger. They therefore reflect significant changes of LHC running conditions and also hardware faults of the detector as described later in Chapter 4.

3. The LHC and the ATLAS detector

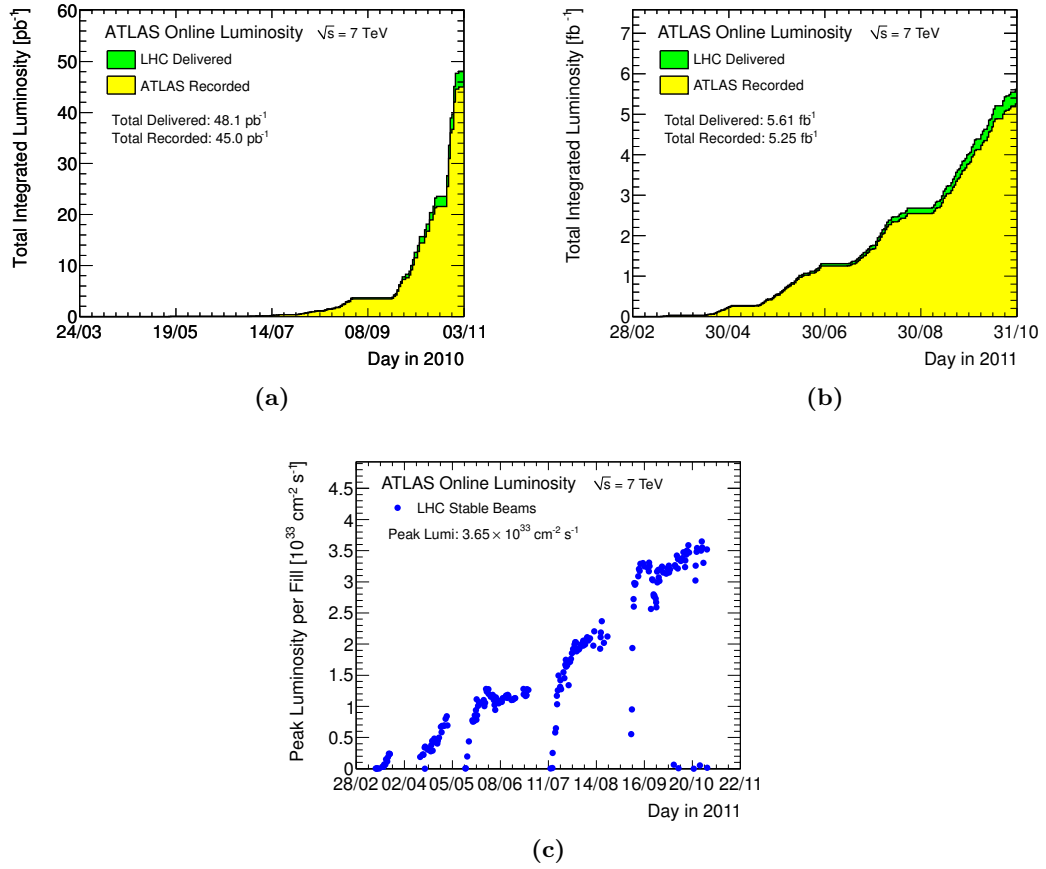


Figure 3.11.: *Cumulative luminosity versus day delivered to (green), and recorded by ATLAS (yellow) during stable beams and for pp collisions at 7 TeV centre of mass energy in (a) 2010 and (b) 2011, and (c) the maximum instantaneous luminosity versus day delivered to ATLAS. The delivered luminosity accounts for the luminosity delivered from the start of stable beams until the LHC requests ATLAS to turn the sensitive detector off to allow a beam dump or beam studies. Given is the luminosity as determined from counting rates measured by the luminosity detectors. These detectors have been calibrated with the use of the van-der-Meer beam-separation method, where the two beams are scanned against each other in the horizontal and vertical planes to measure their overlap function. [162]*

4. Object and event reconstruction

In the proton-proton collisions at the LHC a huge number of particles are created. These particles travel through the ATLAS detector where they leave traces in the different subdetectors depending on their properties. This chapter covers the reconstruction of physics objects that are needed for the identification of top quark pair events in the lepton + jets event topology as described in Sec. 2.2.6.1.

In general, top quarks decay into leptons, bundles of hadronic particles, called jets, and neutrinos, the latter resulting in missing transverse energy. In this analysis τ -leptons are reconstructed as electrons or muons and accounted to the respective channel if they decay leptonically, or as jets if they decay hadronically. In this chapter the corresponding reconstruction algorithms are presented. Since there are three analyses presented in this thesis, the actual objects used in each analysis differ and differences will be described, but the overall reconstruction techniques are the same. In the following the term online refers to actions taking place during data-taking whereas offline refers to post-data taking algorithms.

The task of reconstruction algorithms is to reliably reconstruct physics objects so that they can be compared to the objects created by the Monte Carlo generators as described in Chapter 5. In the QCD-jet dominated environment of the LHC strict lepton identification cuts have to be applied since leptons are the cleanest sign of electroweak physics. To further reduce the amount of hadronic particles being identified as leptons, isolation criteria are introduced. Since the identification algorithms start from the basic detector components, the final physics object needs to be calibrated, which is also described in the following.

4.1. Tracks and vertices

The reconstruction of tracks of charged particles allows for their momentum measurement and aids in particle identification as described later. Algorithms start from energy deposits in the Inner Detector layers. The reconstruction of the tracks' vertices is important to distinguish the primary interaction, i.e. the hard interaction, from additional interactions that might take place in the event and also for the identification of secondary vertices of jets that contain c or b quarks called c -/ b -tagging (see Sec. 4.5).

4.1.1. Track reconstruction

Due to the coverage of the Inner Detector (see Sec. 3.2.3) tracks can be reconstructed up to $|\eta| < 2.5$. A track from a particle traversing the barrel of the ID would typically lead to 3 pixel clusters, 8 SCT strip clusters and more than 30 TRT straw hits. Tracks are

4. Object and event reconstruction

reconstructed in the ID using a sequence of algorithms described in detail in Reference [163]. The so-called inside-out algorithm starts from three hits found in the Pixel or SCT Detectors and adds hits moving away from the interaction point using a combinatorial Kalman filter [164]. Ambiguities in the track candidates found in the silicon detectors are resolved by judging their number of hits and fit quality. After resolving all ambiguities the track candidates are refitted and additional space-point measurements from the TRT are added if they improve the fit quality. Otherwise, the hits are assigned to the track as outliers. If a reconstructed track does not have a hit in a silicon layer, this is referred to as pixel or SCT hole. The inside-out algorithm is the baseline algorithm designed for the efficient reconstruction of primary charged particles. Primary particles are defined as particles with a mean lifetime of greater than 3×10^{-11} s directly produced in a pp interaction or from the subsequent decays or interactions of particles with a lifetime shorter than 3×10^{-11} s [165]. In a second stage, back-tracking is performed: The track search starts from segments reconstructed in the TRT and extends them inwards by adding silicon hits. The purpose of back-tracking is to reconstruct secondaries, which are particles produced in the interactions of primaries.

The coordinates used for tracks and used in the following are different to the four-vectors of reconstructed particles: Since the tracks that are contained in the magnetic field they described by a helix. It is parametrised by the signed transverse (d_0) and longitudinal (z_0) impact parameter and the azimuthal and polar angles θ and ϕ of the track tangent at perigee and the charge signed inverse transverse momentum q/p_T . Ultimately, the tracking performance depends on the accurate placement of the detector hits and their errors. Therefore, the detector was aligned as described in Reference [166]. The current alignment precision is 4 and 10 μm for the pixel and SCT barrel sensors, respectively.

4.1.2. Vertex reconstruction

The identification of vertices is essential to distinguish the primary vertex associated with the hard interaction from additional pileup vertices that might be present in the event (see also Chapter 5). This became even more important with the higher LHC luminosity towards the end of 2011 running where on average up to 18 pp interactions took place simultaneously as shown in Fig. 4.1. Vertex reconstruction starts with vertex seeds that are found by looking for the global maximum in the distribution of z coordinates of the tracks in the event, computed at the point of closest approach to the beam spot center [167]. The vertex position is determined using an iterative vertex finding algorithm [168] taking the seed and neighbouring tracks as input. The compatibility of each track with the vertex is obtained from the χ^2 of the fit. Tracks displaced by more than 7σ from the vertex are used to seed a new vertex and the procedure is repeated until no additional vertices can be found. The beam spot position serves as a stringent constraint in the r - ϕ plane and defines the luminous region in the z -direction [169]. The vertex resolution is roughly 30 μm in the transverse and 50 μm in the longitudinal plane in 2010 data [167]. For 2011 data, the vertex resolution has been slightly improved since the minimum

transverse momentum of the tracks used to define a reconstructible interaction is raised from 100 MeV to 400 MeV [165].

The primary vertex associated with the hard interaction of interest is defined as the vertex with the largest sum of the transverse momenta $\sum p_T$ of the associated tracks since one expects the highest momentum transfer from the hard scattered event. To ensure that the events used in this work stem from a pp collision and not from non-collision background such as beam halos this vertex has to have more than four tracks, otherwise the event is rejected.

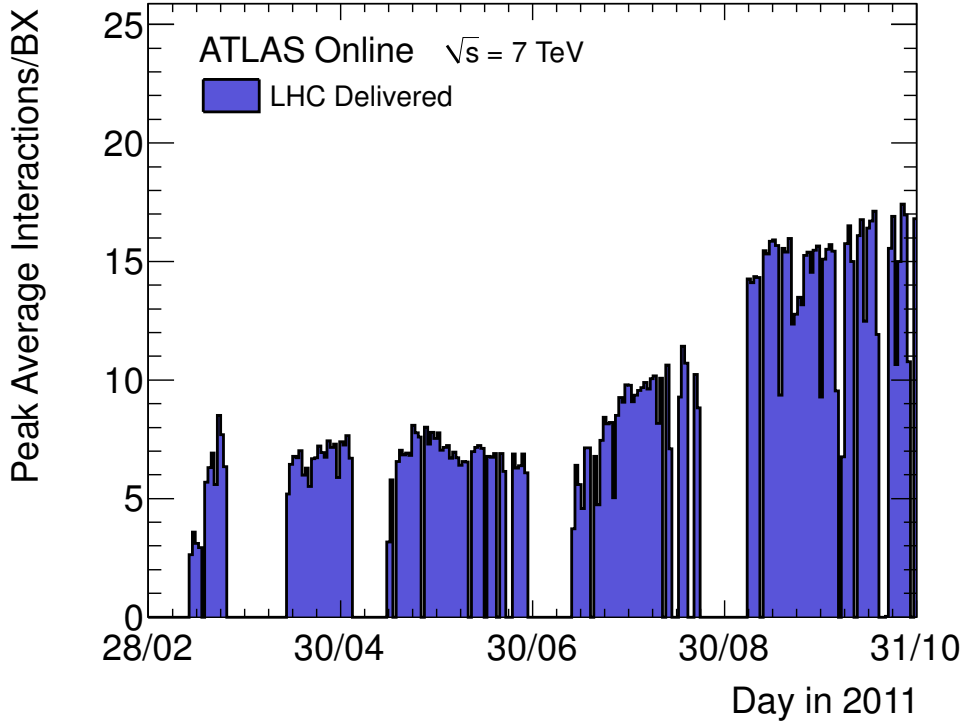


Figure 4.1.: Mean number of interactions per bunch crossing at the peak of the fill for each day in 2011 for data used in physics analyses. The mean is calculated from all bunch crossings in a lumi-block. [165]

4.2. Electrons

Excellent electron identification with high efficiency and high jet rejection rate over a broad energy range is essential to suppress the large multi-jet background while maintaining the top signal. For the analyses presented in this work electrons are reconstructed from energy clusters in the central region of $|\eta_{\text{cluster}}| < 2.47$ in the electromagnetic calorimeter (see Sec. 3.2.4) and then associated to a track in the ID that points to the cluster [170, 171]. The transition region between the barrel and endcap calorimeters,

4. Object and event reconstruction

$1.37 < |\eta| < 1.52$, has a large amount of material in front of the first active calorimeter layer, which spoils identification efficiency and energy calibration and is therefore excluded.

4.2.1. Electron identification and reconstruction

The EM clusters are identified by using a sliding-window algorithm that searches for seed clusters of longitudinal towers with total transverse energy above 2.5 GeV. The window size corresponds to the fine granularity of the calorimeter middle layer of 3×5 in units of 0.025×0.025 in $\eta \times \phi$ space. An electron is reconstructed if a track extrapolated from its last measurement point to the middle layer of the calorimeter is matched to a seed cluster within certain distances in η and ϕ . The electron cluster is subsequently rebuilt using 3×7 (5×5) longitudinal towers of cells in the barrel (endcaps) to take into account the different detector geometry in these regions. The cluster energy is thereupon determined by adding up the estimated energy deposit in the material in front of the EM calorimeter, the measured energy deposit in the cluster, the estimated external energy deposit outside the cluster (lateral leakage), and the estimated energy deposit beyond the EM calorimeter (longitudinal leakage) [147]. The four-vector is computed using the energy of the cluster while the η and ϕ directions are taken from the corresponding track parameters at the vertex. The transverse energy yields $E_T = E_{\text{cluster}} / \cosh \eta$. For the 2010 analysis a transverse energy $E_T > 20$ GeV is required. The 2011 analyses select $E_T > 25$ GeV electrons due to the higher trigger thresholds (see Sec. 4.2.3).

The identification of electrons is based on independent cuts that are using variables from the calorimeter, the tracking system and combinations thereof that provide good separation between isolated or non-isolated signal electrons, background electrons (primarily from photon conversions and Dalitz $\pi^0 \rightarrow e^+e^-\gamma$ decays) and jets faking electrons. In ATLAS, there are in general three different sets of cuts with increasing background rejection power: **loose**, **medium** and **tight** [170]. The **loose** set makes use of shower shape variables of the EM calorimeter middle layer and hadronic leakage variables. The **medium** set adds requirements on the EM calorimeter strip layer variables, track quality and track-cluster matching. The **tight** cut set additionally applies cuts on the ratio of the cluster energy to the track momentum, E/p , and employs particle identification using the TRT, discrimination against photon conversions via a b -layer hit requirement and information about reconstructed conversion vertices. The criteria are summarised in Tab. 4.1. For the 2010 analysis the **tight_withTrackMatch** requirement is used. The additional suffix applies due to the fact that in the previous **tight** cut set definition [170] no cluster-track match is required.

For 2011 data the selection is reoptimised to cope with the new running conditions of the LHC. Since there was more pileup (see Sec. 3.1) and a higher instantaneous luminosity, the electron trigger (see Sec. 4.2.3) rate was heavily increased. Since one did not want to increase the trigger threshold too much, an electron identification with higher rejection power but with minimal reduction impact on efficiency was needed and thus the cuts mentioned above were adjusted accordingly. For the 2011 analysis (a) the **tight** cut set is required and for the 2011 analysis (b) the **tightpp** cut set is used, which

Table 4.1.: Definition of variables used for loose, medium and tight electron identification. [171]

Type	Description	Name
Loose selection		
Acceptance	$ \eta < 2.47$	
Hadronic leakage	Ratio of E_T in the first layer of the hadronic calorimeter to E_T of the EM cluster (used over the range $ \eta < 0.8$ and $ \eta > 1.37$)	R_{had1}
	Ratio of E_T in the hadronic calorimeter to E_T of the EM cluster (used over the range $ \eta > 0.8$ and $ \eta < 1.37$)	R_{had}
Middle layer of EM calorimeter	Ratio of the energy in 3×7 cells over the energy in 7×7 cells centred at the electron cluster position	R_η
	Lateral shower width, $\sqrt{(\sum E_i \eta_i^2)/(\sum E_i) - ((\sum E_i \eta_i)/(\sum E_i))^2}$, where E_i is the energy and η_i is the pseudorapidity of cell i and the sum is calculated within a window of 3×5 cells	$w_{\eta 2}$
Medium selection (includes loose)		
Strip layer of EM calorimeter	Shower width, $\sqrt{(\sum E_i (i - i_{\text{max}})^2)(\sum E_i)}$, where i runs over all strips in a window of $\Delta\eta \times \Delta\phi \approx 0.0625 \times 0.2$, corresponding typically to 20 strips in η , and i_{max} is the index of the highest-energy strip	w_{stot}
	Ratio of the energy difference between the largest and second largest energy deposits in the cluster over the sum of these energies	E_{ratio}
Track quality	Number of hits in the pixel detector (≥ 1)	n_{pixel}
	Number of total hits in the pixel and SCT detectors (≥ 7)	n_{Si}
	Transverse impact parameter ($ d_0 < 5$ mm)	d_0
Track-cluster matching	$\Delta\eta$ between the cluster position in the strip layer and the extrapolated track ($ \Delta\eta < 0.01$)	$\Delta\eta$
Tight selection (includes medium)		
Track-cluster matching	$\Delta\phi$ between the cluster position in the middle layer and the extrapolated track ($ \Delta\phi < 0.02$)	$\Delta\phi$
	Ratio of the cluster energy to the track momentum	E/p
	Tighter $\Delta\eta$ requirement ($ \Delta\eta < 0.005$)	$\Delta\eta$
Track quality TRT	Tighter transverse impact parameter requirement ($ d_0 < 1$ mm)	d_0
	Total number of hits in the TRT	n_{TRT}
Conversions	Ratio of the number of high-threshold hits to the total number of hits in the TRT	f_{HT}
	Number of hits in the b-layer (≥ 1) (if expected)	n_{BL}
	Veto electron candidates matched to reconstructed photon conversions	

4. Object and event reconstruction

has even harsher cuts to reject background. The 2011 analysis (b) additionally applies a cut on the longitudinal impact parameter z_0 of the ID track at the point of closest approach of the track to the primary vertex of $|z_0| < 2$ mm.

Due to hardware problems in the EM calorimeter during data-taking, regions with no or below nominal high-voltage, dead front-end boards or dead optical links and isolated dead or high noise channels are masked in the reconstruction. These are stored in so-called object quality maps in the $\eta - \phi$ plane. Additionally, in 2011 a controller board responsible for six neighbouring front-end boards failed resulting in an area in the LAr calorimeter where reconstruction was not possible for run periods E–H (see ATLAS/LHC performance in Sec. 3.3).

The reconstruction efficiencies in data and Monte Carlo simulation are compared using a so-called tag-and-probe method. By selecting a sample of Z bosons decaying to electrons with high purity one can *tag* the first electron that passes the selection and then *probe* whether there is a second electron with opposite charge fulfilling the same selection criteria. Here, *probe* candidates are electrons with the same kinematic requirements. The invariant mass of the two electrons has to be close to the Z boson mass. Performing this study in data and Monte Carlo one obtains efficiency maps for both and can then correct the efficiencies in the Monte Carlo samples using scale factors in the form of $\text{SF} = \varepsilon_{\text{data}}/\varepsilon_{\text{MC}}$. These change the weight of individual events depending on the kinematics of the electron. The reconstruction efficiency of **tight** electrons in the 2010 data set is shown in Fig. 4.2. The scale factor obtained from 2010 data is a plain $\text{SF}_{\text{reco}} = 1.000 \pm 0.015$. For the analysis using 0.7 fb^{-1} of 2011 data the scale factors are divided in three regions in pseudorapidity of the associated cluster and for the 2011 full data set analysis binned in nine η and six E_T bins to account for regions with different efficiencies while still having sufficient statistic in each bin.

4.2.2. Electron energy calibration and resolution

The electromagnetic calorimeter energy scale was derived from test-beam measurements with uncertainties varying from 0.3% to 1.6% as a function of E_T and η for the region of $|\eta| < 2.47$ used here [171]. Uncertainties are reduced using the well-known masses of the Z boson and the J/ψ particle. Further reduction is achieved by comparing the ratio E/p of the energy E measured in the calorimeter and the momentum p measured by the Inner Detector using $W \rightarrow e\nu$ events. Using these results the energy scale in the Monte Carlo samples is smeared to match the dielectron mass distribution. In 2010 data the electron energy scale is corrected in addition. Distributions showing the outcome of the electron energy calibration are shown in Fig. 4.3.

4.2.3. Electron trigger

In order for a collision event to be stored for further analysis it has to pass one of the ATLAS trigger chains as described in Sec. 3.2.7. For the analyses in this thesis single lepton triggers are used. Here, non-prescaled triggers, i.e. if they fire each event is recorded and none are skipped due to a too high rate, are chosen. This guarantees full

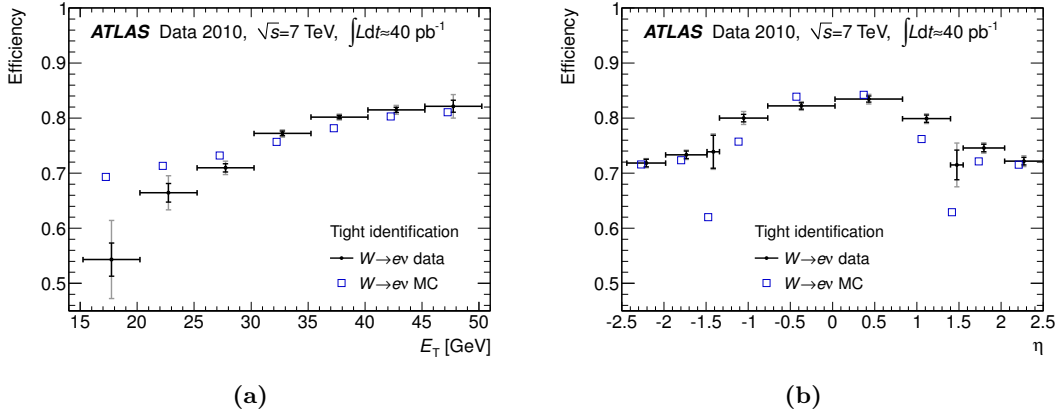


Figure 4.2.: *Electron reconstruction efficiencies used for scale factor construction measured from $Z \rightarrow ee$ events in 2010 data (black dots) and predicted by MC (blue squares) for tight identification as a function (a) of E_T and integrated over $|\eta| < 2.47$ excluding the transition region $1.37 < |\eta| < 1.52$ and (b) of η and integrated over $20 < E_T < 50$ GeV. In the transition region modelling issues are observed which is why this region is excluded for data analysis. The results for the data are shown with their statistical (inner error bars) and total (outer error bars) uncertainties. The statistical error on the MC efficiencies plotted as open squares is negligible. For clarity, the data and MC points are slightly displaced horizontally in opposite directions. [171]*

statistics of the analysed data set but also means that thresholds are moderately higher. The trigger namings are such that they contain the E_T or p_T threshold at which they have reached their efficiency plateau. The offline selection threshold (see Sec. 4.2.1) is chosen a few GeV above to ensure full efficiency.

The L1 trigger selects electromagnetic objects if the energy deposited in the EM calorimeter in two adjacent towers of $\Delta\eta \times \Delta\phi = 0.1 \times 0.1$ size is above a certain threshold. At L2 and EF very similar reconstruction algorithms as at offline level are deployed. At L2 a different seeding and faster tracking algorithms are used. The EF typically uses looser identification cuts to remain fully efficient with respect to the offline objects. Since the trigger menus continuously evolve to account for the increasing LHC luminosity [173, 174] different trigger chains are used for the analyses. These are summarised in Tab. 4.2.

Similar to the reconstruction efficiency, the electron trigger efficiency is corrected for with the help of the tag-and-probe method. The *tag* electron has to fulfil the object selection criteria and additionally has to match a corresponding object of the trigger at question within a cone of $\Delta R = 0.15$. Candidates for *probe* electrons have to pass the selection criteria, have opposite charge and the resulting dielectron mass has to be close to the Z boson mass. If these requirements are met it is tried to find a trigger match

4. Object and event reconstruction

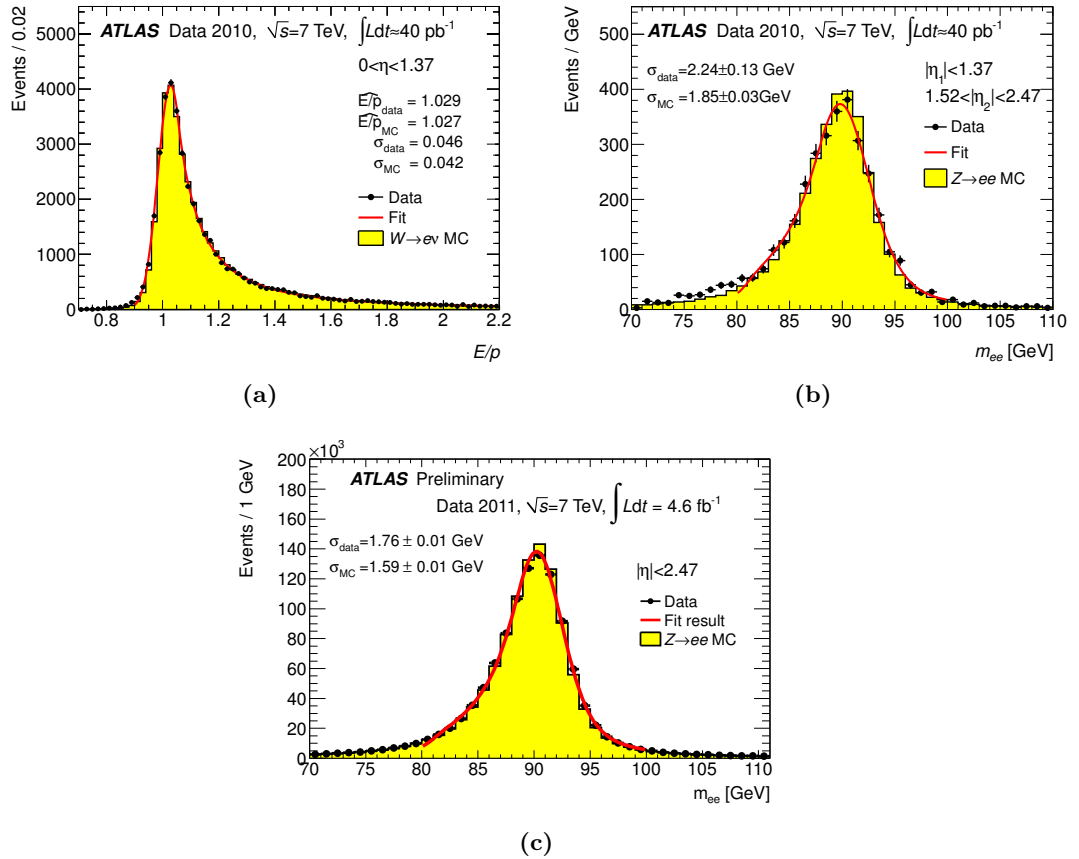


Figure 4.3.: *Electron energy calibration distributions: (a) E/p distributions of electrons and positrons from $W \rightarrow e\nu$ decays for $0 < |\eta| < 1.37$ in data (full circles with statistical error bars) and $W \rightarrow e\nu$ MC (filled histogram). The result of the fit with a Crystal Ball function to the data is also shown (full line). The most probable value ($\widehat{E/p}$) and the Gaussian width (σ) of the fitted Crystal Ball function are given both for the data and the signal MC. (b) Reconstructed dielectron mass distribution for $Z \rightarrow ee$ decays after applying the baseline $Z \rightarrow ee$ calibration for $|\eta| < 2.47$ excluding the crack region. The data (full circles with statistical error bars) are compared to the signal MC expectation (filled histogram). The fits of a Breit-Wigner convolved with a Crystal Ball function are shown (full lines). The Gaussian width (σ) of the Crystal Ball function is given both for data and MC simulation. [171] (c) same as (b) for 2011 data. [172]*

Table 4.2.: *Electron trigger chains used in the 2010 and 2011 run periods (see Sec. 3.3) for the analyses presented in this work. The latter two triggers for run periods L–M 2011 are combined with a logical OR to account for inefficiencies of the e22vh_medium1 trigger at high E_T .*

Run period	L1	L2	EF	analysis
E4–I2 2010	EM13	e15_medium	e15_medium	2010
B2–G5 2011	EM18	e20_medium	e20_medium	2011 (a)
B2–J 2011	EM18	e20_medium	e20_medium	2011 (b)
K 2011	EM16	e22_medium	e22_medium	2011 (b)
L–M 2011	EM16_VH	e22vh_medium1	e22vh_medium1	2011 (b)
L–M 2011	EM30	e45_medium1	e45_medium1	2011 (b)

and therewith the efficiency in data and MC is determined. For the 2010 Monte Carlo a plain scale factor is used whereas for both 2011 analyses eighteen regions in cluster pseudorapidity and six in E_T are distinguished.

4.2.4. Electron isolation

In addition to the identification cuts, calorimeter isolation cuts are applied to avoid misidentification of narrow jets or leptonic decays of jets as primary electrons. Jets consisting mostly of π^0 mesons for instance can also have just one single track, but will likely distribute their energy in a larger area in the calorimeter. The isolation is measured in a cone around the centre of the reconstructed electron as energy in the calorimeter by summing the clusters. The energy of the electron itself is subtracted. The E_T deposited in the calorimeter towers in a cone of radius $R = 0.2$ around the electron position is computed and has to be less than 4 GeV for the 2010 analysis and less than 3.5 GeV for the 2011 analysis (a). For the latter, a p_T -dependent correction is applied to take into account the leakage of the electron energy outside that cone and another correction to account for underlying pileup events. The 2011 analysis (b) employs more advanced isolation criteria. In addition to the calorimeter isolation, track isolation is required by summing the transverse momenta of all tracks in the ID that fall inside a cone of size $\Delta R = 0.3$. Instead of a constant isolation, one aims for uniform isolation efficiency with respect to certain offline electron selection across η and E_T . The selection criteria for both isolation types are consequently obtained with the tag-and-probe method with Z bosons using the full 2011 data set. The *probe* electron is analysed with respect to its isolation properties and hence an efficiency map is derived. The calorimeter isolation variables are corrected for energy leakage into the isolation cone and also for additional energy depositions from pileup events. The working point used for this analysis is at 90% efficiency each for calorimeter and track isolation with the respective cone sizes described above.

The identification efficiency of isolated electrons is corrected for in simulation with

4. Object and event reconstruction

respect to data using tag-and-probe. *Tag* electrons are isolated electrons fulfilling all selection criteria, *probe* candidates have to meet the selection requirements excluding isolation, and as above for reconstruction and trigger efficiencies have opposite charge and lead to a dielectron mass within the Z boson mass window. The efficiency is then obtained by asking for isolation of the *probe* electron. The identification scale factors are determined for eight bins in cluster pseudorapidity and six bins in transverse energy in 2010 and for 2011 using 18 η and (a) five and (b) eight E_T bins.

4.3. Muons

As for electrons, good muon identification and reconstruction have to be ensured to obtain large statistics at a low fake rate. These are provided by the large Muon System of the ATLAS detector as described in Sec. 3.2.5. For the analyses covered in this work muons are reconstructed from tracks in the Muon System and the Inner Detector and combined to a single object. Therefore, due to the coverage of the ID only muons in the central region $|\eta| < 2.5$ are considered.

4.3.1. Muon identification and reconstruction

Muon candidates are reconstructed by searching for track segments in the different layers of the muon chambers using Hough transforms [175], a computationally efficient procedure for detecting lines or tracks. Starting from the outermost layer these segments are then combined using a fit that accounts for material effects obtained either from the observed calorimeter energy deposition or from a parametrisation [176]. This so-called standalone track is then matched by constructing a χ^2 from the track parameters of the ID and the standalone fits. The MuId algorithm used here then re-fits the combined track candidate by starting from the ID track subsequently adding the MS measurements, which is consequently referred to as combined muon. A combined muon can also be found by the MuGir1 algorithm seeded by a track in the ID that is extended to the Muon System. The quality of the muons used in this work is referred to as `tight` since they guarantee a low background level. The transverse momenta of the muons used in this work have to be $p_T > 20$ GeV. For the 2011 analysis (b) the threshold is increased to 25 GeV to match the one for electrons.

In order to reduce the number of muons from secondary decays, additional requirements are applied to the ID track quality of the muon: The muon has to hit one of the b-layer modules if the region is not dead and leave at least another one in the pixel detector. More than five hits in the SCT have to be found while the number of holes in the pixel detector and the SCT together has to stay below three (see Sec. 4.1.1). For the TRT the following cuts are applied where n denotes the number of TRT hits plus the number of TRT outliers (see also Sec. 4.1.1):

- for $|\eta| < 1.9$: $n > 5$ and $n_{\text{outliers}}/n < 0.9$,
- for $|\eta| \geq 1.9$: if $n > 5$ require $n_{\text{outliers}}/n < 0.9$.

As for electrons, the 2011 analysis (b) additionally applies a cut on the longitudinal impact parameter, z_0 , of the ID track at the point of closest approach of the track to the primary vertex of $|z_0| < 2$ mm.

The reconstruction efficiency is obtained using the tag-and-probe method in $Z \rightarrow \mu\mu$ events in the same way as described for electrons in Sec. 4.2.1. The muons have to be oppositely charged and their invariant mass has to be around the Z boson mass. The *tag* muon has to be combined whereas *probe* muon candidates only have to have an ID track with the quality cuts described above and be well separated in $\Delta\phi$. The reconstruction efficiency and the derived scale factors in 2010 data are shown in Fig. 4.4. For the 2010 analysis a plain reconstruction scale factor is used whereas for the 2011 analyses scale factors are split into different regions in p_T , η and ϕ .

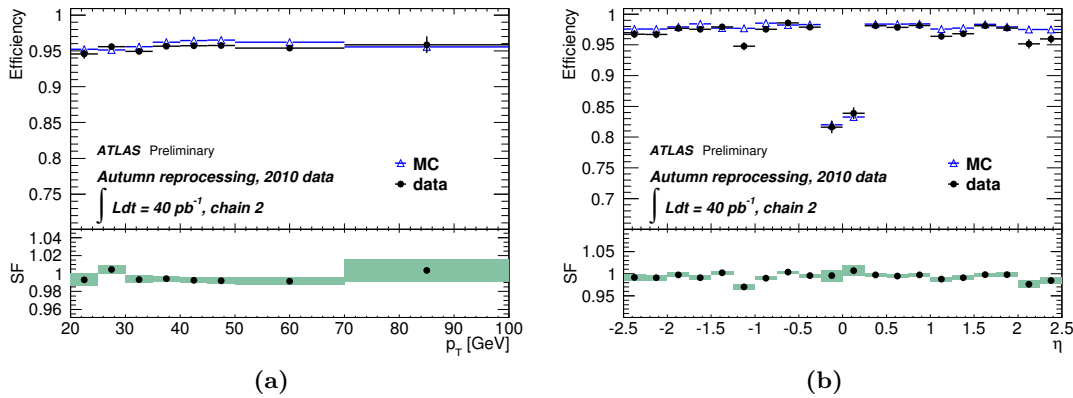


Figure 4.4.: Muon reconstruction efficiencies and scale factors measured from $Z \rightarrow \mu\mu$ events in 2010 data and predicted by MC for combined muons as a function (a) of p_T and integrated over $|\eta| < 2.5$ and (b) of η and integrated over $20 \text{ GeV} < p_T < 100 \text{ GeV}$. The efficiencies obtained from data (dots) without background correction and Monte Carlo simulation (open triangles) including backgrounds, are shown in the upper part of each figure. The corresponding scale factors are shown in the lower part. [177]

4.3.2. Muon momentum calibration and resolution

The muon momentum calibration and resolution is obtained using $Z \rightarrow \mu\mu$ and $W \rightarrow \mu\nu$ events [178]. Z -events are sensitive to the momentum resolution since the width of the reconstructed dimuon invariant mass peak at the Z pole is a convolution of the natural width of the Z boson and the muon momentum resolution. Events with muons from a W boson decay are used to evaluate the difference of the independent momentum measurements of ID and MS. Furthermore, external constraints are used from the analysis of data taken without the magnetic field of the toroid. To account for differences between data and simulation the muon momentum scale is shifted and the

4. Object and event reconstruction

resolution smeared. The resulting invariant mass spectra in the Z boson mass range are shown in Fig. 4.5.

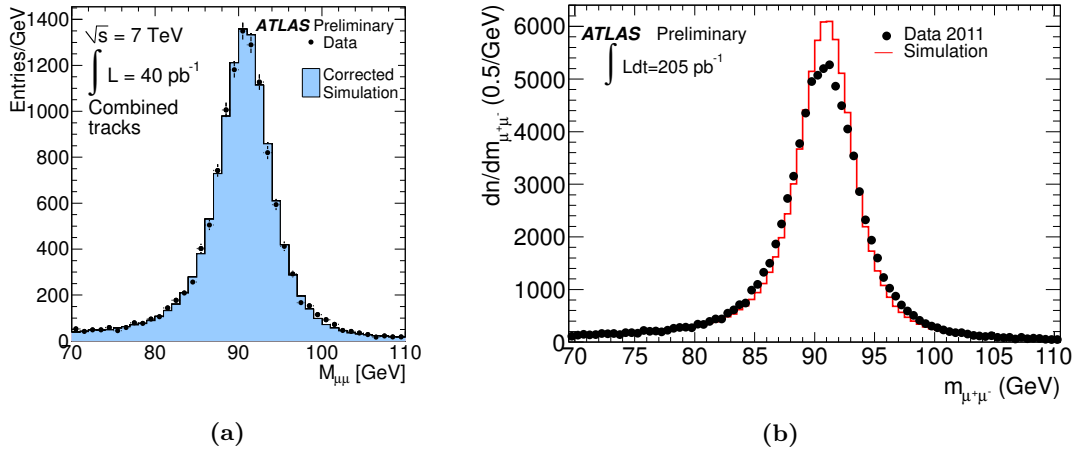


Figure 4.5.: Muon momentum calibration distributions for combined muons with $p_T > 20 \text{ GeV}$: (a) Dimuon invariant mass comparison in the Z boson mass range between 2010 collision data (dots) and simulation (full histogram), after correcting the simulated muon p_T . The distribution is integrated over the full range of η . [178]
(b) Invariant mass distribution of muon pairs with $|\eta| < 2.5$ and calorimeter isolation for 2011 data (dots) and simulation (histogram). [179]

4.3.3. Muon trigger

The muon trigger chambers extend over the whole ϕ range, but only up to $|\eta| < 2.4$. Using Resistive Plate Chambers (RPC) in the barrel ($|\eta| < 1.05$) and Thin Gap Chambers (TGC) in the endcaps ($1.05 < |\eta| < 2.4$) Regions of Interest (RoI) are selected [147]. Based on hit coincidences within different RPC or TGC layers inside the programmed geometrical windows defining the transverse momentum region, the Muon to Central Trigger Processor Interface calculates the number of muonic events for six different transverse momentum threshold signatures. These are fixed ranging from 5 to 40 GeV. The RoI of size $\Delta\eta \times \Delta\phi = 0.4 \times 0.4$ are then passed on to the HLT.

The L2 system accesses the RoI with its full granularity. Trigger decisions are applied in a series of steps based on signature and sequence tables. If a muon candidate is found, the existing measurement is sequentially refined by acquiring additional information from the detectors: a track fit is performed using tracks in the Monitored Drift Tubes and the transverse momentum is evaluated. These muon tracks can be combined with tracks in the Inner Detector that are not available at L1. The L2 algorithm is also capable of discriminating between isolated and non-isolated muon candidates by using information from the calorimeters. For further details refer to References [139, 147].

Table 4.3.: *Muon trigger chains used in the 2010 and 2011 run periods (see Sec. 3.3) for the analyses presented in this work.*

Run period	L1	L2	EF	analysis
E4–F2 2010	MU0	mu10_MSonly	mu10_MSonly	2010
G1–G5 2010	MU0	mu13	mu13	2010
G6–I2 2010	MU10	mu13_tight	mu13_tight	2010
B2–G5 2011	MU10	mu18	mu18	2011 (a)
B2–I 2011	MU10	mu18	mu18	2011 (b)
J–M 2011	MU11	mu18_medium	mu18_medium	2011 (b)

The EF accesses the full event at full granularity using offline algorithms. As for the electron trigger the algorithms are employed around the regions found by L2. The EF starts by reconstructing tracks in the Muon Spectrometer and looks for regions of activity within the detector subsequently performing pattern recognition and full track fitting. The tracks are then extrapolated to their origin. Finally the information obtained is combined with the reconstructed tracks from the inner detector. The muon trigger chain evolved over time during LHC running [173]. The chains used in this work are summarised in Tab. 4.3. The choice of triggers is again based on the preference of using low-threshold but unrescaled triggers. At the initial data taking stage in 2010 there were no combined muon triggers available but muons were instead triggered using the Muon System only. Towards the end of 2011 data taking the `mu18_medium` trigger was introduced. Here, the term `medium` refers to the muon quality as described for `tight` above in Sec. 4.3. The `medium` cut set includes muons that pass `tight` requirements and additionally muons reconstructed with an extended track. Furthermore, muons found by either the `MuGirl` or the `MuTagIMO` algorithm close to the acceptance hole within $|\eta| < 0.2$ (see Sec. 3.2.5) or with at least two muon track segments are included. `MuTagIMO` is an algorithm seeded by a track in the ID that reconstructs muons while relying on the measurement of the transverse momentum in the ID [147].

A wrong timing configuration was used by the RPC in 2011 for a fraction of data-taking period L. This affected the high- p_T thresholds of the L1 trigger, i.e. L1_MU11 and higher, in the barrel region. Therefore, all triggers seeded from there, such as the `mu18_medium` used in this analysis, were compromised and result in typically 20% efficiency loss in this region. This is reflected in the MC simulation.

The muon trigger efficiency in simulation is corrected for the efficiency determined in data using tag-and-probe. The `tag` and `probe` requirements are similar to the one described for the electron trigger in Sec. 4.3.3. For the 2010 analysis a 3×3 binning in $\eta \times \phi$ is used. The 2011 analysis (a) adds several different regions in transverse momentum. The 2011 analysis (b) again uses only $\eta \times \phi$ binning but splits the scale factors into three data taking periods, namely B-I, J-K and L-M, because of the different triggers and the LHC data-taking conditions.

4. Object and event reconstruction

4.3.4. Muon isolation

In addition to the identification requirements, isolation cuts are applied on the muon. These are intended to suppress the contribution of so-called *non-prompt* muons, i.e. muons that stem from secondary decays and not from the hard interaction itself. Since these decays mostly take place in jets containing heavy quarks, demanding isolation shows good rejection power against non-prompt muons.

Thus, calorimeter and track isolation are required as described in Sec. 4.2.4 for electrons. For the 2010 analysis and the 2011 analysis (a) cones of radii $\Delta R = 0.3$ in which the sum of transverse energy or momenta must not exceed 4 GeV are used for both isolation types. The additional rejection factor with respect to non-prompt muons is approximately four [177]. Since it was found that large cone sizes for calorimeter isolation are prone to the presence of additional interactions, isolation was re-optimised for the 2011 analysis (b). Consequently, the calorimeter isolation cone is reduced to $\Delta R = 0.2$ while maintaining the 4 GeV cut. The track isolation cone is kept but the threshold lowered to 2.5 GeV leading to a rejection factor of about 5.5 with respect to requiring no isolation.

The identification efficiency with respect to the additional isolation cuts in data and MC is compared using the tag-and-probe method in $Z \rightarrow \mu\mu$ events similarly as described for electrons in Sec. 4.2.4. The 2010 scale factor is a plain factor whereas the scale factors for the 2011 analyses are divided into different regions in p_T , η and ϕ . The 2011 analysis (b) is furthermore split into the data taking periods B–I, J–K and L–M.

4.4. Jets

Jets are bundles of hadronic particles that form due to confinement (see Chapter 2) Events with top quarks contain several jets of hadrons in the final state. These are reconstructed from energy depositions and charged particle momenta in the detector. The jets point back to the primary interaction, i.e. to the partons the jets originated from, but one has to correct for hadronisation and detector effects. The task of a jet algorithm is to allow comparisons between theoretical predictions, which are usually described by perturbative calculations, and experimental data. The challenge hereby lies in the fact that QCD employs colour-charged quarks and gluons at short distances, while detectors only observe colour singlet bound states, i.e. hadrons, at rather long distances. The jet algorithm associates clusters of *particles* (at parton, particle or detector level) into jets such that one can relate their kinematic properties to those of the energetic partons produced in the hard scattering process.

There are two classes of jet definitions for hadron colliders. One possibility is based on proximity in coordinate space, cone jet algorithms [180, 181]) whereas the other uses proximity in momentum space by successively merging pairs of *particles* in order of increasing relative transverse momentum, k_T algorithms [182, 183]). For this work only the anti- k_T algorithm of the k_T family is used and detailed in the following.

4.4.1. The anti- k_T algorithm

The class of k_T algorithms are so-called cluster type jet-finders based on sequential pairwise recombination of particles. Their computing performance is nowadays competitive with the other commonly used jet algorithms such as cone algorithms [184]. The particles are analysed with respect to their relative transverse momentum squared, defined by:

$$d_{ij} = \min(p_{T,i}^{2s}, p_{T,j}^{2s}) \frac{\Delta R_{ij}^2}{R^2}, \quad \Delta R_{ij}^2 = (\eta_i - \eta_j)^2 + (\phi_i - \phi_j)^2, \quad (4.1)$$

where R is a free distance parameter which is used to control the size of the jets and $p_{T,i/j}$, $\phi_{i/j}$ and $\eta_{i/j}$ are the transverse momentum, azimuthal angle and pseudorapidity of the particles, respectively. The k_T algorithm starts from the calorimeter clusters or towers in four-momentum representation, from now on called object. For each object the geometrically nearest neighbour (in terms of ΔR_{ij}) and its squared p_T with respect to the beam $d_{i,B} = p_{T,i}^{2s}$ is obtained. One then finds the minimal value d_{\min} . If $d_{\min} = d_{i,B}$, the object becomes a jet, otherwise objects i and j are merged. One identifies the objects whose nearest neighbours have changed, updates the d_{ij} values and then finds the new d_{\min} until no objects are left.

Depending on the parameter s , three different classes of clustering algorithms are distinguished. For $s = 1$ one speaks of the original k_T algorithm which clusters soft objects before harder ones are added to the final jet [185]. In case $s = 0$, only the geometrical distance between the objects is considered, the algorithm being called the Cambridge-Aachen algorithm [182]. In this analysis the choice is $s = -1$, i.e. the inverse square of the transverse momenta is compared. This is the anti- k_T algorithm [184, 186], used in ATLAS by default with distance parameters $R = 0.4$ and $R = 0.6$. Since top quark events are characterised by several jets in the final state, the smaller distance parameter $R = 0.4$ is chosen in this work to resolve the jets. The advantage of the anti- k_T algorithm is that hard objects collect adjacent soft ones before these are clustered into harder objects, which figuratively reverts the effect of radiation. If the soft objects are all within a radius less than $2R$ from the hard object, the resulting jet has a conical shape. If two hard objects are within $R < \Delta R < 2R$ the objects in the overlapping region are associated to one of them depending on their d_{ij} leading to more complex jet shapes. If they are within $R < \Delta R$ they are merged and shapes can become more stretched.

In contrast to the majority of cone algorithms the k_T algorithms are all collinear- and infrared-safe, i.e. insensitive to the addition of soft particles and therefore theoretically well behaved with respect to soft gluon emissions [187]. They are furthermore expected to yield more precise particle mass measurements [188] and they allow one to decompose a jet into constituent subjets, which is useful for identifying decay products of fast-moving heavy particles [189].

4. Object and event reconstruction

4.4.2. Jet reconstruction

Offline jets are built from three-dimensional topological calorimeter cell clusters using the `FastJet` program with the four-momentum recombination scheme [190]. The cells are calibrated at the electromagnetic scale as determined in electron test beam measurements and simulation. Topological clusters make optimal use of the calorimeter granularity by putting together all topologically connected cells and analysing them with respect to local signal maxima [191]. They are formed starting from seed cells with high signal-to-noise ratio and then iteratively adding neighbouring cells with a signal-to-noise ratio above a certain threshold to the cluster. Jet finding is done in $(y - \phi)$ coordinates, where y denotes the rapidity. Only topo-clusters with positive energy are considered as input, for details see [192]. Negative clusters might be present due to the calibration scheme and the capacitive coupling of neighbouring cell channels. Jets with $p_T < 7$ GeV are discarded.

4.4.3. Jet calibration

Since the ATLAS calorimeter is non-compensating, the jets' energies need to be calibrated to the energy scale of hadrons, the so-called hadronic scale. Hereby, one needs to take into account additional energy contributions from pileup events and the position of the primary vertex to ensure correct reconstruction. Several calibration schemes are used in ATLAS [192]. For top analyses, the simplest calibration scheme called EM+JES is used, because it allows a rather simple evaluation of the systematic uncertainties. The other schemes that are available, however, yield a better jet energy resolution.

The EM+JES scheme applies corrections as a function of the jet energy and pseudorapidity to jets reconstructed at the electromagnetic scale. This happens in three subsequent steps. First, a pileup correction is performed that subtracts the average supplemental energy due to additional proton-proton interactions within the same bunch crossing based on Monte Carlo studies and in-situ measurements. This takes into account the jet pseudorapidity, the number of reconstructed primary vertices and the bunch spacing. The latter is particularly important for the 50 ns bunch spacing running in 2011 that introduced a sensitivity of the calorimeter signals to the energy flow in past collisions, due to the ATLAS calorimeter signal shapes [193]. The second step corrects the direction of the jet such that the jet originates from the primary vertex of the interaction instead of the geometrical centre of the detector. In the final step the jet energy of reconstructed jets is transferred to the hadronic scale. This is done using an energy response function $\mathcal{R}_{EM}^{\text{jet}} = E_{EM}^{\text{jet}}/E_{\text{truth}}^{\text{jet}}$, correcting the energy of reconstructed jets E_{EM}^{jet} to the energy of their corresponding Monte Carlo truth jet $E_{\text{truth}}^{\text{jet}}$. The average jet energy scale correction as a function of the calibrated jet transverse momentum and the average simulated jet response at EM scale are shown in Fig. 4.6. Eventually, the pseudorapidity of the jet is corrected for a small bias due to poorly instrumented regions of the calorimeter. Jets considered in this work are required to meet $p_T > 25$ GeV and have to be in the central region of the detector of $|\eta| < 2.5$. Jets with negative energy are discarded. These might be present since the offset correction is calculated with respect

to the jets' p_T instead of the E_T . The protection against that was only introduced later in 2011.

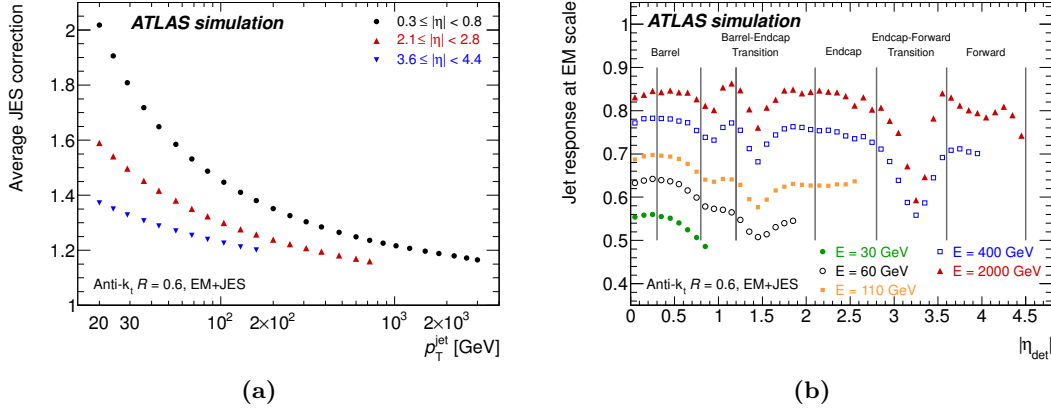


Figure 4.6.: Calibration of EM+JES jets: (a) average jet energy scale correction as a function of the calibrated jet p_T for three representative η -intervals obtained from a nominal Monte Carlo simulated sample, (a) average simulated jet response $\mathcal{R}_{\text{EM}}^{\text{jet}}$ (at EM scale) in bins of EM+JES calibrated jet energy and as a function of the detector pseudorapidity. Both are shown for anti- k_T jets with $R = 0.6$, and results for $R = 0.4$ are found to be similar. [192]

The performance of the jet calibration is validated in several studies such as single hadron response measurements [194] and compared to a combination of in-situ techniques [192]. Well established signatures such as γ +jet [195, 196] and Z +jets events [197, 198] as well as the comparison to charged particle tracks [199] are used. Additional jets found in proximity to a jet lead to a deterioration of the response function [200]. Therefore, a large number of uncertainties are connected with the energy scale which will be discussed and evaluated later in Chapter 8.

4.4.4. Jet energy resolution

The jet energy resolution is obtained in di-jet events using two different methods that are sensitive to different sources of uncertainty [201]. The so-called di-jet balance method is based on momentum conservation in the transverse plane. The asymmetry distribution of the transverse momenta of the two leading jets is fitted with a Gaussian and used to determine the jet p_T resolution. Additional corrections for soft radiation are applied to account for the presence of supplemental soft particle jets not detected in the calorimeter.

The second method, the so-called bi-sector method is based on the definition of an imbalance vector, which is given as the vector sum of the two leading jets in the di-jet event. The vector is zero for perfectly balanced jets and thus sources that give rise to fluctuations can be investigated. The advantage of the definition is that it allows the

4. Object and event reconstruction

expression of the resolution in calorimeter terms only. More details can be found in Reference [201].

For both methods data-MC agreement is compared and shown in Fig. 4.7a. MC simulation describes the jet energy resolution in 2010 data within 14% for central jets with $20 \text{ GeV} < p_T < 80 \text{ GeV}$. The same uncertainty is assumed beyond for $p_T \geq 80 \text{ GeV}$. In order to improve agreement between data and MC, an additional smearing of the jet p_T is used for 2010 MC. This is not needed for the 2011 analyses.

4.4.5. Jet quality and pileup rejection

Additional quality criteria are applied to the jets to ensure reliable measurements. Misreconstructed jets can arise from various sources such as hardware problems, LHC beam conditions, and cosmic-ray showers. Jets that do not meet these criteria are of so-called **bad** quality. To take into account calorimeter noise, jets are checked for their signal shape quality by comparing to the expected pulse shape. Additionally, large energy fractions in the calorimeter point to noise bursts and jets that deposit a large fraction of their energy in the EM calorimeter hint at coherent EM noise. Jet candidates not in-time with the collision events are a signal for cosmic rays or non-collision background. Furthermore, cuts on the sum of the transverse momenta of the associated track divided by the total jet p_T are applied. More details on the cuts can be found in References [192, 202].

For the 2011 analysis (b) a cut on the jet-vertex fraction is applied to reduce the effect of additional pileup events in the same bunch crossing. The jet-vertex fraction measures the probability that a jet originates from a particular vertex. It is calculated by summing up the transverse momenta of the tracks associated with the calorimeter jet if the track stems from the primary vertex divided by the p_T of all tracks associated with the calorimeter jet. Jets with a probability to originate from the primary vertex less than 0.75 are rejected. Scale factors are applied to improve the data-MC agreement for this variable. These have been obtained using a data-Monte Carlo comparison of $Z \rightarrow \mu\mu$ and $Z \rightarrow ee + \text{jets}$ events with specific selections to obtain samples of hard-scattering (signal) jets and of pile-up (background) jets. Based on a tag-and-probe method signal and background efficiencies and inefficiencies are determined and parametrised by an exponential function. The results are validated using truth information. This analysis has not yet been made public.

4.4.6. Jet reconstruction efficiency

The jet reconstruction efficiency is measured using a tag-and-probe method in a di-jet back-to-back topology [201]. Track jets are used as *tag* objects and a second track jet balancing the event in ϕ as *probe* candidate. The efficiency is then obtained by matching calorimeter jets to the *probe* candidate track jet. The comparison between data and Monte Carlo shows good agreement and is depicted in Fig. 4.7b. For high- p_T jets as used in these analyses jet reconstruction is almost fully efficient.

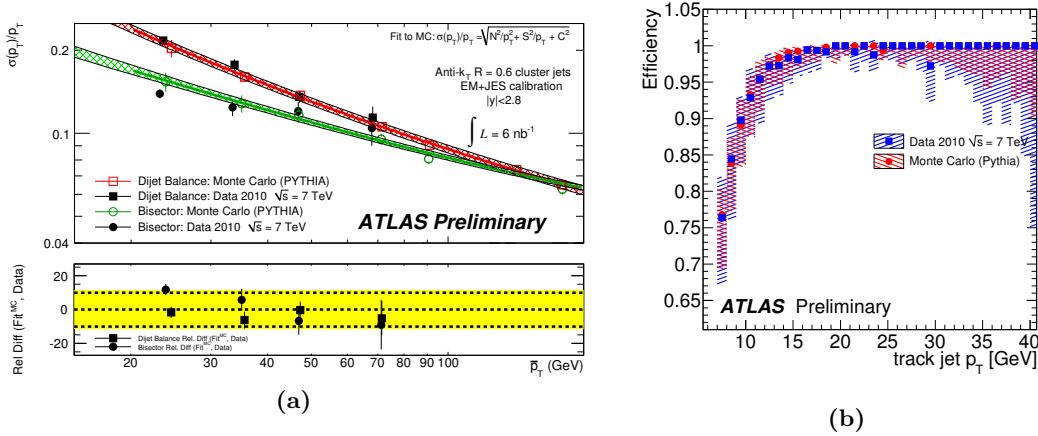


Figure 4.7.: (a) Jet energy resolution for the di-jet balance (squares) and bi-sector (circles) techniques as a function of the average jet p_T in data (black) and MC (red/green). The lower plot shows the relative difference between the Monte Carlo fit and the data results. (b) Selection efficiency relative to track jets as a function of probe track jet p_T in data (blue) and MC (red). The hatched areas indicate the statistical and systematic uncertainties added in quadrature. [201]

4.5. Identification of b -jets

Correct identification of jets stemming from the fragmentation and hadronisation of b quarks, called b -tagging, is an important tool for the analysis and selection of top quark events and therefore used in the 2010 analysis and 2011 analysis (b). It is not used in the 2011 analysis (a) for reasons given in the corresponding analysis Chapter 9. To distinguish b -jets from jets that contain only light quarks one takes advantage of the special properties of b -jets. For instance, fragmentation is hard so that the B -hadron retains about 70% of the original b -quark momentum. Furthermore, B -hadrons have a relatively high mass of greater than 5 GeV. Thus, their decay products carry large transverse momenta with respect to the jet axis and the opening angle of the decay products is large enough to allow spatial separation. However, the most important property is the relatively long life time of about 1.5 ps of hadrons containing a b quark corresponding to an average flight path length of a B -hadron in a jet of about 3 mm in the transverse plane for a jet of 50 GeV. This allows for the reconstruction of secondary vertices, which are the main ingredient for b -tagging.

4.5.1. 2010 analysis b -jet identification and calibration

There are several b -tagging algorithms in ATLAS [147] (B -Physics Chapter), which exploit different properties of b -jets or a combination of them. For the 2010 analysis the JetProb algorithm [203] is employed, which makes use of the property that tracks

4. Object and event reconstruction

from B -hadron decays are expected to have on average a large impact parameter with respect to the interaction point. For each selected track the signed transverse impact parameter significance, $S_{d_0} = d_0/\sigma_{d_0}$, is calculated. The sign is defined by the angle between the jet direction and the line joining the primary vertex to the point of closest approach to the primary vertex. If it is less than $\pi/2$ it is positive, otherwise negative. For tracks originating from the primary vertex the distribution is centered around zero with a random sign, whereas tracks from b - and c -jets tend to have a positive sign. For each track the probability that it originates from the primary vertex, i.e. that it is a light jet, is determined. The probabilities for a jet are then combined with a weighting factor depending on the track multiplicity to a jet probability \mathcal{P}_{jet} . The distribution utilised here employs the transformation $-\log_{10} \mathcal{P}_{\text{jet}}$ and is shown in Fig. 4.8.

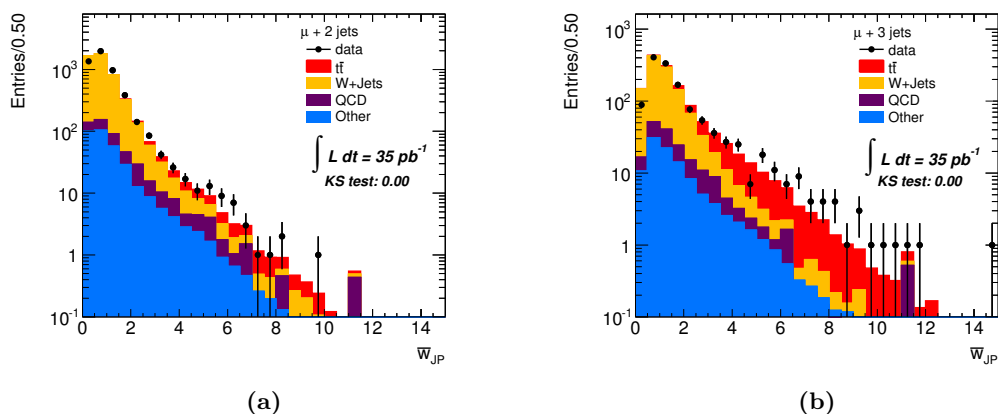


Figure 4.8.: Average of the two jets with highest b -tagging probability obtained with the *JetProb* algorithm using the transformation $-\log_{10} \mathcal{P}_{\text{jet}}$ in 2010 data (dots) compared to simulation (full histogram) for (a) exactly 2, and (b) exactly 3 jets in the muon channel.

As for all objects used in data and MC agreement between data and simulation needs to be investigated and corrected for in simulation if necessary. The efficiencies at which b -jets are identified as well as the misidentification rate of light jets being identified as b -jets needs to be measured in data. This is done at b -tagging efficiency working points that refer to cuts on the b -tagging distribution which yield a certain b -jet identification efficiency in simulation. There are several methods that allow for the calibration of b -tagging. For the *JetProb* algorithm used for the 2010 analysis working points at 50%, 70%, 80% and 90% efficiency have been calibrated with the so-called p_T^{rel} method [204].

This method uses only b -jets that contain a reconstructed muon. It is based on the variable p_T^{rel} , which is defined as the momentum of the muon transverse to the combined muon plus jet axis. Using MC-templates for b -, c - and light-flavour-jets, a fit is performed to the p_T^{rel} spectrum before and after requiring a b -tag at a certain working point. An additional correction to avoid biases from data-MC modelling issues and contamination of the templates is performed. The b -tagging efficiencies for the 50% and 70% working

points obtained with this method are shown in Fig. 4.9.

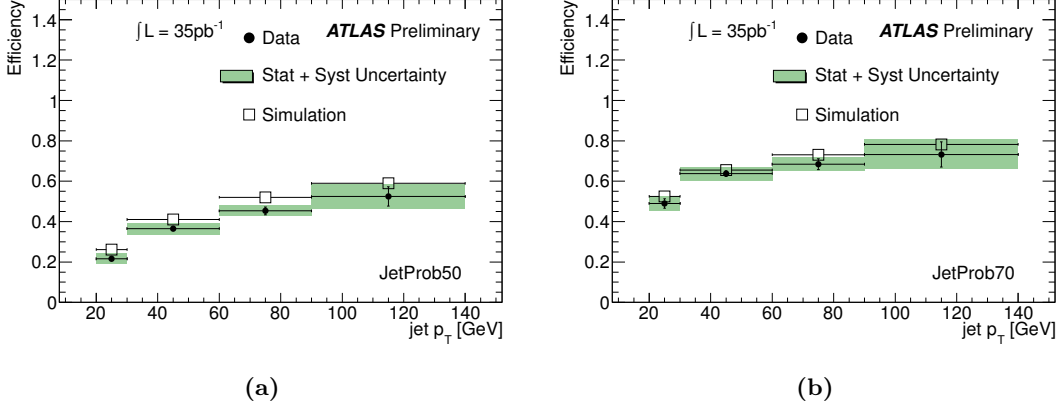


Figure 4.9: b -tagging efficiencies for the *JetProb* algorithm in data (dots) and simulation (open squares) obtained with the p_T^{rel} method as a function of jet p_T for (a) the 50%, and (b) the 70% efficiency working point. Uncertainties in data are shaded in green. [204]

The mistag rate, i.e. the rate at which light jets are b -tagged, is also measured in data using the *SV0-mass method* and confirmed by the *negative tag method*. The *SV0-mass* is the invariant mass of charged particles associated with the inclusively reconstructed secondary vertex. Templates of those distributions are derived from simulation and fit to data after applying b -tagging. By knowing the tagging efficiencies of b - and c -jets and hence the expected event yields for each category the mistag rate can be derived. The negative tag method exploits the idea that the lifetime-signed S_{d_0} distribution is symmetric around zero for light jets due to the finite detector resolution. Thus the negative part of this distribution can be used to determine the light-flavour mistag probability after applying some corrections. More details can be found in Reference [204].

By comparing data and MC for a certain working point scale factors are obtained for each jet for different jet p_T and η regions depending on its true flavour defined as:

$$SF_{\text{jet}}(\text{flavour}, p_T, \eta) = \frac{\varepsilon_{\text{data}}(\text{flavour}, p_T, \eta)}{\varepsilon_{\text{MC}}(\text{flavour}, p_T, \eta)}. \quad (4.2)$$

To calculate the jet weight, one has to differentiate between the case where the jet is tagged in MC:

$$w_{\text{jet}} = SF_{\text{jet}}(\text{flavour}, p_T, \eta), \quad (4.3)$$

and where it is not tagged:

$$w_{\text{jet}} = \frac{1 - \varepsilon_{\text{data}}(\text{flavour}, p_T, \eta)}{1 - \varepsilon_{\text{MC}}(\text{flavour}, p_T, \eta)} = \frac{1 - SF_{\text{jet}}(\text{flavour}, p_T, \eta) \cdot \varepsilon_{\text{MC}}(\text{flavour}, p_T, \eta)}{1 - \varepsilon_{\text{MC}}(\text{flavour}, p_T, \eta)}. \quad (4.4)$$

4. Object and event reconstruction

The total event weight is then the product of all single jet weights.

The 2010 analysis, however, uses the $-\log_{10} \mathcal{P}_{\text{jet}}$ distribution of the `JetProb` algorithm as input for the fit as discussed later in Chapter 7.1. Therefore, no cut on this distribution is used and the result is insensitive to the absolute value of scale factors applied. Nevertheless, the MC distribution needs to be corrected to match the data distribution. Thus, an interpolation between the four calibrated working points is used. For jets with their b -tagging weight between the weight cuts for two working points, passing working point i and failing point j the scale factor yields:

$$SF_{ij} = \frac{\mathcal{P}_{\text{data},i} - \mathcal{P}_{\text{data},j}}{\mathcal{P}_{\text{MC},i} - \mathcal{P}_{\text{MC},j}} = \frac{\mathcal{P}_{\text{MC},i} \cdot SF_i - \mathcal{P}_{\text{MC},j} \cdot SF_j}{\mathcal{P}_{\text{MC},i} - \mathcal{P}_{\text{MC},j}}, \quad (4.5)$$

with the tagging probabilities \mathcal{P} for data or MC at the corresponding working point as defined above. The shape agreement between data and MC can be improved the more working points are calibrated and the closer the scale factors are to 1. For weights below the lowest working point at 90% efficiency the inefficiency scale factor is used, for tag weights above the 50% efficiency point the efficiency scale factor for this working point is applied.

4.5.2. 2011 analysis (b) b -jet identification and calibration

With more data being available and consequently a better detector understanding more powerful b -tagging algorithms can be used. The `MV1` algorithm used for the 2011 analysis (b) is a combination of the `IP3D`, the `SV1` and the `JetFitter` algorithms [205].

The `IP3D` algorithm [147, 205] is an extension of the `JetProb` algorithm described in the previous section. In addition to the signed transverse impact parameter significance, $S_{d_0} = d_0/\sigma_{d_0}$, also the longitudinal significance, $S_{z_0} = z_0/\sigma_{z_0}$, is taken into account making use of correlations. From the comparison of S_{d_0} and S_{z_0} distributions for Monte Carlo simulated events containing b -jets and light u -jets, likelihood functions P_b and P_u are constructed for each track to originate from a b -jet or a u -jet. From these a track weight, w_t , is computed as the ratio of the probabilities:

$$w_t = P_b(S_{a_0}, S_{z_0})/P_u(S_{a_0}, S_{z_0}). \quad (4.6)$$

From all tracks i in the jet passing a quality cut a jet weight is defined:

$$w_{\text{jet}} = \sum_{i \in \text{jet}} \ln w_t^i. \quad (4.7)$$

The `SV1` algorithm [147, 205] belongs to the class of secondary vertex algorithms which seek for the inclusive vertex formed by the decay products of the bottom-hadron, including the products of the subsequent charm-hadron decay. All track pairs that form two-track vertices are selected and used to reject tracks coming from material interactions or other particle decays. The track pairs are then combined into a single effective secondary vertex. To compute a jet weight similar to the one used for the `IP3D` algorithm, again a likelihood ratio is constructed from Monte Carlo simulated events

containing b -jets and u -jets. As inputs a 2D-distribution of the invariant mass of all tracks associated to the vertex vs. the fraction of the jet energy in the secondary vertex and a one-dimensional distribution of the number of two-track vertices are used. In addition, the distance ΔR between the jet axis and the line joining the primary vertex to the secondary one is taken into account.

The `JetFitter` algorithm [147, 205, 206] exploits the topology of weak B - and D -hadron decays inside the jet. In contrast to the `SV1` algorithm it aims to identify both decays by applying a Kalman filter on a common line on which the primary vertex and the b - and c -vertices lie. Templates are created from simulation for b - and c - and light jets and combined into a likelihood similarly as for the `SV1` algorithm with the addition of variables regarding the vertex information such as vertex mass, energy fraction and flight length significance. The `JetFitter` algorithm is the most powerful tagging algorithm regarding light jet rejection for a given b -tagging efficiency.

Since all three algorithms are based on the construction of likelihood ratios, they can easily be combined by adding the weights of the individual algorithms. Since this combination shows a good light jet rejection, the tagger can be used at the 70% efficiency point with a light jet rejection of about 100 [207]. This corresponds to a weight cut of $w_{\text{jet}} > 0.601713$.

The calibration of the tagging and mistagging efficiencies and inefficiencies is performed in three steps. First, the mistag scale factors are determined based on the *SV0-mass method* and cross-checked with the *negative tag method*, both described above in Sec. 4.5.1. The mistag rates are shown in Fig. 4.10. The uncertainties range from 18% in the intermediate p_T range for central jets to up to 49% in the high- p_T region for jets with $1.2 < |\eta| < 2.5$.

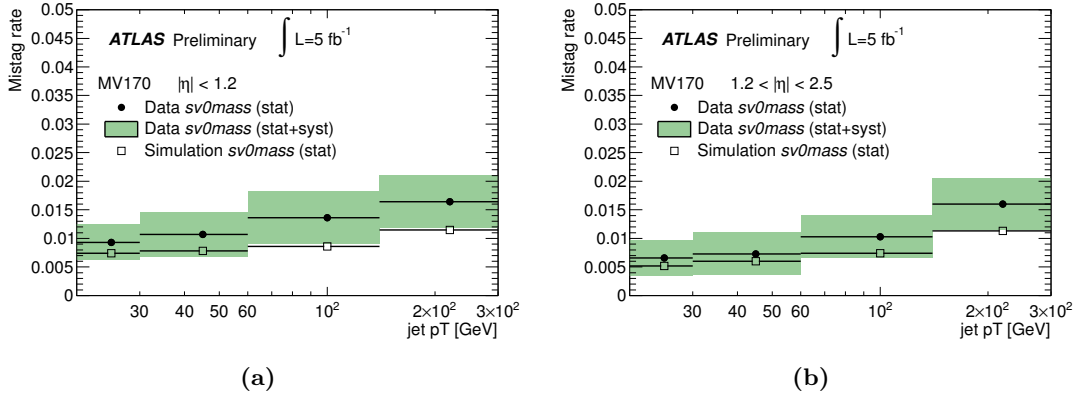


Figure 4.10.: Mistag rates in data (dots) and simulation (open squares) for the MV1 algorithm at 70% efficiency obtained with the *SV0* mass method as a function of jet p_T for (a) $|\eta| < 1.2$, and (b) $1.2 < |\eta| < 2.5$. Uncertainties in data are shaded in green. [208]

In order to obtain uncorrelated c -jet scaling factors, the c -jet efficiency is measured

4. Object and event reconstruction

with the D^{*+} method [209]. Using decays of b or $c \rightarrow XD^{*+} \rightarrow XD^0(\rightarrow K^-\pi^+)\pi^+$ and charge conjugate one can select a pure sample of b - and c -jets. Inside the jet a D^{*+} is reconstructed starting from tracks compatible with the oppositely charged kaon and pion mass hypotheses to obtain the D^0 . The decay chain is then fitted reconstructing both the D^0 and the D^{*+} vertices simultaneously. The flavour composition of the sample is estimated by fitting the so-called D^0 pseudo-proper time which allows discrimination between $c \rightarrow D^{*+}$ and $b \rightarrow D^{*+}$ decays. Eventually, the c -tagging efficiency is obtained by fitting the $\Delta m = m_{K\pi\pi} - m_{K\pi}$ distribution before and after b -tagging using the b -tagging efficiency measured in data using the p_T^{rel} method. By comparing data and simulation one can obtain the correction factors with uncertainties between 10% and 40% depending on the jet p_T .

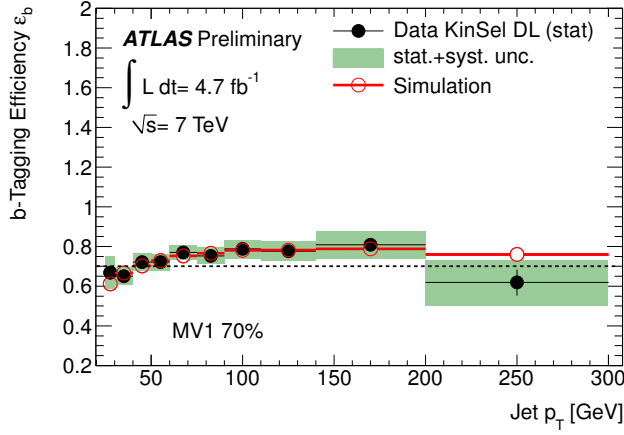
The calibration of the b -tagging efficiency ε_b is performed using a $t\bar{t}$ sample employing a method called *kinematic selection* [210] with a dilepton selection in order not to overlap with the signal lepton + jets selection. Details on the dilepton selection can be found in the reference given. The method relies on the knowledge of the flavour composition of the $t\bar{t}$ signal and background samples. The efficiency is obtained using

$$\varepsilon_b = \frac{1}{f_{b\text{-jets}}} \cdot (f_{b\text{-tag}} - \varepsilon_c f_{c\text{-jets}} - \varepsilon_{\text{light}} f_{\text{light-jets}} - \varepsilon_{\text{fake}} f_{\text{fake}}), \quad (4.8)$$

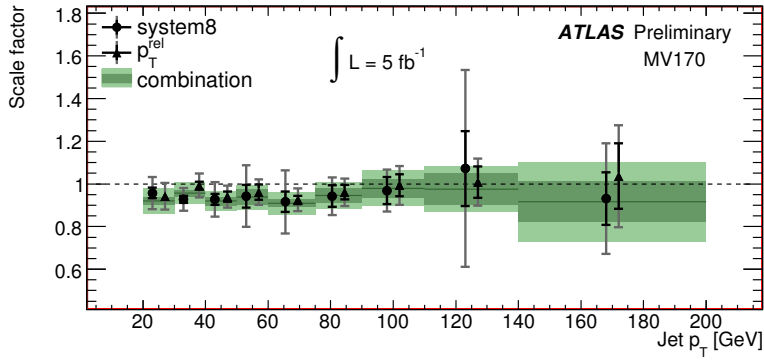
where the f_x denote the expected fractions for the different flavour-jets derived from Monte Carlo and ε_c and $\varepsilon_{\text{light}}$ are the mistag efficiencies for c - and light jets, respectively, to be tagged as b -jets obtained and corrected as described above. The fraction of events from fake lepton or multi-jet background f_{fake} is obtained from data as well as the efficiency $\varepsilon_{\text{fake}}$ to b -tag jets in these events. The derived b -tagging efficiencies in data and MC are shown in Fig. 4.11a. The uncertainties for the resulting scale factors range from 5 to 15% for different regions in p_T . Originally the p_T^{rel} method described in Sec. 4.5.1 and the *System8 method* in a sample of jets containing muons [207] were used to correct the b -tagging efficiencies. The efficiencies are in agreement with the results of the *kinematic selection* method as shown in Fig. 4.11b. However, especially when requiring two b -tagged jets using a calibration method applied in a sample close to the signal topology yields much better data-MC agreement.

4.6. Missing transverse energy

The missing transverse energy or momentum E_T^{miss} is defined as the momentum imbalance in the plane transverse to the beam axis. This imbalance is accounted to particles that cannot be detected by the detector since momentum conservation is expected. In lepton + jets $t\bar{t}$ events the neutrino from the leptonic W boson decay escapes undetected and thus a large amount of E_T^{miss} is expected. The missing transverse energy is obtained



(a)



(b)

Figure 4.11.: Measured b -tagging efficiencies in data compared to simulation for the MV1 algorithm at 70% b -tagging efficiency (a) using the kinematic selection method in the dilepton $t\bar{t}$ analysis [210] used for the 2011 analysis (b), and (b) using the p_T^{rel} (dots) and the System8 method (triangles) and the combination thereof (green area) as comparison [207]. The results are shown with their statistical (inner error bars) and total (outer error bars) uncertainties.

4. Object and event reconstruction

from the negative vector sum of the momenta of all particles detected in the collision:

$$\vec{E}_T^{\text{miss}} = \begin{pmatrix} E_x^{\text{miss}} \\ E_y^{\text{miss}} \end{pmatrix} \quad (4.9)$$

$$E_T^{\text{miss}} = |\vec{E}_T^{\text{miss}}| = \sqrt{(E_x^{\text{miss}})^2 + (E_y^{\text{miss}})^2}, \quad (4.10)$$

where E_x^{miss} and E_y^{miss} are the x and y components of the vector defined as

$$E_x^{\text{miss}} = - \sum_i^{N_{\text{cell}}} E_i \sin \theta_i \cos \phi_i \quad (4.11)$$

$$E_y^{\text{miss}} = - \sum_i^{N_{\text{cell}}} E_i \sin \theta_i \sin \phi_i. \quad (4.12)$$

4.6.1. Reconstruction and calibration of missing transverse energy

The E_T^{miss} reconstruction includes contributions from calorimeter energy deposits and muons reconstructed in the Muon System [211, 212]. Starting from the topological clusters at EM scale, the E_T^{miss} is corrected for physics objects used in the analysis to ensure one-to-one correlation and consistency of all objects. The calorimeter cells are therefore calibrated according to the associated physics objects, namely electrons, jets and so-called soft jets with a transverse momentum less than 20 GeV. Electrons have to pass the identification cuts of the respective analysis as given in Sec. 4.2.1 and a p_T cut of 10 GeV. Jets enter the E_T^{miss} calculation directly if their calibrated p_T is greater than 20 GeV. Otherwise, for jets with $7 \text{ GeV} < p_T < 20 \text{ GeV}$ referred to as soft jets, the associated calorimeter cells are added to the E_T^{miss} without the jet energy scale factor. Topological clusters outside reconstructed objects are added at EM calibration and referred to as cell out terms. For the muon term all combined muons are considered. For muons within $\Delta R = 0.3$ of a reconstructed jet the muon energy deposited in the calorimeter is included in the jet term whereas for isolated muons this energy deposition is added to the muon term. In summary, the E_T^{miss} components are

$$-E_{x,y}^{\text{miss}} = E_{x,y}^{\mu} + E_{x,y}^e + E_{x,y}^{\text{Jet}} + E_{x,y}^{\text{SoftJet}} + E_{x,y}^{\text{CellOut}}, \quad (4.13)$$

where $E_{x,y}^{\mu}$ denotes the muon, $E_{x,y}^e$ the electron, $E_{x,y}^{\text{Jet}}$ the jet, $E_{x,y}^{\text{SoftJet}}$ the soft jet, and $E_{x,y}^{\text{CellOut}}$ the cell out term contributions.

4.6.2. Missing transverse energy performance

The performance of E_T^{miss} has been checked in different control samples. The studies presented here are performed in $Z \rightarrow ll$ and $W \rightarrow l\nu$ samples, but similar studies have also been carried out in $t\bar{t}$ samples. In events of $Z \rightarrow ll$ one does not expect genuine E_T^{miss} , which therefore allows for resolution and noise studies. The leptons can be used to reconstruct the direction of motion of the Z boson. By projecting E_T^{miss} onto this

axis, one is sensitive to the balance between the leptons and the hadronic recoil and thus the E_T^{miss} scale. An imbalance between the leptons and the hadronic recoil of a few GeV is observed, which is mainly due to the contribution of the soft jet and cell out terms. Comparison with Monte Carlo simulation shows the same behaviour. Therefore, one can use the comparison between data and MC and the balance between the sum of these two soft terms and the hard objects to evaluate the scale and resolution systematic uncertainties on the soft terms. The resolution is shown in Fig. 4.12a as a function of $\sum E_T$, the scalar sum of transverse energy of cells in the event associated to the different objects where cells are calibrated according to the scheme described above. It follows a function $\sigma = k \cdot \sqrt{\sum E_T}$ where $k \approx 0.5 \text{ GeV}^{1/2}$ for 2010 data and $0.7 \text{ GeV}^{1/2}$ for 2011 data due to the increased pileup conditions.

Events with genuine E_T^{miss} such as $W \rightarrow l\nu$ events allow the evaluation of the E_T^{miss} scale and linearity. In most distributions data shows reasonable agreement with simulation, but at high $\sum E_T$ large deviations are visible. The linearity in MC shows a bias up to 15% due to the finite resolution of the E_T^{miss} measurement in particular for low values of $\sum E_T$. On average the bias is 1-3% for 2010 and 5% for 2011. The overall uncertainty on the E_T^{miss} scale is estimated by comparing data and MC and shifting MC up and down by 1σ for each term and also taking account uncertainties on electrons, muons and jets as described above in the respective sections. The overall scale uncertainty increases with $\sum E_T$ from about 2% to 10% for $W \rightarrow l\nu$ events as shown in Fig. 4.12b. Even though these events are similar to $t\bar{t}$ events, additionally similar studies have been performed following top event selection criteria. These confirm the behaviour found for W events.

4.7. Overlap removal

In order to avoid duplicate reconstruction of an object by the independent algorithms and to avoid ambiguities so-called overlap removals are performed.

4.7.1. Electron muon overlap removal

If a muon leaves or radiates a significant amount of energy in the EM calorimeter, it can be reconstructed both as a muon and an electron, because the reconstruction algorithms are run independently. In this case they will share the same ID track. Since this dual reconstruction affects the E_T^{miss} reconstruction, such events are removed.

4.7.2. Muon jet overlap removal

Muons that are reconstructed within a cone of $\Delta R = 0.4$ to a jet that passes the quality criteria mentioned above are likely to stem from a leptonic decay of a heavy flavour hadron inside the jet. They are removed to reduce the amount of non-prompt muons and to suppress the multi-jet background.

4. Object and event reconstruction

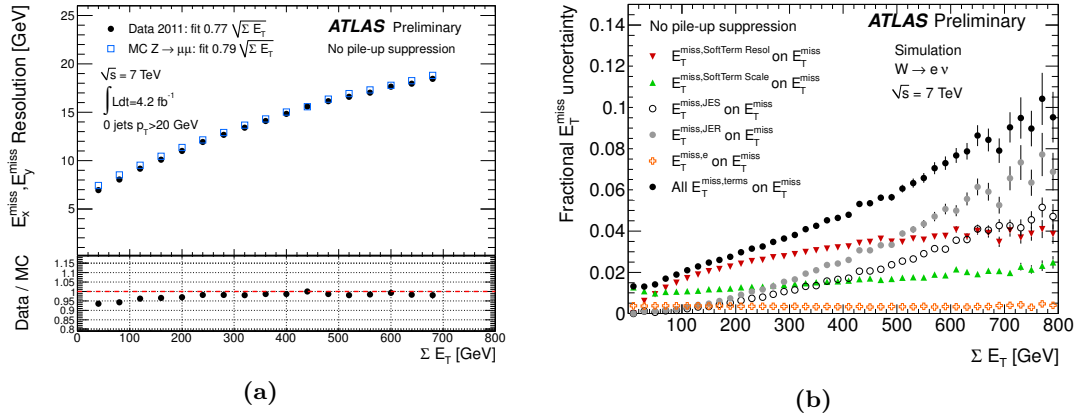


Figure 4.12.: *Missing transverse energy performance in 2011 data: (a) $E_{x,y}^{\text{miss}}$ resolution as a function of ΣE_T in $Z \rightarrow \mu\mu$ events without jets with $p_T > 20 \text{ GeV}$ in data (dots) and MC (open squares). The lower parts of the figures show the ratio between data and MC, and (b) fractional systematic uncertainty on contributions of different term uncertainties on E_T^{miss} uncertainty as a function of ΣE_T in MC $W \rightarrow e\nu$ events. The overall fractional systematic uncertainty on the E_T^{miss} scale, obtained combining the contributions from various terms, is also shown. [212]*

4.7.3. Jet electron overlap removal

Since all calorimeter objects are reconstructed by the jet finder, all electrons are also reconstructed as jets. Therefore, jets that overlap with good reconstructed electrons within $\Delta R = 0.2$ are removed because they are most likely an otherwise double-counted electron. After this step, for the 2011 analysis (b) only, electrons that lie within $\Delta R = 0.4$ are removed as the reconstruction scale factors for electrons are only valid outside this cone.

5. Dataset and event generation

The analyses presented in this thesis cover three different data sets recorded from 2010 to 2011. In particular, these differ by the amount of data analysed and also the LHC running conditions, e.g. different beam parameters leading to different pileup scenarios (see Sec. 3.3) under which they have been taken. The latter therefore have to be properly modelled in simulation. In this chapter the data sets used are briefly described together with the data quality required. Furthermore, details about the Monte Carlo event generation, simulation and additional corrections are given.

5.1. Dataset

The 2010 analysis uses the full available data set recorded by the ATLAS detector during 2010 data-taking (see Sec. 3.3) excluding the initial low luminosity running periods during which the detector was commissioned and trigger inefficiencies were recovered. The total integrated luminosity for run periods 2010 E4–I2 taken from 6th August until 29th October yields 35.3 pb^{-1} with an uncertainty of 3.4% [153].

The 2011 analysis (a) uses the part of the 2011 data set that was available at the time the analysis was prepared for publication in July 2011 consisting of run periods 2011 B2–G5 taken from 22nd March until 11th June. The integrated luminosity of the data set is 695 pb^{-1} . This luminosity estimate has an uncertainty of 3.7% [155].

The full 2011 data set recorded in pp collisions is exploited by the 2011 analysis (b) using run periods 2011 B2–M up to 30th October. The luminosity of the data analysed is 4660 pb^{-1} . The luminosity uncertainty could be reduced to 1.8% [213] thanks to a better understanding of the van-der-Meer scan method.

5.1.1. Data Quality and Good Runs Lists

Even though stable run periods are chosen for the analyses, not all runs can be used. Top quark analyses require the whole detector to be functional since the objects employed are reconstructed from all parts of the detector. Therefore, only data-taking runs and luminosity blocks during which the detector was in a state sufficiently good for further analysis are used. Luminosity blocks are time periods of mostly two minutes length in which the detector and the accelerator can be considered in a constant state. They can be shorter if detector states or trigger prescales change. Only the amount of data with good quality is considered for the luminosity estimates above and for analysis.

5.2. Event generation using Monte Carlo generators

The ATLAS detector is a highly complex device. It is very difficult to predict the response of the millions of readout channels of the detector to a certain physics process. In order to be able to extract usable information from data, accurate modelling of the event kinematics and topology at parton and hadron level is needed. This is usually done by the means of a Monte Carlo simulation and will be described in detail in the following. Based on a set of parton distribution functions (see Sec. 2.2.3), the hard process is generated according to a theoretical model, which is then subject to the parton shower and hadronisation as well as decays described in Sec. 5.2.2. These steps are outlined in Fig. 5.1. Consequently, the stable particles are fed to a full detector simulation that models the interaction of those particles with the detector material and the corresponding detector response. The raw detector data are then subject to the same reconstruction algorithms that are also used for real data. The generation and simulation programs have to be corrected for and adjusted to the real data. Since simulation of events usually happens before or in parallel to data-taking, additional run-dependent corrections are performed which are also described.

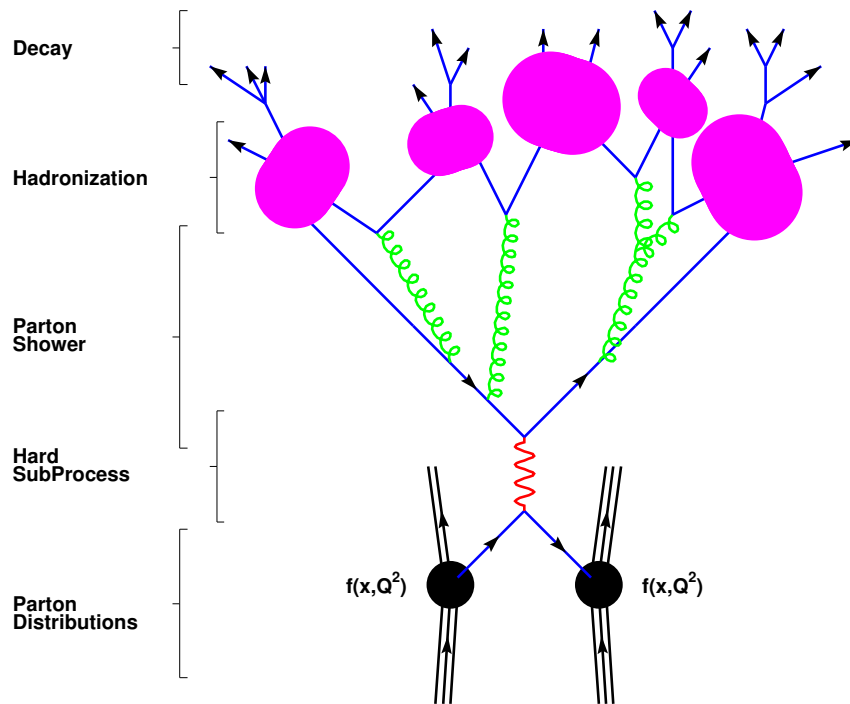


Figure 5.1.: Steps of Monte Carlo event generation as described in the text evolving in time from bottom to top. [214]

5.2.1. Simulation of hard processes and physics events

The basis of theoretical event generation at the LHC is a parametrisation of the incoming partons stemming from the proton, which is given by the parton density functions. They describe the probability to find a quark or gluon within a given proton momentum fraction x from the pp collision taking place at the LHC (see Sec. 2.2.3 for details). Using the incoming partons as input the simulation of hard processes can be performed by event generators, details of the ones employed for this analysis are discussed in Sec. 5.4.1. They produce hypothetical events with the distributions and rates predicted by theory based on the cross-section formulae of the physics process, which are given for top quark pair events in Sec. 2.2.1. Using the cross-section formula the phase space is sampled and candidate events are defined by choosing values for the degrees of freedom from a uniformly distributed random number generator. To actually obtain events with the frequency predicted by theory the candidate events undergo a so-called unweighting procedure giving events a more uniform weight. Cross-section integrators that are made use of to calculate the expected production cross section follow the same principle. The only exception is the last step where instead of unweighting one would use event weights from a large number of candidate events to fill a relevant distribution, e.g. the transverse momentum of an outgoing quark.

Although one can extract physical information from the use of an event generator or cross-section integrator, the process itself is still unphysical, because quarks and gluons are present in the initial and final state. These are confined into hadrons in nature. Furthermore, emission of extra partons plays a major role especially in QCD, which is not accounted for. Therefore one has to include a way to estimate the effects of real and virtual higher-order corrections in perturbation theory and to describe hadronisation effects.

There are different techniques used to compute the exact number of emissions. The so-called Tree Level Matrix Element generators employed in this analysis such as `AlpGEN` [215] use the higher order diagrams that correspond to the emission of real particles for this purpose. Unfortunately, for finite calculations cuts have to be applied at the parton level, e.g. requiring a minimum transverse momentum, influencing physical observables. Another more advanced approach is to use NLO computations also considering virtual contributions (see below). For this purpose resummation and parton shower techniques are used, the second widely used though less accurate than the first.

5.2.2. Parton shower and hadronisation

The showering and hadronisation generators start from the hard process allowing the partons to split (or branch) into pairs of other partons. These again may also branch and so on following a Markov process [216]. An event then consists of a large number of elementary particles, including quarks and gluons. Consequently, the coloured partons are grouped into colour-singlet composite hadrons following a hadronisation model. This model is based on phenomenological models that are tuned to experimental data. Either the QCD-improved version of the factorisation theorem (see Chapter 2.2.2) or

5. Dataset and event generation

phenomenological, non-perturbative models are applied to describe the parton-hadron transition. The latter are employed by PYTHIA [217] and HERWIG [218], both used in this analysis. Eventually, many short-lived resonances will be present after hadronisation which are then decayed.

The showering and hadronisation programs often bring along the possibility to add underlying events, in the case of HERWIG the dedicated underlying event simulation program Jimmy [219] is used while PYTHIA has its own model. The underlying event stems from the coloured remains of the protons that did not take part in the hard collisions, the so-called beam remnants. They are usually included in the hadronisation process, because they might be colour-connected to the hard subprocess. The probability for colour reconnection to take place between two partons can also be adjusted based on experimental data. Furthermore, at the LHC there is the possibility of multiple parton interactions from the beam protons that are also added.

As last step so-called pileup from other pp collisions in the same bunch crossing is also accounted for. The MC samples are overlaid with simulation samples reproducing the bunch train structure of the LHC beams. This is particularly important to take into account out-of-time pileup, i.e. additional collisions taking place before or after the actual bunch crossing of interest. For the 2010 analysis the configuration corresponds to double trains with 225 ns separation. Each train is composed of eight filled bunches with 150 ns bunch separation and an average of 2.2 additional pile-up events simulated with PYTHIA. For the 2011 analyses 50 ns bunch separation is used adding on average 5.5 pileup events to the 2011 analysis (a). For the 2011 analysis (b) four different pileup periods are defined to reflect the changing LHC running conditions ranging from 5.4 ± 0.8 average interactions at the beginning of 2011 up to 11.3 ± 2.4 average interactions towards the end of 2011 pp collisions.

It has to be noted that matrix element generators as well as shower and hadronisation generators are usually treated independently: The matrix element generators compute the hard process at fixed-order (see Sec. 2.2.2) and the parton shower processes the soft and collinear emissions. However, this fails to correctly represent higher order processes in which an additional parton is emitted at the hard scale because parts of this process overlap with the soft one. Combining an NLO matrix element program with a parton shower program therefore leads to double-counting of events. Thus NLO matrix element generators have been developed that take special care of the merging of soft and collinear emissions and hard ones. This approach is employed by MC@NLO [220, 221] and POWHEG [222–224] used for the generation of $t\bar{t}$ samples as described in Sec. 5.4.

5.3. Detector simulation and event reconstruction

The events obtained after applying showering and hadronisation are passed on to a computer simulation of the detector implemented within the ATLAS software framework Athena [225] based on the GEANT4 simulation toolkit [226]. A precise description of the detector geometry (position, dimensions and material of all active and inactive detector parts) is included as well as a simulation of all kinds of physics processes caused

by the interaction of the particles with the material. To provide a highly realistic detector response, the processes simulated in GEANT4 range from very low energies of a few eV such as gas ionisations up to TeV energies. This simulation is in many cases the most time-consuming process and is therefore sometimes performed with simplified parametrisations referred to as fast simulation.

The information obtained in the simulation is then digitised to emulate the detector electronics output one would expect under experimental running conditions. This allows for the use of the same reconstruction algorithms and tools in Monte Carlo simulated and real data.

The event reconstruction is done in two sequential steps. The first step uses only information from one subdetector part described in Sec. 3.2. This means, for example, that muon track segments in the Muon System and the Inner Detector are treated separately. In the second step these information are combined providing an accurate measurement, e.g. by matching the Muon Spectrometer and the Inner Detector tracks segments to a muon track. Details of the event and object reconstruction are given in Chapter 4.

In Monte Carlo simulation also detector issues are reflected. For instance, the hardware problems in the EM calorimeter during data-taking described in Sec. 4.2.1 are taken into account by producing events for four different running conditions and reweighting them to the corresponding data fraction.

Even though the MC samples are generated with additional pileup events as discussed in Sec. 5.2.2, residual differences in the pileup between data and Monte Carlo simulation are corrected for in the 2011 analyses. The Monte Carlo events are re-weighted based on the number of primary vertices. For data these are averaged across all bunch crossings for a given luminosity block. For the 2010 analysis the differences between data and MC are treated as a source of systematic uncertainty.

5.4. Monte Carlo data samples

As discussed before in Sec. 2.2.6, top quark pairs in the lepton + jets channel decay via $t\bar{t} \rightarrow WbWb \rightarrow l\nu bqq'b$ and possibly additional radiation. The signal topology thus consists of a high- p_T lepton, a number of jets, two of them might be b -tagged, and missing transverse energy. There are, however, processes whose final state is very similar. The dominant background to top quarks is the production of leptonically decaying W bosons in association with jets, which are only distinguishable by the kinematic properties in the final state as discussed in Chapter 6. The same applies for events with two W bosons and single top quarks. The latter two processes, however, have a comparably much smaller production cross section than W + jets production that has a cross section two orders of magnitude higher than top production. Other electroweak backgrounds such as Z + jets production arise from the limited detector coverage, particle misidentification and inefficiencies, for instance if a lepton escapes detection. The generation of the signal and background samples is discussed in the following. Another background, the production

5. Dataset and event generation

of multi-jet events, where a jet is identified as a lepton, is difficult to simulate and therefore modelled by events taken from data, which is discussed in Chapter 6.

5.4.1. Simulation of top quark pair events

For the generation of all top quark samples a MC top mass parameter of $m_t = 172.5$ GeV has been used. The PDF sets used are stated in Sec. 2.2.4. The $t\bar{t}$ Monte Carlo samples are normalised from the generator cross section to the “NNLO approx.” cross section given in the same section. This scale factor is usually referred to as k -factor.

The nominal $t\bar{t}$ signal sample for the 2010 and the 2011 analysis (a) has been simulated using MC@NLO [220, 221] in version 3.41. This NLO matrix element generator avoids the double-counting of NLO and shower events by introducing a subtraction term that also removes infrared singularities. NLO approximated terms that also appear in the showering of LO terms are subtracted. This method is therefore dependent on the parton shower program. Currently, fragmentation and hadronisation is only implemented to work with HERWIG [218] version 6.510 and the underlying event is simulated by Jimmy [219] using the ATLAS tune AUET1 [227] for the 2010 analysis and the updated tune AUET2 [228] for the 2011 analyses. Due to the MC@NLO subtraction scheme negative weights are assigned to 10–15% of the events. Monte Carlo samples have been split up into a sample in which both W bosons have been forced to decay hadronically (referred to as fully hadronic sample) and where at least one W boson has been forced to decay leptonically (referred to as (semi-)leptonic sample). The k -factor for the MC@NLO also includes a correction factor for the $W \rightarrow l\nu$ branching ratio which was set to 0.111 instead of 0.108 for the event generation.

To evaluate the cross-section dependency on the top quark mass m_t , samples are generated for m_t ranging from 140 GeV to 210 GeV in 10 GeV steps and around the central point additional mass points at 165, 167.5, 175 and 177.5 GeV. The cross sections are calculated with Hather as described in Sec. 2.2.4 and scaled accordingly.

In contrast to MC@NLO the POWHEG [222–224] generator does not produce negative weights. This is achieved by making sure that the first emission is always generated via the NLO matrix element. The intertwined shower programs used here, HERWIG and PYTHIA, contain a p_T -veto making sure that all subsequent emissions are softer. For the 2011 analysis (b) the 2011 ATLAS tune AUET2B [229] has been used for PYTHIA. A detailed discussion and validation of MC@NLO and POWHEG can be found in Reference [230]. This sample is used as nominal signal sample in the 2011 analysis (b) (see Chapter 10) and for the other two analysis to evaluate the NLO signal generator uncertainties.

To compare with a leading order matrix element generator ALPGEN [215] is used in combination with HERWIG/Jimmy. ALPGEN is a Standard Model process generator with emphasis on final states with large jet multiplicities. Accordingly, the leading order CTEQ6L1 [73] PDF set with α_s also at leading order is used. To allow for a more efficient sample generation the sample is split into slices of additional parton multiplicity: $t\bar{t} + N$ partons and a minimum p_T cut on the parton of $p_T > 15$ GeV is applied and the minimum separation between them has to be $\Delta R = 0.7$. Using the MLM algorithm [231] parton shower and matrix element calculations are matched. The matching parameters

for the parton-jet matching are a minimum transverse momentum of the jet, $p_T = 20$ GeV, and a matching cone of $\Delta R = 0.7$. Jets with transverse momentum or ΔR above this value are taken from a matrix element calculation, jets below this value come from a parton shower. This technique avoids double counting and the number of partons matched to the MLM algorithm defines the parton multiplicity of the sample. Matching up to four partons is applied and beyond all events are merged into a 5+ partons sample. Samples for the lepton + jets and the dilepton channel are generated separately. For the 2011 analysis (b) additionally `AlpGEN` samples in conjunction with `PYTHIA` are used. They are generated using the leading order CTEQ5L [232] PDF set and the Perugia 2011 underlying event tune [233].

To allow for a convenient variation of initial- and final-state radiation, which is not unambiguously possible with the NLO generators, further $t\bar{t}$ samples have been generated with the tree level matrix element generator `AcerMC` [234] and the `MRST2007LOMOD` [88] (2010 analysis) and CTEQ6L1 PDF sets (2011 analysis (b)). The `AcerMC` program has been specifically developed for the generation of Standard Model events at the LHC. Interfacing the program to `PYTHIA` a sample with nominal settings for initial- and final-state radiation is created as well samples where the settings are varied in `PYTHIA` by 1/2 and 2, both separately and at the same time. Since it has been found (see Chapter 8) that this variation creates unphysically large uncertainties, the ISR/FSR variations for the 2011 analysis (b) are based on uncertainties evaluated using data. The ISR variation is based on a jet gap fraction analysis in dileptonic $t\bar{t}$ events [235] and the FSR variation on jet shapes in QCD multi-jet events that have been used for MC tuning [236] creating an envelope around the central value of the energy scale distribution Q_0^2 . For the 2011 analysis (b) `AlpGEN` + `PYTHIA` samples are used that were generated with up and down variations of α_s by factors of two.

5.4.2. Simulation of W/Z + jets events

The W and Z + jets events have been generated using `AlpGEN` [215] with `HERWIG/Jimmy` described above using the CTEQ6L1 [73] PDF set. Feynman diagrams for the processes are shown in Fig. 5.2. The MLM algorithm has been used with the same parameters. Separate samples have been generated for parton multiplicities ranging from zero to five. The W + jets samples are further split according to the W boson decay, which has either been forced to decay into an electron, muon or τ -lepton and their respective neutrino. Similarly, separate samples for the Z boson forced to decay into two leptons of the same flavour have been generated. The Z + jets samples have been generated with dileptons in the invariant mass range of $40 \text{ GeV} < m_{ll} < 2000 \text{ GeV}$. For the calculation of the cross sections, the cross-section integrator `FEWZ` [237] has been used. This program is particularly developed for the calculation of fully exclusive W and Z production. The NNLO cross sections calculated with `FEWZ` and the `MSTW2008NNLO` PDF set for the full kinematic regime yield

$$\sigma_W = \left(10461^{+84}_{-94} \text{ (scale)} \pm 167 \text{ (PDF)} \pm 126 \text{ } (\alpha_s) \right) \text{ pb} \quad (5.1)$$

5. Dataset and event generation

for $W \rightarrow l\nu$ production and

$$\sigma_Z = \left(970_{-6}^{+5} \text{ (scale)} \pm 14 \text{ (PDF)} \pm 9 \text{ } (\alpha_s)\right) \text{ pb} \quad (5.2)$$

for $Z \rightarrow ll$ only. Within the m_{ll} range given above the inclusive cross section for $Z/(\gamma^*) \rightarrow ll$ is calculated to $\sigma_Z = 1.070 \pm 0.054$ nb.

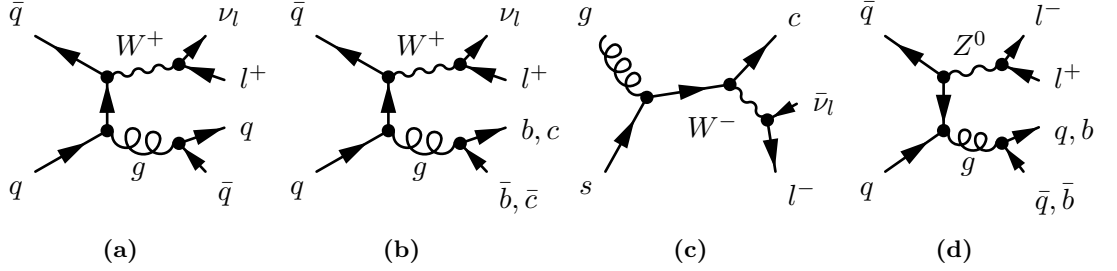


Figure 5.2.: Examples of Feynman diagrams for $W/Z + \text{jets}$ production where q denotes a light quark: (a) $W + \text{light jets}$, (b) $Wb\bar{b}/c\bar{c} + \text{jets}$, (c) $Wc + \text{jets}$, and (d) $Z(b\bar{b}) + \text{jets}$ production. Charge conjugate production modes are implied. Only leptonic decays of the bosons are considered.

The production of a W boson in association with heavy flavour quarks is performed separately to ensure sufficient statistics. $Wb\bar{b} + \text{jets}$, $Wc\bar{c} + \text{jets}$ and $Wc + \text{jets}$ samples have been generated. Since the $Wc + \text{jets}$ process has a comparably large production cross section, a generator cut on the c -parton of $p_T > 10$ GeV is applied and the minimum distance between the c -jet and another light jet has to be greater than $\Delta R = 0.7$. Up to four partons are generated in addition where the $Wc + 4$ partons sample is generated inclusively, i.e. also events with more than 4 partons are merged in this sample. The $Wb\bar{b} + \text{jets}$ and the $Wc\bar{c} + \text{jets}$ samples require $\Delta R > 0.7$ between the two heavy flavour jets and are produced with up to three additional partons, the highest parton multiplicity sample again generated inclusively. Similarly, for the 2011 analysis (b) only, $Zb\bar{b} + \text{jets}$ samples for each lepton flavour with up to three additional partons are generated. The invariant mass of the lepton pair has to be within $30 \text{ GeV} < m_{ll} < 10000 \text{ GeV}$. The heavy flavour samples are scaled with the same k -factors as the light jet samples under the assumption that the relative difference between the LO and the NNLO cross section is independent of the jet flavour. For the 2011 analysis (b) the k -factor for the Wc samples has been recalculated using the MCFM cross section integrator [238] and increased to 1.52 instead of 1.2.

Since there is no possibility in Alpgen to match heavy flavour quark jets explicitly, there exists a significant overlap between the $W + \text{light jets}$ and the $W + \text{heavy flavour jets}$ samples and similarly for the $Z + \text{light jets}$ and the $Zb\bar{b} + \text{jets}$ samples. The same heavy flavour states can arise in multiple samples. To remove the overlap the different strengths of the matrix element calculation and the parton shower are exploited. While the parton shower describes collinear gluon splitting more fittingly, the matrix element

performs better when there is a large opening angle between the quarks. Thus the angular distance ΔR is used for discrimination. If there exists a pair of heavy flavour quarks with $\Delta R > 0.4$ in the $W + \text{light}$ or $Wc + \text{jets}$ sample, the event is vetoed. In return, events from the $Wc\bar{c}$ samples are removed if a $c\bar{c}$ pair lies within $\Delta R < 0.4$ or a $b\bar{b}$ pair is found at $\Delta R > 0.4$. Events from the $Wb\bar{b}$ with a $b\bar{b}$ pair at $\Delta R < 0.4$ are also removed. The samples used for analysis without the vetoed events are then classified as follows. Events from the $W + \text{light jets}$ sample that contain heavy quark pairs are added to the respective heavy flavour quark samples. If there exists a $b\bar{b}$ pair in a $Wc\bar{c} + \text{jets}$ sample event, this event is added to the $Wb\bar{b} + \text{jets}$ sample. The same approach is chosen for the $Z + \text{jets}$ samples, where only the overlap between the $Z + \text{light jets}$ and the $Zb\bar{b}$ samples is removed.

5.4.3. Simulation of other electroweak processes

5.4.3.1. Single top production

The production of single top events is performed with MC@NLO interfaced with HERWIG and Jimmy using a top quark mass of $m_t = 172.5$ GeV and the CTEQ6.6 PDF set. The s - and t -channel as well as the tW production mode are generated separately and scaled to the NNLO cross sections given in Sec. 2.2.5. For the tW process diagrams that also enter $t\bar{t}$ production at the amplitude level are removed to avoid interference terms with LO $t\bar{t}$ production completely. For all production modes the W bosons have been forced to decay leptonically to electrons, muons or τ -leptons without allowing dileptonic events for the Wt -channel. The samples have also been generated for masses between 140 GeV and 210 GeV in 10 GeV steps. Since there are no NNLO calculations at these points, the NLO cross sections are used for normalisation obtained from MC@NLO and cross checked with MCFM.

For the 2011 analysis (b) the tree level matrix element generator AcerMC [234] with PYTHIA and the LO** (LHAPDF 20651) [239] PDF set has been used for t -channel production. In contrast to other generators, it is expected to combine LO and NLO tree level diagrams for the t -channel production in a more physically motivated way [240], properly interpreting the gluon to $b\bar{b}$ splitting at NLO.

5.4.3.2. Diboson production

Diboson production as shown in Fig. 5.3, i.e. the production of WW , WZ , and ZZ boson pairs, has a rather low cross section with $\sigma_{WW} = 44.9 \pm 2.2$ pb, $\sigma_{WZ} = 18.5 \pm 1.3$ pb, and $\sigma_{ZZ} = 9.23 \pm 0.46$ pb calculated with MCFM. In this NLO calculation the Z boson mass has to be greater than $m_Z = 60$ GeV, if a Z boson is produced. The samples are generated and showered by HERWIG with a filter that requires at least one lepton with $p_T > 10$ GeV and $|\eta| < 2.8$. If one of the bosons decays hadronically, the signature is very similar to the one of top quark decays. The samples are normalised to the NLO cross section.

5. Dataset and event generation

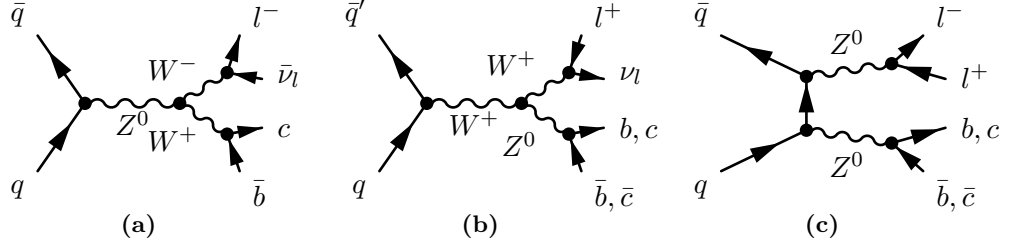


Figure 5.3.: Leading order Feynman diagrams for diboson production: (a) WW , (b) WZ , and (c) ZZ production. Charge conjugate production modes are implied. Only leptonic decays of the W bosons are considered. In addition to the Z -decay into heavy flavour quarks shown here the decay into light quarks is also possible.

5.4.4. Summary of Monte Carlo samples

In Tab. 5.1 the Monte Carlo samples used for the analysis are summarised. A detailed listing with ATLAS MC sample IDs can be found in Appendix A. Information about the theoretical cross sections can be found above and in Sec. 2.2.

Table 5.1.: Summary of Monte Carlo samples used for the analysis. For samples that are split into parton multiplicities the highest parton multiplicity sample is generated inclusively indicated with a “+”-sign.

physics process	generator	comments
$t\bar{t}$ (no all-hadronic) $m_t = 172.5$ GeV	MC@NLO/HERWIG	nominal NLO signal sample
$t\bar{t}$ (no all-hadronic)	POWHEG/HERWIG	NLO generator uncertainty
$t\bar{t}$ (no all-hadronic)	POWHEG/PYTHIA	parton shower uncertainty
$t\bar{t}$ dileptonic + 0...5+ partons	AlpGEN/HERWIG	LO signal sample ¹
$t\bar{t}$ l +jets + 0...5+ partons	AlpGEN/HERWIG	LO signal sample ¹
$t\bar{t}$ dileptonic + 0...5+ partons	AlpGEN/PYTHIA	LO signal sample ¹
$t\bar{t}$ l +jets + 0...5+ partons	AlpGEN/PYTHIA	LO signal sample ¹
$t\bar{t}$ (no all-had.) ISR/FSR variations	AcerMC/PYTHIA	ISR/FSR uncertainty ²
$t\bar{t}$ dileptonic + 0...4+ partons	AlpGEN/PYTHIA	ISR/FSR uncertainty ¹
$t\bar{t}$ l +jets + 0...4+ partons	AlpGEN/PYTHIA	ISR/FSR uncertainty ¹
$t\bar{t}$ (no all-had.) $m_t = 140$ – 210 GeV	MC@NLO/HERWIG	mass variation ²
single top t -channel $W \rightarrow l\nu$	MC@NLO/HERWIG	²
single top t -channel $W \rightarrow l\nu$	AcerMC/PYTHIA	¹
single top s -channel $W \rightarrow l\nu$	MC@NLO/HERWIG	
single top tW production	MC@NLO/HERWIG	
$W \rightarrow e\nu$ + 0...5+ partons	AlpGEN/HERWIG	
$W \rightarrow \mu\nu$ + 0...5+ partons	AlpGEN/HERWIG	
$W \rightarrow \tau\nu$ + 0...5+ partons	AlpGEN/HERWIG	

continued on next page

Table 5.1.: Summary of Monte Carlo samples used for the analysis. For samples that are split into parton multiplicities the highest parton multiplicity sample is generated inclusively indicated with a “+”-sign.

physics process	generator	comments
$W(\rightarrow l\nu)b\bar{b} + 0\dots 3+$ partons	AlpGEN/HERWIG	
$W(\rightarrow l\nu)c\bar{c} + 0\dots 3+$ partons	AlpGEN/HERWIG	
$W(\rightarrow l\nu)c + 0\dots 4+$ partons	AlpGEN/HERWIG	
$Z \rightarrow ee + 0\dots 5+$ partons	AlpGEN/HERWIG	
$Z \rightarrow \mu\mu + 0\dots 5+$ partons	AlpGEN/HERWIG	
$Z \rightarrow \tau\tau + 0\dots 5+$ partons	AlpGEN/HERWIG	
$Z(\rightarrow ee)b\bar{b} + 0\dots 3+$ partons	AlpGEN/HERWIG	¹
$Z(\rightarrow \mu\mu)b\bar{b} + 0\dots 3+$ partons	AlpGEN/HERWIG	¹
$Z(\rightarrow \tau\tau)b\bar{b} + 0\dots 3+$ partons	AlpGEN/HERWIG	¹
WW	HERWIG	
ZZ	HERWIG	
WZ	HERWIG	

¹ used in 2011 analysis (b) only

² used in 2010 and 2011 analysis (a) only

6. Basic event selection and data-driven background estimation

In this chapter the basic event selection for top quark pair events in the lepton + jets channels is described. Based on that, the different QCD multi-jet background estimation methods and models are discussed and the data-driven W + jets background estimation is detailed.

6.1. Selection cuts

The event selection follows the $t\bar{t}$ lepton + jets event topology as described in Sec. 2.2.6.1. In these events one expects a lepton, a neutrino and about four jets. The objects used are detailed in Chapter 4. Based on this event topology a $t\bar{t}$ candidate event has been selected in 2010 collision data (shown in Fig. 6.1), which could be a $t\bar{t}$ decay or one of the background processes discussed in Secs. 5.4.2 and 5.4.3 as well as in this chapter.

The aim of the selection is to obtain a clean sample of top quark pair events with low background contributions while maintaining sufficient statistics of the sample. As different data sets are analysed, the event selection slightly differs not only with regards to the object level cuts as mentioned in Chapter 4, but also regarding the event level cuts. The data-driven background estimation techniques also require a top-like selection, which is usually modified as part of the method and also in order to be largely independent of the signal selection cuts.

For the event to be stored, it has to fire one of the triggers. Here, only electron (Sec. 4.2.3) and muon (Sec. 4.3.3) triggers are used since they provide the cleanest sample a priori. Depending on the lepton flavour, the event is categorised as electron or muon channel. Since one high- p_T lepton is expected, the event must only contain exactly one reconstructed and isolated muon or electron. Furthermore, at least three jets are required although at least four are expected to take into account that jets might lie outside the central detector region. The neutrino from the decay of the W boson gives rise to a cut on the missing transverse energy. Additionally, together with the lepton the transverse mass of the W boson, m_T^W , can be reconstructed and used for further background discrimination as described later. It is calculated via:

$$m_T^W = \sqrt{2p_T^l p_T^\nu (1 - \cos(\phi^l - \phi^\nu))}, \quad (6.1)$$

where p_T^l and ϕ^l are the lepton transverse momentum and azimuthal angle, and the neutrino information are obtained from the E_T^{miss} vector, which is constructed using the x - and y -components of the E_T^{miss} setting the z -component to zero. The 2011 analysis

6. Basic event selection and data-driven background estimation

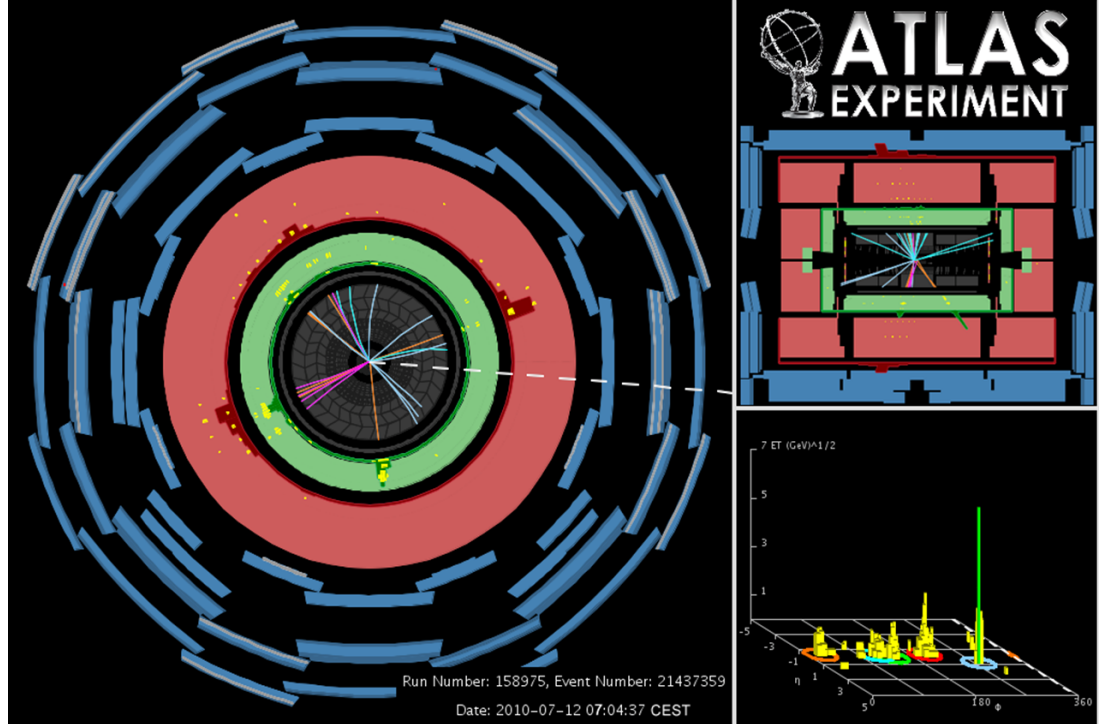


Figure 6.1.: Event display of a $t\bar{t}$ candidate in the electron + jets channel. The electron is shown as the orange downward-pointing track associated to the green cluster, and as the green tower in the η - ϕ lego plot in the bottom right. The direction of the missing transverse energy is shown as the dotted line in the r - ϕ view (left). [241]

(b) additionally requires at least one of the selected jets to be b -tagged (see Sec. 4.5.2). The event selection cuts for the analyses are summarised in Tab. 6.1.

Table 6.1.: Offline event selection cuts for the three analyses. Details of the objects and triggers used can be found in Chapter 4. Event level cuts require full detector functionality (see Sec. 5.1) and non-collision background rejection cuts on the primary vertex (Sec. 4.1.2).

cut	cut applied and threshold if applicable		
	2010 analysis	2011 analysis (a)	2011 analysis (b)
event level requirements	✓	✓	✓
pass trigger	✓	✓	✓
at least one lepton (muon or electron) matching with trigger object	20 GeV	25 GeV ^a / 20 GeV ^{b,c}	25 GeV

continued on next page

Table 6.1.: *Offline event selection cuts for the three analyses. Details of the objects and triggers used can be found in Chapter 4. Event level cuts require full detector functionality (see Sec. 5.1) and non-collision background rejection cuts on the primary vertex (Sec. 4.1.2).*

cut	cut applied and threshold if applicable		
	2010 analysis	2011 analysis (a)	2011 analysis (b)
veto events with additional leptons (muon or electron)	20 GeV	25 GeV ^a / 20 GeV ^{b,c}	25 GeV
count jets (require at least three for signal region)	25 GeV	25 GeV	25 GeV
E_T^{miss}	20 GeV ^a / 35 GeV ^b	25 GeV ^a / 35 GeV ^b	30 GeV
m_T^W	25 GeV ^a	25 GeV ^a	30 GeV
$m_T^W + E_T^{\text{miss}}$	60 GeV ^b	60 GeV ^b	-
at least one b -tagged jet	-	-	✓

^a e + jets channel

^b μ + jets channel

^c upper cut on muon $p_T < 150$ GeV to reduce the influence of inefficiencies found for trigger modelling in MC. Trigger matching only applied in MC.

6.2. QCD multi-jet background estimation

The excellent lepton identification capabilities of the ATLAS detector ensure that the dominant backgrounds to $t\bar{t}$ production are other processes that also produce prompt high- p_T leptons such as W and Z + jets production. There are, however, sizable contributions from processes that do not originate from the direct production of Z or W bosons or the $t \rightarrow W(\rightarrow l\nu)b$ vertex. These are for instance:

- semi-leptonic decays inside b -jets as shown in Fig. 6.2a,
- in-flight decays of π^\pm or K mesons,
- reconstruction of pions as electrons (the π^0 e.g. from the hadronisation of one of the quarks as shown in Fig. 6.2b),
- reconstruction of photons or photon conversions as electrons.

In general, one can classify these events into events with non-prompt leptons and events with hadronic jets identified as leptons. If at the same time the E_T^{miss} is mismeasured, these events have a similar signature as the signal events.

As the production rate of QCD multi-jet events with a cross section of about 1 mb [242] is much higher than the production of events with leptons ($\mathcal{O}(10$ nb), refer to Sec. 5.4),

6. Basic event selection and data-driven background estimation

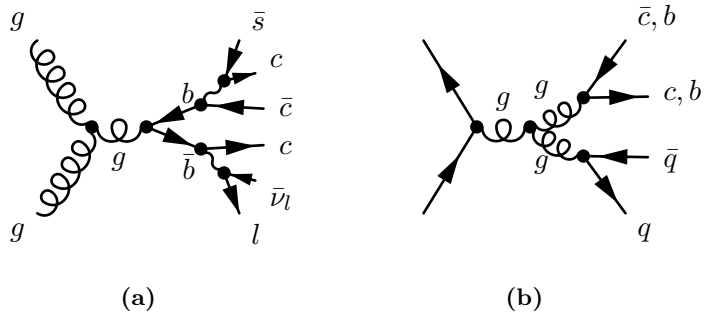


Figure 6.2.: Leading order Feynman diagrams for QCD multi-jet production that might enter the $t\bar{t}$ lepton + jets event selection: (a) leptonic final states of $b\bar{b}$ production, and (b) purely hadronic final states where one collimated jet formed from one of the hadronised quarks might be identified as a lepton.

there is a significant contribution of jets that have been misidentified as leptons in the selected data sample. However, since the fraction of multi-jet events passing the event selection compared to the total number of multi-jet events is very small, one cannot produce sufficient statistics in the Monte Carlo simulation. Furthermore, the multi-jet background is mostly from very rare response of the detector and therefore hard to simulate. Therefore, the approaches chosen here extract samples from collision data that allow modelling of the QCD background. There are two different approaches pursued in this work: The template fitting methods aim to obtain a sample from data that is able to model the multi-jet background while being orthogonal to the signal selection. Using a fit in a sideband region the multi-jet contribution in the signal sample is estimated. The matrix methods are based on the definition of a *loose* and a *tight* sample in data and the selection efficiencies of real and fake leptons therein in order to solve for the fake lepton rate. Both are described in the following. The methods used for the individual analyses are summarised in Sec. 6.2.3.

6.2.1. Template fitting methods

The template fitting methods obtain a multi-jet model from data, i.e. events including full kinematic information for all objects. In order to obtain a normalisation for the model a template fit is performed to signal-selected data using the model and simulation samples for all other processes. The fit is usually performed using a sideband region of an observable where the multi-jet background dominates, which is here the E_T^{miss} distribution.

Two different multi-jet modelling approaches have been developed. The *anti-electron method* utilises electron objects that have been selected by inverting electron identification cuts. This method is used for QCD multi-jet background estimation in the electron channel of the 2010 analysis. The *jet-electron method* selects jets and uses them as lepton objects.

6.2.1.1. Anti-electron method

The original idea for the *anti-electron method* stems from the CDF experiment (see e.g. [243]). For application at ATLAS it has initially been developed and used for the re-discovery of the top-quark at the LHC [244]. The *anti-electron method* employs electron identification cuts described in Sec. 4.2.1 that are designed to reject fake electrons. By inverting a selection of these one obtains a sample which contains predominantly fake electrons while being largely independent of the kinematic properties of the event. The data set is obtained from collision data by requiring at least one of the electron or photon triggers of the the data-taking period to fire. The particle identification cuts under study are applied to hadronic leakage, track quality and measurements in the strips and the middle sampling of the electromagnetic calorimeter. Several combinations of these cuts have been evaluated. The electron-like object has to fulfil all kinematic requirements including isolation. In case there are no signal electrons or muons, this electron is chosen as the candidate electron, and the rest of the event selection cuts are applied. As these electrons are similar to the signal electrons, they are called anti-electrons. For the 2010 analysis and the 2011 analysis (a) it has been found that requiring the hadronic leakage cut to fail yields best agreement between data and simulation, see the description of the fit method in Sec. 6.2.1.3.

Since the missing transverse energy for each event is calculated using only electrons that pass the electron identification cuts (refer to Secs. 4.2.1 and 4.6) the E_T^{miss} needs to be recalibrated treating the anti-electron as an electron and not as a hadronic jet.

6.2.1.2. Jet-electron method

The *jet-electron method* follows a very similar idea as the *anti-electron method* described above but employs jet objects instead of electron objects. The selection is therefore based on a data set that is obtained from jet-triggered events. The triggers used have a fixed rate based on a random acceptance decision at L1 and L2 levels where the EF requirement is sliced in jet p_T .

Similar to anti-electrons, the object used to model the lepton has to fulfil the same kinematic cuts as the signal lepton in p_T and η , but calibrated at EM scale. Therefore, also the E_T^{miss} is recalibrated. The jet-electron candidate furthermore has to have a large fraction of its energy deposited in the electromagnetic calorimeter of 80 to 95%. To suppress the selection of real electrons from photon conversions at least four tracks have to be associated with the jet. As above, no signal leptons must be present in the event. The *jet-electron model* is used for the 2011 analysis (b) for both electron and muon channel as cross check and for shape uncertainty evaluation. The only difference in the selection is the different η range.

6.2.1.3. Fit procedure

To estimate the number of expected QCD multi-jet events both approaches utilise a binned likelihood of the model and all other considered processes taken from simulation fit to data for a given number of jets, in the following also referred to as jet multiplicity

6. Basic event selection and data-driven background estimation

bin. Since multi-jet events are not expected to have on average a large value of E_T^{miss} this distribution is particularly sensitive to the QCD contribution. Furthermore, one can avoid any correlation with the extraction of the signal process by performing the fit in the E_T^{miss} sideband ($E_T^{\text{miss}} < 35$ GeV). In the fit the multi-jet template and the $t\bar{t}$ signal template are allowed to float freely. Except for the multi-jet template all other processes are normalised to their cross section expectation. The other background processes have Gaussian constraints roughly based on their cross section uncertainty varying from 10% for single top processes up to 30% for $W + \text{jets}$. The diboson contribution is added to the $Z + \text{jets}$ processes.

The uncertainties on the QCD prediction are evaluated as follows. As statistical uncertainty the uncertainty on the fit and the extrapolation uncertainty from the fit region to the signal region of each QCD model are taken. In order to check the linearity of the fitting procedure pseudo experiments are performed. The pseudo experiments are constructed by varying the QCD contribution from 0.5 to 1.5 of the fitted rate. A linear correlation between the input and the fitted QCD contribution is found and the slope is in perfect agreement with unity, i.e. the fitting procedure is bias free. The uncertainty on the slope (gradient) in each jet multiplicity bin is taken as a systematic uncertainty of the method in this bin. Furthermore, for the *anti-electron model* an alternative model is created to evaluate the shape uncertainty. Based on these studies for analyses not using b -tagging a total uncertainty of 50% and for analyses using b -tagging a total uncertainty of 100% on the multi-jet background contribution is assumed. The higher uncertainty on the b -tagged estimates is due to the unknown heavy flavour contribution and the lower statistics of the model. A more detailed discussion of the uncertainties can be found in Appendix B.

The results of the fits in 2010 data split into jet multiplicity bins using the *anti-electron model* are shown in Fig. 6.3. The performance of the method is evaluated using χ^2 and Kolmogorov-Smirnov (KS) [245] statistical tests. These tests measure the difference between two distributions and express the compatibility as a p-value of the test statistic. A few selected benchmark distributions to assess the validity of the model to describe the multi-jet background in the signal region can be found in Fig. 6.4. Further distributions, studies conducted as well as linearity checks are given in Appendix B. The *anti-electron model* has also been used for the first measurement of top quark pair production at ATLAS [244], the measurement of the cross section for the production of a W boson in association with b -jets [246], and the search for $t\bar{t}$ resonances [247].

The fitted QCD multi-jet fractions with respect to 2010 data without b -tagging using the *anti-electron model* are summarised in Tab. 6.2. The fit results for the 2011 analysis (b) are not listed here since this model is only used to evaluate the QCD shape uncertainty with the normalisation taken from the *matrix methods* described below. To acquire sufficient statistics in 2011 data the b -tagging requirement is loosened using the 85% b -tagging efficiency working point corresponding to a weight cut of greater than 0.0714225 instead of using the 70% point.

6.2. QCD multi-jet background estimation

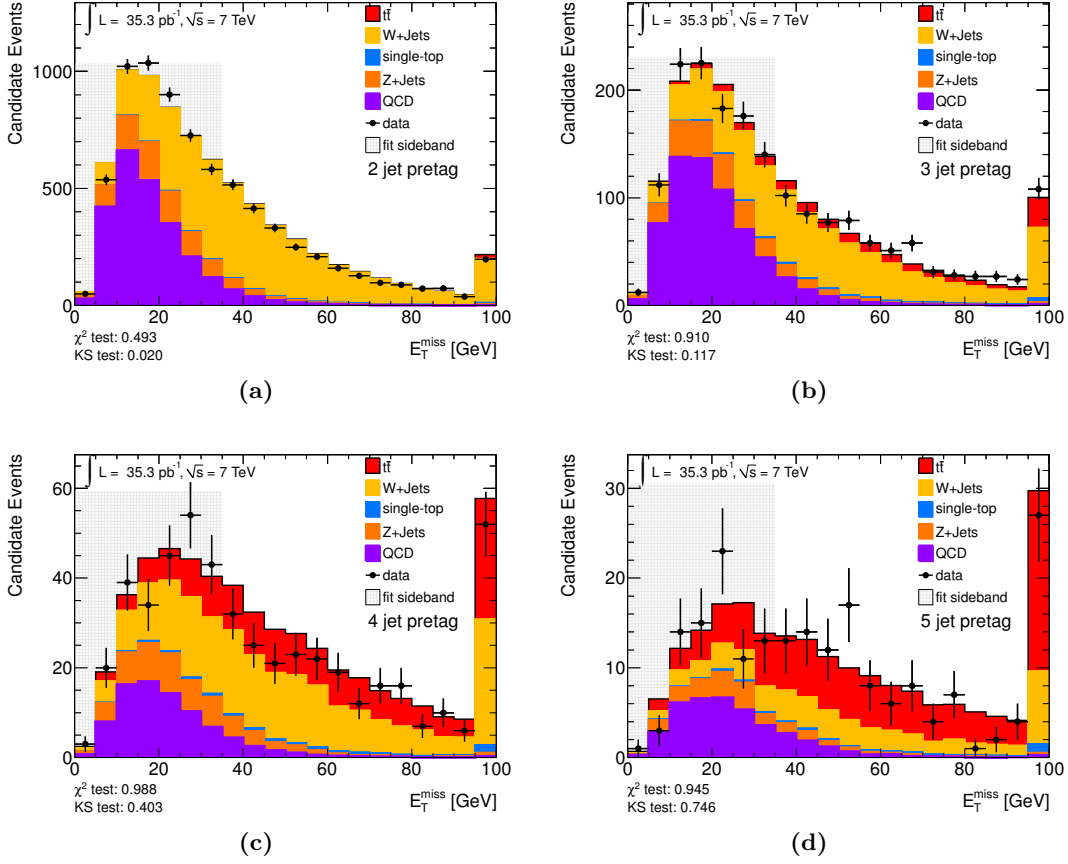


Figure 6.3.: QCD multi-jet background fit results using the anti-electron model (purple) in the (a) 2 jet exclusive, (b) 3 jet exclusive, (c) 4 jet exclusive, and (d) 5 jet inclusive jet multiplicity bin. The fit is performed in the E_T^{miss} sideband (shaded), $E_T^{\text{miss}} < 35$ GeV. In the bottom left of each panel the χ^2 and KS test between data and the simulation stack plus QCD model are shown.

Table 6.2.: Number of selected data signal events, predicted QCD events and fraction in 35 pb^{-1} of 2010 data in the signal region with a given number of jets in the sample without b -tagging requirement using the anti-electron model. Uncertainties are statistical only.

	data events	QCD events	fake fraction
2 jets	2567	161.1	$(6.3 \pm 0.7)\%$
3 jets	755	63.0	$(8.3 \pm 1.2)\%$
4 jets	261	11.8	$(4.5 \pm 2.3)\%$
≥ 5 jets	123	7.9	$(6.4 \pm 3.2)\%$

6. Basic event selection and data-driven background estimation

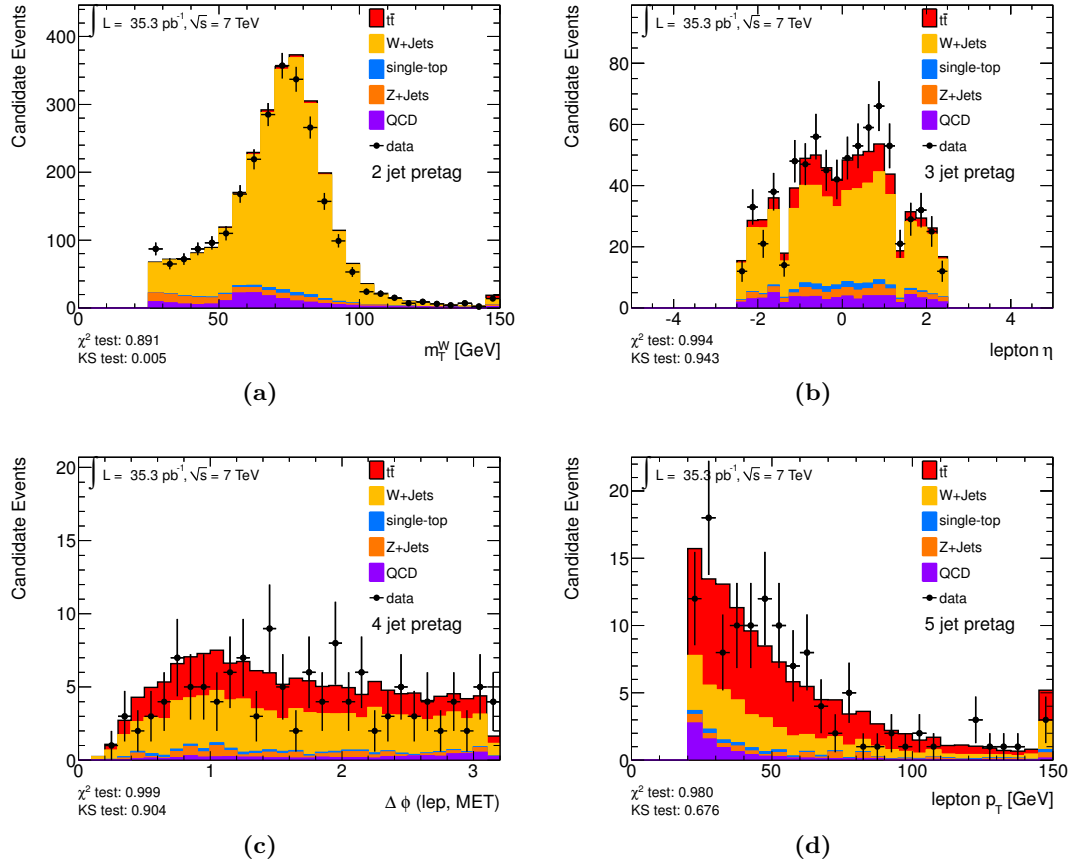


Figure 6.4.: Control plots for QCD multi-jet background evaluation using the anti-electron model after applying the E_T^{miss} cut: (a) transverse mass of the W boson in the 2 jet exclusive jet bin, (b) lepton η in the 3 jet exclusive jet bin, (c) $\Delta\phi$ between the lepton and the E_T^{miss} vector in the 4 jet exclusive bin, and (d) lepton p_T in the 5 jet inclusive jet bin. In the bottom left of each panel the χ^2 and KS test between data and the simulation stack plus QCD model are shown.

6.2.2. Matrix methods

The *matrix method* pursues a very different approach compared to the fitting methods. The method obtained its name from the system or matrix of equations used to calculate the number of QCD multi-jet events in the signal region. The *matrix method* exploits differences in lepton identification-related properties between prompt isolated leptons from W and Z decays referred to as *real leptons* in the following and those in which the leptons are either non-isolated or result from misidentification of photons or jets referred to as *fake leptons*. Two different samples are defined using the full signal event selection that only differ in the lepton identification criteria: a *tight* sample for which usually the standard signal selection criteria are applied and a *loose* sample with less harsh requirements, the former being a subset of the latter.

The assumption of the *matrix method* is that the number of selected events in the *loose* and the *tight* sample, N^{loose} and N^{tight} , can be expressed as a linear combination of the numbers of events with real and fake leptons, N^{real} and N^{fake} , respectively. The following system of equations is defined:

$$N^{\text{loose}} = N_{\text{real}}^{\text{loose}} + N_{\text{fake}}^{\text{loose}}, \quad (6.2)$$

$$N^{\text{tight}} = \varepsilon_{\text{real}} N_{\text{real}}^{\text{loose}} + \varepsilon_{\text{fake}} N_{\text{fake}}^{\text{loose}}, \quad (6.3)$$

where $\varepsilon_{\text{real}}$ and $\varepsilon_{\text{fake}}$ represent the probability for a *real* or *fake* lepton satisfying the *loose* criteria to also match the *tight* ones. One can thus write these as:

$$\varepsilon_{\text{real}} = \frac{N_{\text{real}}^{\text{tight}}}{N_{\text{real}}^{\text{loose}}}, \quad (6.4)$$

$$\varepsilon_{\text{fake}} = \frac{N_{\text{fake}}^{\text{tight}}}{N_{\text{fake}}^{\text{loose}}}. \quad (6.5)$$

If both efficiencies are estimated in control samples outside the signal region that contain either only *real* or *fake* leptons one can solve the equations for the number of events with a *fake* lepton in the *tight* sample, i.e. in the signal sample:

$$N_{\text{fake}}^{\text{tight}} = \frac{\varepsilon_{\text{fake}}}{\varepsilon_{\text{real}} - \varepsilon_{\text{fake}}} \left(\varepsilon_{\text{real}} N^{\text{loose}} - N^{\text{tight}} \right). \quad (6.6)$$

To obtain physical distributions from the efficiencies events in data that pass the *loose* selection are weighted. For events that pass the *loose* selection while failing the *tight* one the weight

$$w(x) = \frac{\varepsilon_{\text{real}}(x) \times \varepsilon_{\text{fake}}(x)}{\varepsilon_{\text{real}}(x) - \varepsilon_{\text{fake}}(x)} \quad (6.7)$$

is applied whereas for events passing both selections

$$w(x) = \frac{(\varepsilon_{\text{real}}(x) - 1) \times \varepsilon_{\text{fake}}(x)}{\varepsilon_{\text{real}}(x) - \varepsilon_{\text{fake}}(x)} \quad (6.8)$$

6. Basic event selection and data-driven background estimation

is used, where x is a parametrisation of the lepton kinematics, e.g. the η and E_T/p_T coordinates.

In order to reduce the influence of statistical fluctuations the data set obtained with the *loose* lepton definition should yield significantly higher statistics than the *tight* one. The *loose* lepton definitions as well as their efficiency parametrisation and the definition of control regions is given in the following.

6.2.2.1. Electron channel

In the electron channel the *matrix method* is used for the 2011 analyses. For the 2011 analysis (a) the *loose* electron has to pass the **medium** electron identification cuts as described in Sec. 4.2.1 with an additional hit in the innermost layer of the Pixel Detector. The isolation requirements are loosened to $E_T < 6$ GeV deposited in the calorimeter towers in a cone of radius $R = 0.2$ around the electron position (cf. Sec. 4.2.4). If a *loose* electron is identified the E_T^{miss} is recalibrated to correctly treat it as electron object. The efficiency for real leptons, $\varepsilon_{\text{real}}$, is measured using the *tag-and-probe method* in $Z \rightarrow ee$ events as described in Sec. 4.2. Hereby, the *loose* electrons serve as *tag* objects and the efficiency is parametrised in 18 bins in η and six bins in E_T . The efficiency for fake leptons, $\varepsilon_{\text{fake}}$, is determined in data in events with at least one jet and $5 \text{ GeV} < E_T^{\text{miss}} < 20$ GeV and is also parametrised in η . The evaluation of systematic uncertainties is performed by defining a different control region, using a different $\varepsilon_{\text{fake}}$ parametrisation, and taking $\varepsilon_{\text{real}}$ from the Monte Carlo simulation. Furthermore, the contribution of real electrons to the *loose* sample is varied based on MC. It should be noted that the *tight* data set is not strictly a subset of the *loose* one, since events with a **medium** and a **tight** electron enter the *tight* data set, but are rejected from the *loose* one because there is more than one lepton of at least **medium** quality. This leads to small inconsistency that is however negligible compared to the other uncertainties. Based on these studies, a total uncertainty of 50% is assigned to the multi-jet contribution.

For the 2011 analysis (b) the *loose* electron requirement is to pass **medium** electron identification cuts as described in Sec. 4.2.1. Additionally, the electron object must not stem from a photon conversion. The isolation requirements are loosened to $E_T < 6$ GeV deposited in the calorimeter towers in a cone of radius $R = 0.2$ around the electron position and the sum of transverse momenta of all tracks in the ID must not exceed 6 GeV within a cone of size $\Delta R = 0.3$ (cf. Sec. 4.2.4). As above, if a *loose* electron is identified the E_T^{miss} is recalculated to correctly treat it as electron object. As above, the *real* lepton efficiency, $\varepsilon_{\text{real}}$, is measured using the *tag-and-probe method* in $Z \rightarrow ee$ events and parametrised in 18 η and 5 E_T bins. The *fake* lepton efficiency is determined in a control region with $E_T^{\text{miss}} < 20$ GeV in events with at least one jet where the contribution from W and Z events is estimated using simulation. A minimum distance between the jet with highest momentum and the electron of $\Delta R > 0.7$ is required and additionally the distance to the closest jet is used in the efficiency parametrisation. For the uncertainty determination different background subtraction methods are evaluated, the signal and fake control regions are varied as well as the fit ranges (some details can be found in Ref. [248]). A total uncertainty of 50% is assigned to the multi-jet prediction.

6.2.2.2. Muon channel

The *matrix method* in the muon channel is used for all analyses with small differences with regards to the regions used for the *fake* efficiency determination and the *loose* muon definition. For the *loose* selection the muon track and calorimeter isolation criteria are dropped (see Sec. 4.3.4) while keeping the muon jet overlap removal as described in Sec. 4.7.2. The efficiency for real muons is measured using the *tag-and-probe method* in $Z \rightarrow \mu\mu$ events as described in Sec. 4.3.1 and parametrised in muon η and p_T . The *loose* efficiency is measured in events with at least one jet with $p_T > 25$ GeV and $|\eta| < 2.5$. For the 2010 analysis a selection region is used where the significance of the impact parameter of the associated track with respect to the primary vertex, $S_{d_0} = \frac{d_0}{\sqrt{\text{cov}(d_0)}}$ (see Sec. 4.1.1), has to be $S_{d_0} > 3$. The contamination of the latter region with muons from the hard scattering process is found to be very low. The 2011 analysis (a) uses a region that is orthogonal to the signal selection requiring $m_T^W < 20$ GeV for the *fake* efficiency measurement while the 2011 analysis (b) additionally requires $m_T^W + E_T^{\text{miss}} < 60$ GeV. The 2011 analyses use the impact parameter region as cross check and the 2010 analysis the low m_T^W and $m_T^W + E_T^{\text{miss}}$ region. For all control regions the expected contributions from W and $Z + \text{jets}$ production are subtracted using Monte Carlo predictions. The measured efficiencies are parametrised in absolute values of η and for the 2011 analysis (b) also in leading jet p_T to account for hadronic activity from hard jets affecting the muon isolation. Furthermore, the efficiency measurements for the 2011 analysis (b) are split into two LHC running periods to account for higher pileup towards the end of 2011. Comparing with the control regions the total uncertainty on the yield prediction is estimated to 50% for all analyses.

6.2.3. Discussion of QCD multi-jet estimation methods

Several QCD multi-jet estimation methods are used in this work as described above. For each of the analyses different approaches are chosen. The reasons for that are manifold. For a template fit to data in order to extract the $t\bar{t}$ cross section as described in Chapter 7 a full model as obtained from the *anti-electron* and *jet-electron* methods would be preferable, since these models are completely orthogonal to the signal selection and the normalisation is obtained in sideband regions. Even though the *matrix methods* determine the efficiencies used in sideband regions, they reuse data events and are therefore not independent of the signal selection which might cause undesired correlations, in particular when the *loose* and *tight* definitions are very similar.

The fake lepton models, however, are particularly difficult to obtain in the first place, because there are several possibilities for an object to fake a lepton and by defining the anti- or jet-electron the correct mixture needs to be obtained as well as the right propagation to the missing transverse energy. Furthermore, it is challenging to maintain such a model over time since trigger thresholds and definitions and also lepton identification cuts evolve. In contrast to that, the *matrix methods* do not need to define an orthogonal fake lepton object, but just have to loosen the lepton identification and/or isolation cuts and a region where fake leptons are expected to dominate over real leptons. It is hereby

6. Basic event selection and data-driven background estimation

important to determine a reasonable fake efficiency parametrisation but less crucial to obtain a correct mixture of fake leptons. Since the *matrix methods* by definition always have larger statistics than the signal data set, they usually provide rather smooth shapes while the fake lepton models in particular towards the end of 2011 data-taking suffer from low statistics. As a consequence this leads to unphysical spikes in the multi-jet background distributions which can only partly be countered by smoothing algorithms. Unfortunately this is causing the fit to scale the QCD multi-jet background down, which is why the results of the *matrix methods* are used as nominal multi-jet background for the 2011 analyses and the fake lepton models only as cross check and to evaluate the shape uncertainty. The use of the different methods in the analyses is summarised in Tab. 6.3.

Table 6.3.: *Summary of the use of the different QCD multi-jet background estimation methods in the analysis: used as nominal model (✓), as cross check and shape uncertainty (✗) or not used (-).*

Estimation method	Usage in analysis		
	2010	2011 (a)	2011 (b)
anti-electron model ($e + \text{jets}$)	✓	✗	-
alternative anti-electron model ($e + \text{jets}$)	✗	-	-
jet-electron model ($e + \text{jets}$)	-	-	✗
jet-electron model ($\mu + \text{jets}$)	-	-	✗
matrix method ($e + \text{jets}$)	-	✓	✓
matrix method ($\mu + \text{jets}$)	✓	✓	✓
alternative matrix method ($\mu + \text{jets}$)	✗	✗	-

6.3. Data-driven estimation of the $W + \text{jets}$ background

At the LHC the rate of W^+ production is higher than that of W^- production because the parton density of up quarks is larger than the one of down quarks at a proton-proton collider. Furthermore, the theory prediction of the ratio of W^+ to W^- production is well understood [88, 249] and in particular better than the prediction of the total cross section of W bosons in association with three or more jets. Since the production of all other dominant processes is charge symmetric—the single top contribution is relatively small and taken from simulation—the charge asymmetry can be exploited to estimate the $W + \text{jets}$ background normalisation. Hereby, the charge of the W boson is associated with the charge of the selected lepton. The formula used to extract the number of $W + \text{jets}$ events for a jet multiplicity bin is given by:

$$N_W = N_{W^+} + N_{W^-} = \frac{N_{W^+}^{\text{MC}} + N_{W^-}^{\text{MC}}}{N_{W^+}^{\text{MC}} - N_{W^-}^{\text{MC}}} \cdot (D^+ - D^-) = \frac{r^{\text{MC}} + 1}{r^{\text{MC}} - 1} \cdot (D^+ - D^-), \quad (6.9)$$

6.3. Data-driven estimation of the $W + \text{jets}$ background

Table 6.4.: $W + \text{jets}$ scale factors for the 2011 analysis (a) obtained with the charge asymmetry method using the signal selection for a given jet bin. Uncertainties are statistical only.

jet bin	$\mu + \text{jets}$ channel	$e + \text{jets}$ channel
1 jet	0.983 ± 0.034	0.948 ± 0.080
2 jets	0.942 ± 0.076	0.907 ± 0.058
3 jets	0.870 ± 0.097	0.881 ± 0.123
4 jets	0.849 ± 0.142	0.839 ± 0.166
≥ 5 jets	0.687 ± 0.180	1.098 ± 0.331

where $N_{W^{+/-}}^{\text{MC}}$ is the number of events of positively or negatively charged $W + \text{jets}$ events obtained from MC simulation and $D^{+/-}$ the total number of events with a positively/negatively charged lepton in data. The ratio $r^{\text{MC}} = \frac{\sigma(pp \rightarrow W^+)}{\sigma(pp \rightarrow W^-)}$ is evaluated using the signal event selection on the $W + \text{jets}$ MC samples. Smaller contributions, e.g. from single top production, are subtracted from Eq. 6.9. The scale factors to be applied to selected $W + \text{jets}$ events after scaling them to the theory cross section obtained with this method for the 2011 analyses (a) and (b) are given in Tabs. 6.4 and 6.5, respectively. The apparent difference between the electron and the muon estimates for the 2011 analysis (a) for events with five and more jets is due to limited statistics in both the data and simulation samples and covered by the systematic uncertainties. The b -tagged $W + n$ jets estimates, $W_{\geq 1\text{tag}}^n$, used in the 2011 analysis (b) are obtained by using so-called *tagging fractions*. The *tagging fraction*, f_{tag}^n , is the ratio between the number of $W + \text{jets}$ events with at least one b -tagged jet and the number of events without tagged jets for a given number of jets (jet bin). It is derived from data after subtraction of all backgrounds for events with two jets. The ratio between the tagging fractions in the n jet bin and the 2 jet bin, $f_{\text{tag}}^{2 \rightarrow n}$, is computed using simulation. With the pretag yields, W_{pretag}^n , the b -tagged $W + n$ jets estimates are then given by:

$$W_{\geq 1\text{tag}}^n = W_{\text{pretag}}^n \cdot f_{\text{tag}}^2 \cdot f_{\text{tag}}^{2 \rightarrow n}. \quad (6.10)$$

The systematic uncertainties are dominated by the heavy flavour fraction that is also measured in data as described below in Sec. 6.3.1. All other uncertainties are comparably small. Details are given in Sec. 7.2.

The $W + \text{jets}$ estimates for the 2010 analysis were initially also estimated using a data-driven technique called *Berends-Giele scaling* [250]. It is based on the hypothesis that the ratio of $W + n$ jets to $W + (n + 1)$ jets is constant as a function of n [251]. Thus, the number of $W + \text{jets}$ events in a given jet bin, n , can be estimated using:

$$N_W^n = N_W^2 \left(\frac{N_W^2}{N_W^1} \right)^{n-2}, \quad (6.11)$$

6. Basic event selection and data-driven background estimation

Table 6.5.: $W + \text{jets}$ scale factors for the 2011 analysis (b) obtained with the charge asymmetry method using the signal selection with at least one b -tagged jet for a given jet bin with full uncertainty.

jet bin	$\mu + \text{jets}$ channel	$e + \text{jets}$ channel
1 jet	$1.05^{+0.26}_{-0.23}$	$0.98^{+0.28}_{-0.27}$
2 jets	$0.97^{+0.13}_{-0.12}$	$0.88^{+0.16}_{-0.15}$
3 jets	$0.89^{+0.12}_{-0.11}$	0.81 ± 0.14
4 jets	$0.95^{+0.17}_{-0.15}$	$0.83^{+0.14}_{-0.16}$
≥ 5 jets	$0.90^{+0.22}_{-0.20}$	$0.82^{+0.24}_{-0.20}$

Table 6.6.: Scale factors for the heavy flavour fractions in the $W + \text{jets}$ background for the 2011 analysis (b) in the 2 jet exclusive bin. The statistical and systematic uncertainties are summed in quadrature.

channel	$Wb\bar{b}/Wc\bar{c} + \text{jets}$	$Wc + \text{jets}$	$W \text{ light} + \text{jets}$
$\mu + \text{jets}$	1.24 ± 0.34	$0.98^{+0.37}_{-0.31}$	$0.97^{+0.07}_{-0.08}$
$e + \text{jets}$	$1.41^{+0.31}_{-0.39}$	$0.73^{+0.39}_{-0.35}$	1.00 ± 0.09

where the number of $W + \text{jets}$ events in the 1 and the 2 jet bin, N_W^1 and N_W^2 , are measured in data after subtracting all backgrounds using MC. Since this estimate worsens the data-MC agreement, the original normalisation from Monte Carlo simulation is used for the final analysis instead of this approach, but the extrapolation uncertainty to the high multiplicity jet bins is adapted as discussed in Sec. 7.2.

6.3.1. Data-driven estimation of the heavy flavour content in the $W + \text{jets}$ background

The heavy flavour content in the $W + \text{jets}$ background is estimated using the *tag-counting method* in the 1 and 2 jet bin. After subtracting the non- $W + \text{jets}$ background the number of data events can be written as a function of the contributions of the $W + \text{light}$ flavour, $Wb\bar{b}$, $Wc\bar{c}$ and $Wc + \text{jets}$ processes. For estimates in the b -tagged sample these fractions are multiplied by the tagging probability for each process. By solving a system of equations scaling factors for each of the processes are obtained. 2010 data require that the fraction of $Wb\bar{b}$ and $Wc\bar{c} + \text{jets}$ is increased by a factor of 1.30 ± 0.65 with respect to the theoretical prediction while keeping the integral of all $W + \text{jets}$ events constant. For the 2011 analysis (b) the fractions are determined for the electron and the muon channel separately. The scale factors are summarised in Tab. 6.6. Their uncertainties are discussed in Sec. 7.2.

7. Measurement and signal extraction method

In order to perform a cross section measurement one needs to select events, N_{data} , in a collision data set of known integrated luminosity, \mathcal{L} , and compare it to predicted events, e.g. from MC simulation, taking into account both signal and potential background processes. With known signal acceptance, α , due to detector geometry and event selection one can determine the cross section using

$$\sigma = \frac{N_{\text{signal}}}{\alpha \cdot \mathcal{L}} = \frac{N_{\text{data}} - N_{\text{background}}}{\alpha \cdot \mathcal{L}}, \quad (7.1)$$

where N_{signal} and $N_{\text{background}}$ are the number of signal and background events, respectively. There are several different methods to extract the cross section as discussed in the following.

For the first measurement of the $t\bar{t}$ cross section at ATLAS analysing a data set of 2.9 pb^{-1} of 2010 data an event-counting approach was chosen [244], simply plugging numbers into Eq. 7.1. This approach is commonly employed when there is only limited statistics available, in this case only two dozens of signal events were expected. Tight cuts such as requiring at least four jets were applied to gain a clean signal sample. The background contributions were obtained similarly as described in Chapter 6: The QCD multi-jet background is completely taken from data while the $W + \text{jets}$ background normalisation is estimated using the ratio of events in the two to the one jet bin and extrapolating into the signal region. For all other backgrounds simulation estimates are used.

With the availability of the full 2010 data set and later the 2011 data set and consequently much higher statistics multi-dimensional distributions can be used instead of counting experiments. Therefore, the measurement of the top quark pair cross section in this work is based on a template fit. A priori normalisations are still taken from side-band regions or theory, but the fit is furthermore sensitive to the normalisation of both signal and background contributions in the signal region. This is in particular achieved by using variables that discriminate the $t\bar{t}$ signal from the dominant $W + \text{jets}$ and QCD multi-jet background. By combining kinematic variables such as lepton η with event shape variables into a single variable one can further increase the discrimination power. The shape of the discriminant, however, does not only help normalise the different processes, but also contains information regarding systematic shifts that might be preferred by data. This can be exploited by a technique called profile likelihood, which includes several sources of systematic uncertainty as so-called nuisance parameters in the fit used for the 2010 analysis and the 2011 analysis (a). Further background discrimination and

7. Measurement and signal extraction method

suppression is achieved by the use of b -tagging information in the 2010 and the 2011 analysis (b).

Additionally, the sample analysed is extended to 3-jet final states and split into three sub-samples according to the jet bin (multiplicity) for the electron and the muon channel: 3 jets exclusive, 4 jets exclusive and 5 jets inclusive, i.e. five and more jets. By exploiting the 3 jet bin additional sensitivity to the normalisation of the $W + \text{jets}$ background is gained. Since the ratio of $W + n$ jets to $W + (n+1)$ jets is roughly constant as a function of n [251] as described in Sec. 6.3, a measurement of the $W + \text{jets}$ normalisation allows to constrain the $W + \text{jets}$ background in the higher jet bins where the $t\bar{t}$ signal dominates. Naively, one would not expect $t\bar{t}$ events in the lepton + jets channel in the 3 jet bin, because the event topology (see Sec. 2.2.6.1) suggests the presence of at least four jets, two from the decays of the top quarks and two from the hadronic W decay. However, since only jets within $|\eta| < 2.5$ are considered and jets might also escape detection for other reasons, about one third of all $t\bar{t}$ events is present in this bin. Nevertheless, this bin is dominated by the $W + \text{jets}$ background that decreases with increasing jet multiplicity as shown in Fig. 7.1.

In this chapter the discriminating variables are described in Sec. 7.1 and combined into a likelihood discriminant in Sec. 7.1.1. This discriminant is affected by systematic uncertainties which are described in Sec. 7.2. The idea of the likelihood fit method is discussed in Sec. 7.3 including its extension to the profile likelihood method.

7.1. Discriminating variables

The choice of variables for the likelihood discriminant is based on a few criteria. The foremost important criterion is good discrimination against the $W + \text{jets}$ background. Since a projective likelihood method is employed (see Sec. 7.3), the correlation between the variables should be small in order to allow for optimal performance. To prevent accidental higher order correlations between the variables a small set of variables is used. These have to be well understood, i.e. the data-MC agreement should be good in control regions. The 2010 analysis additionally aims to reduce the sensitivity to the jet energy scale uncertainty (see Sec. 7.2) that was expected to be the dominant uncertainty. However, having studied the fit method in more detail, the 2011 analysis (a) explicitly tries to be sensitive to this uncertainty to constrain it using data as briefly motivated above and discussed below in Sec. 7.3. The 2011 analysis (b) pursues an approach similar to the 2011 analysis (a) but does not explicitly aim to be sensitive to the jet energy in the choice of variables, because it is already sensitive to it due to the measurement method described in Chapter 10. A detailed summary of all variables studied as well as their discrimination power can be found in Reference [248].

Based on these criteria and studies all three analyses use the following common variables:

- pseudorapidity of the lepton, η ,
- transformed form of aplanarity, $\exp(-8 \times \mathcal{A})$,

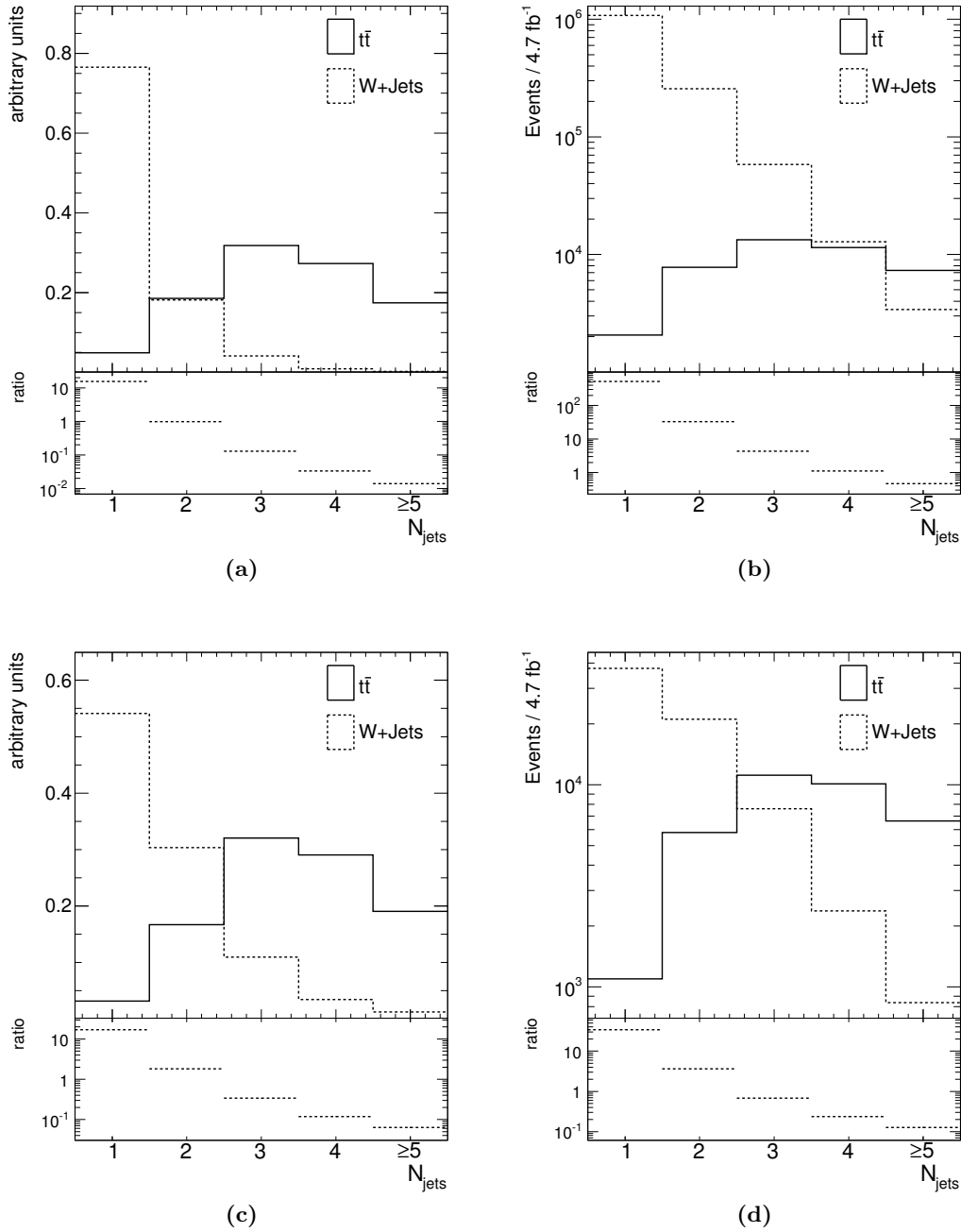


Figure 7.1.: Expected fraction (left) and number of selected events (right) for the 2011 analysis (b) using 4.7 fb^{-1} in the $e + \text{jets}$ channel based on simulation of $t\bar{t}$ production and the dominant $W + \text{jets}$ background process, shown as a function of the number of selected jets in the event without b-tagging requirement (top) and with at least one selected b-jet (bottom). The ratio of $W + \text{jets}$ to $t\bar{t}$ is shown in the bottom part of each plot.

7. Measurement and signal extraction method

- sum of transverse momenta of the third and fourth jet divided by the sum of z -components of all selected objects and transformed to $\exp(-4 \times H_{T,3p})$,

where the aplanarity is defined as the 1.5 times the smallest eigenvalue, $\mathcal{A} = \frac{3}{2}\lambda_3$, of the sphericity tensor:

$$S^{\alpha\beta} = \frac{\sum_i^{N_{\text{obj}}} p_i^\alpha p_i^\beta}{\sum_i^{N_{\text{obj}}} |\vec{p}_i|^2}, \quad (7.2)$$

for $\alpha, \beta = 1, 2, 3$. The eigenvalues are defined such that $\lambda_1 \geq \lambda_2 \geq \lambda_3$ and $\lambda_1 + \lambda_2 + \lambda_3 = 1$. For a planar event $\mathcal{A} \approx 0$ and for an isotropic one $\mathcal{A} \approx \frac{1}{2}$. The sums in Eq. 7.2 run over the four leading jets (three jets in the 3 jet bin) and the charged lepton.

The variable $H_{T,3p}$ is defined as:

$$H_{T,3p} = \sum_{i=3}^{N_{\text{jets}}} (p_T^i) / (p_z^\nu + p_z^l + \sum_{i=0}^{N_{\text{jets}}} p_z^i), \quad (7.3)$$

where p_z^ν and p_z^l are the momentum z -components of the neutrino and lepton, respectively, and the sum runs up to $N_{\text{jets}} = 4$. Here, p_z^ν is obtained by assuming that the missing transverse energy in the event stems from the neutrino only, i.e. $E_T^{\text{miss}} = p_T^\nu$ and using the mass of the W boson of $m_W = 80.425$ GeV as constraint. One can formulate a quadratic equation for p_z^ν with solutions:

$$p_z^\nu = \frac{\mu \cdot p_z^l}{p_T^{l2}} \pm \sqrt{\frac{\mu^2 \cdot p_z^{l2}}{p_T^{l4}} - \frac{E^{l2} \cdot p_T^{\nu2} - \mu^2}{p_T^{l2}}}, \quad (7.4)$$

with

$$\mu = \frac{m_W^2}{2} + p_T^l \cdot p_T^\nu \cdot \cos \Delta\phi, \quad (7.5)$$

where E^l is the energy of the lepton and $\Delta\phi$ the azimuthal angle between the charged lepton and the E_T^{miss} vector. In case Eq. 7.4 has two solutions the one closer to zero is chosen. If there is no real solution the value of E_T^{miss} is iteratively scaled down until a real solution is found.

Because of the veto against electrons in the transition region $1.37 < |\eta| < 1.52$, the pseudorapidity distribution of the lepton in the electron channel has a hole. In order to avoid empty bins, the η distribution in the electron channel is shifted such that:

$$\eta = \begin{cases} \eta^{\text{det}} & \text{for } |\eta^{\text{det}}| < 1.37, \\ \eta^{\text{det}} - 0.15 & \text{for } 1.52 < \eta^{\text{det}} < 2.47, \\ \eta^{\text{det}} + 0.15 & \text{for } -2.47 < \eta^{\text{det}} < -1.52. \end{cases} \quad (7.6)$$

For the muon channel no transformation is used.

The variables exploit the fact that top quark pair events contain on average more energy than $W + \text{jets}$ events. Furthermore, due to the large mass of the top quark its decay products are mostly found in the central region of the detector. From Figs. 7.2

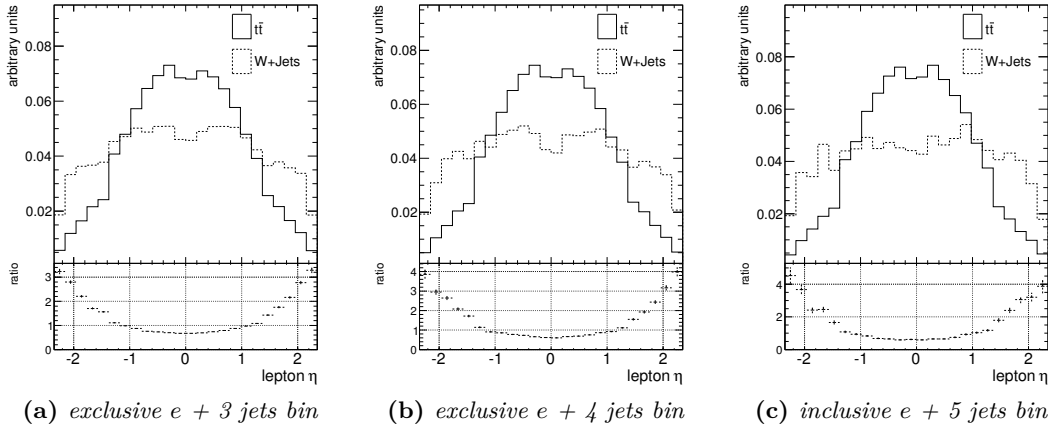


Figure 7.2.: Lepton η distribution in the $e + 3$, 4 , and ≥ 5 jets bin for $t\bar{t}$ production and the dominant $W + \text{jets}$ background process without b -tagging requirement. The ratio of $W + \text{jets}$ to $t\bar{t}$ is shown in the bottom part of each plot.

to 7.4 one can see that the variables selected show good discrimination between the $t\bar{t}$ signal and the $W + \text{jets}$ background. The transformations of \mathcal{A} and $H_{T,3p}$ mentioned above are chosen such that the distributions spread over a wider range and the difference in statistics between the bins is smaller. All three variables have no or only very low sensitivity to the jet energy scale uncertainty, the lepton pseudorapidity by definition and the other two since they consider momentum ratios of several objects in the event and therefore reduce the effect of energy shifts.

For the 2010 analysis an additional variable is employed to increase separation: the average **JetProb** b -tagging weight of the two selected jets with highest b -tagging probability, \bar{w}_{JP} . It is defined as

$$\bar{w}_{\text{JP}} = \frac{w_{\text{jet}_1} + w_{\text{jet}_2}}{2}, \quad (7.7)$$

where $w_{\text{jet}_{1/2}}$ are the b -tagging weights of the two jets in the form of $-\log_{10} \mathcal{P}_{\text{jet}}$ as described in Sec. 4.5.1. This variable is independent of the other kinematic variables. The choice for the **JetProb** algorithm over the **SV0** algorithm is due to the availability of more calibration points that lead to better data-MC agreement (refer to Sec. 4.5.1). Most of the $W + \text{jets}$ events do not contain b -jets so that one might as well just consider the first b -tagged jet. However, the tagging algorithm also selects a considerable amount of c -jets and the production of $Wc/Wc\bar{c} + \text{jets}$ is non-negligible. Since one expects two b -jets in the final state of a $t\bar{t}$ event, using the two selected jets with highest b -tagging probability yields better separation. Good agreement between data and simulated events is achieved for the 4 and 5 jet bin. However, for the 3 jet bin for low b -tagging probabilities larger discrepancies are found that are not covered by the mistagging uncertainties. It is thus decided to not use this variable in the 3 jet bin, also because studies show that fluctuations of the variable in this bin have large influence on the cross section

7. Measurement and signal extraction method

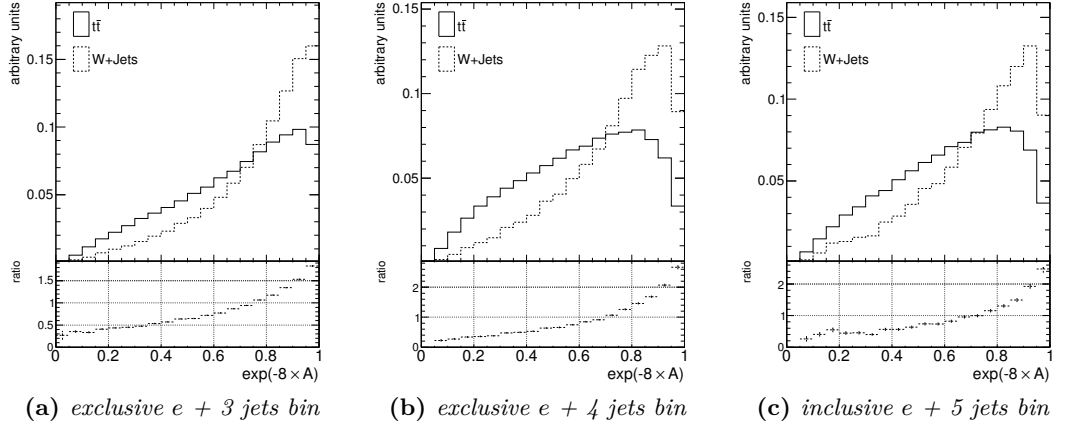


Figure 7.3.: Transformed form of aplanarity, $\exp(-8 \times A)$, distribution in the $e + 3$, 4 , and ≥ 5 jets bin for $t\bar{t}$ production and the dominant $W + \text{jets}$ background process without b -tagging requirement. The ratio of $W + \text{jets}$ to $t\bar{t}$ is shown in the bottom part of each plot.

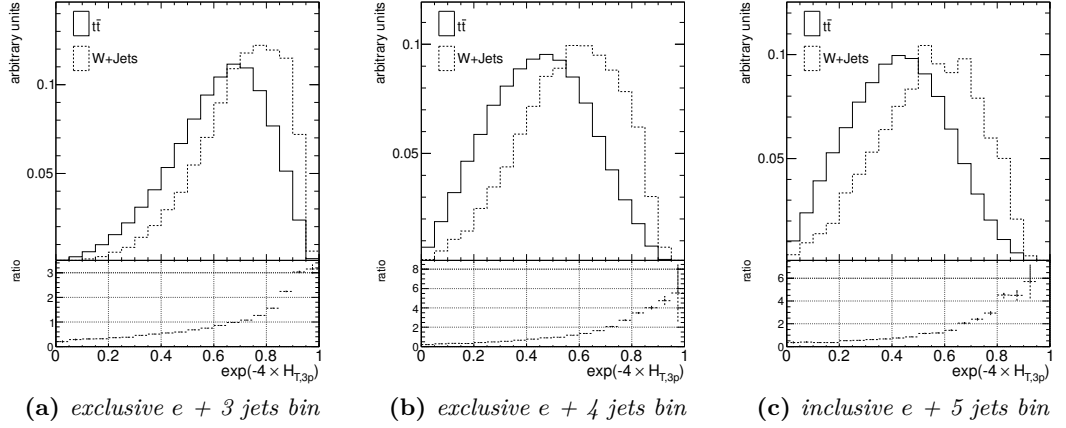


Figure 7.4.: $\exp(-4 \times H_{T,3p})$ distribution in the $e + 3$, 4 , and ≥ 5 jets bin for $t\bar{t}$ production and the dominant $W + \text{jets}$ background process without b -tagging requirement. The ratio of $W + \text{jets}$ to $t\bar{t}$ is shown in the bottom part of each plot.

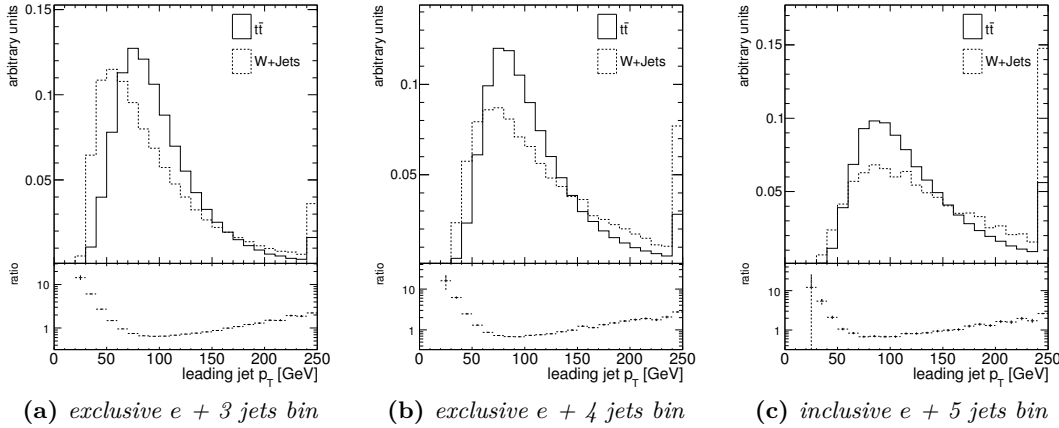


Figure 7.5.: Leading jet p_T distribution in the $e + 3$, 4 , and ≥ 5 jets bin for $t\bar{t}$ production and the dominant $W + \text{jets}$ background process without b -tagging requirement. The ratio between the two processes is shown in the bottom part of each plot in logarithmic scale. The last bin represents the overflow bin.

measurement.

The 2011 analysis (a) employs only kinematic event information to avoid the comparably large uncertainties from the b -tagging calibration and the heavy flavour content in the $W + \text{jets}$ sample. Instead, in addition to the three variables discussed above the transverse momentum of the leading jet is used in the likelihood discriminant. On average, harder jets are produced in $t\bar{t}$ production than in $W + \text{jets}$ production. For higher jet multiplicities, however, this effect washes out so that the leading jet p_T shows lower discrimination in the 5 jet bin. Nevertheless, this variable is chosen over other jet energy scale sensitive variables for its robustness and since it does not have correlations with other jets and their uncertainties. The distributions for the different jet bins are shown in Fig. 7.5.

The 2011 analysis (b) pursues a different measurement approach as described in Chapter 10. Since its intention is to measure efficiencies within the $t\bar{t}$ sample harder background rejection cuts are applied to obtain a cleaner sample. Therefore, at least one of the selected jets is required to be b -tagged using the MV1 tagger at the 70% efficiency working point (refer to Sec. 4.5.2). Since the individual discriminating variables lose discrimination power against the $W + \text{jets}$ background in a b -tagged sample, again a combination of variables in the form of a projective likelihood to separate the $t\bar{t}$ sample from the background is employed. For the purpose of this measurement the three discriminating variables described above, namely lepton η , $\exp(-8 \times \mathcal{A})$, and $\exp(-4 \times H_{T,3p})$, are exploited. The leading jet p_T is not used since sensitivity to the jet energy scale is already inherent in the measurement method (see Chapter 10).

7. Measurement and signal extraction method

7.1.1. Projective likelihood discriminant

The combination of the variables described above into one discriminant, \mathcal{D} , is performed using a projective likelihood approach. The discriminant based on n_{var} variables can be expressed as signal over signal-plus-background probability for an event i in the form of Ref. [252] such that

$$\mathcal{D}(i) = \frac{\mathcal{L}_S(i)}{\mathcal{L}_S(i) + \mathcal{L}_B(i)}, \quad (7.8)$$

where

$$\mathcal{L}_{S(B)}(i) = p_{S(B)}(x_1(i), x_2(i), \dots, x_{n_{\text{var}}}(i)), \quad (7.9)$$

which can—under the assumption that the probabilities for each variable $x_k(i)$ are not correlated with each other—be factorised into

$$\mathcal{L}_{S(B)}(i) = \prod_{k=1}^{n_{\text{var}}} p_{S(B),k}(x_k(i)), \quad (7.10)$$

where $p_{S(B),k}$ is the signal (background) probability distribution function (PDF) for the k th input variable x_k . The PDFs are normalised such that

$$\int_{-\infty}^{+\infty} p_{S(B),k}(x_k) dx_k = 1, \quad \forall k. \quad (7.11)$$

Correlated input variables lead to a degradation of the method since cancellation effects occur in Eq. 7.8 and the PDF cannot be factorised anymore in the form of Eq. 7.10.

The projective likelihood variable is implemented in the TMVA framework [252] in version 4.1.0 that is embedded in the data analysis framework ROOT [253], which is used in version 5.28 throughout this work. The discriminant, \mathcal{D} , and the probability density functions, $p_{S(B),k}$, are created in a so-called training process in which the $t\bar{t}$ events enter as signal and only the W + light jets events as background, because they pose the dominant background. The W + heavy flavour jets samples only do not enter the training for the 2011 analysis (a), since the analysis is insensitive to any heavy flavour contributions. To ensure statistical independence of the training and the evaluation sample, the simulation samples are split in two using the events of each sample alternately for one of the steps only. This is not strictly necessary for a projective likelihood and therefore not done for the 2011 analysis (b). As there is no parametric form known for the input distributions they enter the training process unbinned and are then empirically approximated by spline functions of various degrees fitted to histogrammed versions of the input. The binning of the histograms is hereby based on an average number of events per bin and varies for the different channels, jet bins, and analyses. Additionally, a smoothing procedure of the spline functions is set manually to achieve good agreement between input histogram and fitting function.

In the evaluation step the discriminant, \mathcal{D}_i , is calculated for each event, i , and templates are created for data, the multi-jet estimates, and for all simulation samples separately. The likelihood functions are shown in the respective analysis chapters. For the

Table 7.1.: *Discriminating variables used for the analyses as defined in the text. For the 2010 analysis and the 2011 analysis (a) the variables are combined into a projective likelihood discriminant, \mathcal{D} .*

Variable	2010 analysis	2011 analysis (a)	2011 analysis (b)
lepton η	✓	✓	✓
$\exp(-8 \times \mathcal{A})$	✓	✓	✓
$\exp(-4 \times H_{T,3p})$	✓	✓	✓
\bar{w}_{JP}	✓	-	-
leading jet p_T	-	✓	-

fit described below the discriminants are obtained separately for the $e + \text{jets}$ and the $\mu + \text{jets}$ channel for each jet bin and combined into one global discriminant. Using 20 bins for each channel the global discriminant contains 120 bins for each analysis. The variables used for the different analyses are summarised in Tab. 7.1.

7.2. Systematic uncertainties

Systematic uncertainties arise from the limited knowledge, precision and understanding of the parameters that enter the measurement. Therefore, they also affect the likelihood discriminant described above and the acceptance of events. In general, one can distinguish between experimental uncertainties that are present when reconstructing objects with the detector and theoretical uncertainties that arise when comparing different physics models based on simulation. In contrast to statistical uncertainties, systematic uncertainties do not decrease with the increase of the data set, but require dedicated studies for their understanding, even though a larger data set often allows for more detailed studies that lead to a reduction of the uncertainties. As an example, the effect on the likelihood discriminant from experimental detector and theoretical modelling uncertainties is shown in Fig. 7.6. The individual uncertainties are discussed in the following. For some uncertainties below it is stated that they are treated as so-called *nuisance parameters*, which means that they are treated as additional parameters in the fit. Details of this procedure are discussed in Sec. 7.3.1.

7.2.1. Experimental uncertainties

7.2.1.1. Jet energy scale

In the jet-populated environment of $t\bar{t}$ events the jet energy scale uncertainty is expected to be one of the dominant uncertainties. The jet energy calibration is subject to a large number of studies based among others on different detector components and simulation models to reach a good level of understanding of the correlations between the various uncertainty components. The contributions of the single components to the total jet energy scale uncertainty for the 2010 analysis are shown in Fig. 7.7. They are mostly

7. Measurement and signal extraction method

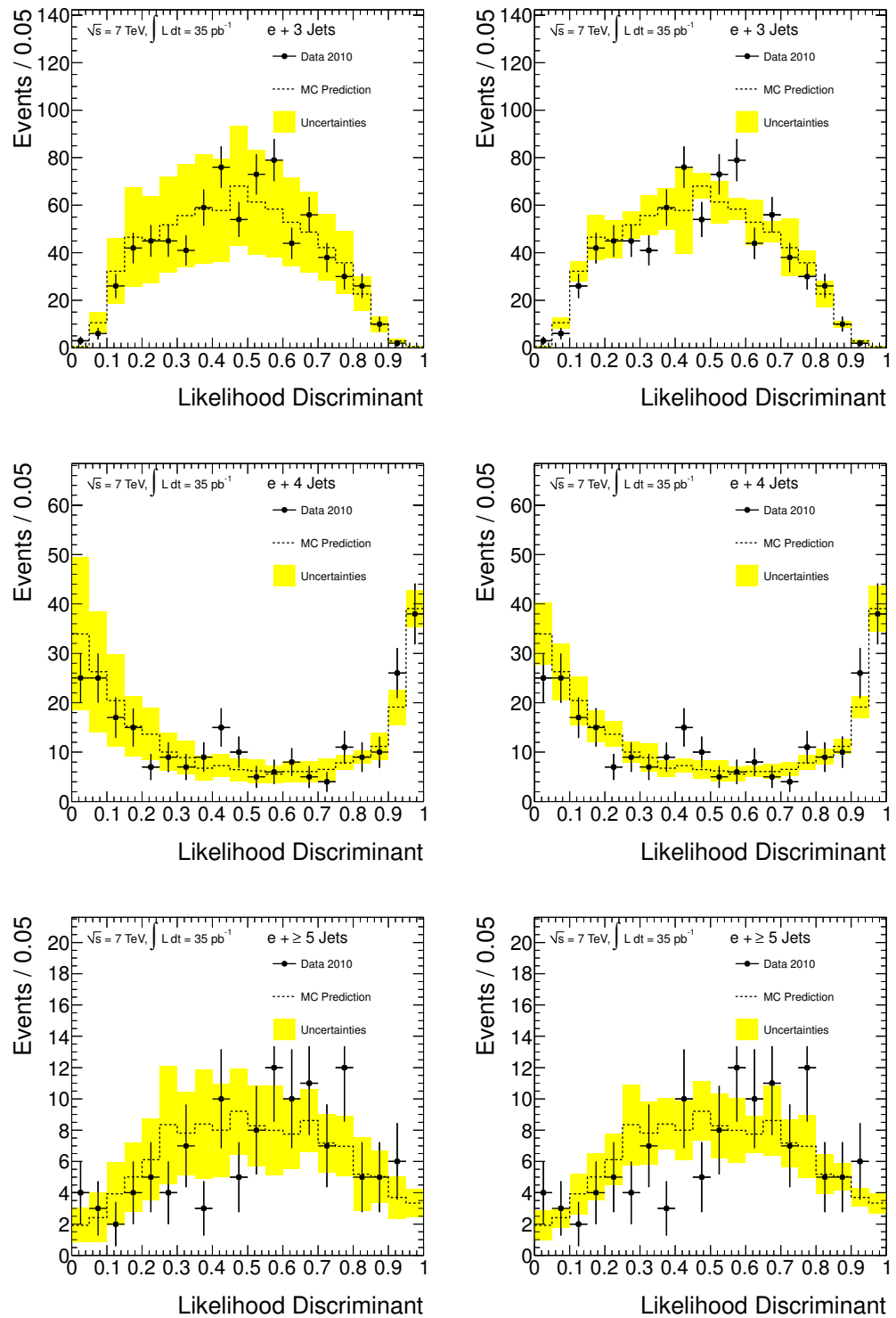


Figure 7.6.: Quadratic sum of all sources of systematic uncertainties for physics modelling uncertainties (left) and detector related uncertainties (right) for the sum of predicted events for the 2010 analysis, including the data-driven QCD multi-jet estimate, compared to data in the $e + \text{jets}$ channel. [248]

dominated by the single particle calorimeter response and for more forward jets with lower transverse momentum also the η -intercalibration, details are given in the following and in Ref. [192].

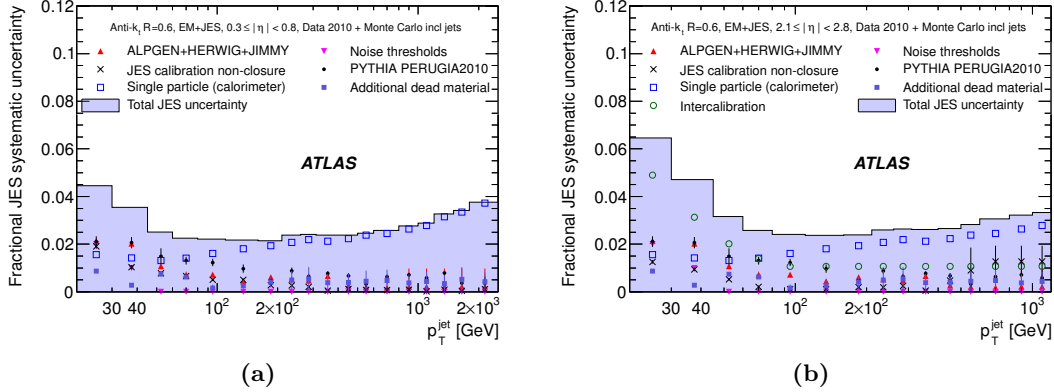


Figure 7.7.: Fractional jet energy scale systematic uncertainty as a function of p_T for jets in the pseudorapidity region (a) $0.3 \leq |\eta| < 0.8$ in the calorimeter barrel, and (b) $2.1 \leq |\eta| < 2.8$ in the calorimeter endcap. The total uncertainty is shown as the solid light shaded area. The individual sources are also shown together with uncertainties if applicable. [192]

The 2011 analysis (a) is particularly sensitive to the jet energy scale. This analysis but also the 2010 analysis reach a significant reduction of the connected uncertainty using the profile likelihood technique. In order not to ignore correlations between the uncertainty components they are evaluated separately in both analyses instead of creating a global envelope. For the 2011 analysis (b) a total of 64 systematic variations is provided. After evaluating their effect on top quark analyses, the set of parameters was reduced and merged to 16. However, since the 2011 analysis (b) does not aim for highest precision but for a clean and well understood sample and no profiling is used (see Sec. 7.3.2), an envelope of all uncertainties is used. This is addressed in more detail in the analysis chapter (Chapter 10).

Calorimeter response The calorimeter response to single particles is evaluated using several measurements based on Monte Carlo truth studies and test beam data: The single hadron energy measured in a cone around an isolated track is compared to the track momentum for tracks up to $p_T = 20$ GeV. Furthermore, pion response measurements performed in the 2004 combined test-beam are taken into account for transverse momenta from 20 to 350 GeV [254]. Additional uncertainties are related to low- p_T particles that do not reach the calorimeter or are not reconstructed in a topological cluster due to the noise thresholds, the response to particles with $p_T > 400$ GeV, the electromagnetic scale of particles not measured in-situ, and also the response to neutral hadrons based

7. Measurement and signal extraction method

on simulation. The total envelope obtained by adding uncertainties and observed biases linearly is determined to be about 1.5 - 4%, depending on the jet transverse momentum.

η -intercalibration Since different calorimeter technologies are used in ATLAS and because of varying amounts of dead material in front of the calorimeters, the calorimeter response to jets is not uniform. It is therefore studied by comparing the transverse momenta of a well-calibrated central jet and a jet in the forward region in dijets events, i.e. events with only two jets at high transverse momenta, to obtain calibration constants. Two different approaches are pursued: one, where the p_T -balance is always evaluated with respect to jets in the central region and another so-called *matrix method* that exploits the full event statistics by using *left* and *right* jets, where $\eta^{\text{left}} < \eta^{\text{right}}$. Based on a matrix of equations the calibration factors are extracted. Since both methods yield comparable results, but the latter exploits more statistics, it is used for the evaluation of uncertainties. Comparison of 2010 data with simulation at $p_T > 60$ GeV shows good agreement within 2%, but at lower transverse momentum larger discrepancies are observed in the more forward regions as reflected in Fig. 7.7b. Using 2011 data and corresponding simulation samples uncertainties for jets with $p_T > 40$ GeV less than 1% for $|\eta| < 1.0$ and less than 2.5% for $|\eta| < 2.8$ are found [255].

Pileup The offset to the jet transverse energy due to multiple proton-proton collisions is evaluated from the average energy in calorimeter towers in minimum bias events at the electromagnetic scale. The uncertainties of those corrections are studied in several analyses where selection conditions such as the trigger choice are varied. Up to $|\eta| < 1.9$ track jets are used for comparison and beyond the dijet balance method. The uncertainty grows with increasing number of primary vertices in the event from 1–2% in case of two measured vertices up to 3–6% for four vertices for jets with $p_T = 20$ GeV in 2010 data. For jets with $p_T > 200$ GeV the uncertainty is less than 1%. Similar results with up to 7% uncertainty at low p_T are found for the 2011 analyses, that suffer from a significantly higher amount of pileup. For jets with $p_T > 40$ GeV the systematic bias in the jet p_T measurement is at most 3% at the highest pileup activities experienced in 2011 [193].

Noise term The topological clusters that are used to reconstruct the jets are formed from cells above a certain signal-to-noise ratio as described in Sec. 4.4.2. Differences between the calorimeter noise in simulation and data can lead to biases in the reconstruction. To evaluate this effect the noise thresholds are varied and the difference in jet response and offset are taken as systematic uncertainty. It is found that this variation only affects jets with $p_T < 45$ GeV leading to 1% uncertainty.

Parton shower model The default samples for the jet energy scale studies summarised here are created using the PYTHIA program [217] for event generation and showering, the latter with ATLAS-specific underlying event tunes [229]. To evaluate the influence of the parton shower on the jet calibration, the jet response is compared to events generated with the Alpgen matrix element generator [215] interfaced with HERWIG [218] (see also

Sec. 5.2.2). For evaluation of the uncertainty for the full 2011 data set exploited by 2011 analysis (b) the HERWIG++ program [256] is used for showering. The difference is quoted as uncertainty. At the time of writing this result is not yet published.

Underlying event model The coloured beam remnants that need to be taken into account in the hadronisation step in the form of an underlying event model as discussed in Sec. 5.2.2 also affect the jet energy scale. To assess the effect, events simulated with the ATLAS tune are compared to events obtained using the PERUGIA tunes [233] that are based on measurements performed by the Tevatron and LEP experiments.

Close-by jets In top quark pair events, in which a large number of jets is present, additional uncertainties on the jet energy scale arise when two jets are close to each other. In this case the calorimeter response might be degraded due to overlapping energy depositions. This effect is studied by comparing calorimeter and track jets in data and simulation [192, 200]. Depending on the jet transverse momentum and the distance between the jets the response is found to vary between 1.7% and 2.8%. The 2010 analysis treats this uncertainty as a separate nuisance parameter (see Sec. 7.3.1) whereas this term is quadratically added to all other jet energy scale uncertainties in the 2011 analysis (a) since the uncertainty has been obtained in 2010 data and this way differences are accounted for. For the 2011 analysis (b) an updated estimate is used that is not yet published.

Flavour composition Jets that are initiated from gluons tend to contain more particles. Therefore, these jets have on average lower transverse momenta than jets stemming from light quarks, which in return penetrate further into the calorimeter. Additionally, gluon jets tend to be wider before interacting with the detector, which is amplified by the magnetic field immersing the Inner Detector because their low- p_T charged particles are stronger bent than the higher- p_T particles in light quark jets. If the quark-gluon flavour composition in data differs from the simulation samples an additional uncertainty arises. Using a large sample of jets the average flavour composition can be obtained using templates from designated simulation samples. These templates are then used in γ -jet events and in multi-jet samples where additional jets mostly stem from gluon radiation to evaluate the difference in jet response. It is found that light quark jets have a 5–6% higher response than gluon jets at low p_T . This difference decreases to about 2% at high p_T [192, 257]. Depending on how well the flavour composition of a given process is known, the uncertainties on the jet energy scale due to flavour composition can be reduced from about 6% to 1%. In this work the flavour composition for the $t\bar{t}$ samples is taken from simulation. For the 2011 analysis (a) the same composition is used for all other simulation samples and the obtained uncertainty added to all other jet energy scale uncertainties as above for the close-by jet uncertainty. The 2010 analysis and the 2011 analysis (b) assume no a priori knowledge about the quark-gluon flavour composition for all background simulation samples which is therefore conservatively taken as 50:50 while the one for $t\bar{t}$ is again taken from simulation. Using the full 2011 data set it was

7. Measurement and signal extraction method

observed that the gluon jet response is slightly underestimated by PYTHIA. Therefore, an additional flavour response uncertainty is taken into account for the 2011 analysis (b) by evaluating the difference in gluon response between the PYTHIA and HERWIG++ samples.

b-jet energy scale The b -jet energy scale differs from the global jet energy scale uncertainty in particular due to the presence of semi-leptonic decays that contain neutrinos and the different fragmentation models of the parton shower programs. The calorimeter jet response uncertainties for b -jets is evaluated in single hadron response measurements using samples of inclusive dijet and $b\bar{b}$ dijet events. The additional uncertainty found is less than an additional 0.5% with respect to inclusive dijet samples. The uncertainty arising from the modelling of the b -quark production mechanism and fragmentation is determined from variations of the Monte Carlo simulation such as comparing different MC generators and underlying event tunes, varying the detector material in front and in between the calorimeters, and using different fragmentation functions. The resulting additional uncertainty for b -jets is shown in Fig. 7.8. It is about 2% up to $p_T \approx 100$ GeV and below 1% beyond. This uncertainty is added in quadrature to the nominal jet energy scale uncertainty. No update for 2011 simulation is available and hence the 2010 values are used.

7.2.1.2. Jet reconstruction efficiency

The jet reconstruction efficiency is based on studies in 2010 data [192, 201]. Using a *tag-and-probe* method in dijet events jets are reconstructed from tracks where the higher-momentum track jet has to match a calorimeter jet. The *probe* track jet has to be located in the opposite hemisphere ($\Delta\phi \geq 2.8$). The reconstruction efficiency is then determined as the fraction of probe track jets that match a calorimeter jet. Based on comparison of efficiencies in data and simulation the uncertainty is propagated to the measurement by randomly dropping jets in simulation based on their transverse momentum and pseudorapidity. Differences between data and simulation are basically only found for jets with $p_T < 30$ GeV and therefore the uncertainty is negligible above.

7.2.1.3. Jet energy resolution

The jet energy resolution described in Sec. 4.4.4 is found to be worse in 2010 data than in simulation. To account for this, the transverse momentum of jets in 2010 simulation is smeared to match data. To obtain the uncertainty for this correction no smearing is applied. For the 2011 analyses no additional smearing is applied, but the smearing procedure is used to derive the uncertainty of the jet energy resolution.

7.2.1.4. b-tagging calibration

The b -tagging and mistagging calibration described in Secs. 4.5.1 and 4.5.2 for the 2010 analysis and the 2011 analysis (b), respectively, are varied independently within their uncertainties. Since four different calibration points are used for the 2010 analysis, in

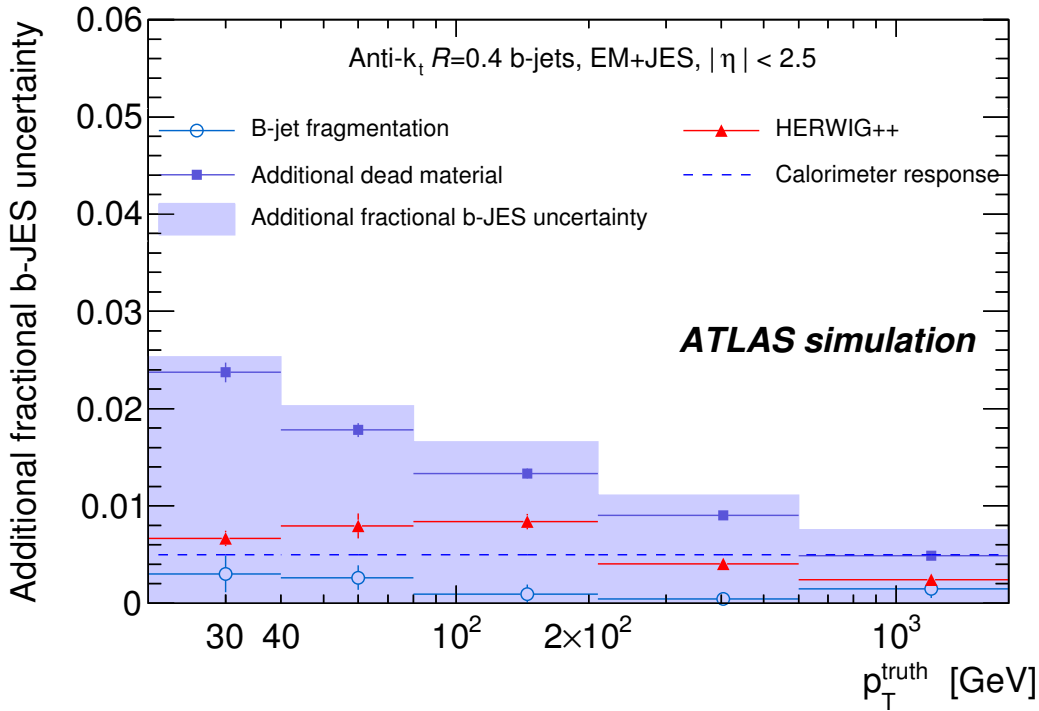


Figure 7.8.: Additional fractional b -jet JES uncertainty as a function of the truth jet transverse momentum for anti- k_T jets with $R = 0.4$ for $|\eta| < 2.5$. Shown are systematic Monte Carlo variations using different modelling of the b -quark fragmentation and physics effects as well as variations in the detector geometry and the uncertainty in the calorimeter response to b -jets as evaluated from single hadron response measurements. Uncertainties on the individual points are statistical only. [192]

total eight different $\pm 1\sigma$ uncertainties are considered. They enter the minimisation process as independent nuisance parameters (see Sec. 7.3.1), namely four b -tagging and four mistagging parameters. Even though the correlation coefficients between the nuisance parameters are of $\mathcal{O}(50\text{--}70)\%$ since they are obtained using the same methods, no correlation is assumed. This is a conservative approach, since less shape cancellations are possible. For the 2011 analysis (b) a cut on the b -tagging calibration is applied and only one calibration point is used. Therefore, the b -tagging, mistagging, and additionally the c -tagging calibration are varied independently at this point and added in quadrature.

7.2.1.5. Jet vertex fraction scale factors

To evaluate the systematic uncertainty on the jet vertex fraction scale factors (described in Sec. 4.4.5) the requirements to consider a reconstructed jet to stem from the hard scattering process are varied in simulation and the effect on the signal efficiency and

7. Measurement and signal extraction method

inefficiency scale factors is determined. The uncertainties for the background pileup (in-)efficiencies are assumed to be twice as large as found for the signal ones. Since the scale factors are parametrised by an exponential function also the fit uncertainty is taken into account and added in quadrature.

7.2.1.6. Missing transverse energy

The uncertainties from the energy scale and resolution corrections on leptons and jets are propagated into the calculation of the missing transverse energy, since these objects enter the E_T^{miss} calculation directly as described in Sec. 4.6.1. Additional uncertainties are added from contributions of calorimeter cells not associated to any jets (**CellOut**), and soft jets ($7 \text{ GeV} < p_T < 20 \text{ GeV}$) by varying both simultaneously within their uncertainties. For the 2011 analysis (a) an additional flat 10% uncertainty, fully correlated to the above two terms, is added to account for uncertainties from the pileup model. Due to the failure of a controller board responsible for six front-end boards of the EM calorimeter (see Sec. 4.2.1) an additional uncertainty is applied to cover the effect that this defect is not fully implemented in simulation for the 2011 analysis (a). The 2010 analysis uses fully correlated uncertainties on the **CellOut** and **SoftJet** terms whereas the 2011 analysis (a) combines **CellOut**, **SoftJet** and pileup terms into one nuisance parameter in the minimisation (see Sec. 7.3.1). The 2011 analysis (b) treats the **CellOut** and **SoftJet** terms as uncorrelated.

7.2.1.7. Lepton scale factors

The lepton reconstruction, trigger and identification scale factors discussed in Chapter 4 are used to correct efficiencies in simulation to the ones measured in data. Their uncertainties are derived by varying the lepton and signal selections and from the uncertainty in the evaluation of the backgrounds.

7.2.1.8. Lepton momentum/energy scale and resolution

Based on $Z \rightarrow ll$ events the muon momentum scale, the electron energy scale, and the momentum/energy resolution for both were determined in data and simulation. The correction factors and associated uncertainties were derived to match the simulation to observed distributions in collision data. For muons, the 2010 analysis uses an envelope of the Muon Spectrometer and Inner Detector track resolution smearing uncertainties. For the 2011 analyses these are treated separately.

7.2.2. Model uncertainties

Most model uncertainties are only considered for the signal process since they are covered for the background processes by their other associated uncertainties unless stated otherwise below. The signal generator, i.e. the matrix element, and the parton shower uncertainties are treated separately since they treat a different kind of physics as described in Sec. 5.2.

7.2.2.1. NLO signal generator

For the 2010 analysis and the 2011 analysis (a) the nominal signal samples generated with the NLO generator `MC@NLO` interfaced with `HERWIG/Jimmy` are compared to the NLO generator `POWHEG`, which also uses `HERWIG/Jimmy` for hadronisation, showering and underlying event simulation (see Sec. 5.4.1 for details). For the 2011 analysis (b) the nominal $t\bar{t}$ sample is generated using `POWHEG` interfaced with `PYTHIA`. Since no other next-to-leading order generator sample interfaced with `PYTHIA` is available `POWHEG + HERWIG/Jimmy` is compared to `MC@NLO` also in conjunction with `HERWIG/Jimmy` to evaluate the uncertainty. Both samples are normalised to the `POWHEG+PYTHIA` fiducial cross section (see Chapter 10 for definition).

7.2.2.2. Parton shower

Since `MC@NLO` can currently only be interfaced with `HERWIG`, the parton shower uncertainty is evaluated comparing `POWHEG` in conjunction with `HERWIG/Jimmy` as above to `POWHEG + PYTHIA`. For the 2011 analysis (b) `POWHEG + HERWIG/Jimmy` is compared to `POWHEG + PYTHIA`. As for the NLO generator uncertainty, the `POWHEG + HERWIG/Jimmy` is normalised to the `POWHEG + PYTHIA` fiducial cross section.

7.2.2.3. Initial and final state radiation

As described in Sec. 5.4.1 six different samples for the variation of initial (ISR) and final state radiation (FSR) are generated using `AcerMC` with different `PYTHIA` settings. Since `AcerMC` generates different events than `MC@NLO`, all variation samples are normalised to the ratio of `AcerMC` generated with nominal ISR/FSR settings to the nominal `MC@NLO` sample in each bin of the distribution. For the 2011 analysis (b) `AlpGEN + PYTHIA` samples are used for which the α_s value at the matching scale has been varied by factors of 2. The variation samples have been generated with updated parameters based on uncertainties evaluated using data are used (see also Sec. 5.4.1). Similarly as above, all variation samples are normalised to the ratio of the nominal `AlpGEN + PYTHIA` prediction to the nominal `POWHEG + PYTHIA` sample in each bin of the distribution.

7.2.2.4. Parton distribution functions

For the 2010 analysis and the 2011 analysis (a) the `CTEQ6.6` PDF set is employed for the $t\bar{t}$ signal generation and therefore the corresponding error set is used to reweight the signal sample for each 44 of the errors separately and template distributions are created. With those an envelope for the up- and down-variation of the PDFs is created. The positive and negative fluctuations are added in quadrature for each bin of the discriminant \mathcal{D} separately to create $\pm 1\sigma$ templates. Both rate and shape variations are taken into account. The latter are found to be small, but governed by changes in the lepton pseudorapidity. The 2011 analysis (b) using the `CT10` PDF set follows the full `PDF4LHC` recommendations [258] by evaluating the envelope of the variations of the `CT10`, `MSTW2008NLO`, and `NNPDF2.3` [259] PDF sets, the latter with $\alpha_s(m_Z) =$

7. Measurement and signal extraction method

0.120 to match with MSTW2008NLO, at 68% confidence level. The original *PDF4LHC* recommendations still recommend NNPDF2.0 [260] since the updated version had not been tested in detail at the time of publication. Discussion with the authors, however, resulted in a switch to the latest available version 2.3, which takes into account LHC data and therefore yields slightly smaller uncertainties.

7.2.2.5. $W + \text{jets}$ generator parameters

The dominant $W + \text{jets}$ background is simulated using *AlpGEN* as described in Sec. 5.4.2. Since at the time of analysis all other available $W + \text{jets}$ samples suffered either from low statistics or insufficient tuning the shape uncertainty of this process is evaluated by varying generator settings at generator truth level. Parameters varied are related to the factorisation and renormalisation scale as well as matching thresholds of the MLM algorithm (see Sec. 5.4.1) and the underlying event model (refer also to a more detailed description of these in Appendix C). The largest deviation from the nominal settings is found when varying the functional form of the factorisation scale and the minimum parton p_T required for the matching with jets. Weights for these are extracted based on the leading jet transverse momentum distribution for each jet bin separately.

7.2.2.6. $W + \text{heavy flavour}$ contribution

The $W + \text{heavy flavour}$ jets contribution is estimated in events with one and two jets as described in Sec. 6.3.1. The $Wb\bar{b}$ and $Wc\bar{c}$ contributions are hereby treated together due to their similar production mechanism but separately from the Wc contribution. Their scale factors and associated uncertainties are given in Sec. 6.3.1. The uncertainties are derived from two different methods to measure the scale factors and account for differences between the results. However, since the measurement is performed in events with one and two jets, an additional uncertainty has to be quoted when extrapolating to higher jet multiplicities used in this work. Detailed Monte Carlo studies, which are described in Appendix C, show that a 25% extrapolation uncertainty from the 2 jet bin to the 3, 4 and ≥ 5 jet bin is sufficient to cover the uncertainties in the Monte Carlo model. This can be seen from Fig. 7.9 where the ratio of the $W + \text{heavy flavour}$ jets samples to the $W + \text{light flavour}$ jets sample is shown. The ratio remains constant over all jet bins within an envelope of about 25%. For the 2011 analysis (b) the $W + \text{heavy flavour}$ jets contribution is evaluated as a shape uncertainty only because the overall $W + \text{jets}$ normalisation is taken from data.

7.2.2.7. QCD multi-jet model

For the 2010 analysis and the 2011 analysis (a) an alternative QCD model is derived using the *anti-electron method* in the electron + jets channel as described in Sec. 6.2.1.1 and Appendix B. The nature of the heavy flavour contribution of the multi-jet background in the $e + \text{jets}$ and the $\mu + \text{jets}$ channel is, however, different (see mechanism described in Sec. 6.2). This is also due to the fact that electrons and muons are reconstructed in different subdetectors. Due to the sensitivity of the 2010 analysis to this contribution the

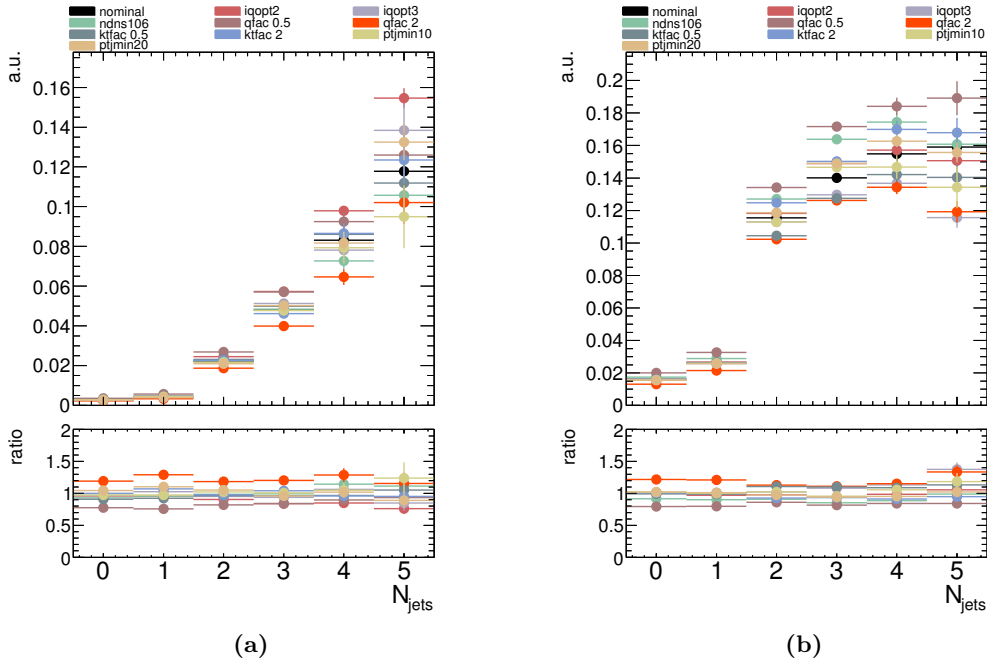


Figure 7.9.: *Effect of the systematic variations of the generator parameters on the ratio of the jet multiplicity distribution. Shown in arbitrary units in the top plot is the ratio of the (a) $Wb\bar{b}$, and (b) $Wc + \text{jets}$ sample to the $W + \text{light flavour jets}$ sample. The 5 jet bin is inclusive. The bottom plot shows the ratio of each variation with respect to the nominal settings. Uncertainties are statistical only. The acronyms used in the legend to describe the systematic variations are explained in Appendix C.*

use of the *anti-electron model* leads to very unstable results in the muon + jets channel. Thus, instead an additional *matrix method* selection is employed with an alternative selection of events containing *loose* but not *tight* muons in the region $m_T^W < 10$ GeV. For the 2011 analysis (b) the jet-electron model is used as alternative model in both channels.

7.2.2.8. Background normalisation and luminosity

The dominant $W + \text{jets}$ and QCD multi-jet background normalisations are taken from data as detailed in Secs. 6.2 and 6.3 with the exception that for the 2010 analysis the a priori normalisation for the $W + \text{jets}$ background is taken from simulation. As described in Sec. 7.3.1 for the 2010 analysis and the 2011 analysis (a) the uncertainties on the normalisation are included in the fit as Gaussian constraints.

For these two analyses the $W + \text{jets}$ background the uncertainties associated with the *Berends-Giele scaling* are employed: The theoretical uncertainty for inclusive $W + \text{jets}$ production is 4%. Studies show that the ratio of $W + n$ jets to $W + (n + 1)$ jets is

7. Measurement and signal extraction method

constant as a function of n with an uncertainty of 24%. Propagating this to the signal jet multiplicity bins results in uncertainties of 42% for events with three jets, 48% for events with four jets and 54% for the prediction of events with five or more jets. Both the $W + \text{jets}$ as well as the QCD multi-jet contributions are treated uncorrelated in each jet bin and channel. This is in particular important for the 2010 analysis, where the a priori normalisation for the $W + \text{jets}$ events is taken from simulation. Relying on the `AlpGEN` prediction only for $W + n$ jets to $W + (n + 1)$ jets would otherwise introduce a large uncertainty since variations of Q^2 have a large effect on the ratio for high jet multiplicities.

For the 2011 analysis (b) the uncertainties from the W charge asymmetry measurement are used and considered uncorrelated in each channel and jet bin. They range from 12–29% increasing with jet multiplicity (see Sec. 6.3).

The other, smaller, electroweak backgrounds are treated as fully correlated among the two channels and all jet multiplicities. The 10% uncertainty on single top quark production and 5% uncertainty on diboson production are taken from theory predictions. Since the $Z + \text{jets}$ background is rather small, no detailed normalisation studies as for the $W + \text{jets}$ processes are conducted, but a plain 30% uncertainty is assumed based on previous studies.

In addition to the single process normalisation a global luminosity uncertainty for the analysed data sets is taken into account since all simulation samples are scaled to the same integrated luminosity. Thus the uncertainties given in Sec. 3.3 for the different analyses are added in quadrature to the normalisation uncertainty.

Studies of the stability of the QCD prediction (see also Appendix B) yield an uncertainty of 50% for both the electron and muon channel. The prediction for each jet bin is treated independently. For the 2011 analysis (b) the QCD background is treated as one parameter in each channel.

7.2.2.9. Pileup model

As described in Sec. 5.2.2 the Monte Carlo simulation samples are overlaid with pileup events. In contrast to the 2011 analyses, the 2010 simulation samples are not reweighted to match the bunch structure in data, but instead this is considered as a systematic uncertainty. To evaluate this uncertainty, scale factors are extracted based on the number of primary vertices in a given event by comparing the $t\bar{t}$ signal sample with data. Keeping the normalisation of each sample constant those scale factors are applied to the simulation sample before the event selection. For the 2010 analysis it is found that the Monte Carlo simulation contains more pileup than is present in data. For the 2011 analyses no uncertainty is quoted.

7.2.2.10. Monte Carlo statistics

Due to the limited number of Monte Carlo simulation events, in particular $W + \text{jets}$ events in the 2010 analysis and the 2011 analysis (a), the cross section measurement can be affected. To evaluate this effect on the fit the statistics in each bin of the nominal

templates is sampled assuming Gaussian statistics using pseudo experiments and the influence on the expected uncertainty is extracted. For the 2010 analysis the uncertainty arising from limited MC statistics is included as a nuisance parameter in the fit. The uncertainty found for the 2011 analysis (a), however, is comparably large and use of it as a nuisance parameter gives too much freedom to the fit. This effect partially spoils the sensitivity to other nuisance parameters. Therefore, the uncertainty is evaluated in separate pseudo experiments (see Sec. 7.4 below). For the 2011 analysis (b) the effect of Monte Carlo statistics is found to be negligible, also because no profile likelihood method is used.

7.3. Likelihood fit method

7.3.1. Likelihood function

Based on the discriminant templates described above, the aim of the method is to obtain the best value of the top quark pair cross section, $\sigma_{t\bar{t}}$, from a fit of the simulation and multi-jet templates to data. Hereby, knowledge of the contributing processes and also, with the exception of the 2011 analysis (b), the uncertainties are exploited. The fit is performed using an extended maximum likelihood function using the minimiser package `Minuit2` [261]. The likelihood is defined as the product of independent Poisson probabilities for each of the bins:

$$\mathcal{L}_0(\vec{\mu}) = \prod_k \frac{\mu_k^{n_k} \exp[-\mu_k]}{n_k!}, \quad (7.12)$$

where n_k is the observed number of events in bin k and μ_k is the expected number of events in bin k from the sum of all signal and background templates, $\mu(\vec{\beta}) = \sum_j \beta_j \nu_{jk}$. In this sum, ν_{jk} is the expected numbers of events in bin k from template j . The notations $\vec{\beta}$ and $\vec{\delta}$ are used to indicate the dependence on all parameters β_j or δ_i . The expected number of events is obtained from MC templates normalised to the luminosity of the data sample according to their theory cross section described in Sec. 5.4 for all samples but QCD multi-jet and for the 2011 analyses also the $W + \text{jets}$ samples, where the normalisation is obtained from data-driven methods described in Chapter 6. The parameters β_j are the free parameters in the maximum likelihood fit. They describe the deviation from the nominal template normalisation and are nominally set to $\beta_j = 1.0$. Since the uncertainties on the contribution of the individual processes are known, the fit allows Gaussian constraints Δ_j on all parameters β_j but the parameters of interest. This is realised by multiplying \mathcal{L}_0 with

$$\prod_j \frac{1}{\sqrt{2\pi}\Delta_j} \exp\left[-\frac{(\beta_j - 1)^2}{2\Delta_j^2}\right]. \quad (7.13)$$

For positively defined observables such as cross sections, e.g. the β -parameters fitted here, one has to be careful when using Gaussian constraints. To avoid negative results,

7. Measurement and signal extraction method

one can truncate the Gaussian at or just above zero, which might, however, lead to problems in the fit. An alternative option to this approach is to use the log-normal probability density function. Adapting from Ref. [262] for the use in the likelihood function the term can be defined as:

$$\prod_j \frac{1}{\sqrt{2\pi}\Delta_j\beta_j} \exp\left[-\frac{(\ln\beta_j)^2}{2\Delta_j^2}\right]. \quad (7.14)$$

This transforms into the Gaussian term given in Eq. 7.13 for $\beta_j^{\text{Gauss}} = \ln\beta_j^{\text{log-normal}}$. The log-normal constraint adds a large penalty term to the likelihood when the β -parameter tends towards zero but shows the same behaviour as the Gaussian constraint otherwise. For the 2010 and the 2011 analysis (a) no problems are found when using the Gaussian constraints. The log-normal constraint was, however, tested for the 2011 analysis (b) to replace the Gaussian one, but is eventually not used, because nevertheless too large compensation effects between the $W + \text{jets}$ background and the $t\bar{t}$ signal were found. Instead all backgrounds are fixed.

For the 2010 analysis and the 2011 analysis (a) selected systematic uncertainties that influence the shape and normalisation of the templates are also included in the fit as so-called *nuisance parameters*, δ_i . For each bin the number of expected events becomes a function of the nuisance parameters, i.e. $\mu_k(\vec{\delta})$. The uncertainties are hereby represented by their $\pm 1\sigma$ variation. Hence, for each process and uncertainty there exist three templates, the nominal one and one each for the variations. Initially, the nuisance parameters have the value $\delta_i = 0.0 \pm 1.0$, representing the nominal situation with 1σ uncertainties. To allow the use of a nuisance parameter in the fit it has to be continuous, i.e. the height of histogram bins is varied between, and possibly beyond, input histograms according to the parameter value. To achieve this, a quadratic interpolation is performed between the templates for $\delta_i \in [-1, 1]$ using Lagrange polynomials and a linear extrapolation of the templates for $|\delta_i| > 1$. This way the continuation can be made differentiable [263]. This procedure is also referred to as vertical morphing since the shape continuously morphs as the δ_i parameter changes. The implementation in the likelihood function is given as the product of the expected number of events, ν_{jk} , with the product of shift parameters, $\prod_i \epsilon_{jik}(\delta_i)$, using the following explicit formulae for interpolation and extrapolation of the terms:

$$\epsilon_{jik}(\delta_i) = \begin{cases} \lambda_{jik}^+ + (\delta_i - 1) \left\{ \left(\frac{3}{2}\lambda_{jik}^+ - 1 \right) + \left(\frac{1}{2}\lambda_{jik}^- - 1 \right) \right\} & \text{for } \delta_i > 1, \\ \frac{1}{2}\delta_i \left\{ (\delta_i - 1)\lambda_{jik}^- + (\delta_i + 1)\lambda_{jik}^+ \right\} - (\delta_i - 1)(\delta_i + 1) & \text{for } |\delta_i| \leq 1, \\ \lambda_{jik}^- + (\delta_i + 1) \left\{ \left(-\frac{1}{2}\lambda_{jik}^+ + 1 \right) + \left(-\frac{3}{2}\lambda_{jik}^- + 1 \right) \right\} & \text{for } \delta_i < -1, \end{cases}$$

where λ_{jik}^\pm are the ratios of the templates for nuisance parameters i for $\delta_i = \pm 1$ and the nominal templates.

When performing the fit, the resulting errors on the nuisance parameters give an idea whether the fit is able to constrain the uncertainties based on the information in data. If an error remains at 1, the expected systematic uncertainty is either reflected in data

or no sensitivity exists. If it is less than 1, the fit is able to constrain the uncertainty. In rare cases the error can get larger than 1, which means that it contributes stronger to the total uncertainty than initially expected.

Since a continuous interpolation is used for the templates, only systematic uncertainties that are expected to be continuous in $\delta_i \in [-1, 1]$ are treated as nuisance parameters. All other uncertainties are evaluated using pseudo experiments as described below in Sec. 7.4. In summary, the full likelihood function for the 2010 analysis and the 2011 analysis (a) is given by

$$\mathcal{L}_0(\vec{\beta}, \vec{\delta}) = \prod_k \frac{\mu_k^{n_k} \exp[-\mu_k]}{n_k!} \times \prod_j \frac{1}{\sqrt{2\pi}\Delta_j} \exp\left[-\frac{(\beta_j - 1)^2}{2\Delta_j^2}\right] \times \prod_i \frac{1}{\sqrt{2\pi}} \exp\left[-\frac{\delta_i^2}{2}\right], \quad (7.15)$$

where

$$\mu_k = \mu_k(\vec{\beta}, \vec{\delta}) = \sum_j \beta_j \nu_{jk} \left[\prod_i \epsilon_{jik}(\delta_i) \right]. \quad (7.16)$$

The 2011 analysis (b) uses

$$\mathcal{L}_0 = \prod_k \frac{\mu_k^{n_k} \exp[-\mu_k]}{n_k!} \times \prod_j \frac{1}{\sqrt{2\pi}\Delta_j \beta_j} \exp\left[-\frac{(\ln \beta_j)^2}{2\Delta_j^2}\right], \quad (7.17)$$

with the same definitions as above without $\vec{\delta}$ dependence. As described in Sec. 7.2.2.8 the Gaussian constraint is not used for the non- $t\bar{t}$ processes mentioned before, but employed for a different background discussed in Chapter 10.

7.3.2. Minimisation and profiling

The maximum likelihood fitter minimises $-\ln(\mathcal{L})$, where constant terms in Eq. 7.15 are dropped before minimisation. The Hessian symmetric uncertainties on all parameters are obtained from the second derivatives of $-\ln(\mathcal{L})$ at the minimum including the full covariance matrix. Asymmetric uncertainties are extracted based on the MINOS technique implemented in `Minuit`.

The fitter is also capable of profiling the multi-parameter likelihood function to extract a one-dimensional likelihood, $\lambda(\beta_0)$, that only depends on one parameter of interest, here assumed to be $\beta_0 = \sigma_{t\bar{t},\text{measured}}/\sigma_{t\bar{t},\text{predicted}}$ [264]. First the profile likelihood is obtained by minimising the likelihood with respect to all parameters (index *allmin*). In the second step the ratio of the likelihood value at the minimum and the value obtained from a minimisation with respect to all parameters but β_0 , which is kept fixed in the fit indicated with *min* is formed. Taking the logarithms ($\log \mathcal{L}$) therefore yields the difference:

$$-\ln(\lambda(\beta_0)) = -\ln\left(\mathcal{L}(\beta_0, \beta_1^{\min}, \dots, \delta^{\min}, \delta^{\text{bin},\min})\right) + \ln\left(\mathcal{L}(\vec{\beta}^{\text{allmin}}, \vec{\delta}^{\text{allmin}}, \vec{\delta}^{\text{bin},\text{allmin}})\right) \quad (7.18)$$

7. Measurement and signal extraction method

As can be shown, the logarithm of the profile likelihood has all desired properties of a log-likelihood function. Thus the uncertainties on β_0 can be extracted from the minimum $-\ln((\lambda(\beta_0^{\min}))) \pm 0.5$, which helps to understand the dependency of β_0 on each fit parameter. Since this multi-parameter fit can easily lead to unwanted effects or biases, the fit procedure and its sensitivity to various effects need to be studied carefully, which is addressed in the respective analysis chapters.

7.4. Performance and uncertainty evaluation using pseudo experiments

To evaluate the performance and stability of the measurement approach and to evaluate the impact of uncertainties so-called *pseudo experiments* are performed: Pseudo or artificial data of the likelihood discriminant, \mathcal{D} , is created from the Monte Carlo templates. For each template bin a random number is drawn from a Poisson distribution with mean value λ , where λ is the original sum of the signal and background templates in the bin. The pseudo data are then fit using the nominal templates. The fit values are filled into histograms, which are fit with a Gaussian to extract the mean value.

7.4.1. Use of pseudo experiments in the 2010 and 2011 analysis (a)

For the 2010 analysis and the 2011 analysis (a) the procedure described above is typically repeated 1000 times for each investigation. For the pseudo experiments the nuisance parameters are limited to $|\delta_i| < 1.25$ since no knowledge of the behaviour of the nuisance parameters beyond this point is assumed. Furthermore, this ensures that the fit converges more often. Otherwise, a larger number of time-consuming pseudo experiments would need to be performed.

To evaluate the effect of a single systematic uncertainty that is included in the fit as a nuisance parameter the fit to data is performed without the nuisance parameter in question. The quadratic difference in relative uncertainty between the two fits is taken as a measure of the contributions of the systematic uncertainty to the total uncertainty. This is, however, not an exact method, because correlations among the uncertainties are neglected, but it gives a good idea of the size of the systematic uncertainty.

For systematic variations, e.g. the study of parameters that are found or expected to be non-continuous, the shifted templates at $\pm 1\sigma$ are used to draw random numbers from. The result of all pseudo experiments is compared to the procedure where pseudo experiments are performed from the nominal templates. The difference in the mean of the Gaussians is quoted as uncertainty. Additionally, for each pseudo experiment the deviation of the fit result from the default value divided by the uncertainty on the fit result, often called pull, is calculated. This value yields information whether uncertainties are biased or over-/underestimated. If the pull width is smaller than one, it hints at an overestimation of the uncertainties with respect to data and vice versa. Shifts of the pull distribution could be the result of biases that might have to be corrected for.

To evaluate the a priori expected uncertainty, the $t\bar{t}$ normalisation, $\beta_0 = 1$, is kept constant while random variations of all other processes β_i with $i > 0$ and nuisance parameters δ_i within their $\pm 1\sigma$ range are utilised. These shifts are drawn from a unit Gaussian distribution, renormalised, and the δ parameters are morphed as described in Sec. 7.3.1. The pseudo data distribution is then drawn from the sum of the templates and fit with the nominal ones. Repeating this procedure without the nuisance parameters yields the statistical uncertainty. By subtracting the statistical uncertainty from the total expected uncertainty in quadrature one arrives at the expected systematic uncertainty.

7.4.2. Use of pseudo experiments in the 2011 analysis (b)

Since the 2011 analysis (b) does not make use of profiling, all systematic uncertainties are evaluated in pseudo experiments. These are created by drawing a random number for each systematic variation and pseudo experiment using the $\pm 1\sigma$ variation templates, which are bin-wise linearly interpolated between the nominal template and extrapolated beyond. Since in contrast to the other two analyses the uncertainties are not included in the fit, discrete and continuous uncertainties are not distinguished. However, in order to take into account possible correlations between the individual systematic variations all uncertainties are varied at the same time. Because of the large number of uncertainties the uncertainties are limited to $|\delta| < 3\sigma$ to ensure that the majority of fits to the pseudo data converges. In return, this means that there is a relative 0.3% uncertainty on the error obtained, which is clearly negligible. In order to account for the large number of systematic variations, 200,000 pseudo experiments are performed. In order to evaluate the statistical uncertainty 10,000 pseudo experiments are evaluated.

7.5. Summary of uncertainties

The systematic uncertainties and their treatment in each analysis is summarised in Tab. 7.2. Details of each individual component are given above. Even though the 2010 analysis and the 2011 analysis (a) are similar, some of the uncertainties are treated differently. For the 2011 analysis (a) no b -tagging or heavy flavour uncertainties are considered since they have no effect on the likelihood discriminant. However, since additional Monte Carlo studies varying the amount of initial and final state radiation show that these parameter are continuous, ISR and FSR uncertainties are treated as two nuisance parameters in the fit. No pileup uncertainty is quoted since the simulation samples are generated according to the pileup conditions in data. The close-by jets and flavour composition components of the jet energy scale uncertainty are added to all other JES uncertainties except for the pileup and the b -jet JES component for technical reasons. This leads to an overestimation of these uncertainties. One-sided templates such as obtained for the jet reconstruction efficiency uncertainty are symmetrised around the nominal one to obtain $\pm 1\sigma$ bounds.

7. Measurement and signal extraction method

Table 7.2.: Sources of systematic uncertainties and their treatment in the cross section extraction as nuisance parameter (\checkmark), outside the fit (\times) or where not applicable or treated otherwise (-). The first set of uncertainties is related to assumptions on the physics model, while the second set is related to detector and reconstruction effects.

Systematic uncertainty	Usage in analysis			Comments
	2010	2011 (a)	2011 (b)	
Background normalisation	-	-	-	1
Signal generator	\times	\times	-	
Parton shower model	\times	\times	\times	
ISR and FSR	\times	\checkmark	\times	
PDF	\times	\times	\times	
W + jets generator settings	\times	\times	-	
W + heavy flavour contribution	\checkmark	-	\times	
QCD multi-jet model	\times	\times	-	
Pileup model	\checkmark	-	-	
Monte Carlo statistics	\times	\times	\times	
Muon/electron scale factors	\checkmark	\checkmark	\times	
Muon momentum scale and resolution	\checkmark	\checkmark	\times	
Electron energy scale	\checkmark	\checkmark	\times	
Electron energy resolution	\checkmark	\checkmark	\times	
Calorimeter response (JES)	\checkmark	\checkmark	\times	2
η -intercalibration (JES)	\checkmark	\checkmark	\times	2
Noise term (JES)	\checkmark	\checkmark	\times	2
Parton shower model (JES)	\checkmark	\checkmark	\times	2
Underlying event model (JES)	\checkmark	\checkmark	\times	2
Pileup influence on JES	\checkmark	\checkmark	\times	2
Close-by jets (JES)	\checkmark	-	\times	2,3
Flavour composition (JES)	\checkmark	-	\times	2,3
b -Jet energy scale	\checkmark	\checkmark	\times	
Jet energy resolution	\checkmark	\checkmark	\times	
Jet reconstruction efficiency	\checkmark	\checkmark	\times	
E_T^{miss} uncertainties	\checkmark	\checkmark	\times	
b -tagging calibration	\checkmark	-	\times	
Mistagging calibration	\checkmark	-	\times	

¹ included in statistical uncertainty through Gaussian constraints

² 2011 analysis (b) uses envelope of JES uncertainties

³ included in other JES components for 2011 analysis (a)

8. Cross section measurement using b -tagging

The cross section measurement using b -tagging and kinematic information exploits a collision data set of 35 pb^{-1} recorded in 2010. This analysis is the first precision measurement of top quark-antiquark pair production in the lepton + jets channel at the ATLAS experiment after the initial measurement of the top quark at the ATLAS experiment [244] briefly discussed at the beginning of Chapter 7. The analysis has been published as preliminary conference result [265] and in the version presented here also as a journal article [266]. In the following, the results of the event selection are presented in Sec. 8.1. Since the analysis method is already explained in detail in Chapter 7, only the differences with respect to the other analyses presented in this work are detailed. The cross section extraction can be found in Sec. 8.2 with subsequent stability tests in Sec. 8.3. The chapter is concluded by a discussion of the result and its extension to other measurements in Sec. 8.4.

8.1. Results of event selection and multivariate signal and background separation

The event selection—requiring at least three jets, exactly one lepton, and cuts on E_T^{miss} and m_T^W —is described in Chapter 6. The event yields after selection are shown in Fig. 8.1 and Tabs. 8.1 and 8.2. Good agreement between the expected and observed yields is found.

8. Cross section measurement using b -tagging

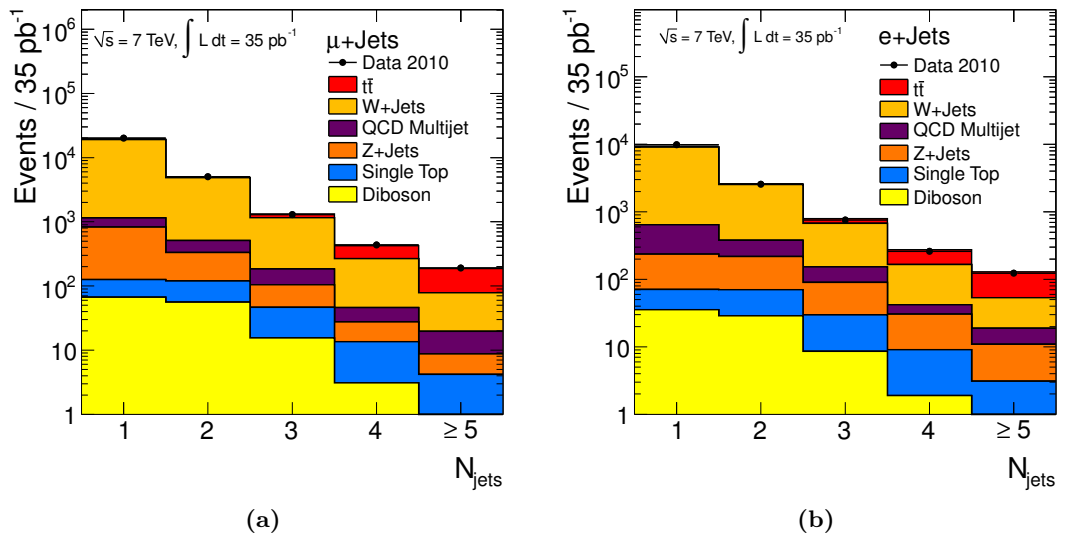


Figure 8.1.: Observed and expected event yields for the 2010 analysis in the (a) $\mu + \text{jets}$ and (b) $e + \text{jets}$ channel. [248]

8.1. Results of event selection and multivariate signal and background separation

Table 8.1.: Selected events in the $\mu + \text{jets}$ channel split up by the different jet multiplicities. Uncertainties are from limited MC statistics, theoretical cross sections, JES, luminosity and ISR/FSR for $t\bar{t}$. Control region is shaded.

	1 jet	2 jets	3 jets	4 jets	≥ 5 jets
$t\bar{t}$	20 \pm 9	85 \pm 22	165 \pm 23	156 \pm 18	109 \pm 27
$W + \text{jets}$	18000 \pm 2100	4330 \pm 990	980 \pm 410	220 \pm 140	59 \pm 38
Fakes (QCD multi-jet)	316 \pm 95	180 \pm 54	79 \pm 24	19 \pm 6	11 \pm 3
Single top	58 \pm 10	64 \pm 11	31 \pm 7	10.5 \pm 3.6	3.6 \pm 2.1
$Z + \text{jets}$	700 \pm 140	210 \pm 50	59 \pm 26	13.9 \pm 9.6	4.5 \pm 3.6
Diboson (WW, WZ, ZZ)	67 \pm 10	56 \pm 9	16 \pm 4	3.1 \pm 1.8	0.6 \pm 0.8
signal/background ratio	0.001	0.02	0.14	0.58	1.39
Total Predicted	19200 \pm 2400	4930 \pm 1140	1330 \pm 500	420 \pm 180	187 \pm 74
Data Observed	20076	5039	1289	436	190

Table 8.2.: Selected events in the $e + \text{jets}$ channel split up by the different jet multiplicities. Uncertainties are from limited MC statistics, theoretical cross sections, JES, luminosity and ISR/FSR for $t\bar{t}$. Control region is shaded.

	1 jet	2 jets	3 jets	4 jets	≥ 5 jets
$t\bar{t}$	15 \pm 5	63 \pm 12	117 \pm 17	109 \pm 15	76 \pm 19
$W + \text{jets}$	8500 \pm 1100	2160 \pm 500	520 \pm 220	124 \pm 77	35 \pm 23
Fakes (QCD multi-jet, $\gamma + \text{jets}$)	410 \pm 200	160 \pm 80	64 \pm 32	12 \pm 6	8 \pm 4
Single top	36 \pm 7	42 \pm 8	21 \pm 5	7.3 \pm 2.9	2.7 \pm 1.7
$Z + \text{jets}$	170 \pm 40	147 \pm 43	60 \pm 28	21 \pm 15	7.8 \pm 6.0
Diboson (WW, WZ, ZZ)	36 \pm 6	29 \pm 6	9 \pm 3	1.9 \pm 1.5	0.4 \pm 0.6
signal/background ratio	0.002	0.02	0.17	0.66	1.41
Total predicted	9140 \pm 1360	2610 \pm 650	790 \pm 310	270 \pm 120	129 \pm 55
Data observed	9849	2568	755	261	123

8. Cross section measurement using b -tagging

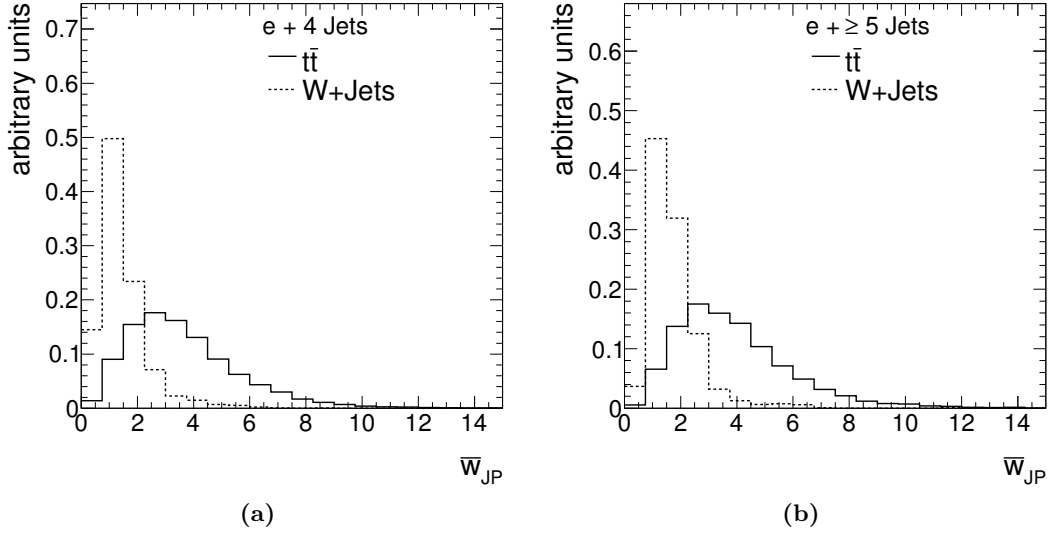


Figure 8.2.: *Distribution of the average JetProb weight of the two selected jets with highest b -tagging probability, \bar{w}_{JP} , in the $e + 4$ and ≥ 5 jets bin for $t\bar{t}$ production and the dominant $W + \text{jets}$ background process. [248]*

The analysis employs the input variables lepton η , a transformed form of aplanarity, $\exp(-8 \times \mathcal{A})$, and $\exp(-4 \times H_{T,3p})$ as well as the average JetProb weight of the two selected jets with highest b -tagging probability as detailed in Sec. 7.1 combined into a projective likelihood discriminant. The major difference to the other analyses described in the following chapters is the direct use of the b -tagging weight. Top quark pair events always contain two real b -jets in the final state whereas $W + \text{jets}$ events contain mostly light flavour jets. The advantage over applying a cut on the distribution at a given efficiency point as done in the 2011 analysis (b) (see Chapter 10) is that one can add the variable into the likelihood discriminant ensuring a comparably large data sample can be analysed while gaining discrimination power. Furthermore, additional shape information helps to constrain the background prediction. The distribution of the JetProb weight of the two selected jets with highest b -tagging probability for $t\bar{t}$ and $W + \text{jets}$ production in different jet bins is shown in Fig. 8.2. This variable is a very powerful discriminator and therefore needs to be corrected carefully for differences found between data and simulation, which is detailed in Sec. 4.5.1.

For the \bar{w}_{JP} distributions agreement between data and simulation for events with at least four jets as shown in Fig. 8.3 is obtained. One can, however, observe already in the 4 jet bin that there are larger discrepancies for low b -tagging probabilities, i.e. low \bar{w}_{JP} , which are not found to be fully covered by the uncertainties. This effect worsens for the 3 jet bin, where the $W + \text{jets}$ background, which only in the comparably rare case of $Wb\bar{b} + \text{jets}$ production contains two real b -jets, dominates. Since the \bar{w}_{JP} variable has high discrimination power but studies show that the fit is very sensitive to changes

8.1. Results of event selection and multivariate signal and background separation

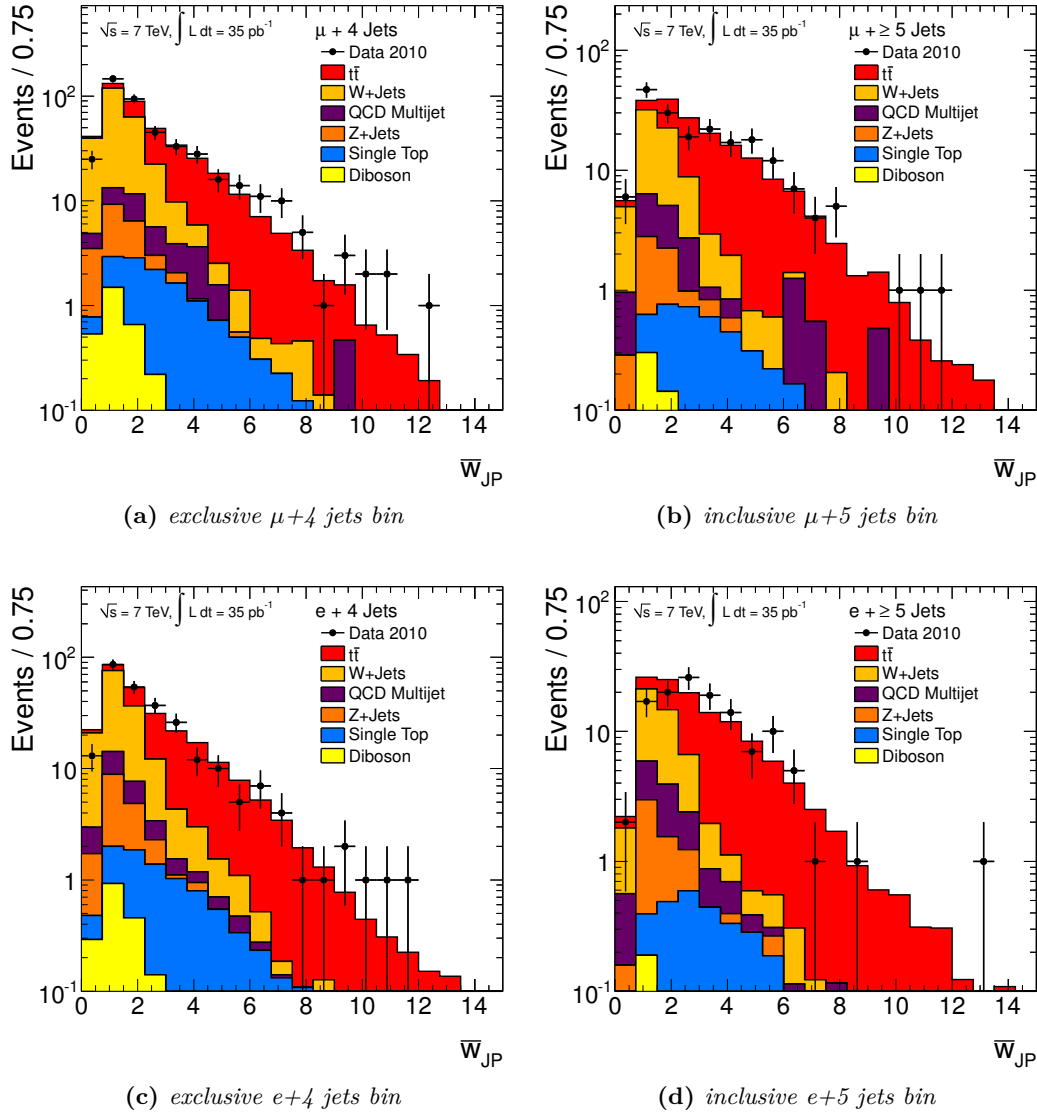


Figure 8.3.: The input variable \bar{w}_{JP} for the $\mu + \text{jets}$ and the $e + \text{jets}$ channel in the signal regions.

in the low \bar{w}_{JP} region, this variable is only used in events with 4 and ≥ 5 jets, where it is well understood. This leads to a reduction in separation power of the likelihood discriminant for events with three jets, but since the fit is performed in all three jet bins simultaneously these events still pose an important constraint and help to extract additional information on background normalisation and systematic uncertainties.

For the other three input variables comparisons of data with the predictions are shown in Figs. 8.4 to 8.6. Largely good agreement is found and discrepancies observed are

8. Cross section measurement using b -tagging

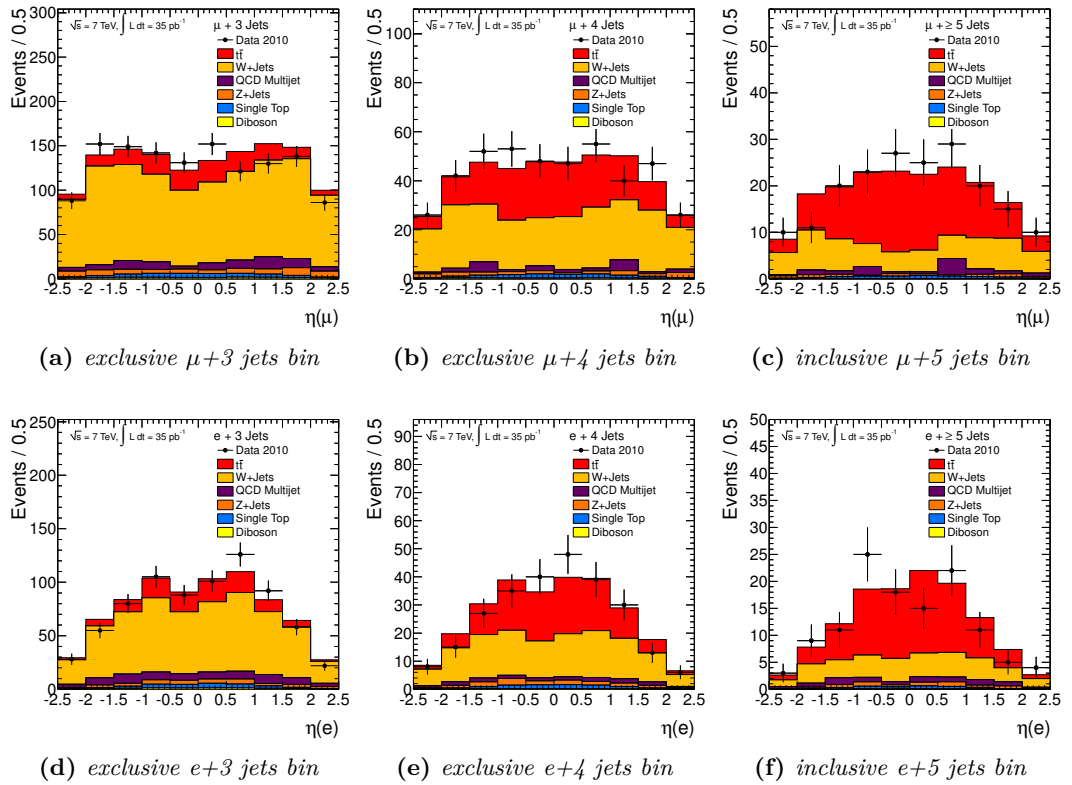


Figure 8.4.: The input variable η^ℓ for the μ +jets and the e +jets channel in the signal regions.

covered by the systematic uncertainties, which are, however, not shown in the figures but only for the final discriminant below.

The combined projective likelihood discriminant is shown in Fig. 8.7. One speaks of good separation power when the discriminant shows small overlap between signal and background and/or a significant shape difference is visible between them. In this analysis the best separation power is achieved in the 4 jet bin. The apparent shape difference between the 3 and the 4 jet bin is due to the exclusion of \bar{w}_{JP} in the 3 jet bin and consequent degradation of separation power. The overall separation power for events with five and more jets is slightly diminished in comparison to events with fewer jets since the background events become more top-like and therefore the distribution of the discriminant is flatter. Additionally, in the electron channel for five and more jets the discrimination power is also found to be lower due to the low number of expected events. This is explained by the lower selection efficiency in the electron channel.

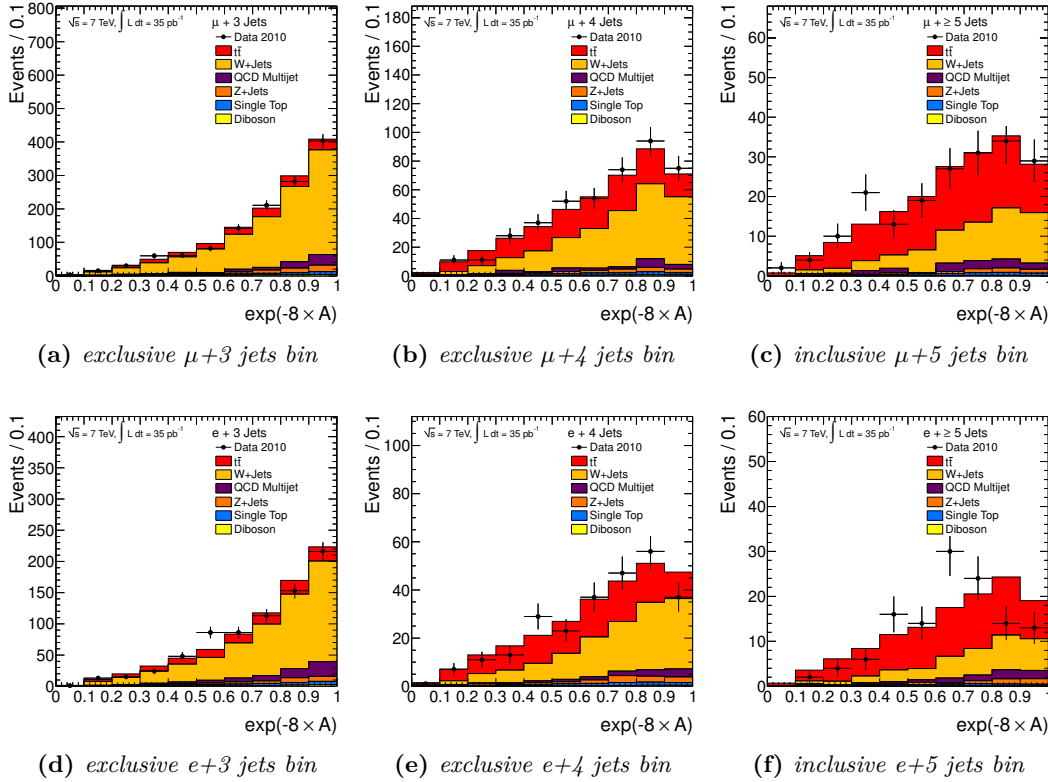


Figure 8.5.: The input variable $\exp[-8 \times A]$ for the $\mu + \text{jets}$ and the $e + \text{jets}$ channel in the signal regions.

8.2. Cross section extraction

The $t\bar{t}$ cross section is extracted using the profile likelihood method, which is described in Sec. 7.3.2. Only systematic uncertainties that are expected or shown to be continuous are included in the fit as nuisance parameters (see Sec. 7.2) while the non-continuous uncertainties are evaluated using pseudo experiments (see Sec. 7.4).

8.2.1. Expected uncertainties

The expected combined statistical and systematic uncertainties are obtained using the recipe described in Sec. 7.4. Performing 1,000 pseudo experiments including all nuisance parameters the expected total uncertainty amounts to 8.3% taken from the Gaussian fit shown in Fig. 8.8. The corresponding pull distribution is shifted away from zero to -0.09 and has a width of 0.92, i.e. smaller than the desired value of 1, due to the extrapolation cut-off at 1.25 on the nuisance parameters as discussed in Sec. 7.3.1. By removing the cut-off the fit fails more often but the width moves towards 1. The statistical uncertainty is found to be 6.1% performing the fit without nuisance parameters. Subtracting the

8. Cross section measurement using b -tagging

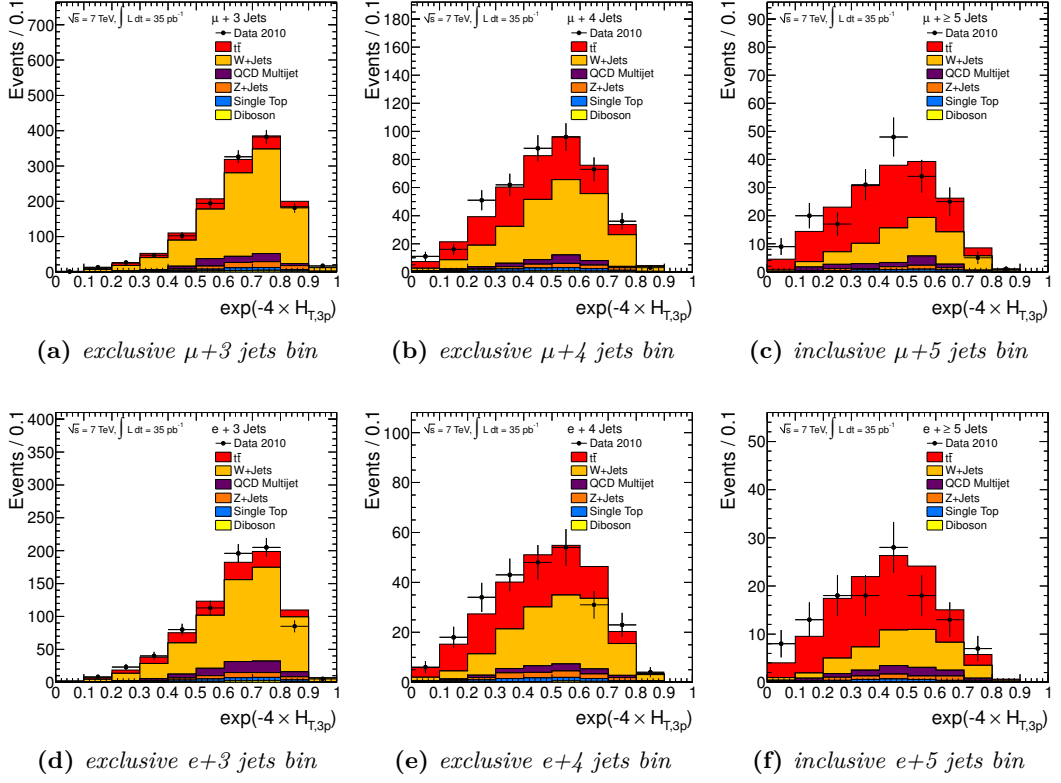


Figure 8.6.: *The input variable $\exp[-4 \times H_{T,3p}]$ for the μ +jets and the e +jets channel in the signal regions.*

statistical uncertainty from the total uncertainty in quadrature yields an expected total systematic uncertainty of 5.6% from the fit.

The stability of the fit is furthermore evaluated by performing pseudo experiments as detailed in Sec. 7.4 in which the assumed $t\bar{t}$ cross section is varied in steps of 10 pb from 120 to 200 pb to investigate the linearity of the fit. For each of the input cross sections 1,000 experiments are drawn, the fit is performed and the average fit value of all experiments for a given cross section is extracted assuming a Gaussian shape. A linear fit to the mean values of those results as a function of the input cross section is expected to yield a gradient of 1 and no offset for a fully unbiased setup. In case a significant shift is found, this non-linearity needs to be propagated to the final measurement result to make the extracted cross section independent of the expected signal cross section.

The fit presented in Fig. 8.9a shows good linearity over the full range, but a small offset of -1.6 pb. Therefore, the signal cross section obtained by the fit in the following is corrected via:

$$\sigma_{t\bar{t}} = \frac{\sigma_{t\bar{t},\text{fit}} + 1.6}{0.994} \text{ pb}, \quad (8.1)$$

also taking into account the change in slope by a factor of 0.994. This shift is also visible

8.2. Cross section extraction

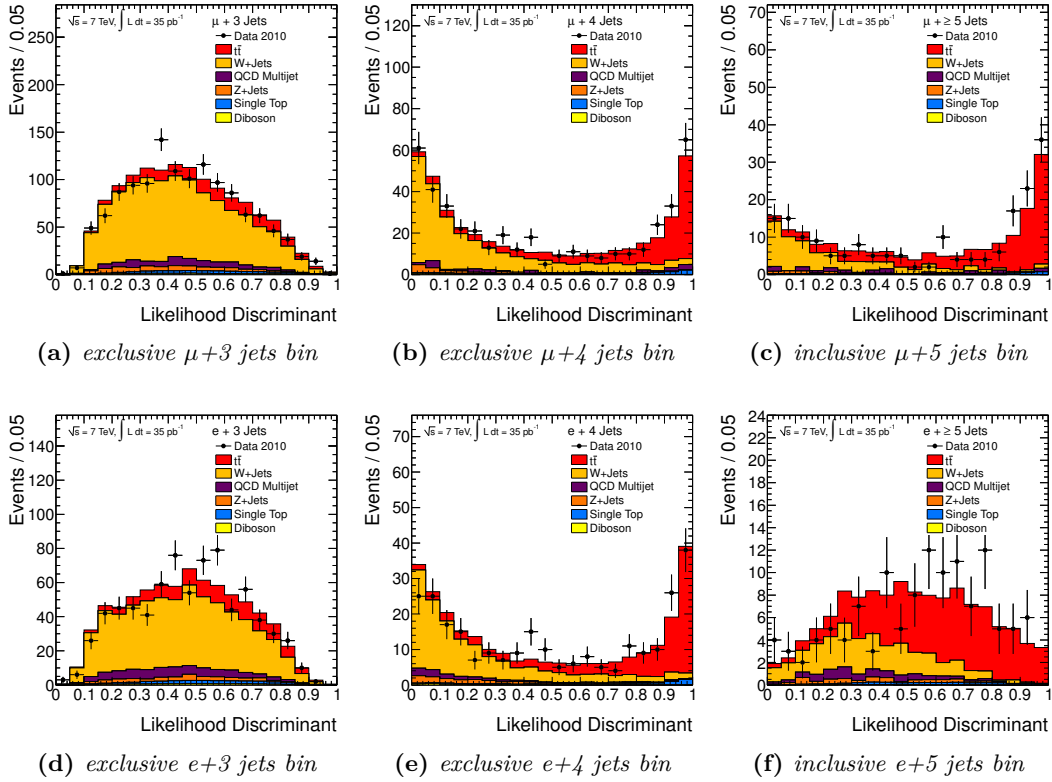


Figure 8.7.: Likelihood discriminant for the $\mu + \text{jets}$ and the $e + \text{jets}$ channel in the signal regions.

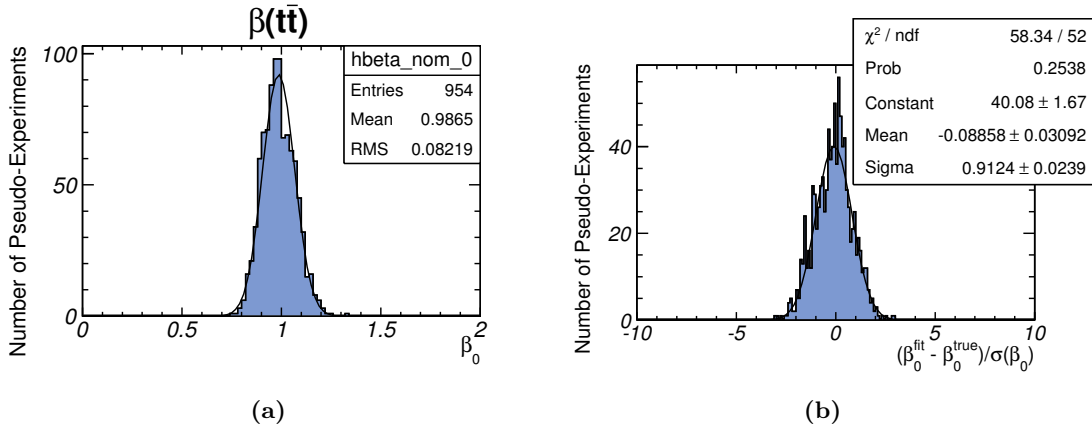


Figure 8.8.: Distribution of (a) fitted $t\bar{t}$ cross section parameter, β_0 , and (b) its pull using 1,000 pseudo experiments. Systematic uncertainties that are treated outside the fit are not considered here.

8. Cross section measurement using b -tagging

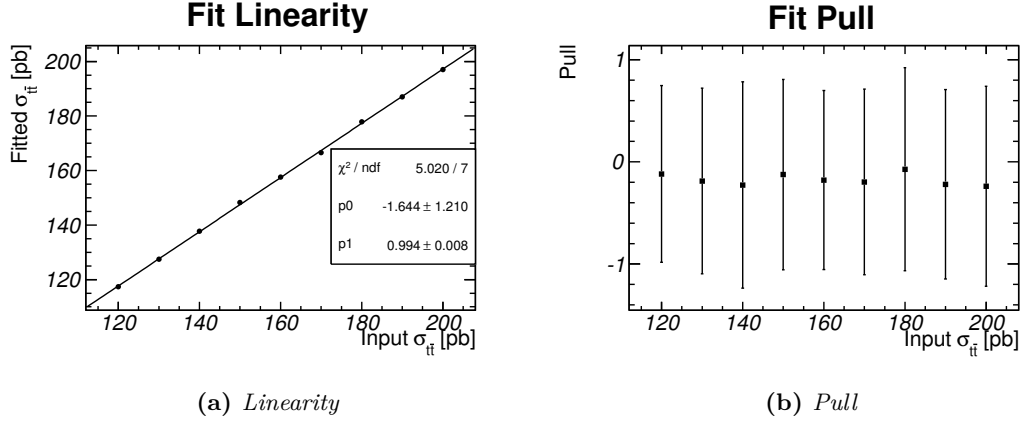


Figure 8.9.: (a) Linearity test and (b) pull distribution as a function of input $t\bar{t}$ cross section.

in the individual pull distributions at the cross section values. One might furthermore argue that since the width of the pulls is less than 1 the uncertainties are slightly over-estimated, which would mean that a more conservative estimate is quoted. However, as discussed above this effect is also due to the fact that the uncertainties are cut off at 1.25σ , which can be removed without changing the overall result but takes significantly more time since the fit fails more often.

The uncertainties on the total signal-plus-background prediction are shown in comparison with data in Fig. 8.10. The uncertainty bands include all contributions except the ISR/FSR and showering ones since they use different central value templates. The error band is centered around the sum of predicted signal and background events in each bin. One can see that the data points are well covered by the systematic uncertainties considered in the analysis.

8.2.2. Fit results

Applying the minimum log-likelihood fit including all continuous systematic uncertainties and Monte Carlo statistics uncertainties of the templates of discriminant \mathcal{D} to data in all six analysis channels yields a $t\bar{t}$ production cross section of

$$\sigma_{t\bar{t}} = 184^{+16}_{-15} \text{ pb.} \quad (8.2)$$

Correcting for the linearity shift yields

$$\sigma_{t\bar{t}} = 187^{+16}_{-15} \text{ pb.} \quad (8.3)$$

The fit result is shown in Fig. 8.11. The χ^2 and Kolmogorov-Smirnov [245] tests of the compatibility of the fitted sum of signal and background templates with data show very good agreement. The individual fit values of all processes and nuisance parameters are

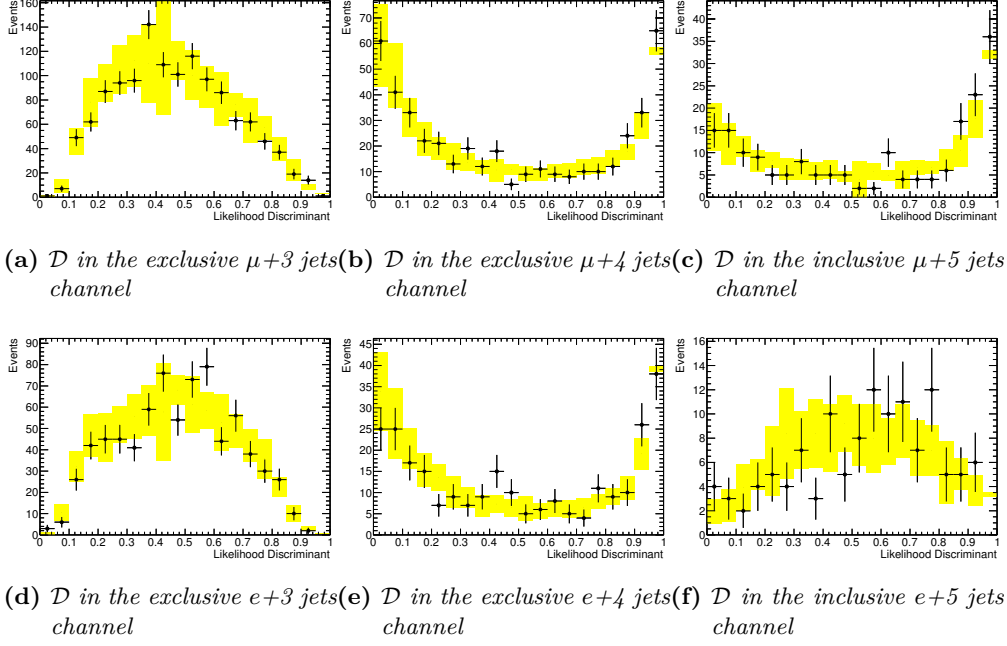


Figure 8.10.: Error bands for the distributions of D of the sum of predicted signal and background events overlaid on the discriminant distributions in data for the six different analysis channels.

given in Tab. 8.3.

Table 8.3.: Resulting fit parameters and Hessian symmetric uncertainties from the fit in all six analysis channels.

Parameter	Value	Hessian error
$\beta(t\bar{t})$	1.1142	0.0918
$\beta(W \rightarrow \mu + 3 \text{ jets})$	0.8700	0.0841
$\beta(W \rightarrow \mu + 4 \text{ jets})$	0.8519	0.1230
$\beta(W \rightarrow \mu + 5 \text{ jets})$	0.7415	0.2076
$\beta(W \rightarrow e + 3 \text{ jets})$	0.9014	0.1015
$\beta(W \rightarrow e + 4 \text{ jets})$	0.8407	0.1537
$\beta(W \rightarrow e + 5 \text{ jets})$	0.5492	0.2633
$\beta(Z + \text{jets})$	1.1189	0.2815
$\beta(\text{Single top})$	1.0059	0.1059
$\beta(\text{Diboson})$	1.0007	0.0600
$\beta(\text{QCD in } \mu + 3 \text{ jets})$	0.8961	0.4786
$\beta(\text{QCD in } \mu + 4 \text{ jets})$	0.9931	0.4730
$\beta(\text{QCD in } \mu + 5 \text{ jets})$	0.6472	0.4718

continued on next page

8. Cross section measurement using b -tagging

Table 8.3.: Resulting fit parameters and Hessian symmetric uncertainties from the fit in all six analysis channels.

Parameter	Value	Hessian error
$\beta(\text{QCD in } e + 3 \text{ jets})$	1.0680	0.4880
$\beta(\text{QCD in } e + 4 \text{ jets})$	1.0107	0.4966
$\beta(\text{QCD in } e + 5 \text{ jets})$	0.8565	0.4912
$\delta(b\text{-tag working point 1})$	-0.6763	1.0609
$\delta(b\text{-tag working point 2})$	0.6062	0.9607
$\delta(b\text{-tag working point 3})$	-0.0890	0.9099
$\delta(b\text{-tag working point 4})$	0.1376	0.8712
$\delta(\text{mistag working point 1})$	0.3651	0.9975
$\delta(\text{mistag working point 2})$	-0.3292	0.9727
$\delta(\text{mistag working point 3})$	0.2834	0.9886
$\delta(\text{mistag working point 4})$	0.0279	0.9947
$\delta(\text{Jet reconstruction})$	1.0277	0.5341
$\delta(\text{Jet energy resolution})$	0.5942	0.9116
$\delta(Wb\bar{b}/c\bar{c} \text{ fraction 3 jets})$	-0.6014	0.9564
$\delta(Wb\bar{b}/c\bar{c} \text{ fraction 4 jets})$	0.2517	0.8627
$\delta(b\bar{b}/c\bar{c} \text{ fraction 5 jets})$	-0.3720	0.9242
$\delta(Wc \text{ fraction 3 jets})$	0.4486	0.9460
$\delta(Wc \text{ fraction 4 jets})$	0.0665	0.9758
$\delta(Wc \text{ fraction 5 jets})$	-0.1275	0.9975
$\delta(\text{Pileup})$	0.2230	0.7710
$\delta(\mu \text{ SFs})$	-0.0563	0.9874
$\delta(e \text{ SFs})$	0.0837	0.9398
$\delta(\mu \text{ momentum smearing})$	-0.1202	1.3489
$\delta(e \text{ energy scale})$	0.1472	0.7577
$\delta(e \text{ energy smearing})$	0.2214	0.7646
$\delta(E_T^{\text{miss}})$	0.1082	0.9111
$\delta(\text{JES Eta})$	1.0496	0.4629
$\delta(\text{JES Calo})$	-0.5960	0.4951
$\delta(\text{JES Alpgen})$	-0.5506	0.5959
$\delta(\text{JES Noise})$	-0.2108	0.7986
$\delta(\text{JES Pileup})$	0.1552	0.6668
$\delta(\text{JES Perugia})$	-0.0310	0.3277
$\delta(\text{JES b-Jet})$	-0.3104	0.6816
$\delta(\text{JES flavour})$	0.5871	0.7088
$\delta(\text{JES close-by})$	-0.3157	0.5178

The linear correlation coefficients of the fit parameters are shown in Fig. 8.12. One can observe that as expected the $W + \text{jets}$ processes in particular in the same lepton channel are correlated. At the same time they are anti-correlated with the QCD tem-

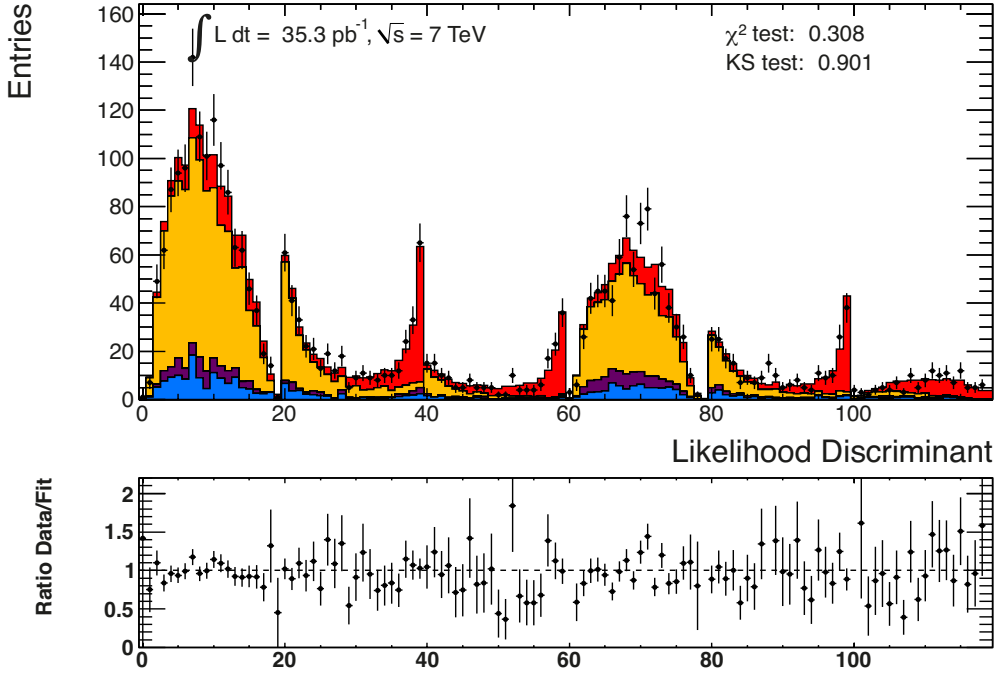


Figure 8.11.: Result of the combined profile likelihood fit in the six lepton + jets channels to data. Statistics tests of the compatibility of the fitted stack of templates with data are shown as well.

plates in the same jet bin and lepton channel since they have very similar likelihood discriminant shapes. Furthermore, since the W + jets templates are fitted separately in all analysis channels (see Sec. 7.2.2), they are sensitive to changes in the jet energy scale, especially the flavour composition uncertainty which is conservatively constructed with 50% quark and 50% gluon fraction. Some of the jet energy scale uncertainties are also correlated among each other. Shifts of the lepton scale factors have an effect on the W + jets background in the corresponding lepton channel as well. The $t\bar{t}$ signal template is correlated with several b -tagging related uncertainties since it contains two real b -jets in contrast to most other backgrounds.

As described in Sec. 7.3.2 the one-dimensional profile likelihood, $\lambda(\beta_0)$, only depending on β_0 , is obtained by minimising the likelihood with respect to all parameters. Keeping β_0 fixed at its minimum value, the log-likelihood value at the minimum is subtracted from a minimisation with respect to all parameters but β_0 . The result of the so-called profiling procedure is shown in Fig. 8.13. One can see that within $-\ln((\lambda(\beta_0^{\min}))) \pm 0.5 = [1.034, 1.215]$, i.e. 1σ , and also within a much larger range, no discontinuities or jumps are found, which confirms that the fit is stable and the nuisance parameters included in the fit do not bias the result. The small jump at $\beta_0 \approx 0.2$ is far away from the fit minimum ($\gg 5\sigma$) and has no effect on the final fit result. To study the stability of the fit in even more detail, the behaviour of the normalisation and nuisance parameters, $\vec{\beta}$

8. Cross section measurement using b -tagging

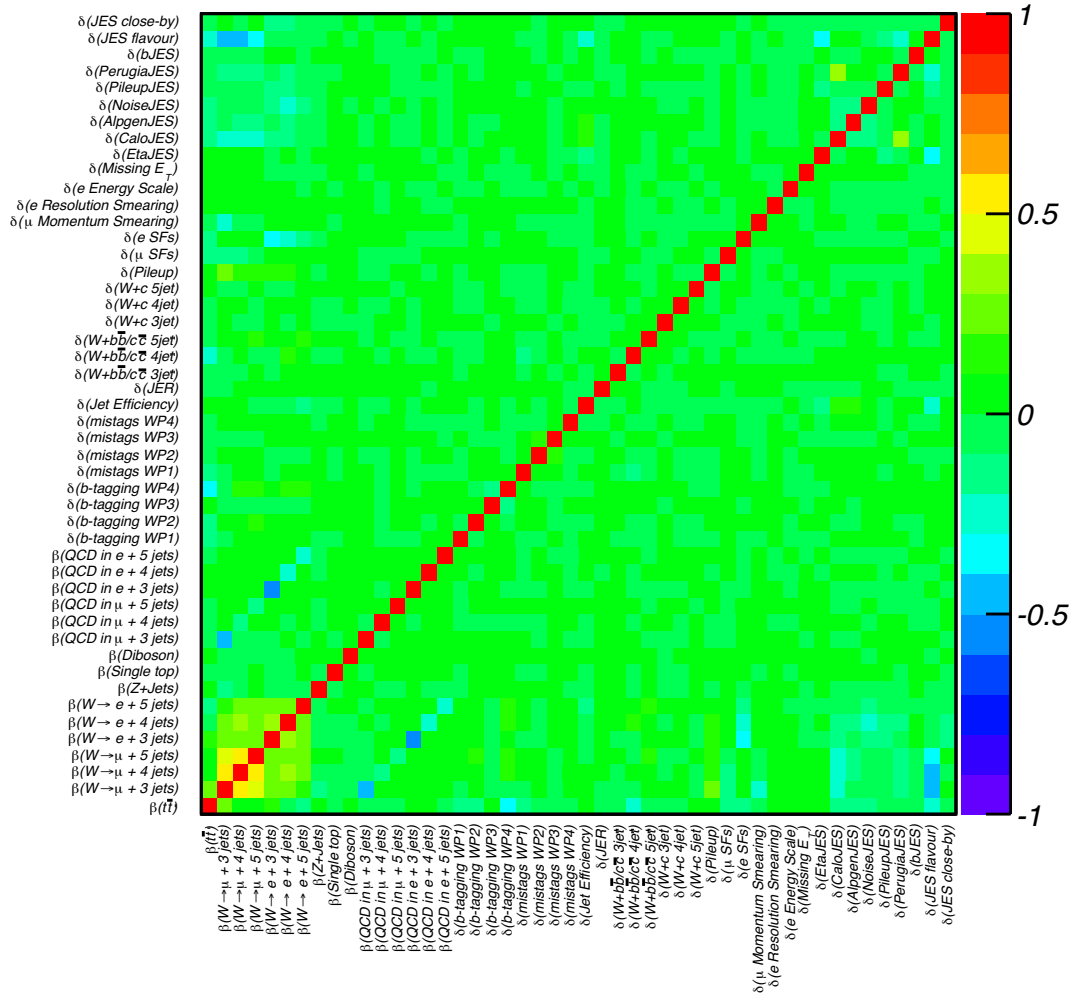


Figure 8.12.: Correlation matrix of the fit parameters β_i and δ_j as obtained from the fit in all six analysis channels. Shown are the linear correlation coefficients.

and $\tilde{\delta}_i$, is evaluated with respect to the value of β_0 . This is shown in Appendix D. Any discontinuities observed occur far away from the minimum. The 1σ interval is in perfect agreement with the uncertainty obtained from the fit.

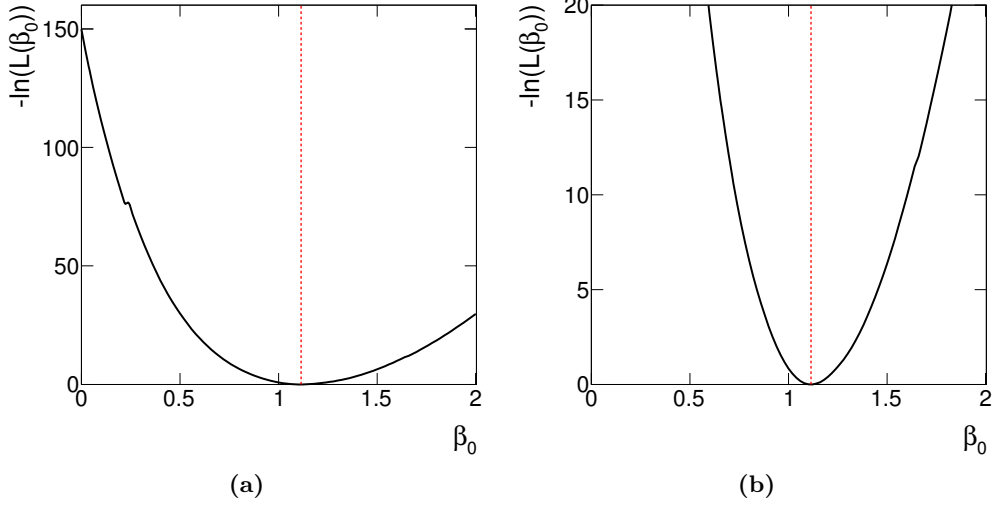


Figure 8.13.: Negative log-likelihood value as function of β_0 , $-\ln(L(\beta_0^{\min}))$, obtained from the profiling procedure in the fit showing (a) the range $\beta_0 = [0, 2]$, and (b) the enlarged region around the fitted value of $\beta_0 = 1.1142$ that is indicated with the red dotted line.

The results when performing the fit separately in the muon and the electron + jets channels are shown in Fig. 8.14 and summarised in Tab. 8.4 where also a comparison to the combined fit is given. One can observe good data-MC agreement in the $\mu + \text{jets}$ channel while agreement in the $e + \text{jets}$ channel is worse than in the muon channel, but mostly statistically limited. Nevertheless, since the top quark pair cross section is extracted as a single parameter over all channels information from the $e + \text{jets}$ channel adds constraining power to the combined fit and leads to an overall agreement between data and simulation.

8.2.3. Observed uncertainties

The observed uncertainties are summarised in Tab. 8.5. They are split into statistical uncertainty as well as systematic uncertainties evaluated in pseudo experiments and in the fit. No direct access to the uncertainties that are included in the fit exists. Therefore, to evaluate their effect on the measurement, they are removed from the fit one-by-one and the quadratic difference to the full fit is taken as uncertainty (see Sec. 7.4).

The observed statistical uncertainty of $(+5.8 / - 5.7)\%$ is found to be slightly smaller than the expected one. The uncertainty obtained from the full fit of 8.2% is only minimally smaller than the expected one, which is largely a result of the smaller statistical

8. Cross section measurement using b -tagging

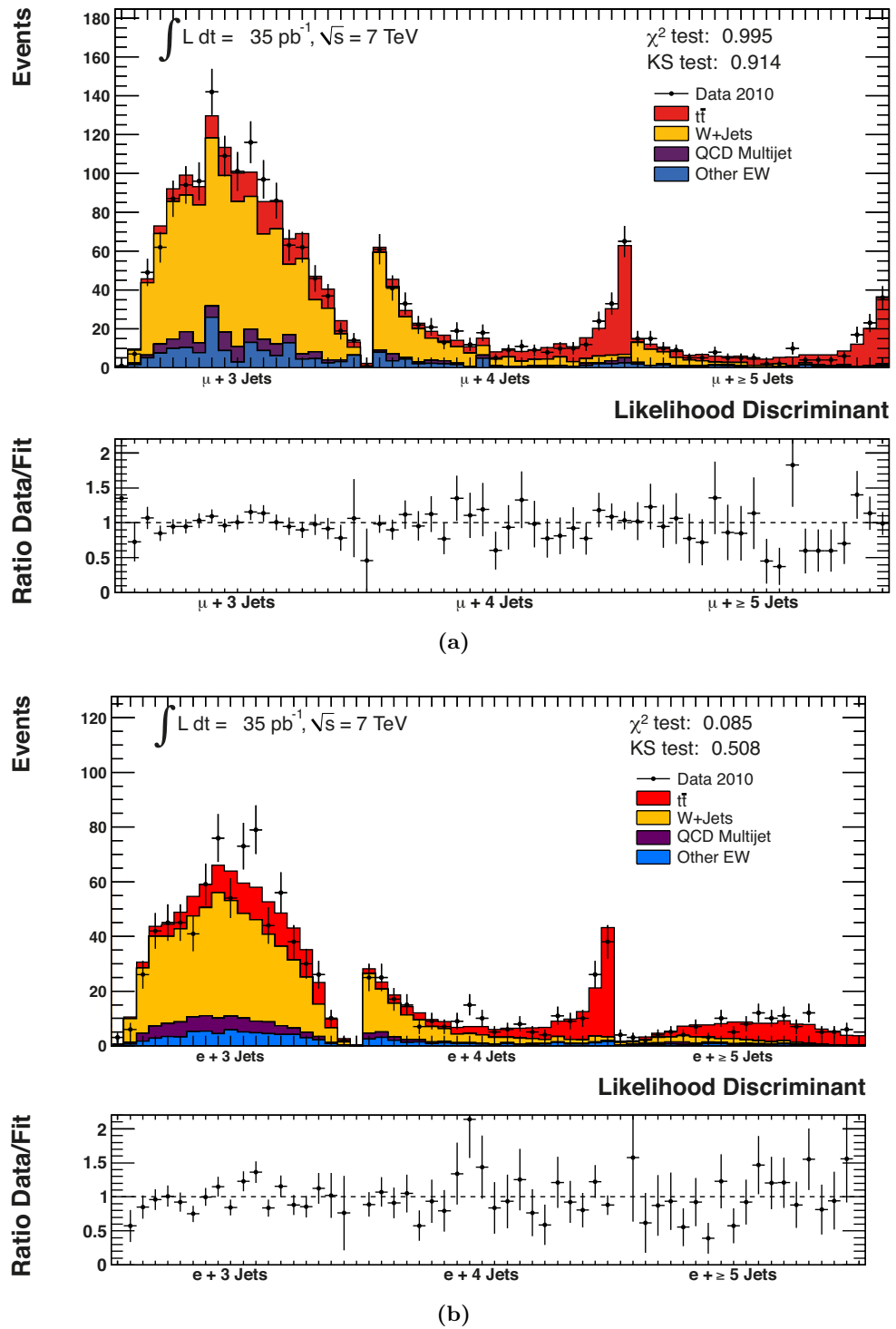


Figure 8.14.: Results for the cross section fit with all nuisance parameters included for (a) the $\mu + \text{jets}$, and (b) the $e + \text{jets}$ channel.

Table 8.4.: *Cross section results for the $\mu + \text{jets}$ and $e + \text{jets}$ channel fits compared to the combined six channel result: statistical only, full fit, and corrected for using the linearity fit results. Only uncertainties included in the fit are taken into account here.*

channel	statistical only [pb]	full fit [pb]	full corrected [pb]
$e + \text{jets}$	185^{+14}_{-13}	181^{+19}_{-18}	184^{+19}_{-18}
$\mu + \text{jets}$	193^{+17}_{-17}	191^{+23}_{-22}	196^{+24}_{-23}
combined	188^{+11}_{-11}	184^{+16}_{-15}	187^{+16}_{-15}

uncertainty. The dominant systematic uncertainties found in the fit are in decreasing order of their size b -tagging calibration, jet energy scale, and the heavy flavour content of the $W + \text{jets}$ sample. While the b -tagging probability distribution \bar{w}_{JP} shows very good discrimination between signal and background, it is associated with comparably large uncertainties due to the limited number of only four calibration points and the calibration method itself. As can be seen in Tab. 8.3 from the size of the uncertainty on the δ parameter (see discussion in Sec. 7.3), the fit is hardly able to constrain these. This similarly holds true for the $W + \text{jets}$ heavy flavour fraction. The jet energy scale is also expected to be one of the dominant uncertainties because of the several jets in top quark pair events. The jet energy scale uncertainty is split into several components, most of which the fit is able to constrain significantly. The JES component with the largest contribution is the quark-gluon flavour composition described in Sec. 7.2.1.1, which employs a rather conservative approach of a 50:50 quark-gluon fraction with 50% uncertainty for the background samples.

The non-continuous uncertainties evaluated in pseudo experiments have a large contribution to the total uncertainty since they cannot be reduced below the intrinsic input. Dominating in this analysis are the modelling of initial and final state radiation and the uncertainty on the generator matrix element model. This is more an effect of the measurement approach than physically motivated, which is addressed in Chapter 10. The uncertainties are mostly caused by large acceptance corrections inaccessible to the experiment.

8.3. Method and stability tests

Since the analyses presented in this work use the profile likelihood method, which helps to reduce systematic uncertainties significantly, the sensitivity of the fit to the size and the shape of systematic uncertainties is evaluated in various studies. This is in particular important to demonstrate that the uncertainties are not underestimated. If these cross checks showed that individual aspects are not covered by the determined uncertainties, additional uncertainties would need to be quoted. In the following detailed examples

8. Cross section measurement using b -tagging

Table 8.5.: *Table of estimated uncertainties. For each systematic uncertainty included in the fit the quadratic difference between the relative uncertainties of the full fit and the fit without the systematic in question is quoted. The remaining systematic uncertainties are added in quadrature afterwards.*

Statistical error (%)	+5.8	-5.7
Object selection (%)		
Jet energy scale	+3.9	-2.9
Jet reconstruction efficiency	+0.01	-0.3
Jet energy resolution	+0.3	-0.01
Electron scale factors	+1.6	-1.4
Muon scale factors	+1.2	-1.1
Electron smearing	+0.0	-0.0
Muon smearing	+0.4	-0.4
Electron energy scale	+0.5	-0.3
Missing E_T	+0.01	-0.01
Background modelling (%)		
W + jets heavy flavour content	+2.7	-2.4
W + jets shape ¹	+1.0	-1.0
QCD shape ¹	+0.8	-0.8
$t\bar{t}$ signal modelling (%)		
ISR/FSR ¹	+5.2	-5.2
NLO generator ¹	+4.2	-4.2
Hadronisation ¹	+0.4	-0.4
PDF ¹	+1.5	-1.5
Others (%)		
b -tagging calibration	+4.1	-3.8
Simulation of pileup	+0.01	-0.01
Templates statistics ¹	+1.1	-1.1
Total systematic uncertainty (%)	+9.7	-9.1
Luminosity uncertainty (%)	+3.7	-3.7
Total uncertainty (%)	+11.9	-11.3

¹ evaluated outside the fit

of the studies performed are given and methodological aspects of the profile likelihood method are addressed.

8.3.1. Use of envelope of uncertainties

For some uncertainties it could be that the $\pm 1\sigma$ template variations are envelopes whereas the shape of single contributions inside them might fluctuate heavily or be very different. Having only access to the smoother envelope the worry is that the fit might artificially decrease the uncertainty returned. This is in particular important for the jet energy scale related ones, which are already split into several sub-components. They could, however, be split even further, if an artificial decrease of the uncertainties was found. This effect is evaluated in pseudo experiments by replacing the templates of a given systematic variation by different functional shapes that only partly fill out the original variation template. This is illustrated in Fig. 8.15. The functional shapes used are linearly increasing and decreasing functions as well as sine and cosine waves with different periods. It is found that the uncertainties returned are smaller than the one found for the original systematic uncertainty and therefore no underestimation takes place.

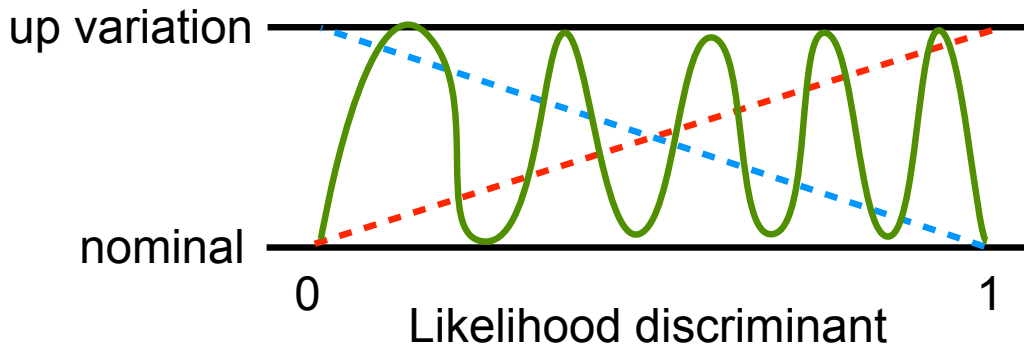


Figure 8.15.: *Illustration of shape variations inside a given systematic variation template for a given jet bin to evaluate the stability of the fit as described in the text. Shown here are linearly rising (red) and falling (blue) as well as sinusoidal (green) shapes.*

8.3.2. Uncertainty absorption

When performing the fit the fit algorithm takes into account the various correlations among the nuisance parameters. Even though the nuisance parameters are eliminated in the final profile likelihood fit and have no relevance in the profiling procedure, but only in the global minimisation, more confidence in the method can be gained by investigating the pull distributions of the nuisance parameters (see Sec. 7.4). As an example the b -tagging shape uncertainty at the lowest working point as one of the largest uncertainties

8. Cross section measurement using b -tagging

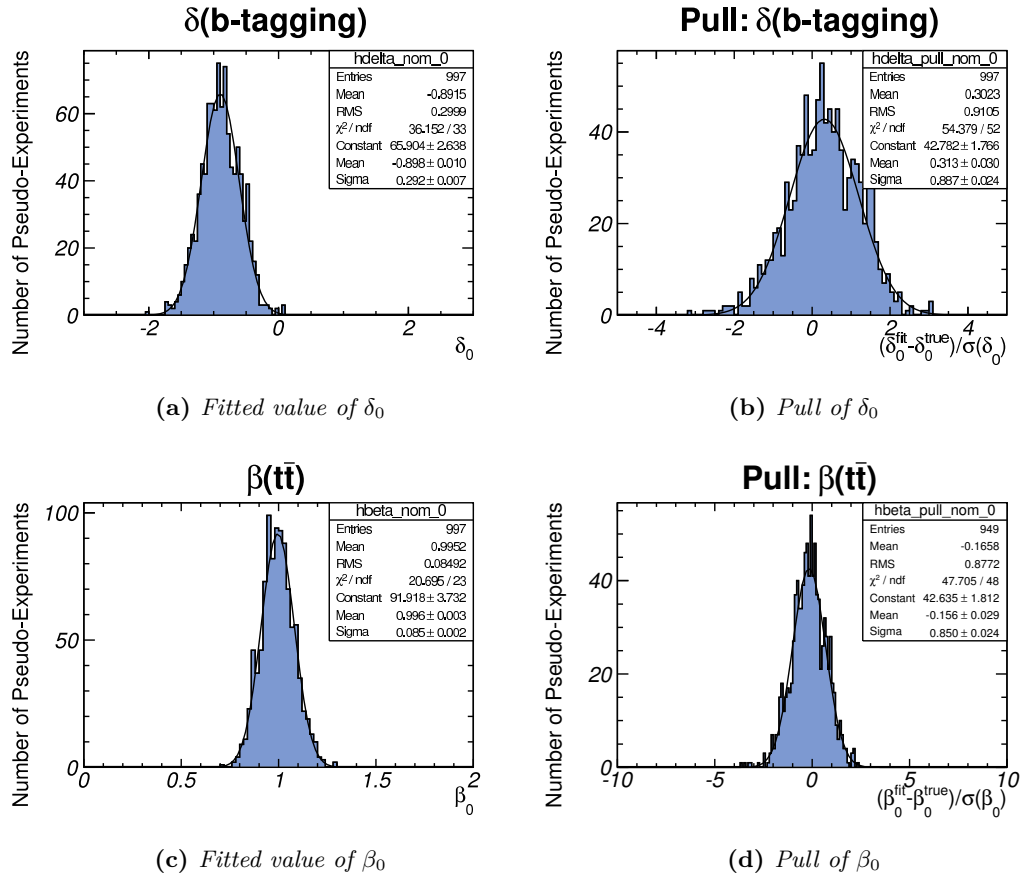


Figure 8.16.: Results of 1,000 pseudo experiments with b -tagging shape at working point 1 shifted to -1σ .

is examined. Pseudo experiments with the nuisance parameter value fixed to $\delta_{b\text{-tag WP1}} = -1$ return a fitted value of $\delta_{b\text{-tag WP1, fit}} = -0.9$ as shown in Fig. 8.16. The shift of 0.1 with respect to the input value is due to the Gaussian constraint on the nuisance parameters, which tries to push the parameter towards zero. The pull distribution of the nuisance parameter shows a shift of the mean of around 0.3. This is on the one hand due to the correlation with the other b -tagging working points. On the other hand this can also be explained by the behaviour of the nuisance parameter in the fit shown in more detail in Sec. D.1 of Appendix D, which prefers such a δ_i value less than zero for $\beta_0 \approx 1$. The width of the pull stays around 0.9. One can furthermore see that the $t\bar{t}$ cross section is hardly affected by the shift of the b -tagging parameter as shown in Fig. 8.16 as well. Repeating the same exercise with jet energy scale nuisance parameters and also varying several nuisance parameters at the same time results in a very similar behaviour and is therefore not shown for the sake of brevity.

8.3.3. Effect of acceptance corrections

The signal modelling uncertainty is only quoted as difference between the two NLO generators MC@NLO and POWHEG with their nominal settings. However, scale variations, which might have a large effect on acceptance, are not explicitly taking into account (refer also Chapter 10). The approximate NNLO predictions discussed in Sec. 2.2.4 are mostly inclusive and not differential therefore not allowing to evaluate changes in acceptance. Instead, the MCFM cross section integrator [238] is used in version 6.1 to calculate the $t\bar{t}$ cross section at fixed order NLO. Within MCFM a selection similar to the one used in the analysis is implemented to investigate the impact of scale variations. The cut on the transverse mass of the W boson is initially not applied to have a larger phase space for comparison. Varying both renormalisation and factorisation scales independently between $m_t/2$ and $2m_t$ (with $m_t = 172.5$ GeV) event yields within acceptance are extracted. These are normalised to the total NLO cross sections for the same scale variations obtained using Hathor [94]. The largest variations are found when shifting both factorisation and normalisation scale to their extreme values $m_t/2$ or $2m_t$ at the same time and yield +1.3% and -1.2%. Applying the W transverse mass cut on top results in even smaller variations of +0.4% and -0.9%. Given that the NLO signal modelling uncertainties taken into account in the analysis are significantly larger than the observed acceptance uncertainty, no additional uncertainty is quoted.

8.3.4. Correlation effects in jet energy scale uncertainties

A total of nine different jet energy scale (JES) uncertainty components are taken into account as nuisance parameters in the fit. At the same time, they constitute one of the dominant uncertainties of the analysis. Therefore, they provide a very nice environment to perform detailed studies regarding the effect of correlations, variable-dependencies and shifts on the fit method.

The calorimeter response JES component posing one of the largest contributions to the jet energy scale uncertainty could be split further into sub-components to consider additional correlations in transverse momentum and pseudo-rapidity (refer also to discussion above in Sec. 8.3.1). Studies show, however, that for those sub-components there is a correlation of more than 80% in the majority of the selected events. To conservatively study this effect, the calorimeter JES uncertainty is split into three components: One component making up 50% of the calorimeter JES uncertainty is constructed as fully correlated across the full jet p_T -range while the other two are designed to have a linearly increasing or decreasing uncertainty depending on the jet p_T making up the other half of the calorimeter JES uncertainty. It is found that the effect of decorrelation is hardly visible in the discriminant. Furthermore, the fit result remains constant yielding the same quality with respect to χ^2/ndf (number of degrees of freedom) and the KS test. The uncertainty on the $t\bar{t}$ cross section is even slightly reduced. The nuisance parameters do not change significantly confirming that a finer splitting of components is not required. In general, however, if one has better or more detailed knowledge on systematic uncertainties available, one should try to exploit it. Nevertheless, one also

8. Cross section measurement using b -tagging

has to take into account that each additional nuisance parameter does not only increase the number of free parameters in the fit, but might also coincidentally cause correlation effects with completely different parameters. Therefore, each nuisance parameter should carefully be investigated with regards to its behaviour in the fit. If the additional splitting of an individual nuisance parameter does not change the overall fit result, keeping the envelope might be more desirable since it will most likely lead to more stable fit results due to the smaller number of degrees of freedom.

A more special case is the influence of correlations on the missing transverse energy. All changes in the jet energy scale are propagated to E_T^{miss} assuming full correlation. To evaluate if this has an effect on the result the likelihood discriminant is constructed without any propagation of the calorimeter response JES component to E_T^{miss} and compared to the default discriminant (which assumes full correlation). The distributions are found to be almost identical meaning that this effect is negligible.

Regarding the sensitivity to systematic shifts and dependencies of the JES uncertainty several tests are performed. The jet transverse momenta might for instance be globally miscalibrated, which should be covered by the JES uncertainty returned by the fit. Shifting the nominal jet energy scale to a 1.5% lower value for all simulation samples the fit result changes to a 0.8% higher value with uncertainties only moving minimally confirming coverage by the JES uncertainty. The JES-independent nuisance parameters show no change while the JES-related ones tend to larger negative values reflecting the miscalibration. Instead of a global miscalibration there might also be miscalibrations as a function of the jet kinematics. This effect is evaluated by introducing linear dependencies of JES components on η or p_T of the jets. These are found to be reflected in the fit result, but all changes are covered by the contribution of the given component uncertainty. The statistical tests comparing data-MC agreement do not change significantly while the systematic shifts are clearly visible in the fitted δ values of the nuisance parameters, i.e. sensitivity to shifts and dependencies is confirmed and reflected in the uncertainties.

If the size or effect of an uncertainty is exactly reflected in the actual measurement, i.e. the variations found in data span the full range of the respective shape and/or normalisation uncertainty, it cannot be constrained further. To investigate whether it is in this case overconstrained by the fit or not, templates for a JES uncertainty component are scaled to the value obtained from the fit. The uncertainty component chosen for this test is the Perugia JES component that describes the effect of using a different underlying event model on the jet energy scale (see Sec. 7.2.1.1). This component is used since it is significantly constrained by the fit and the preferred fitted value is close to the original one ($\delta = 0$). The reason for such a choice is that it is technically much easier to correctly create the new templates with smaller uncertainty if they can be assumed to be symmetric around the central value. The fit results for the Perugia JES parameter is $\delta = -0.03102 \pm 0.3277$. One has to keep in mind that this is not a measurement of the actual uncertainty. The new templates are created by scaling the 1σ templates down to the uncertainty of δ using quadratic interpolation as also done in the fit. Before performing the fit with the new templates for Perugia JES, the Gaussian constraint for this nuisance parameter is removed from the likelihood in order not to influence the other fit parameters. The fit result as well as all other nuisance parameters remain

stable. The new fitted value of Perugia JES is $\delta = -0.04372 \pm 0.9321$. The uncertainty is smaller than unity since the shift of the δ value from zero was ignored. The uncertainty returned from the nominal fit is convoluted with the Gaussian constraint. This can be corrected for by calculating the Gaussian penalty term resulting from the δ -shift of -0.04372 , which amounts to 0.0019. Taking this into account by scaling the 1σ templates to $0.3277 + 0.0019 \approx 0.33$ and repeating the fit yields $\delta = -0.04761 \pm 1.0150$, which confirms the previous assumption.

The behaviour of the fit is investigated further by limiting the number of nuisance parameters in the fit to only one or two to evaluate the effect of correlations in a small test setup. The fit is first performed with the original $\pm 1\sigma$ templates which are then scaled to the uncertainty returned by the fit. Running with one parameter (Perugia JES) only and keeping the Gaussian constraint returns an uncertainty of 0.88 on the corresponding δ value. Dropping the Gaussian constraint yields an uncertainty of 0.999 as expected. In the next step the Calo JES component is added to the fit and the δ uncertainty for Perugia JES is obtained. After scaling to the latter value it is found that the fit leaves Calo JES at about the original value and the δ uncertainty for Perugia JES is just above one, i.e. again the expected values are found.

In summary, one can conclude that no underestimation of uncertainties is found to take place using the profile likelihood method. The use of too many nuisance parameters for a single uncertainty component to describe additional but small correlations has no effect on the overall fit result. Systematic miscalibrations and linear dependencies of the jet energy scale are reflected in the fit result and in each case covered by the extracted uncertainties. No overconstraining of nuisance parameters is found.

8.4. Discussion of results

Having performed the cross section measurement as described above, the result cannot only be used for comparison with other measurements and theory predictions as done below, but also allows for combination with other analysis channels to gain higher precision. Furthermore, the tools and methodology developed open the door for related measurements such as an indirect top quark mass measurement.

8.4.1. Lepton + jets cross section measurement

Using a profile likelihood method adding externally in pseudo experiments evaluated uncertainties the $t\bar{t}$ production cross section is measured in the lepton + jets channel based on kinematic variables and b -tagging information to

$$\sigma_{t\bar{t}} = 187 \pm 11 \text{ (stat.) } {}_{-17}^{+18} \text{ (syst.) } \pm 6 \text{ (lumi.) pb} = 187 {}_{-21}^{+22} \text{ pb}, \quad (8.4)$$

in a data set of $\mathcal{L} = 35 \text{ pb}^{-1}$ recorded with the ATLAS experiment in proton-proton collisions at a centre-of-mass energy of $\sqrt{s} = 7 \text{ TeV}$. The measurement is performed in events with 3, 4 and ≥ 5 jets assuming a top quark mass of $m_t = 172.5 \text{ GeV}$. The total uncertainty amounts to 11.7% which makes this result the most precise measurement

8. Cross section measurement using b -tagging

of the top quark pair cross section in 2010 LHC data. It is limited by the systematic uncertainties, where the dominant ones are found to be related to the $t\bar{t}$ signal modelling. The result is in agreement with theory predictions discussed in Sec. 2.2.4.

Further measurements of the top quark pair production cross section with the ATLAS experiment that also exploit b -tagging information are presented in Reference [265] together with the preliminary version of the result shown here. Measurements without the use of b -tagging have also been performed [267]. They are all found to be in agreement with each other. The second-most precise result using 2010 LHC data is provided by the CMS Collaboration also using a profile likelihood method. It exploits events that contain at least one b -tagged jet using the secondary vertex mass (see ATLAS definition in Sec. 4.5.1) as discriminant [268]. The analysis extends down to events containing at least one jet allowing to measure the heavy flavour content in the $W + \text{jets}$ background.

8.4.2. Combination of cross section measurements

In order to gain even more precision the top quark production measurements in the different channels can be combined. The preliminary version of the 2010 lepton + jets result [265] presented in this work yielding

$$\sigma_{t\bar{t}} = 186 \pm 10 \text{ (stat.) } {}_{-20}^{+21} \text{ (syst.) } \pm 6 \text{ (lumi.) pb} = 186 {}_{-23}^{+24} \text{ pb}, \quad (8.5)$$

has been combined with the corresponding analysis in the dilepton channel [269] and later also with the dilepton channel measurement using 0.7 fb^{-1} of 2011 data [270]. The dilepton analyses are based on a simple cut-and-count method split into three channels using events with at least two jets and either exactly two electrons, two muons or one each. No b -tagging requirement is employed. While the data samples of each channel are orthogonal, many of the systematic uncertainties are correlated and can therefore be combined in a profile likelihood fit.

Thus, for the combination of the three dilepton channel results a likelihood function is employed in which the systematic uncertainties are implemented as nuisance parameters. The likelihood is a product of the Poisson term for the number of observed events in each channel, the luminosity uncertainty and several Gaussian constraint terms for the nuisance parameters. Constraint terms on common uncertainties are only included once and linear interpolation between the nominal and the $\pm 1\sigma$ variations is used.

To combine the lepton + jets channel results with the dilepton channel ones the likelihood function in the lepton + jets channel is approximated with a multivariate Gaussian since the implementation of the full likelihood was not possible in the combination framework. The covariance matrix is obtained from the Hessian matrix of the negative log-likelihood function evaluated at the best fit point. The dimension of the Gaussian corresponds to the parameter of interest, $\sigma_{t\bar{t}}$, and the number nuisance parameters. As shown above in Fig. 8.13 the likelihood is very symmetric and parabolic and further tests have been performed that the approximation yields the same result in profiling.

Fitting this combined model to the observed 2010 data results in a top quark pair

production cross section of [269]

$$\sigma_{t\bar{t}} = 180 \pm 9 \text{ (stat.)} \pm 15 \text{ (syst.)} \pm 6 \text{ (lumi.) pb} = 180 \pm 18 \text{ pb.} \quad (8.6)$$

The combination is dominated by the more precise lepton + jets measurement which therefore also holds true for connected uncertainties. The largest uncertainties are the heavy flavour content in the W + jets background, b -tagging calibration, ISR/FSR modelling and jet energy scale. The measurement has a precision of 10%.

For the combination of the 2011 dilepton measurement with the 2010 lepton + jets result the same technique is chosen. The integrated luminosity measurements are assumed to be a common source of systematic uncertainty. The combined top quark pair production cross section is determined to [271]

$$\sigma_{t\bar{t}} = 176 \pm 5 \text{ (stat.)} \pm_{-10}^{+13} \text{ (syst.)} \pm 7 \text{ (lumi.) pb} = 176 \pm_{-13}^{+16} \text{ pb.} \quad (8.7)$$

The uncertainty is reduced to 9.1% with the same dominating uncertainties with addition of the fake lepton background in the dilepton channel.

8.4.3. Indirect top quark mass determination

The measurement of the top quark pole mass, m_t , from the $t\bar{t}$ cross section provides complementary information to direct methods that usually rely explicitly on the details of the kinematic mass reconstruction. Since m_t directly enters the calculation of the top quark pair cross section as shown in Sec. 2.2.4 a measurement of the top quark cross section in dependence on m_t as implemented in the Monte Carlo generator allows for a mass extraction by comparing to theoretical predictions.

To obtain a parametrisation of the experimentally determined cross section as a function of m_t the cross section measurement is repeated replacing the nominal $t\bar{t}$ and single top Monte Carlo samples with samples that have been generated with m_t ranging from 140 GeV to 210 GeV in 10 GeV steps. It is assumed that the systematic uncertainties are independent of m_t so that only the statistical uncertainty is determined. This assumption is confirmed by determining full uncertainties at the extreme mass points of 140 and 210 GeV and using only these two points and the nominal one to determine the top quark mass as described below. The difference between this extraction and the extraction using all mass points is quoted as a systematic uncertainty. As parametrisation of the experimental result the fit to the data points uses a third order polynomial. The cross section values obtained from the likelihood fit are summarised in Tab. 8.6.

The top quark pair cross section predictions of References [87, 89, 90] are used in this study parametrised as:

$$\sigma_{t\bar{t}}(m_t) = \left(\frac{1}{m_t}\right)^4 (a + b(m_t - 170) + c(m_t - 170)^2 + d(m_t - 170)^3) \text{ pb,} \quad (8.8)$$

where m_t is given in GeV. In Fig. 8.17a the parametrisations for the theoretical predictions and the experimental points are shown as a function of m_t . To extract the

8. Cross section measurement using b -tagging

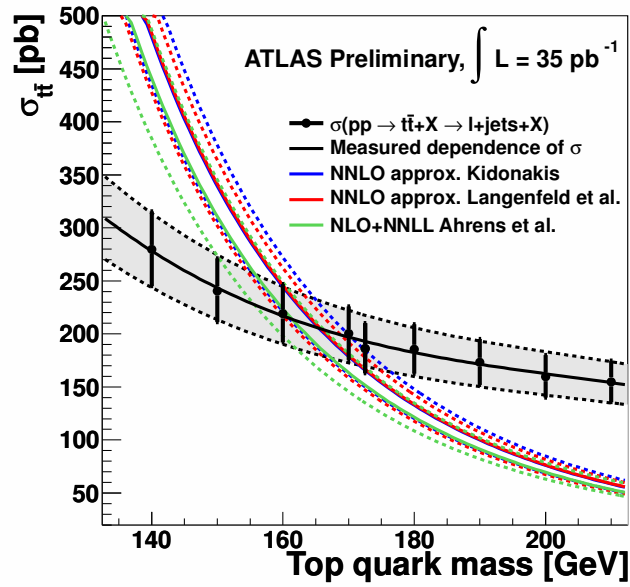
Table 8.6.: *Top quark pair cross section dependence on m_t with statistical uncertainties.*

m_t [GeV]	$\sigma_{t\bar{t}}$ [pb]	m_t [GeV]	$\sigma_{t\bar{t}}$ [pb]
140.0	$279.6^{+14.5}_{-14.2}$	180.0	$185.5^{+9.5}_{-9.3}$
150.0	$240.7^{+11.8}_{-11.5}$	190.0	$173.2^{+8.9}_{-8.7}$
160.0	$219.0^{+11.1}_{-10.9}$	200.0	$159.7^{+8.2}_{-8.1}$
170.0	$200.4^{+10.2}_{-10.0}$	210.0	$154.9^{+8.0}_{-7.8}$
172.5	$186.3^{+9.9}_{-9.7}$		

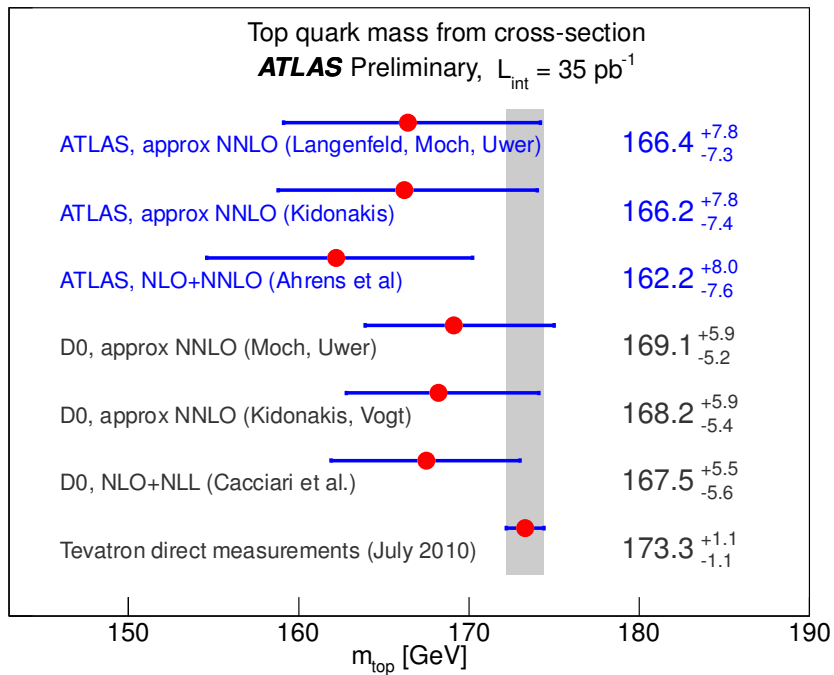
top quark mass a likelihood approach is chosen consisting of the theoretical and the experimental probability density distributions each constructed from Gaussian likelihood functions with width of the associated uncertainties. The top quark pole mass using the theoretical prediction given in Reference [87] is determined to

$$m_t = 166.4^{+7.8}_{-7.3} \text{ GeV}. \quad (8.9)$$

The result includes an uncertainty of 0.4 GeV due to the identification of the top quark pole mass with the top quark mass used in the generator that has been determined by shifting the top quark generator mass by ± 1 GeV [272]. This measurement has been published as a preliminary conference result in Reference [273]. The extracted mass is compared to the values obtained using the other theoretical predictions mentioned above and also the values obtained by the D0 Collaboration [274]. The CMS Collaboration also published a result based on a $t\bar{t}$ cross section measurement in the dilepton channel using a data set of 1.1 fb^{-1} yielding $m_t = 170.3^{+7.3}_{-6.6}$ GeV [275]. It can be seen in Fig. 8.17b that m_t determined with the method described here shows a tendency towards smaller values than found in direct top quark mass measurements, but are compatible with the Tevatron top quark mass average of 173.2 ± 0.9 GeV [62] and also the combination of the LHC results of 173.3 ± 1.4 GeV [276]. Further discussion can be found in Ref. [277].



(a)



(b)

Figure 8.17.: Top quark mass extraction from top quark pair cross section: (a) Measured dependence of the cross section on the top quark mass and dependence on theoretical predictions, and (b) comparison of different results in comparison to direct Tevatron top quark mass measurements. [273]

9. Cross section measurement using kinematic information only

The top quark pair production cross section measurement using kinematic information only in the lepton + jets channel analyses 0.7 fb^{-1} of 2011 collision data. This analysis is based on the 2010 measurement described in the previous Chapter 8 aiming to eliminate the limitations of the preceding result. It has been published as a preliminary conference result [278]. In this chapter first the results of the event selection are shown in Sec. 9.1. Differences with respect to the other analyses presented in this work are detailed. The cross section extraction can be found in Sec. 9.2 with a brief review of the stability tests in Sec. 9.3 and subsequent discussion and extension of the result in Sec. 9.4.

9.1. Results of event selection and multivariate signal and background separation

The event selection can be found in Chapter 6. It is based on requiring at least three jets, exactly one lepton and applying additional cuts on E_T^{miss} and m_T^W . The event yields after selection including the dominant uncertainties on the predictions are shown in Fig. 9.1 and Tabs. 9.1 and 9.2. The uncertainties are from jet energy scale uncertainties, theoretical uncertainties, uncertainty on the luminosity and the limited MC statistics. For the signal the uncertainty on ISR/FSR modelling is contained as well. Good agreement between the expected and observed yields is found.

9. Cross section measurement using kinematic information only

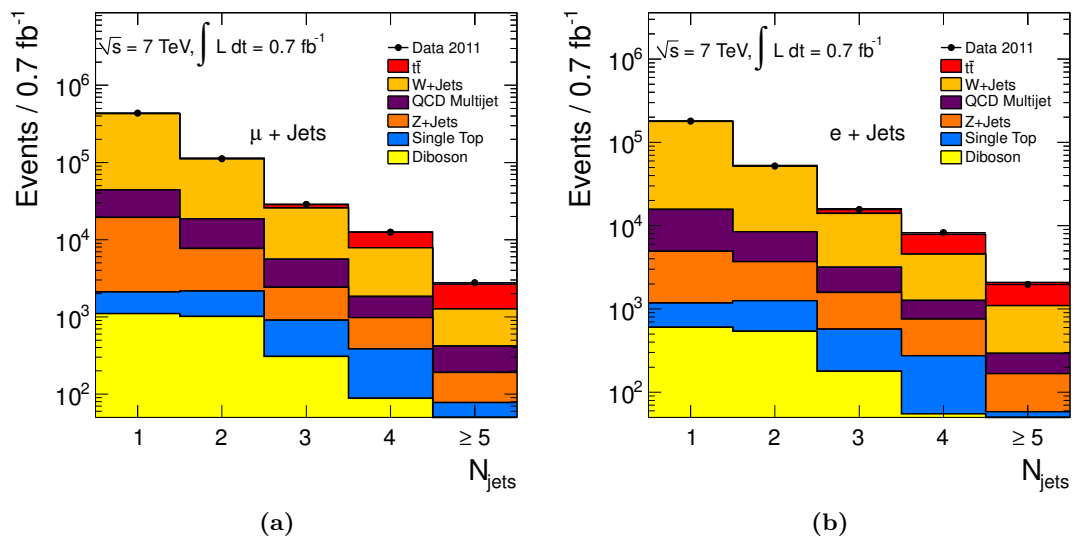


Figure 9.1.: Observed and expected event yields for the 2011 analysis (a) in the $\mu + \text{jets}$ and (b) $e + \text{jets}$ channel. [248]

9.1. Results of event selection and multivariate signal and background separation

Table 9.1.: Selected events in the μ +jets channel for a given jet multiplicity. Uncertainties shown take into account dominant uncertainties as described in the text. The W + jets and QCD multi-jet production background normalisation is obtained from data-driven methods described in Chapter 6.

	1 jet	2 jets	3 jets	4 jets	≥ 5 jets
$t\bar{t}$	320 ± 70	1340 ± 340	2700 ± 500	2710 ± 390	2030 ± 520
W + jets	380000 ± 120000	93000 ± 43000	20000 ± 12000	4600 ± 3200	1100 ± 900
Fakes (QCD multi-jet)	25000 ± 12000	11000 ± 5500	3200 ± 1600	900 ± 400	290 ± 150
Single top	1000 ± 250	1100 ± 500	590 ± 150	210 ± 70	84 ± 34
Z + jets	17000 ± 6000	5500 ± 2600	1500 ± 900	440 ± 300	150 ± 120
Diboson (WW, WZ, ZZ)	1100 ± 130	1000 ± 110	310 ± 60	69 ± 21	18 ± 9
signal/background ratio	0.0007	0.01	0.11	0.44	1.25
Total predicted	430000 ± 120000	110000 ± 40000	28000 ± 12000	9000 ± 4000	3700 ± 1300
Data observed	433931	111741	28643	8680	3814

Table 9.2.: Selected events in the e +jets channel for a given jet multiplicity. Uncertainties shown take into account dominant uncertainties as described in the text. The W + jets and QCD multi-jet production background normalisation is obtained from data-driven methods described in Chapter 6.

	1 jet	2 jets	3 jets	4 jets	≥ 5 jets
$t\bar{t}$	230 ± 60	1010 ± 250	1930 ± 330	1840 ± 280	1460 ± 470
W + jets	162000 ± 53000	43000 ± 20000	11000 ± 6000	2500 ± 1700	1030 ± 840
Fakes (QCD multi-jet, γ + jets)	11000 ± 5000	4800 ± 2400	1600 ± 800	510 ± 250	180 ± 90
Single top	570 ± 140	710 ± 170	390 ± 110	160 ± 50	65 ± 26
Z + jets	3700 ± 1500	2400 ± 1300	1000 ± 640	330 ± 230	150 ± 130
Diboson (WW, WZ, ZZ)	600 ± 70	540 ± 140	180 ± 40	45 ± 16	10 ± 6
signal/background ratio	0.001	0.02	0.14	0.52	1.02
Total predicted	180000 ± 50000	53000 ± 21000	16000 ± 7000	5400 ± 2000	2900 ± 1200
Data observed	179469	51820	15614	5398	2812

As the 2010 analysis described in the previous chapter the 2011 analysis (a) employs the input variables lepton η , a transformed form of aplanarity, $\exp(-8 \times \mathcal{A})$, and $\exp(-4 \times H_{T,3p})$. However, instead of using b -tagging information the transverse momentum of the jet with highest transverse momentum is used. The reason for this choice is manifold: The b -tagging related uncertainties and the W + heavy flavour fraction uncertainty were shown to be among the dominant uncertainties of the 2010 analysis and even though b -tagging is a powerful tool to reject W + jets background the connected uncertainties diminish the gain in separation power. Furthermore, due to the higher statistics more calibration points for the b -tagging weight distribution would be needed to allow for better data-MC agreement which were not available at the time of the analysis. Another important reason for the new variable choice is that the variables for the 2010 analysis were chosen to be largely insensitive to variations of the jet energy scale. Therefore, the comparably large related uncertainties could only be constrained by fitting in three jet bins per channel simultaneously. Adding the leading jet p_T gains additional sensitivity of the profile likelihood method to the jet energy scale variations promising a further reduction of uncertainties. The separation power against $t\bar{t}$ production is shown in Fig. 7.5 in Chapter 7 where in particular in the lepton + 3 and 4 jets channels separation is clearly visible.

Data-Monte Carlo comparisons of the four input variables are shown in Figs. 9.2 to 9.5. Generally, good agreement is found. For the leading jet p_T distribution some modelling issues at low p_T can be observed, but the exponentially falling tail is well described. In events with five and more jets some smaller discrepancies can be seen, which are, however, also due to the lower statistics.

The leading jet p_T together with the other three variables is combined into a projective likelihood discriminant as described in Sec. 7.1.1. Since no heavy flavour sensitive variables are used, the W + heavy flavour samples which have rather low statistics are not used in the training process, but included in the evaluation. The data-MC comparison for the likelihood discriminant before the fit for all channels is shown in Fig. 9.6 already giving good agreement.

9.2. Cross section extraction

As for the 2010 analysis, the $t\bar{t}$ cross section is extracted using the profile likelihood method described in Sec. 7.3.2. Only systematic uncertainties that are expected or shown to be continuous are included in the fit as nuisance parameters while the non-continuous uncertainties are evaluated using pseudo experiments (see Sec. 7.4).

9.2.1. Expected uncertainties

With the method described in Sec. 7.4 the expected combined statistical and systematic uncertainties are estimated in pseudo experiments. Some of the systematic uncertainties are treated differently with respect to the 2010 analysis as discussed in Sec. 7.5.

Including all nuisance parameters the expected combined statistical and systematic uncertainty amounts to 3.6% taken from the Gaussian fit shown in Fig. 9.7. The pull

9. Cross section measurement using kinematic information only

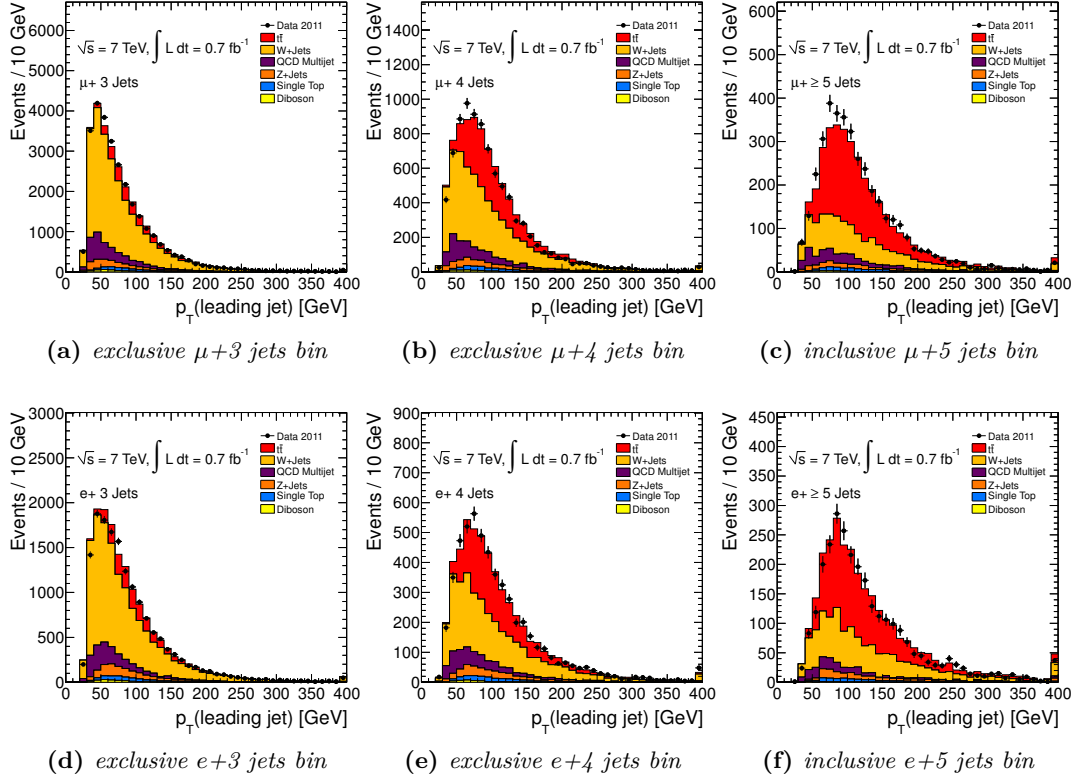


Figure 9.2.: *Transverse momentum of the leading jet in data and Monte Carlo simulated events in the signal regions.*

distribution has a width slightly smaller than 1 which can be fixed by removing the extrapolation cut-off at 1.25 on the nuisance parameters as discussed in Sec. 8.2.1. Adding the additional systematic uncertainties evaluated externally in quadrature to the uncertainty from the fit yields (+5.5/−5.4)%. The statistical uncertainty is found to be 2.4% performing the fit without nuisance parameters. Subtracting this number from the total uncertainty in quadrature an expected total systematic uncertainty of 5.2% from the fit without luminosity uncertainty is obtained.

The linearity of the fit is evaluated in pseudo experiments as detailed in Secs. 7.4 and 8.2.1 by scaling the $t\bar{t}$ template to nine cross section values between 120 pb and 200 pb while keeping all background samples at their nominal value. Each of the resulting β_0 distributions is fit with a Gaussian to extract mean and standard deviations and a linear least squares fit of the mean as a function of the input cross section is performed where the uncertainty used at each input cross section is the standard deviation divided by the square root of the number of pseudo experiments. The fit presented in Fig. 9.8a shows good linearity over the full range. The small offset is not corrected for. The uncertainty returned by the fit is compared against the uncertainty from pseudo experiments using the pull distributions. These are obtained by subtracting the fit value from the input

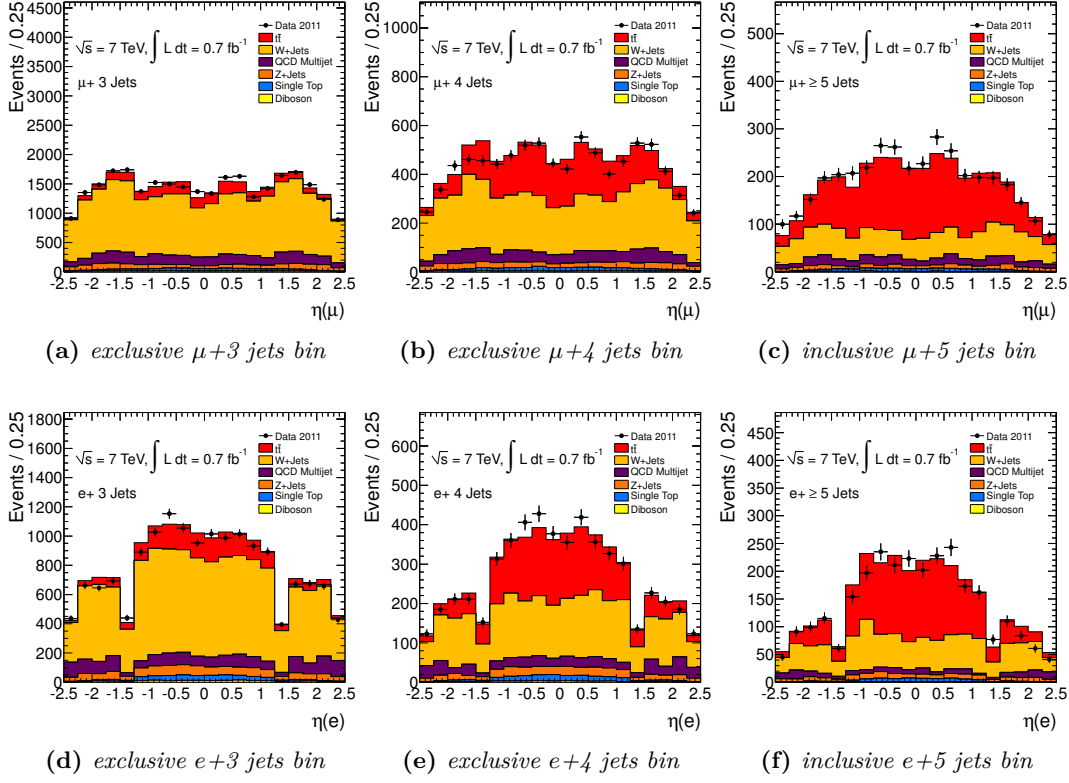


Figure 9.3.: Lepton pseudorapidity in data and Monte Carlo simulated events in the signal regions.

value and dividing by the Hessian error returned by the fit. All pulls shown in Fig. 9.8b are close to one, but slightly smaller due to the 1.25σ extrapolation cut off discussed above.

9.2.2. Fit results

The minimum log-likelihood fit including all continuous systematic uncertainties of discriminant \mathcal{D} to data in all six analysis channels yields a $t\bar{t}$ production cross section of

$$\sigma_{t\bar{t}} = 187.5^{+7.0}_{-6.9} \text{ pb.} \quad (9.1)$$

The fit result is shown in Fig. 9.9. The χ^2 and Kolmogorov-Smirnov tests of the compatibility of the fitted sum of signal and background templates with data show excellent agreement. Individual fit values of all processes and nuisance parameters can be found in Tab. 9.3. As before, initial values for the physics processes are $\beta_i = 1$ with their uncertainties implemented as Gaussian constraints whereas for the nuisance parameters $\delta_i = 0 \pm 1$ is used. If the uncertainty on the nuisance parameter after fitting is found to be less than 1 the fit is able to constrain the uncertainty using data. Otherwise, the

9. Cross section measurement using kinematic information only

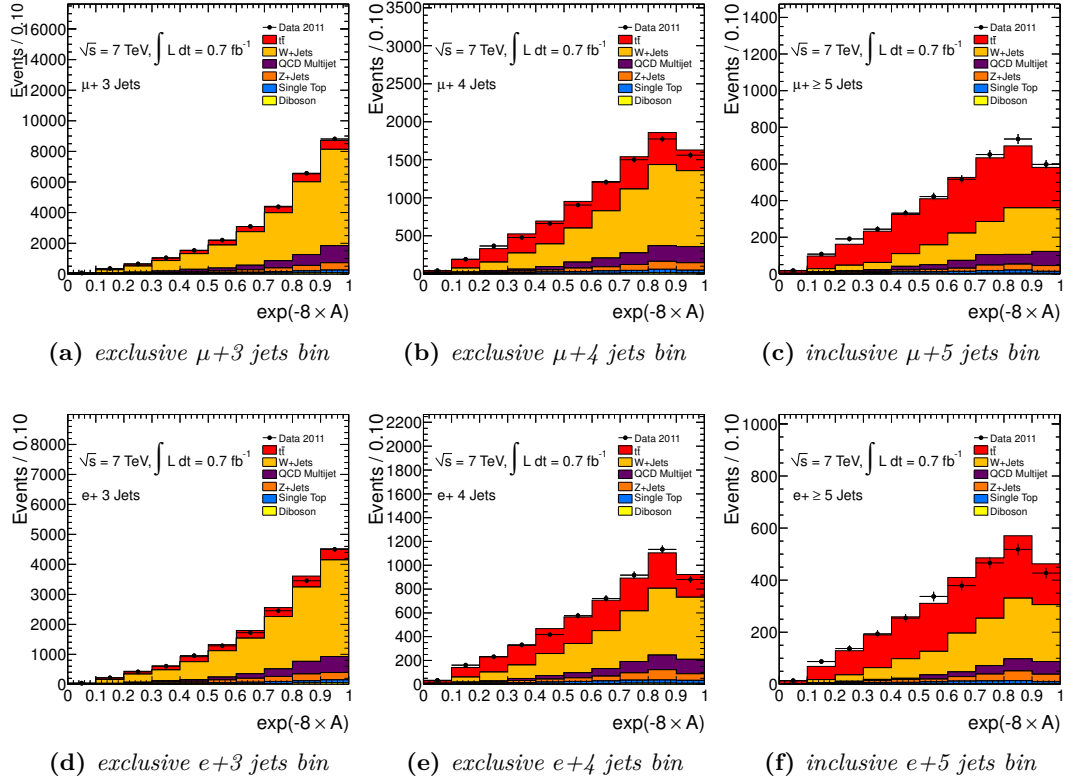


Figure 9.4.: Transformed version of event aplanarity for data and Monte Carlo simulated in the signal regions.

expected systematic uncertainty is either reflected in data or no sensitivity exists. An uncertainty larger than one as for the muon energy scaling indicates that this parameter contributes more strongly to the total uncertainty than initially expected. Since this uncertainty is comparably small and the uncertainty on the nuisance parameter just above one no underestimation of uncertainties is expected.

As can be seen in Tab. 9.3 the fit is able to constrain most jet energy scale related uncertainties to values significantly smaller than 1. This is expected and intended by the addition of the leading jet p_T variable to the the likelihood discriminant which gives strong sensitivity of the fit to the jet energy scale. Furthermore, with the exception of jet energy resolution all jet related nuisance parameters can be constrained. In contrast to that the fit is hardly able to constrain the lepton kinematic related uncertainties as these uncertainties are mostly well reflected in data.

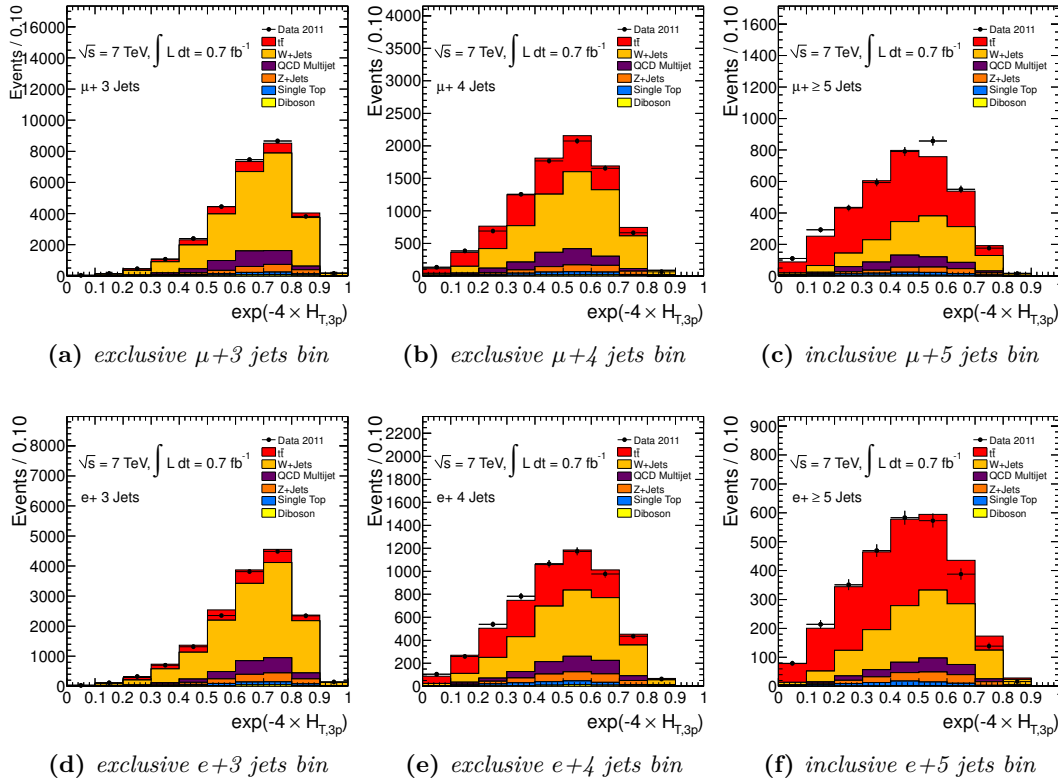


Figure 9.5.: Variable $H_{T,3p}$ in its transformed form for data and Monte Carlo simulated events in the signal regions.

Table 9.3.: Resulting fit parameters and uncertainties from the fit in all six analysis channels to 0.7 fb^{-1} of data. The first error value is the symmetric Hessian uncertainty from the second derivative of the log-likelihood function, the second and third are the asymmetric MINOS errors from scanning the likelihood function around the minimum.

Parameter	Value	Hessian error	Error up	Error down
$\beta(tt)$	1.0875	0.0432	0.0427	-0.0421
$\beta(W \rightarrow \mu + 3 \text{ jets})$	0.9738	0.0687	0.0710	-0.0684
$\beta(W \rightarrow \mu + 4 \text{ jets})$	0.8649	0.1026	0.1083	-0.1061
$\beta(W \rightarrow \mu + 5 \text{ jets})$	0.9114	0.1557	0.1589	-0.1510
$\beta(W \rightarrow e + 3 \text{ jets})$	1.0510	0.0555	0.0597	-0.0588
$\beta(W \rightarrow e + 4 \text{ jets})$	1.0376	0.0987	0.1057	-0.1025
$\beta(W \rightarrow e + 5 \text{ jets})$	0.8296	0.1206	0.1267	-0.1257
$\beta(Z + \text{ jets})$	0.9572	0.2604	0.2745	-0.2728

continued on next page

9. Cross section measurement using kinematic information only

Table 9.3.: Resulting fit parameters and uncertainties from the fit in all six analysis channels to 0.7 fb^{-1} of data. The first error value is the symmetric Hessian uncertainty from the second derivative of the log-likelihood function, the second and third are the asymmetric MINOS errors from scanning the likelihood function around the minimum.

Parameter	Value	Hessian error	Error up	Error down
$\beta(\text{Single top})$	1.0052	0.1066	0.1069	-0.1065
$\beta(\text{Diboson})$	1.0037	0.0620	0.0620	-0.0620
$\beta(\text{QCD in } \mu + 3 \text{ jets})$	1.2376	0.2928	0.3307	-0.3426
$\beta(\text{QCD in } \mu + 4 \text{ jets})$	1.2720	0.3730	0.4234	-0.4152
$\beta(\text{QCD in } \mu + 5 \text{ jets})$	0.8291	0.3861	0.4044	-0.4095
$\beta(\text{QCD in } e + 3 \text{ jets})$	0.6113	0.2157	0.2286	-0.2339
$\beta(\text{QCD in } e + 4 \text{ jets})$	0.6152	0.3195	0.3406	-0.3462
$\beta(\text{QCD in } e + 5 \text{ jets})$	0.4164	0.3984	0.4221	-0.4170
$\delta(\text{AlpgenJES})$	0.4155	0.4143	0.2725	-0.4030
$\delta(\text{bJES})$	0.0964	0.6818	0.5956	-0.6241
$\delta(\text{CaloJES})$	0.0051	0.4264	0.3410	-0.3654
$\delta(\text{NoiseJES})$	-0.3515	0.3979	0.5469	-0.3047
$\delta(\text{PerugiaJES})$	-0.8653	0.1734	0.1824	-0.1397
$\delta(\text{EtaJES})$	-0.1943	0.2129	0.2166	-0.1978
$\delta(\text{PileupJES low } p_T/\text{central})$	0.5219	0.1669	0.1539	-0.1633
$\delta(\text{PileupJES low } p_T/\text{forward})$	0.4685	0.2566	0.2361	-0.2791
$\delta(\text{PileupJES high } p_T/\text{central})$	0.6366	0.4684	0.3133	-0.4291
$\delta(\text{PileupJES high } p_T/\text{forward})$	0.0430	0.9105	0.6602	-0.6345
$\delta(\text{Jet reconstruction efficiency})$	0.1998	0.1357	0.1345	-0.1344
$\delta(\text{Jet energy resolution})$	0.1752	0.9544	0.9510	-0.9565
$\delta(\text{FSR})$	0.0661	0.2086	0.1897	-0.2239
$\delta(\text{ISR})$	0.3392	0.1978	0.1801	-0.2263
$\delta(\mu \text{ SFs})$	0.0923	0.8187	0.7793	-0.7362
$\delta(\mu \text{ momentum smearing at MS})$	-0.1197	0.8364	0.7873	-0.8234
$\delta(\mu \text{ momentum smearing at ID})$	-0.2356	0.9337	0.9757	-0.8533
$\delta(\mu \text{ energy scale})$	0.0437	1.0838	1.0485	-0.9946
$\delta(e \text{ SFs})$	-0.2300	0.9290	0.9152	-0.8999
$\delta(e \text{ resolution smearing})$	0.3176	0.7668	0.6538	-0.7566
$\delta(e \text{ energy scale})$	-0.7455	0.5967	0.7997	-0.5331
$\delta(E_T^{\text{miss}} \text{ LAr})$	0.0605	0.5062	0.5167	-0.5230
$\delta(E_T^{\text{miss}} \text{ SoftJet})$	0.4466	0.4641	0.3333	-0.6785

Considering the linear correlation matrix between the individual fit parameters shown in Fig. 9.10 one can observe strong correlations between some of the fit parameters, which are in particular stronger than in the 2010 analysis as shown in Sec. 8.2.2. The $W + \text{jets}$ processes show a positive correlation of about 50% within the same lepton

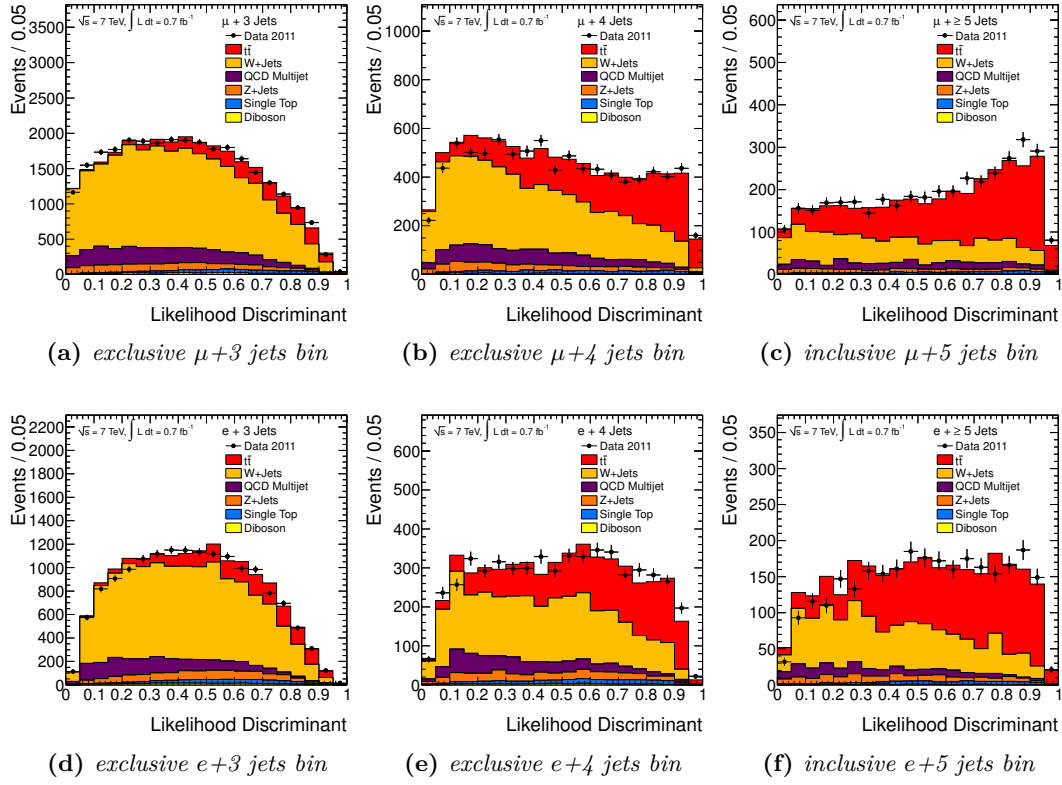


Figure 9.6.: Comparison of the likelihood discriminant \mathcal{D} in data and Monte Carlo simulated events for all fit channels.

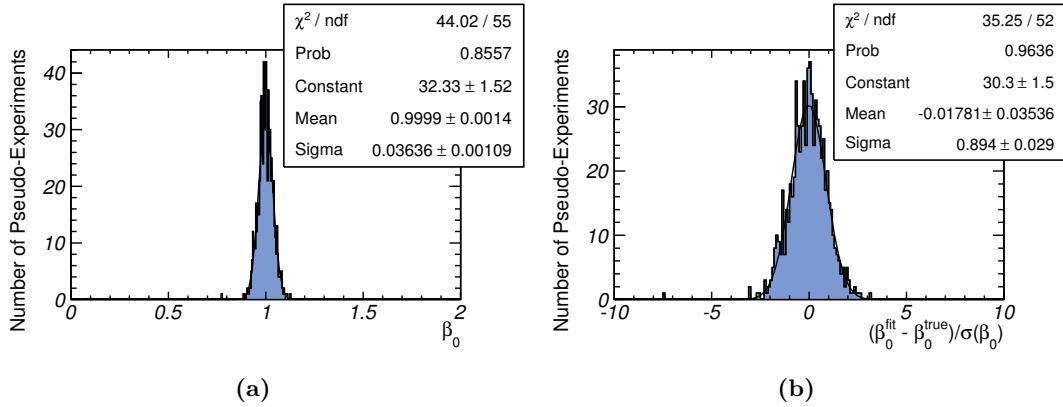


Figure 9.7.: Distribution of (a) fitted $t\bar{t}$ cross section parameter, β_0 , and (b) its pull using 1,000 pseudo experiments. Systematic uncertainties treated outside the fit are not considered here.

9. Cross section measurement using kinematic information only

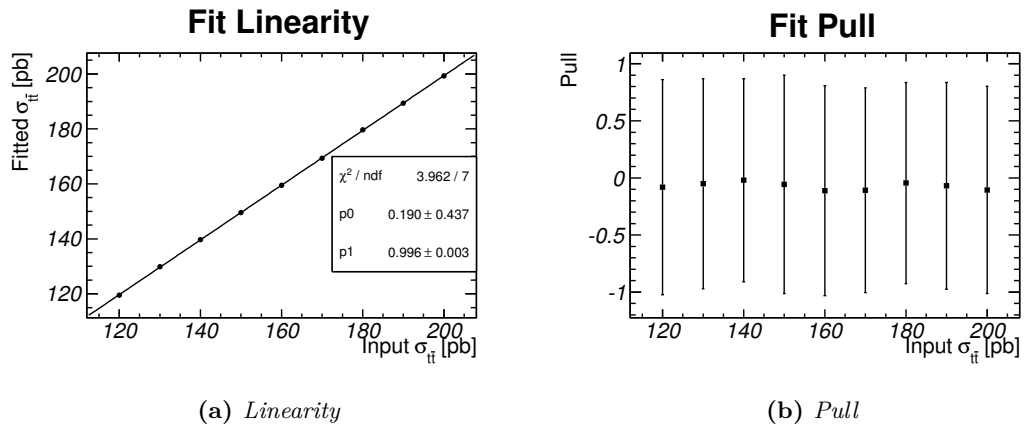


Figure 9.8.: (a) Linearity test and (b) pull distribution as a function of input $t\bar{t}$ cross section.

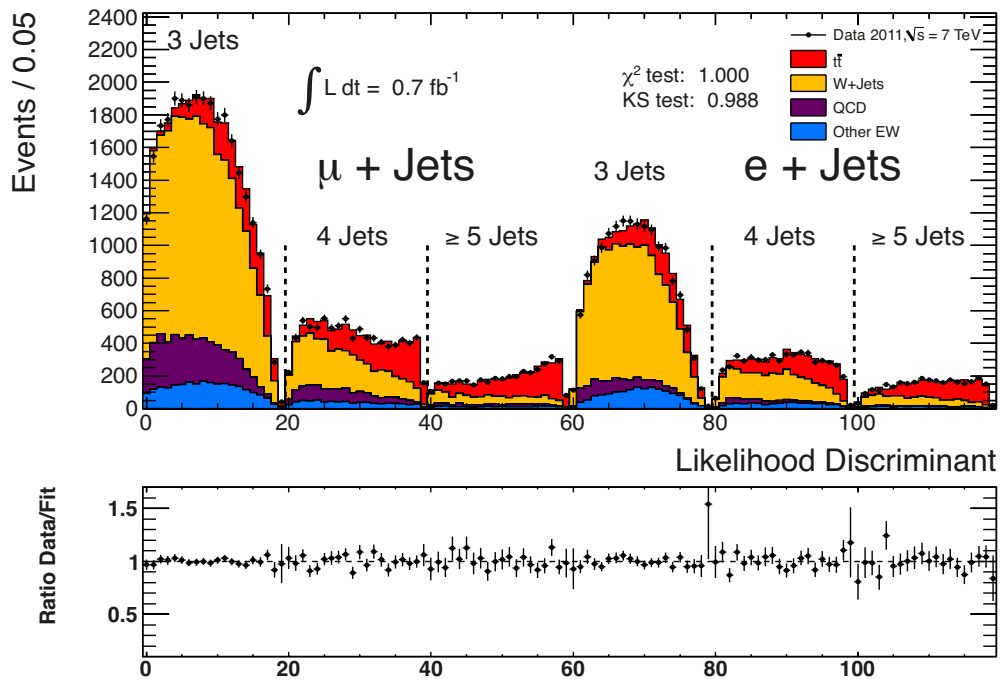


Figure 9.9.: Result of the combined profile likelihood fit in the six lepton + jets channels to data. Statistics tests of the compatibility of the fitted stack of templates with data are shown as well.

channel. This can be explained by $W + \text{jets}$ being the dominant background: Since the $t\bar{t}$ signal is fitted as a single parameter over all jet bins and the $W + \text{jets}$ normalisation has been obtained from data, i.e. close to what the fit will return, any normalisation change to one of the $W + \text{jets}$ templates will affect the other two. One can furthermore observe a strong anti-correlation between the $W + \text{jets}$ and the QCD multi-jet templates in each fit channel. This is due to the very similar shape of both templates meaning that if a template is scaled up the other one will be scaled down replacing the former. Several jet energy scale related nuisance parameters show strong correlations or anti-correlations as expected since they affect the leading jet p_T distribution. Furthermore, high anti-correlation factors are found for the signal and the $W + \text{jets}$ templates and the muon scale factors. Unfortunately, the muon trigger efficiency scale factor uncertainty was found to be overestimated. Since this uncertainty mainly affects the overall normalisation and less the likelihood discriminant shape a shift of the scale factor affects the total number of events leading to a shift of the templates in the opposite direction. This scale factor is furthermore basically independent of the jet bin so that all $W + \text{jets}$ templates in the muon channel are affected. The normalisation of the nuisance parameter is, however, close to the initial value so that no bias is found. A similar but clearly smaller behaviour can be observed for the electron channel.

To evaluate the behaviour of the likelihood function around the minimum the one-dimensional profile likelihood, $\lambda(\beta_0)$, is obtained by minimising the likelihood with respect to all parameters in the profiling procedure (see Sec. 7.3.2). The result is shown in Fig. 9.11. Within $-\ln((\lambda(\beta_0^{\min})) \pm 0.5) = [1.0455, 1.1304]$, i.e. $\pm 1\sigma$, and also for a much larger range the likelihood is continuous and no jumps are observed. This confirms the stability of the fit and that the nuisance parameters included in the fit do not bias the result. The behaviour of each normalisation and nuisance parameter with respect to β_0 is shown in Appendix E. The values far away from the fitted β_0 have no effect on the actual preferred values of the parameters. They are mostly caused by cancellation effects between different parameters, i.e. one increasing while another is decreasing. The 1σ interval is minimally smaller than the uncertainty obtained from the fit.

Performing the fit separately in the muon and the electron + jets channels yields the results summarised in Tab. 9.4. Additionally results of the fit without nuisance parameters and comparison to the full fit is shown. In Fig. 9.12 the likelihood discriminant distributions for the single channel fits are shown. In both channels very good agreement is found, the $e + \text{jets}$ channel having less statistics due to the event selection.

9.2.3. Observed uncertainties

In Tab. 9.5 the observed uncertainties are summarised split into statistical and systematic uncertainties where the latter are partially evaluated inside the fit or in pseudo experiments. The size of uncertainties which are included in the fit is extracted by removing them from the fit one-by-one. The quadratic difference to the full fit is quoted as uncertainty as described in Sec. 7.4. Since some of the parameters are correlated with each other, which cannot be taken into account in this procedure, the quadratic sum is 0.5% larger than the one directly taken from the fit. The uncertainties that

9. Cross section measurement using kinematic information only

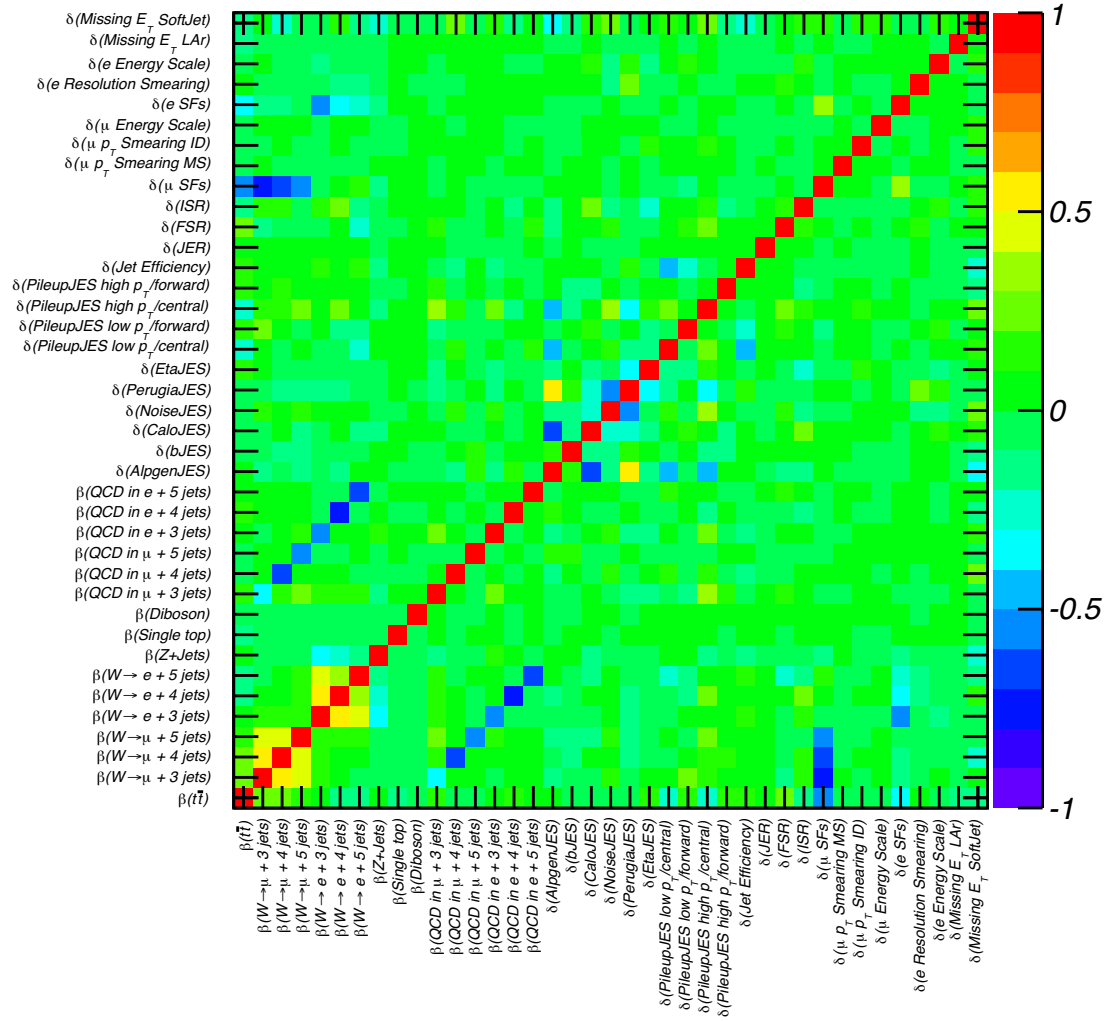


Figure 9.10.: Correlation matrix of the fit parameters β_i and δ_j as obtained from the fit in all six analysis channels. Shown are the linear correlation coefficients.

Table 9.4.: Cross section results for the $\mu + \text{jets}$ and $e + \text{jets}$ channel fits compared to the combined six channel result with statistical uncertainties only and the full fit. Only uncertainties included in the fit are taken into account here.

channel	statistical only [pb]	full fit [pb]
$e + \text{jets}$	$189.3^{+6.7}_{-6.6}$	$178.7^{+10.0}_{-9.6}$
$\mu + \text{jets}$	$186.9^{+5.1}_{-5.1}$	$183.7^{+9.8}_{-9.8}$
combined	$187.5^{+4.1}_{-4.1}$	$179.0^{+7.0}_{-6.9}$

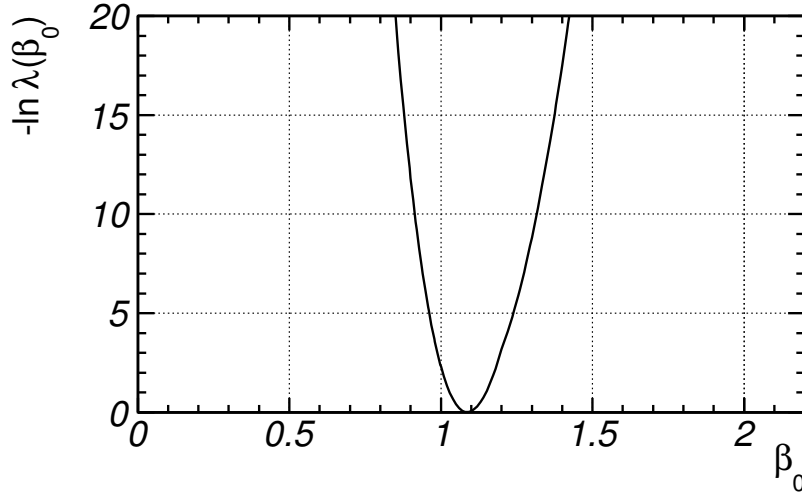


Figure 9.11.: *Negative log-likelihood value as function of β_0 , $-\ln(\lambda(\beta_0^{\min}))$, obtained from the profiling procedure in the fit.*

are evaluated externally add up to 3.8%. The observed statistical uncertainty of the fit amounts to 2.2% reflecting the expected one. The full fit uncertainty including all nuisance parameters yields 3.9% and is 0.3% higher than expected. A detailed listing of the size of each individual uncertainty component can be found in Appendix Sec. E.2.

The measurement is dominated by the signal generator modelling uncertainty which also has a large impact on the 2010 analysis. However, the ISR and FSR modelling uncertainty, which in contrast to the 2010 analysis is included in the fit can be constrained significantly even though it remains one of the largest ones. Of the other uncertainties treated as nuisance parameters the largest ones are the jet energy scale and for the reasons discussed above also the muon scale factors. Unfortunately, the available Monte Carlo statistics used for the analysis is limited reducing the precision of the measurement. Most of the uncertainties have a size comparable to the one found for the 2010 analysis.

9.3. Method and stability tests

The method and stability tests performed for the analysis are very similar to the 2010 analysis and are therefore not detailed. Additionally, it is investigated whether the fit is sensitive to shifts of nuisance parameters. In order to test this, pseudo experiments where a nuisance parameter is shifted to its $\pm 1\sigma$ value are performed. The fit returns the injected value in all cases confirming the sensitivity and therefore the ability to constrain nuisance parameters. Repeating the procedure with several simultaneously

9. Cross section measurement using kinematic information only

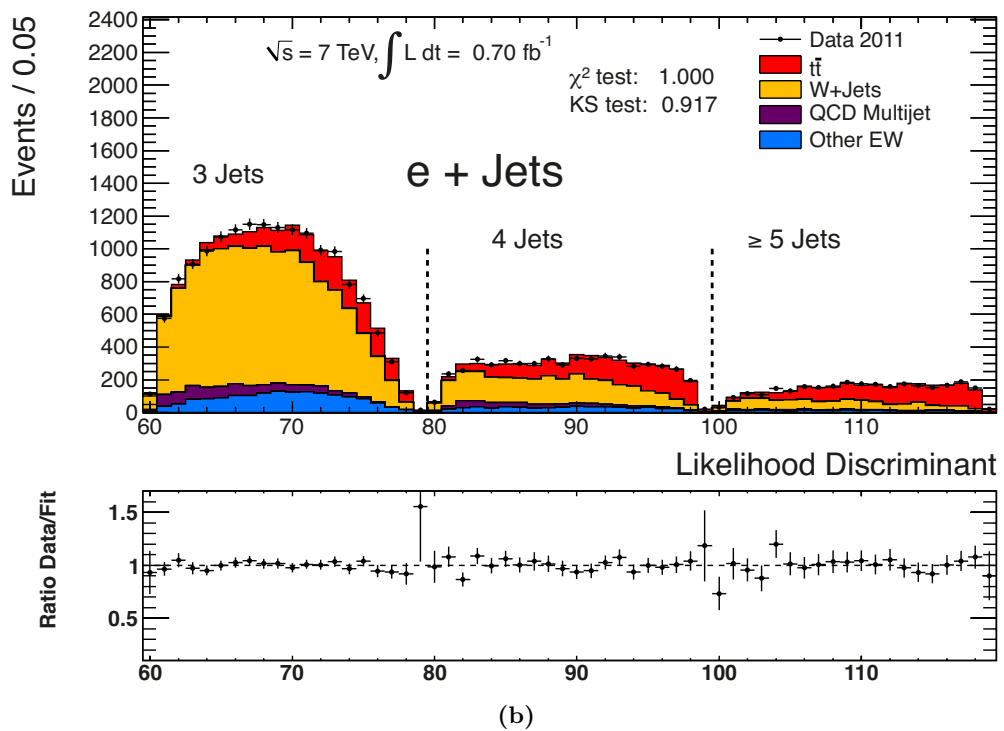
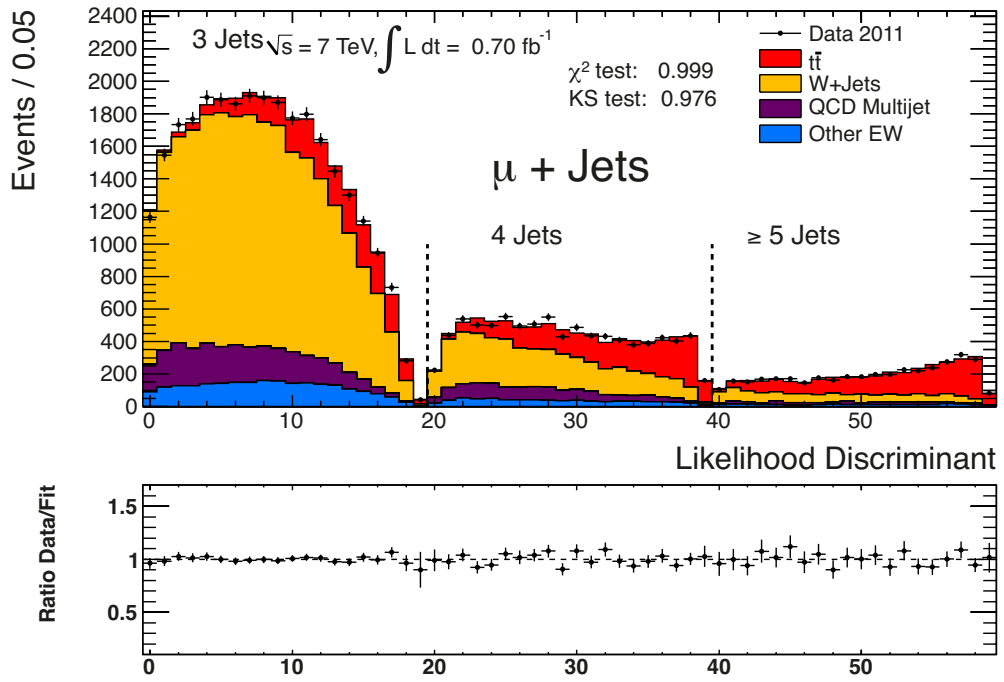


Figure 9.12.: Results for the cross section fit with all nuisance parameters included for (a) the $\mu + \text{jets}$, and (b) the $e + \text{jets}$ channel.

Table 9.5.: *Table of estimated uncertainties. For each systematic uncertainty included in the fit the quadratic difference between the relative uncertainties of the full fit and the fit without the systematic in question is quoted. The remaining systematic uncertainties are added in quadrature afterwards.*

Statistical uncertainty (%)	+2.19	-2.18
Objects selection (%)		
Jet energy scale	+1.57	-2.14
Jet reconstruction efficiency	+0.28	-0.72
Jet energy resolution	+0.87	-0.87
Muon scale factors	+1.81	-1.93
Muon smearing and scale	+1.01	-0.93
Muon momentum scale	+0.90	-0.82
Electron scale factors	+1.24	-1.37
Electron smearing	+0.43	-0.50
Electron energy scale	+0.76	-0.80
Missing transverse energy	+1.10	-0.93
Background modelling (%)		
W + jets shape ¹	+0.49	-0.49
QCD multi-jet shape ¹	+0.37	-0.37
Signal modelling (%)		
ISR/FSR	+1.68	-1.27
NLO generator ¹	+3.06	-3.06
Hadronisation ¹	+0.53	-0.53
PDF ¹	+1.01	-1.01
Others (%)		
MC template statistics ¹	+1.80	-1.80
Quadratic sum of systematic uncertainties (%)	+5.39	-5.54
Total systematic uncertainty (fit) (%)	+4.99	-4.95
Luminosity uncertainty (%)	+3.70	-3.70
Total uncertainty (%)	+6.59	-6.55

¹ evaluated outside the fit

9. Cross section measurement using kinematic information only

shifted nuisance parameters shows the same behaviour.

9.4. Discussion of results

9.4.1. Lepton + jets cross section measurement

The top quark pair cross section in the lepton + jets channel using 0.7 fb^{-1} of data recorded at $\sqrt{s} = 7 \text{ TeV}$ with the ATLAS experiment is measured to

$$\sigma_{t\bar{t}} = 179.0 \pm 4.1 \text{ (stat.)} \pm 8.8 \text{ (syst.)} \pm 6.6 \text{ (lumi.) pb} = 179.0_{-11.7}^{+11.8} \text{ pb}, \quad (9.2)$$

using a profile likelihood method and kinematic information only. To this result the luminosity uncertainty as well as the uncertainties that have been evaluated outside the fit have been added. This corresponds to a total uncertainty of only 6.6%, showing a clear improvement with regards to the 2010 analysis and making this measurement of $\sigma_{t\bar{t}}$ the most precise in the lepton + jets channel to date. The measurement is in agreement with theory predictions discussed in Sec. 2.2.4. The result is limited by the systematic uncertainties, where the dominant ones are found to be related to the $t\bar{t}$ signal modelling and initial and final state radiation. Furthermore, jet energy scale uncertainties and the lepton scale factors play an important role. Analysing a larger data set would not increase precision. However, more statistics usually helps to understand and constrain the uncertainties better. It also becomes more and more apparent that the different $t\bar{t}$ generators require more detailed studies. Furthermore, a coherent treatment of initial and final state radiation in NLO generators needs to be developed and the ISR/FSR settings themselves determined in data. The increased statistics of the LHC data set now allow for measurements of the differential top quark pair production cross section as a function of several variables (see e.g. [279]) and also measurement of the jet multiplicity in these events [280]. Another improvement of the analysis presented here is a fiducial cross section measurement described in the next Chapter 10.

9.4.2. Combination of cross section measurements

As described for the 2010 analysis in Sec. 8.4.2 precision of the measurement of the top quark-antiquark pair production cross section can be further improved by combining the lepton + jets measurement with measurements in other channels. The 2011 analysis (a) is therefore combined with the dilepton channel result described in Sec. 8.4.2 also using 0.7 fb^{-1} of 2011 data [270] and the first ATLAS measurement in the all-hadronic channel [281] in 1 fb^{-1} using a binned likelihood fit to the χ^2 distribution obtained from a kinematic fit assuming the $t\bar{t}$ hypothesis. The same global profile likelihood methodology as for the previous combinations is used, here assuming full correlation between 26 of the 88 uncertainties. The combination yields [282]

$$\sigma_{t\bar{t}} = 177 \pm 3 \text{ (stat.)} _{-7}^{+8} \text{ (syst.)} \pm 7 \text{ (lumi.) pb} = 177_{-10}^{+11} \text{ pb}, \quad (9.3)$$

resulting in a precision of 6%. The result is clearly dominated by the lepton + jets measurement due to its high precision. Dominant uncertainties are lepton identification and jet energy scale uncertainties as well signal modelling uncertainties related to the choice of the signal generator, ISR/FSR variations and PDF uncertainties.

Recently, this result has been combined with the CMS analyses into a LHC top quark pair production cross section measurement. Due to the different treatment of systematic uncertainties in the two experiments a likelihood approach proves difficult. Thus, an alternative technique called *Best Linear Unbiased Estimator (BLUE)* method [283, 284] is employed. The idea of this method is to determine a set of weights to arrive at a weighted sum of the input measurements which minimises the total uncertainty on the combined result. In this procedure statistical and systematic uncertainties and their correlations are taken into account. The ATLAS measurements [270, 278, 281] used for the combination are summarised above. Four CMS measurements are taken into account: a single lepton measurement using b -tagging [268], two measurements in the dilepton channel, where one uses electrons and muons [285] and the other one requiring $\mu\tau$ in the final state [286], and one in the all-hadronic channel [287]. The combination of the CMS results yields

$$\sigma_{t\bar{t}} = 165.8 \pm 2.2 \text{ (stat.)} \pm 10.6 \text{ (syst.)} \pm 7.8 \text{ (lumi.) pb}, \quad (9.4)$$

which corresponds to a total uncertainty of 8%. When combining the ATLAS result with the CMS one assumptions about the correlations between different uncertainties have to be made. These have carefully been checked by varying the correlation coefficients of dominant uncertainties between 0 and 1 and evaluating the effect on the final result. The LHC combination yields [288]

$$\sigma_{t\bar{t}} = 173.3 \pm 2.3 \text{ (stat.)} \pm 7.6 \text{ (syst.)} \pm 6.3 \text{ (lumi.) pb}. \quad (9.5)$$

The weighting of the individual results is such that the ATLAS result makes up two thirds of the measurement because of its smaller uncertainty. The total correlation between the ATLAS and CMS measurements is found to be 30%. The combined cross section has an uncertainty of 5.8% improving the ATLAS result slightly. Dominant uncertainty is the uncertainty on the luminosity determination followed by detector and signal modelling. The summary of all results used for the combination and the combination result itself in comparison with the theory prediction are shown in Fig. 9.13.

Only very recently the CMS Collaboration published another even more precise $t\bar{t}$ cross section measurement in the dilepton channel [289]. Analysing a data set of 2.3 fb^{-1} they determine the cross section to

$$\sigma_{t\bar{t}} = 161.9 \pm 2.5 \text{ (stat.)}^{+5.1}_{-5.0} \text{ (syst.)} \pm 3.6 \text{ (lumi.) pb}, \quad (9.6)$$

exploiting the distribution of the number of jets and b -tagged jets using a profile likelihood technique.

9. Cross section measurement using kinematic information only

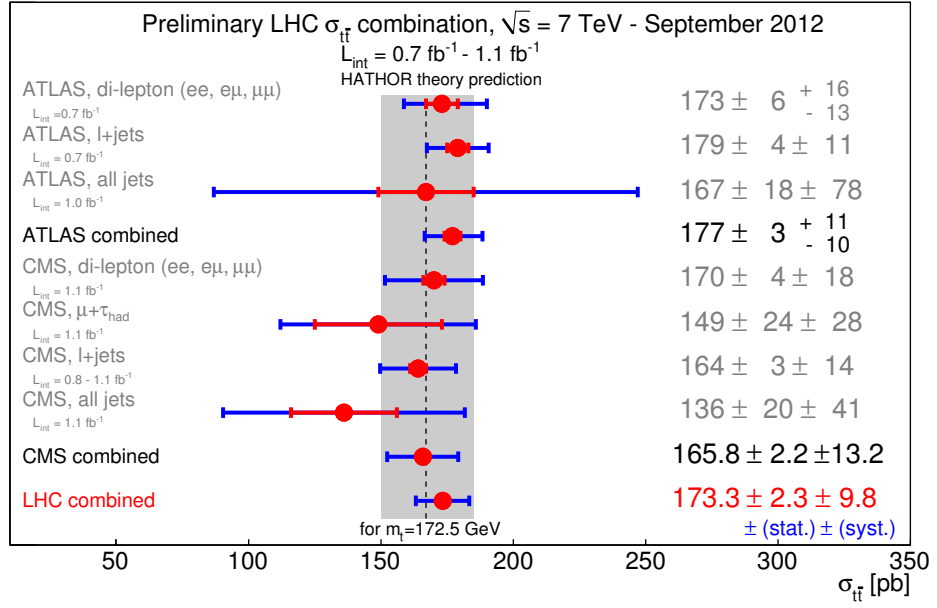


Figure 9.13.: Top quark pair cross section measurements at the ATLAS and CMS experiments and their combination in comparison to the theory value of $\sigma_{t\bar{t}} = 167^{+17}_{-18}$ pb obtained by HATHOR version 1.2. [94]. [288]

9.4.3. Parametrisation of the cross section as a function of the top quark mass

As discussed in Secs. 2.1.3.1 and 8.4.3 the $t\bar{t}$ cross section depends on the top quark mass. In order to make the measurement independent of the generator employed top quark mass the measurement is repeated with statistical uncertainties only in the mass range $140 \text{ GeV} \leq m_t \leq 210 \text{ GeV}$ in 10 GeV steps assuming that the systematic uncertainties are independent of the top quark mass as shown in Sec. 8.4.3. Both the single top and the $t\bar{t}$ samples are replaced accordingly. Around the nominal top quark mass of $m_t = 172.5$ GeV a linear behaviour is observed. Therefore, a linear fit is performed in the range $160 \text{ GeV} \leq m_t \leq 190 \text{ GeV}$ with only the statistical uncertainties considered. The difference between the statistical only and the full fit result is accounted for by shifting the linear fit result by the difference found at the nominal top quark mass. It yields:

$$\sigma_{t\bar{t}}(m_t [\text{GeV}]) = (411.9 - 1.35m_t) \text{ pb.} \quad (9.7)$$

The fit result is shown in Fig. 9.14. This result has been used by Ref. [91] to indirectly determine the top quark mass similarly as described in Sec. 8.4.3. They extract a top quark pole mass of

$$m_t = (169.8^{+4.9}_{-4.7}) \text{ GeV,} \quad (9.8)$$

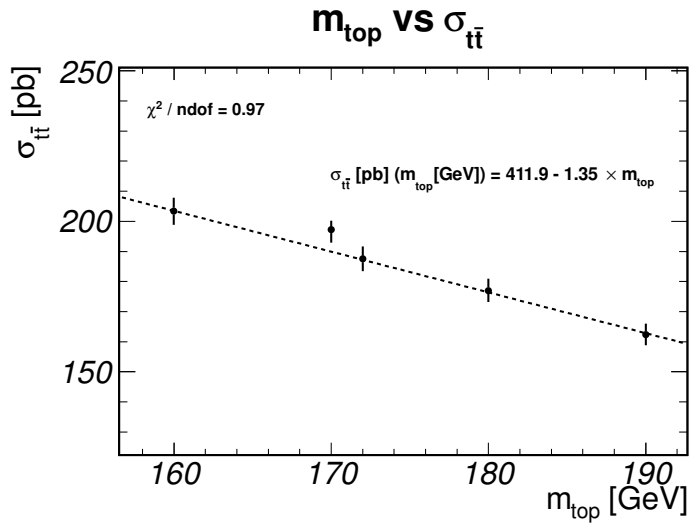


Figure 9.14.: *Dependence of the top quark cross section, $\sigma_{t\bar{t}}$, on the top quark mass, m_t , used for Monte Carlo event generation around the m_t world average value fit with a linear function. Uncertainties shown are statistical only.*

which is in agreement with the directly obtained world average value of 173.2 ± 0.9 GeV [62] within 1σ .

10. Fiducial cross section measurement

The cross section measurements presented in previous chapters are already systematically limited. Further improvements can only be made by a better and more detailed understanding of the different contributions to the total uncertainty. On the one hand, these can roughly be divided into experimental and theoretical uncertainties as described in Sec. 7.2. On the other hand, one can also categorise them as efficiency and acceptance corrections. Efficiency corrections have to be performed due to inefficiencies and object smearing caused by detector effects. Acceptance corrections are corrections for events that are outside the sensitivity of the detector. Experiment cannot make statements about the latter and therefore has to take these corrections completely from theory. This is also reflected in the size of the systematic uncertainties for the two measurements presented so far. While the uncertainties related to detector effects could be significantly constrained due to the profile likelihood method, the acceptance corrections had to be fully propagated to the measurement uncertainty. With the availability of high statistics LO generator samples for comparison and a larger collision data set these uncertainties become by far the dominant ones as motivated in Sec. 10.1. Therefore, the measurement approach needs to be changed, which is described in the following.

In order to be largely independent of acceptance corrections, the measurement should be limited to objects which are inside the detector acceptance and where sufficient statistics is available. Therefore, a selection reproducible at generator level has to be performed. For this selection it is important that the theory objects used are close to the ones considered in experiment. One has to take into account that the detector mostly measures decay products and not the objects from the hard scattering process. In Monte Carlo simulation, the decay and radiation is implemented by the showering and hadronisation programs (see Sec. 5.2). At this stage, the so-called particle level, the MC objects include all phenomenological effects and are as close as possible to the objects measured by the detector without actually using or simulating the detector. To account for detector effects, the selection performed at this level follows the one for the reconstructed objects excluding experimentally difficult or inaccessible regions. The phase space volume that is spanned by the events passing the particle level selection is referred to as fiducial volume, i.e. the volume assumed as a fixed basis of comparison for the measurement. The measurement is therefore referred to as fiducial cross section measurement. In this context, the term phase space refers to the momenta and angular positions of the objects of interest.

To fully correct for experimental effects one would have to correct each single object by its efficiency. This would mean trying to match each object at particle level with a reconstructed object. For instance, for each particle level jet a match at reconstruction level would be looked for and the kinematic properties of the particle jet would be

10. Fiducial cross section measurement

corrected. Leptons would be approached similarly and possibly E_T^{miss} might also be corrected for detector effects such as out-of-cone corrections. In this case one would obtain a measurement completely independent of theory predictions.

However, $t\bar{t}$ final states contain a large number of different objects, which affect each other and therefore a full object-based correction is very difficult. Instead, the approach chosen here is to use a MC generator to model lepton + jets states in $t\bar{t}$ events and perform a data-driven efficiency reweighting to adjust the lepton + jets states to data. In this way the corrections for efficiency and resolution such as scale factors reflect the data.

The particle level selection as well as the results of the event selection at reconstruction and particle level are given in Sec. 10.1. Furthermore, the measurement method is described in more detail. The cross section extraction is given in Sec. 10.2. The discussion of the result, its additional interpretation and the comparison to other measurements are given in Sec. 10.3.

10.1. Event selection and measurement approach

The reconstruction and selection of events are described in Chapter 4 and Sec. 6.1, respectively. As before, the selection is based on requiring at least three jets, exactly one lepton and applying additional cuts on E_T^{miss} and m_T^W . In contrast to the other two analyses at least one b -tagged jet is required to further suppress the W + jets background yielding a cleaner sample of $t\bar{t}$ events. Asking for a second b -jet, however, would spoil the measurement due to large uncertainties of the b -tagging calibration. Events with two jets are used as a control region. The results of the reconstruction level selection are shown in Tabs. 10.1 and 10.2 as well as Fig. 10.1 for a total of five different combinations of $t\bar{t}$ signal generators and/or parton shower programs, all background processes and data. As for the other analyses all generators are normalised to the same approx. NNLO cross section given in Sec. 2.2.4. The NLO samples are hereby scaled from the generator cross section by factors of 1.12 (POWHEG+HERWIG) to 1.146 (MC@NLO+HERWIG) and the LO samples by 1.687 (ALPGEN+HERWIG dilepton decay channel) to 2.123 (ALPGEN+PYTHIA lepton + jets decay channel). All generators predict the same number of events in the 2 jet bin within 1% in perfect agreement with data in the μ + jets channel but a 4–6% lower number than in data in the e + jets channel, the latter, however, most likely due to the W + jets background prediction. This is covered by the respective systematic uncertainty (see Sec. 6.3), which is, however, not shown. Predictions for events with three jets are lower than in data differing up to 5%. Significant differences between the signal generators, however, start to emerge for events with four jets and beyond. While the POWHEG predictions yield 2–5% too few events than found in data in the 4 jet bin for both channels both ALPGEN predictions linked with HERWIG and PYTHIA generate 2–4% too many events compared to data. Similar to ALPGEN, MC@NLO+HERWIG predicts around 2% too many events the 4 jet bin showing best agreement of all generators. The signal generators predict yields differing by 9–12% from each other, taking background processes into account by 7–9%. For the almost background-free events with five and

more jets the difference in the predictions between the different signal generators amounts to a total of 25%. The combined signal plus background yields show disagreements with data at the 10% level. `MC@NLO+HERWIG` predicts 9–10% too few events than data while both `AlpGEN` predictions yield 9–11% too many events. `POWHEG+PYTHIA` shows best agreement with data within 3% with a small overestimation while `POWHEG+HERWIG` tends towards slightly lower values. A cross section measurement as performed in the previous chapters would have to quote these differences found as uncertainty spoiling the whole measurement.

To a large extent the different behaviour of the generators can be explained by the different behaviour of leading order and next-to-leading order generators. The next-to-leading order generators generate only the first additional parton emission while all other additional radiation has to be produced by the parton shower. In contrast to that, the leading order generator `AlpGEN` generates additional partons from the matrix element. On average this leads to a harder jet spectrum and therefore a higher number of predicted events at high jet multiplicities. In order to be able to perform a sensitive cross section measurement the effect of acceptance corrections needs to be reduced. Thus, the first step is to restrict the measurement to the phase space within the acceptance of the detector by performing an additional selection at particle level.

As discussed above, the particle level selection aims to be as close to the reconstruction level selection as possible. The selection here follows the approach pursued in Ref. [280], for which detailed studies regarding the correspondence of reconstruction level vs. particle level objects were performed. Only objects from stable particles, i.e. a mean lifetime $\tau > 0.3 \cdot 10^{-10}$ s, are considered. The selected objects have to be within the acceptance of the detector. Leptons are only considered as candidates if they are found to be in the decay chain of a W boson, i.e. stemming directly from the W decay or from τ leptons decays. As for reconstructed objects, leptons are required to have a transverse momentum of $p_T > 25$ GeV. To emulate the reconstruction level electron clustering algorithm that takes into account bremsstrahlung photons found within in a cone of radius $\Delta R = 0.1$ are added to the electron four-vector. The allowed η regions reflecting the reconstruction level selection are $|\eta| < 2.47$ for muons and $|\eta| < 1.37$ and $1.52 < |\eta| < 2.5$ for electrons. Jet finding is performed using the anti- k_t algorithm with cut-off parameter $R = 0.4$ ignoring intermediate states of decaying particles, neutrinos and muons. Particles from the underlying event are included, whereas particles from overlaid inelastic non-diffractive events (pileup, see Sec. 5.2.2) are not. Only jets with $|\eta| < 2.5$ and a transverse momentum $p_T > 25$ GeV are considered. Jets are regarded as b -tagged, when a B hadron with $p_T > 5$ GeV is found within a cone of $\Delta R = 0.3$ of the jet centre. The closest jet within $\Delta R = 0.2$ of a selected electron is removed to prevent double-counting of objects.

The lepton + jets selection requires exactly one selected electron or muon with the properties described above. Events are vetoed if a second lepton within the same pseudorapidity range and transverse momentum $p_T > 15$ GeV is present to reduce the amount of dileptonic events. The missing transverse energy, determined from all neutrinos in the event, has to be greater than 25 GeV. This cut is 5 GeV lower than at reconstruction level to account for a bias due to the finite resolution of the E_T^{miss} measurement [212]. This

10. Fiducial cross section measurement

Table 10.1.: Selected events in the $\mu + \text{jets}$ channel for a given jet multiplicity. Uncertainties shown are statistical only. The predicted sum of events is calculated for each $t\bar{t}$ generator. The $W + \text{jets}$ and QCD multi-jet production background normalisation is obtained from data-driven methods described in Chapter 6.

	2 jets	3 jets	4 jets	≥ 5 jets
POWHEG+PYTHIA $t\bar{t}$	6760 \pm 40	12870 \pm 50	11150 \pm 50	8700 \pm 50
POWHEG+HERWIG $t\bar{t}$	6400 \pm 20	12400 \pm 20	11370 \pm 20	8950 \pm 20
MC@NLO $t\bar{t}$	6780 \pm 20	13190 \pm 30	11980 \pm 30	7880 \pm 20
AlpGEN+PYTHIA $t\bar{t}$	6310 \pm 30	12690 \pm 40	11950 \pm 40	9750 \pm 40
AlpGEN+HERWIG $t\bar{t}$	6360 \pm 40	12840 \pm 60	12180 \pm 60	9850 \pm 50
$W + \text{jets}$	5640 \pm 90	1690 \pm 40	460 \pm 20	127 \pm 9
$Wb\bar{b} + \text{jets}$	5450 \pm 70	2180 \pm 40	830 \pm 20	290 \pm 10
$Wc\bar{c} + \text{jets}$	4190 \pm 60	1670 \pm 40	610 \pm 20	210 \pm 10
$Wc + \text{jets}$	9600 \pm 80	2230 \pm 40	550 \pm 20	150 \pm 10
single-top t -channel	2700 \pm 10	1437 \pm 9	527 \pm 5	180 \pm 3
single-top Wt	888 \pm 9	955 \pm 10	453 \pm 7	203 \pm 5
single-top s -channel	249 \pm 2	94 \pm 1	25 \pm 1	7 \pm 0
$Z + \text{jets/dibosons}$	1280 \pm 20	510 \pm 10	160 \pm 6	60 \pm 4
QCD multi-jets	2580 \pm 20	960 \pm 10	332 \pm 8	159 \pm 6
sum predicted (POWHEG+PYTHIA)	39320 \pm 160	24600 \pm 100	15100 \pm 70	10090 \pm 50
sum predicted (POWHEG+HERWIG)	38960 \pm 150	24130 \pm 80	15320 \pm 50	10340 \pm 30
sum predicted (MC@NLO)	39350 \pm 150	24930 \pm 80	15930 \pm 50	9270 \pm 30
sum predicted (AlpGEN+PYTHIA)	38870 \pm 150	24420 \pm 90	15890 \pm 60	11140 \pm 50
sum predicted (AlpGEN+HERWIG)	38920 \pm 150	24570 \pm 100	16130 \pm 70	11240 \pm 50
data	39118	25174	15626	10183

effect is only visible up to 40 GeV above which the difference between reconstruction and particle level E_T^{miss} amounts only to 3–5%. The transverse mass of the W boson, calculated from the lepton and the missing transverse energy vector as before, has to be greater than 30 GeV as on reconstruction level. At least three jets have to pass the selection criteria, one of which has to be b -tagged as described above. The particle level and the reconstruction level selection cuts are summarised in Tab. 10.3.

The particle level selected data set is subdivided according to the jet multiplicity. This way, the different contributions can be adjusted in the likelihood fit and the measurement becomes practically independent of the differences found in jet multiplicity for the different generators. This approach is close to the Bayesian reweighting procedure described in References [290, 291], which reweights the particle level selected events to data. The measurement does not depend on the absolute normalisation of the different signal generators anymore, but only on efficiencies with respect to the particle level selection. Since the aim of this analysis is an inclusive cross section measurement the jet bins are not unfolded separately as e.g. in Ref. [280], which is much more difficult. Instead, all uncertainties are treated combined for all jet multiplicity bins.

10.1. Event selection and measurement approach

Table 10.2.: Selected events in the $e + \text{jets}$ channel for a given jet multiplicity. Uncertainties shown are statistical only. The predicted sum of events is calculated for each $t\bar{t}$ generator. The $W + \text{jets}$ and QCD multi-jet production background normalisation is obtained from data-driven methods described in Chapter 6.

	2 jets	3 jets	4 jets	≥ 5 jets
POWHEG+PYTHIA $t\bar{t}$	5770 \pm 40	10730 \pm 50	9310 \pm 50	7100 \pm 40
POWHEG+HERWIG $t\bar{t}$	5570 \pm 20	10690 \pm 20	9780 \pm 20	7670 \pm 20
MC@NLO $t\bar{t}$	5810 \pm 20	11150 \pm 20	10120 \pm 20	6630 \pm 20
AlpGEN+PYTHIA $t\bar{t}$	5370 \pm 20	10730 \pm 40	10200 \pm 40	8230 \pm 40
AlpGEN+HERWIG $t\bar{t}$	5580 \pm 30	10990 \pm 50	10420 \pm 50	8320 \pm 40
$W + \text{jets}$	4240 \pm 70	1090 \pm 30	300 \pm 10	90 \pm 10
$Wb\bar{b} + \text{jets}$	4440 \pm 70	1790 \pm 40	620 \pm 20	220 \pm 10
$Wc\bar{c} + \text{jets}$	3480 \pm 60	1340 \pm 30	460 \pm 20	180 \pm 10
$Wc + \text{jets}$	5480 \pm 50	1220 \pm 20	260 \pm 10	62 \pm 5
single-top t -channel	2230 \pm 10	1197 \pm 8	433 \pm 5	149 \pm 3
single-top Wt	772 \pm 9	813 \pm 9	402 \pm 7	173 \pm 5
single-top s -channel	200 \pm 1	74 \pm 1	19 \pm 0	5 \pm 0
$Z + \text{jets/dibosons}$	1210 \pm 20	650 \pm 10	254 \pm 7	118 \pm 5
QCD multi-jets	2360 \pm 60	970 \pm 50	300 \pm 40	170 \pm 30
sum pred. (POWHEG+PYTHIA)	30190 \pm 140	19880 \pm 90	12370 \pm 70	8260 \pm 50
sum pred. (POWHEG+HERWIG)	29990 \pm 140	19840 \pm 80	12840 \pm 50	8830 \pm 40
sum pred. (MC@NLO)	30230 \pm 140	20310 \pm 80	13170 \pm 50	7790 \pm 40
sum pred. (AlpGEN+PYTHIA)	29790 \pm 140	19880 \pm 90	13260 \pm 60	9390 \pm 50
sum pred. (AlpGEN+HERWIG)	30000 \pm 140	20150 \pm 100	13480 \pm 70	9480 \pm 60
data	31553	20958	13023	8448

Table 10.3.: Particle level vs. reconstruction level event selection cuts. Details of the reconstructed objects used can be found in Chapter 4. Basic event level cuts are not shown here.

particle level	reconstruction level
exactly one lepton (dressed e or μ), $p_T > 25$ GeV and $\eta < 2.5$	exactly one isolated lepton (e or μ), $p_T > 25$ GeV and $\eta < 2.5$
veto second lepton (dressed e or μ), $p_T > 15$ GeV and $\eta < 2.5$	veto second isolated lepton (e or μ), $p_T > 25$ GeV and $\eta < 2.5$
at least three jets, anti- k_T ($R = 0.4$), $p_T > 25$ GeV and $\eta < 2.5$	at least three jets, anti- k_T ($R = 0.4$), $p_T > 25$ GeV and $\eta < 2.5$
at least one b -tagged jet, B hadron with $p_T > 5$ GeV within $\Delta R = 0.3$ of the jet	at least one b -tagged jet, MV1 algorithm at 70% efficiency
$E_T^{\text{miss}} > 25$ GeV, all neutrinos in the event	$E_T^{\text{miss}} > 30$ GeV
$m_T^W > 30$ GeV	$m_T^W > 30$ GeV

10. Fiducial cross section measurement

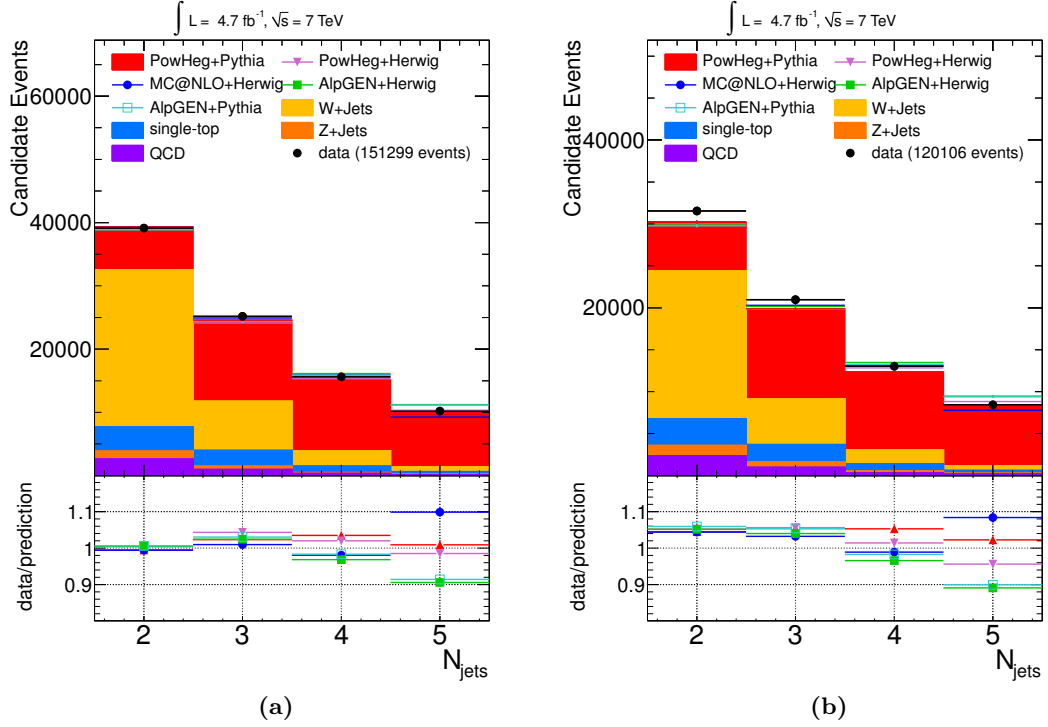


Figure 10.1.: Observed (black dots) and expected event yields for the 2011 analysis (b) in the (a) $\mu + \text{jets}$ and (b) $e + \text{jets}$ channel. The full histogram (red) is the POWHEG+PYTHIA prediction, all other $t\bar{t}$ generator predictions including background are shown as given in the legend. The data/prediction ratio for each generator is shown below.

As the event topology is rather complex and tight selection criteria are applied 60% of the events passing the particle level selection in the muon channel and 65% of the events in the electron channel do not pass the reconstruction level selection of the respective channel. Conversely, about 25% of the reconstruction level selected events do not pass the selection at particle level. The major reasons for signal events failing at reconstruction level while passing all particle level cuts are lepton trigger and identification inefficiencies followed by failing the E_T^{miss} cut. At particle level the majority of events failing when passing the reconstruction level selection are due the missing transverse energy and transverse W mass cuts as well as the dilepton veto. The latter is explained by migrations in the detector area, e.g. when in dilepton events one lepton escapes detection at reconstruction level or fails the tight identification cuts and is thus identified as single lepton event. The acceptance loss due to the cut into the falling E_T^{miss} spectrum has to be endured since it is needed to reject QCD multi-jet events.

In the following, events passing both reconstruction and particle level cuts are referred to as **truth lepton + N jets** events according to the number of jets, N , selected at

particle level. In case an event passes the reconstruction level selection of the respective lepton channel only, it is referred to as out-of-phase-space selected, in short *oops*. Events passing only particle level cuts are not considered further because they are not needed for the analysis. The expected number of $t\bar{t}$ events for the different Monte Carlo generators split according to the jet multiplicity from the particle level selection together with the selection efficiencies is shown in Tabs. 10.4 and 10.5 for the $\mu + \text{jets}$ and the $e + \text{jets}$ channel, respectively. The comparison of the prediction using POWHEG+PYTHIA for the $t\bar{t}$ signal simulation with data is shown in Fig. 10.2. As expected, the majority of all reconstruction level selected events in a given jet bin ends up in the same particle level jet multiplicity bin. The relative migrations between the different jet bins are very similar for the different generators indicating that the fiducial selection helps to absorb the differences between the generators.

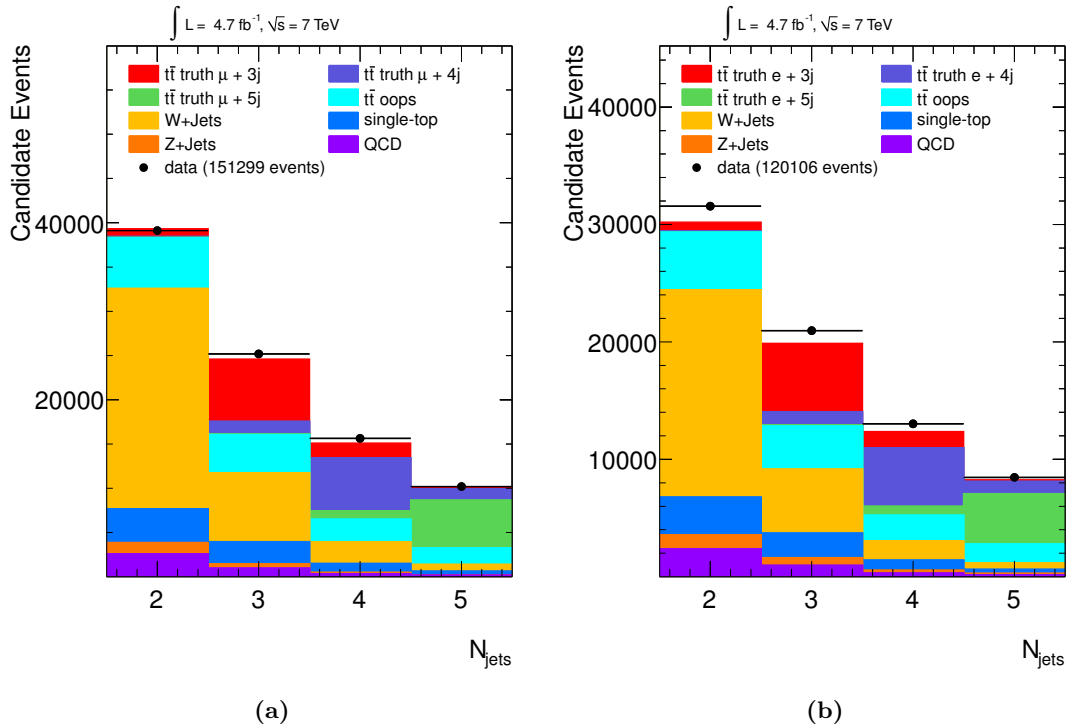


Figure 10.2.: Observed and expected event yields for the 2011 analysis (b) for the POWHEG+PYTHIA split according to the particle selection in the (a) $\mu + \text{jets}$ and (b) $e + \text{jets}$ channel.

As central $t\bar{t}$ generator for this measurement POWHEG+PYTHIA is chosen since it yields best data Monte Carlo simulation agreement in terms of the jet multiplicity prediction before the fit, in particular in the signal-dominated region with five and more jets. Different choices of the central generator would have been possible as well and would have led to the same final result since any difference found between the different generators

10. Fiducial cross section measurement

Table 10.4.: Selected $t\bar{t}$ events in the $\mu + \text{jets}$ channel for a given jet multiplicity. Uncertainties shown are statistical only. The samples are split according to the particle level selection as described in the text. Particle level selection efficiencies shown require at least 3 selected jets at reconstruction level.

particle level selected channel	efficiency [%]	reconstruction level selected		
		3 jets	4 jets	≥ 5 jets
POWHEG+PYTHIA				
$t\bar{t}$ truth $\mu + 3$ jets	40.5 ± 0.2	7048 ± 40	1681 ± 20	174 ± 6
$t\bar{t}$ truth $\mu + 4$ jets	44.3 ± 0.2	1385 ± 17	5973 ± 37	1268 ± 17
$t\bar{t}$ truth $\mu + 5$ jets	43.5 ± 0.2	119 ± 5	949 ± 14	5375 ± 36
$t\bar{t}$ oops	-	4316 ± 31	2546 ± 24	1883 ± 21
POWHEG+HERWIG				
$t\bar{t}$ truth $\mu + 3$ jets	38.8 ± 0.1	6630 ± 17	1605 ± 9	181 ± 3
$t\bar{t}$ truth $\mu + 4$ jets	43.3 ± 0.1	1663 ± 8	6181 ± 17	1238 ± 8
$t\bar{t}$ truth $\mu + 5$ jets	42.8 ± 0.1	179 ± 2	1157 ± 7	5741 ± 17
$t\bar{t}$ oops	-	3926 ± 13	2427 ± 11	1786 ± 9
MC@NLO				
$t\bar{t}$ truth $\mu + 3$ jets	40.1 ± 0.1	7301 ± 19	1714 ± 9	173 ± 3
$t\bar{t}$ truth $\mu + 4$ jets	44.4 ± 0.1	1633 ± 9	6804 ± 19	1262 ± 8
$t\bar{t}$ truth $\mu + 5$ jets	44.0 ± 0.1	147 ± 2	1048 ± 7	5010 ± 17
$t\bar{t}$ oops	-	4114 ± 14	2411 ± 11	1437 ± 9
AlpGEN+PYTHIA				
$t\bar{t}$ truth $\mu + 3$ jets	41.3 ± 0.1	6917 ± 28	1754 ± 15	214 ± 5
$t\bar{t}$ truth $\mu + 4$ jets	45.0 ± 0.1	1423 ± 12	6487 ± 28	1404 ± 13
$t\bar{t}$ truth $\mu + 5$ jets	43.6 ± 0.2	122 ± 3	1011 ± 11	6035 ± 30
$t\bar{t}$ oops	-	4230 ± 22	2694 ± 18	2099 ± 17
AlpGEN+HERWIG				
$t\bar{t}$ truth $\mu + 3$ jets	40.9 ± 0.2	7002 ± 42	1772 ± 22	187 ± 7
$t\bar{t}$ truth $\mu + 4$ jets	45.0 ± 0.2	1628 ± 20	6727 ± 44	1444 ± 20
$t\bar{t}$ truth $\mu + 5$ jets	44.4 ± 0.2	157 ± 6	1165 ± 17	6342 ± 38
$t\bar{t}$ oops	-	4048 ± 29	2519 ± 24	1880 ± 19

Table 10.5.: Selected $t\bar{t}$ events in the $e + \text{jets}$ channel for a given jet multiplicity. Uncertainties shown are statistical only. The samples are split according to the particle level selection as described in the text. Particle level selection efficiencies shown require at least 3 selected jets at reconstruction level.

particle level selected channel	efficiency [%]	reconstruction level selected		
		3 jets	4 jets	≥ 5 jets
POWHEG+PYTHIA				
$t\bar{t}$ truth $e + 3$ jets	35.4 ± 0.2	5830 ± 37	1390 ± 18	148 ± 6
$t\bar{t}$ truth $e + 4$ jets	39.9 ± 0.2	1128 ± 15	4984 ± 34	1044 ± 16
$t\bar{t}$ truth $e + 5$ jets	39.7 ± 0.3	96 ± 4	761 ± 13	4286 ± 32
$t\bar{t}$ oops	-	3679 ± 29	2177 ± 22	1621 ± 20
POWHEG+HERWIG				
$t\bar{t}$ truth $e + 3$ jets	34.7 ± 0.1	5620 ± 16	1357 ± 8	144 ± 3
$t\bar{t}$ truth $e + 4$ jets	40.1 ± 0.1	1426 ± 8	5238 ± 16	1066 ± 7
$t\bar{t}$ truth $e + 5$ jets	41.1 ± 0.1	150 ± 2	995 ± 6	4849 ± 15
$t\bar{t}$ oops	-	3491 ± 13	2188 ± 10	1612 ± 9
MC@NLO				
$t\bar{t}$ truth $e + 3$ jets	35.3 ± 0.1	6087 ± 17	1437 ± 9	143 ± 3
$t\bar{t}$ truth $e + 4$ jets	40.4 ± 0.1	1357 ± 8	5651 ± 17	1047 ± 8
$t\bar{t}$ truth $e + 5$ jets	41.5 ± 0.1	119 ± 2	879 ± 6	4137 ± 15
$t\bar{t}$ oops	-	3588 ± 13	2150 ± 10	1303 ± 9
AlpGEN+PYTHIA				
$t\bar{t}$ truth $e + 3$ jets	36.2 ± 0.2	5791 ± 26	1453 ± 13	162 ± 4
$t\bar{t}$ truth $e + 4$ jets	41.2 ± 0.2	1185 ± 11	5499 ± 26	1169 ± 12
$t\bar{t}$ truth $e + 5$ jets	41.0 ± 0.2	103 ± 3	846 ± 10	5059 ± 28
$t\bar{t}$ oops	-	3648 ± 20	2402 ± 17	1839 ± 17
AlpGEN+HERWIG				
$t\bar{t}$ truth $e + 3$ jets	36.6 ± 0.2	5913 ± 38	1467 ± 20	169 ± 7
$t\bar{t}$ truth $e + 4$ jets	41.6 ± 0.2	1389 ± 19	5752 ± 40	1198 ± 18
$t\bar{t}$ truth $e + 5$ jets	41.9 ± 0.2	142 ± 6	984 ± 15	5292 ± 34
$t\bar{t}$ oops	-	3550 ± 27	2221 ± 22	1661 ± 18

10. Fiducial cross section measurement

in the fiducial volume is quoted as an uncertainty.

10.1.1. Fit procedure

As described in Sec. 7.3.2 a likelihood fit is employed to determine the fiducial cross section. In the fit procedure the selected events for a given particle jet multiplicity referred to as templates in the following are allowed to float freely in order to let them adjust to jet multiplicity distribution found in data. The `truth lepton + N jets` templates are hereby independent of the overall normalisation, but only depend on the selection efficiency in the fiducial region as described in Appendix Sec. F.1. Since the fraction of events in the reconstruction level selected data set failing the particle level selection (`oops`) amounts to around 25% it cannot be neglected. However, as these events are not in the fiducial phase space defined for comparison with theory, they have to be treated as an additional background. Detailed study of this contribution shows that it is a mixture of the other three templates. Furthermore, its relative contribution to the total reconstruction level selected $t\bar{t}$ sample is about the same for all signal generators varying only by a relative 8%. In the likelihood fit an additional Gaussian constraint is introduced that keeps the fraction of the out-of-phase-space selected events constant with respect to the overall $t\bar{t}$ normalisation within its statistical uncertainty. Since this uncertainty is very small, the relative `oops` contribution is basically fixed. In this way the overall normalisation of all $t\bar{t}$ events is allowed to change. Without constraining the `oops` template it could arbitrarily compensate parts of the other $t\bar{t}$ three templates biasing the measurement and spoiling the fiducial particle level comparison between the different generators. However, any effect or bias from the `oops` template on the measurement is reflected in the total uncertainty of the result because the difference between the fiducial cross sections found for the different generators enters the systematic uncertainty.

In contrast to the cross section measurements performed in the previous chapters all background processes are fixed. This is in particular done to avoid compensation effects observed between the different $t\bar{t}$ signal generators and the dominant $W + \text{jets}$ background. It is therefore even more important that the $W + \text{jets}$ normalisation is taken from data (see Sec. 6.3) in order not to obtain very large uncertainties. As described in Sec. 6.2 the QCD multi-jet background normalisation and shape are also determined from data. The single top background is theoretically well understood and the $Z + \text{jets}$ and diboson backgrounds are very small and therefore taken from theory.

10.1.2. Multivariate signal and background separation

In order to cleanly separate the $t\bar{t}$ signal from the $W + \text{jets}$ background a projective likelihood discriminant built from three of the discriminating variables used for the previously described analyses in this work is used. These are the pseudorapidity of the lepton, η , the transformed form of aplanarity, $\exp(-8 \times \mathcal{A})$, and the sum of transverse momenta of the third and fourth jet divided by the sum of z -components of all selected objects and transformed to $\exp(-4 \times H_{T,3p})$. The robustness and separation power of the variables are discussed in Sec. 7.1. Using only one of these variables, e.g. lepton

η only, shows too little separation power with respect to $W + \text{jets}$ events making the measurement too dependent on the individual generator kinematics.

Good agreement between data and simulation is found for all input distributions shown in Figs. 10.3 to 10.5 for POWHEG+PYTHIA with the reconstruction level selection applied only. The resulting projective likelihood is given in Fig. 10.6. Spikes stem from training templates, but are well modelled in data so that no additional smoothing is needed. Additionally, the size of systematic uncertainties is shown in the data/prediction ratio. They are split into correlated and anti-correlated uncertainties depending on their correlation with the final inclusive cross section result. The uncertainties are discussed in Sec. 10.2.1 below. As one can see discrepancies between data and predictions are covered by the uncertainties. Lepton η as an example for the individual input distributions and the likelihood discriminant itself split according to the particle level selection are shown in Figs. 10.7 and 10.8, respectively.

10.2. Cross section extraction

In order to extract the $t\bar{t}$ cross section no profile likelihood is employed in contrast to the full phase space analyses described in the previous chapters. Instead, a simple binned likelihood fit is used for the sake of stability and simplicity. Therefore, all uncertainties are evaluated using pseudo experiments as described in Sec. 7.4. As described above, all non- $t\bar{t}$ background processes are kept fixed in the fit to avoid undesired correlations or compensation effects between the $t\bar{t}$ and the background templates. The background normalisation uncertainty is hence also evaluated in pseudo experiments.

The total fiducial cross section, $\sigma_{t\bar{t}}$, is extracted as linear sum of the single fiducial $t\bar{t}$ cross section values, σ_i , obtained from the fit to data. Only the three processes which are both particle and reconstruction level selected contribute, because the `oops` events are outside the fiducial phase space. The uncertainty is obtained using Gaussian error propagation as described in Appendix Sec. F.2.

10.2.1. Evaluation of systematic uncertainties

As described in Sec. 7.4.2 all uncertainties are evaluated in pseudo experiments at the same time. In addition to the uncertainties discussed in Sec. 7.2 the shape and normalisation of the `oops` template are evaluated. The normalisation is assumed to be uncorrelated in each jet bin using the largest deviations from the POWHEG+PYTHIA prediction found for the other generators. The shape uncertainty is taken from MC@NLO since it shows the largest deviation. Furthermore, the difference found when comparing to the leading order generator ALPGEN is quoted. The results of the pseudo experiments for statistical uncertainty only as well as for the total uncertainty are shown in Fig. 10.9. The smaller number of events in the histograms with respect to the performed pseudo experiments is due to fits that did not converge. Since the generator uncertainties are strictly one-sided uncertainties and even symmetrising around the nominal templates shifts the central value of the pseudo experiments they are evaluated separately and added to the total uncertainty in quadrature. The total uncertainty within the fiducial

10. Fiducial cross section measurement

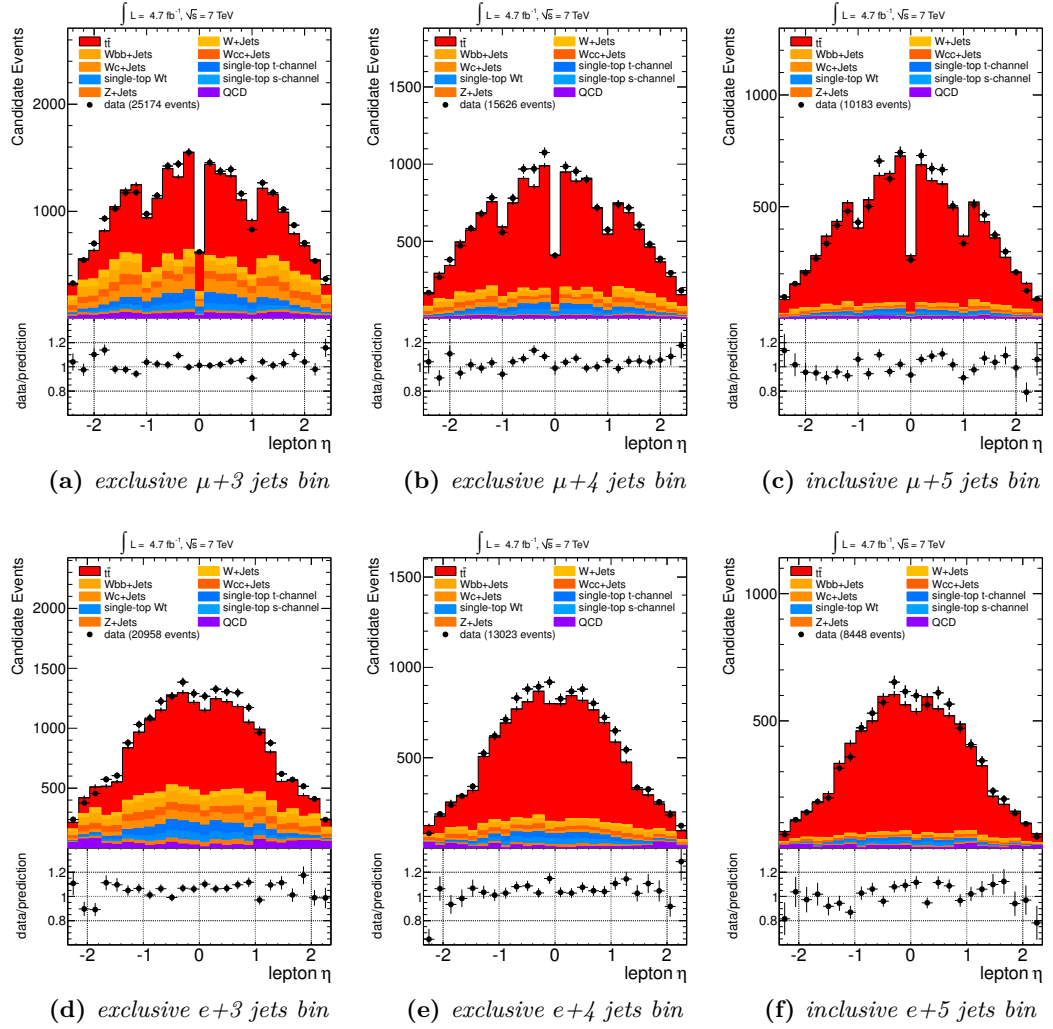


Figure 10.3.: *Lepton pseudorapidity in data and Monte Carlo simulated events in the signal region. The data/prediction ratio is shown at the bottom of each plot.*

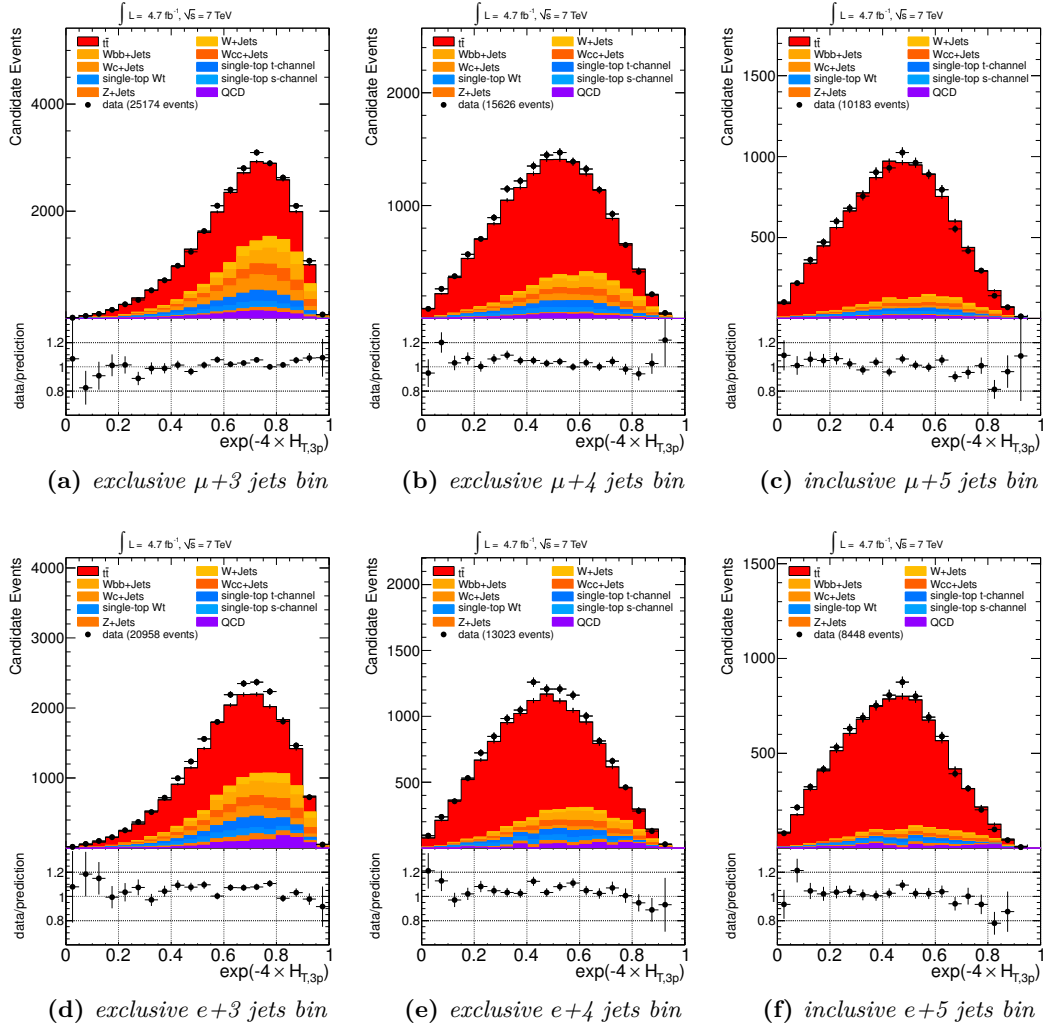


Figure 10.4.: Transformed version of $H_{T,3p}$ in data and Monte Carlo simulated events in the signal region. The data/prediction ratio is shown at the bottom of each plot.

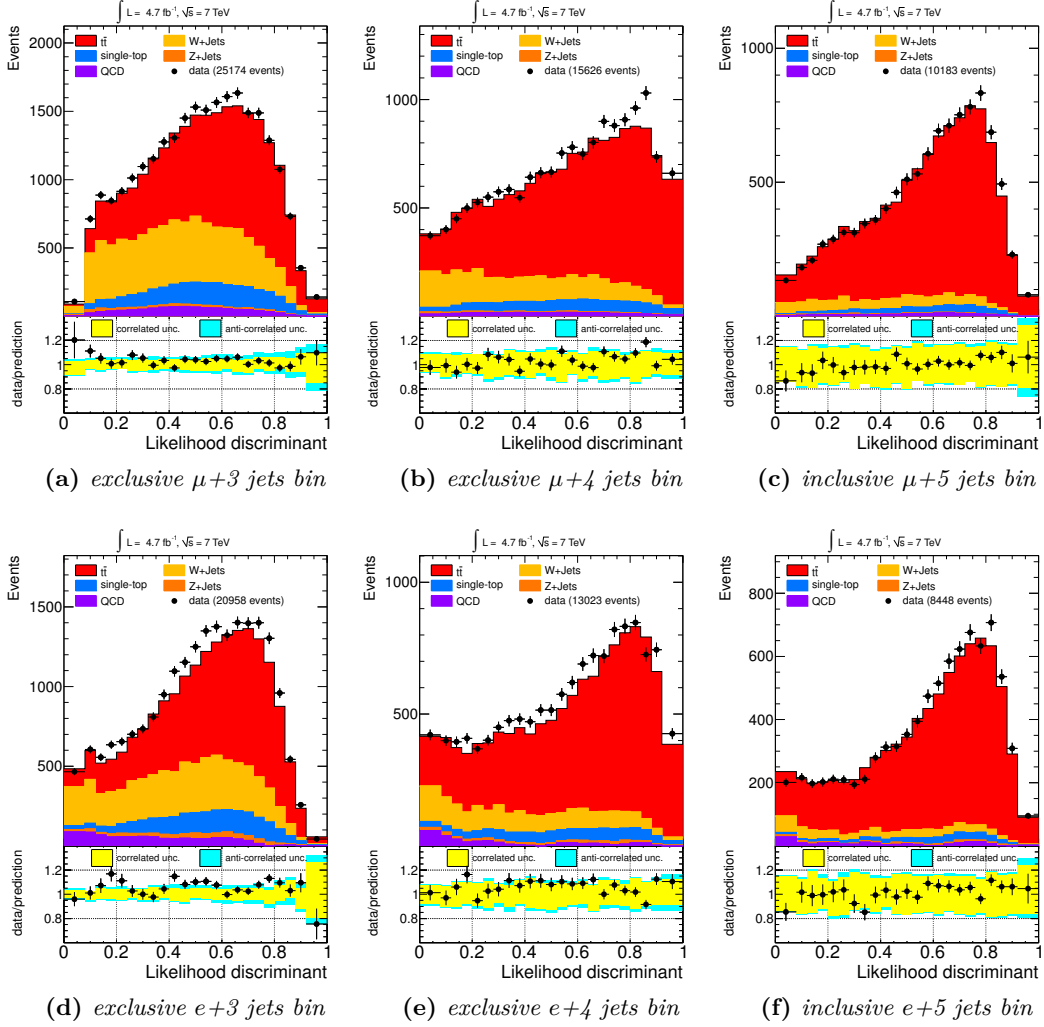


Figure 10.6.: Projective likelihood discriminant in data and Monte Carlo simulated events in the signal region. The data/prediction ratio is shown at the bottom of each plot. Furthermore, the size of the correlated (yellow) and anti-correlated (cyan) uncertainties added in quadrature excluding the signal modelling ones are shown as discussed in the text.

10. Fiducial cross section measurement

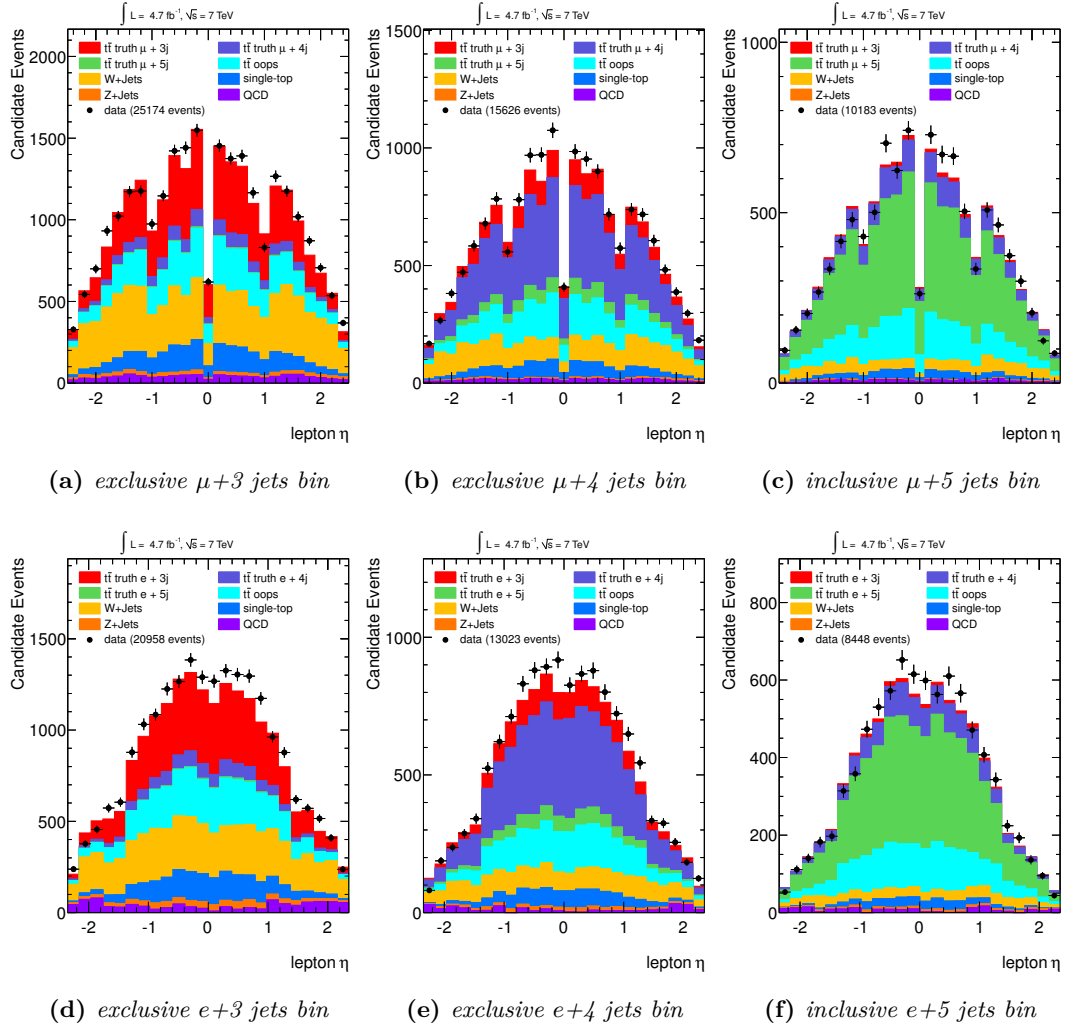


Figure 10.7.: *Lepton pseudorapidity in data and Monte Carlo simulated events in the signal region split according to particle level selection.*

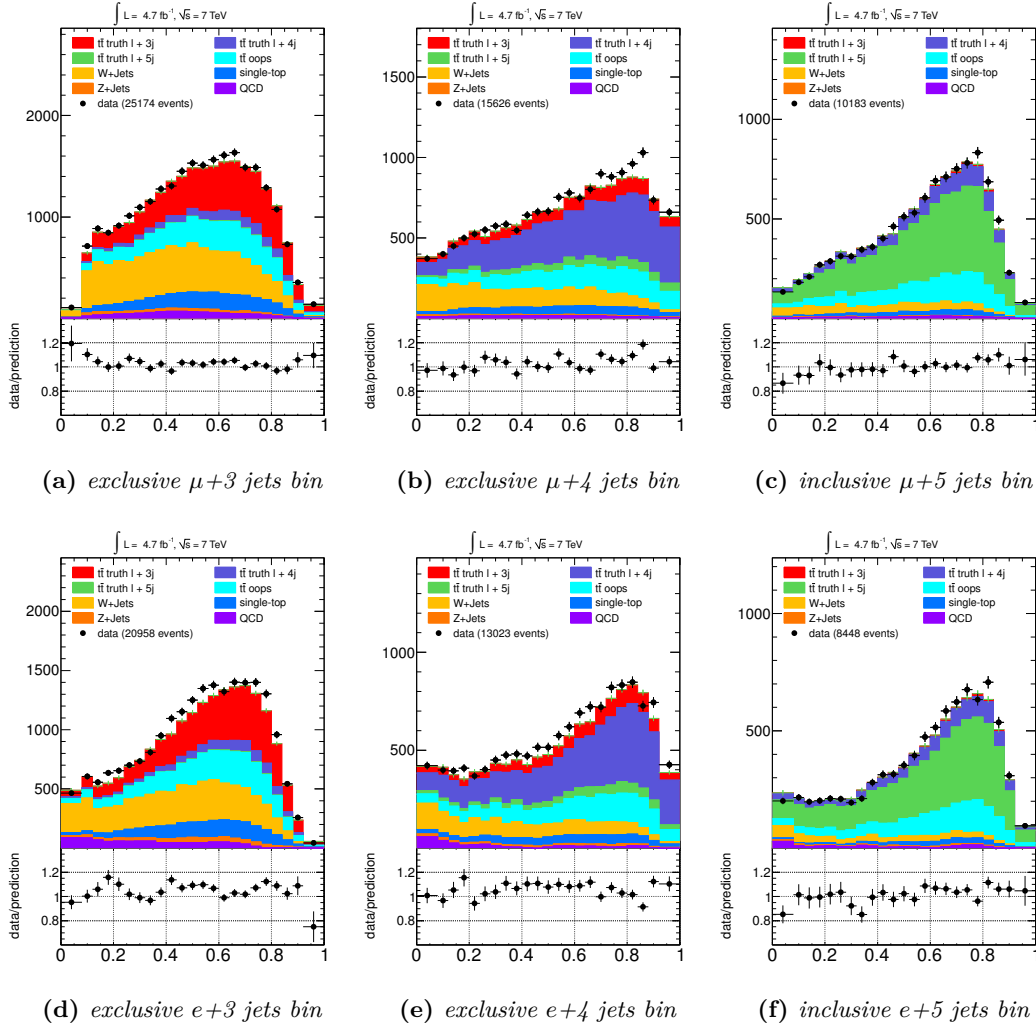


Figure 10.8.: Projective likelihood discriminant in data and Monte Carlo simulated events in the signal region split according to particle level selection..

10. Fiducial cross section measurement

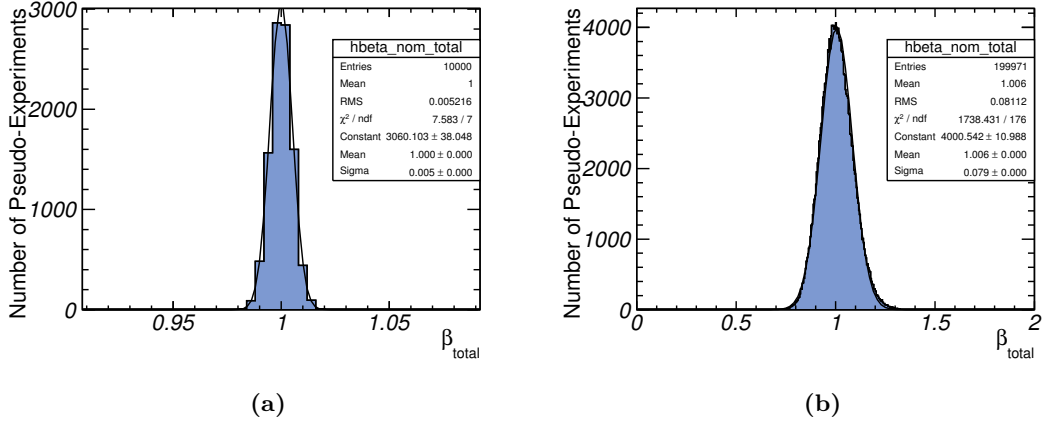


Figure 10.9.: *Distribution of the fitted fiducial $t\bar{t}$ cross section parameter, β_{total} : (a) considering statistical uncertainty only from 10,000 pseudo experiments, and (b) most uncertainties in the fiducial volume using 200,000 pseudo experiments. Generator uncertainties are evaluated separately.*

volume amounts to (+8.4/−7.8)%. The pseudo experiments show a shift of 0.6% towards larger values largely due to the asymmetric behaviour of the jet energy scale variation and the `oops` template normalisation uncertainty. This effect is not corrected for since in contrast to the previous analyses described the uncertainties are not included in the central fit result and the shift is covered by the uncertainties. For the same reasons the total uncertainty is asymmetric and the χ^2 over the number of degrees of freedom of the Gaussian fit also bad.

The effect and behaviour of single systematic uncertainties is assessed by evaluating the uncertainty at its $\pm 1\sigma$ bound. This is shown in Fig. 10.10 as an example for the jet energy scale and the b -tagging calibration uncertainty. For both uncertainties an up-shift of the uncertainties yields a higher cross section value, i.e. they both show correlated behaviour with the cross section. The figures show a two-dimensional distribution of the $t\bar{t}$ cross section value, β , which is nominally set to 1, vs. the value, δ , of the systematic uncertainty used for the respective pseudo experiment where $\delta = \pm 1$ represents the $\pm 1\sigma$ bound. The projection onto the β -axis of a slice of width ± 0.02 at $\pm 1\sigma$ is fit with a Gaussian. By calculating the difference to the mean of the β distribution, i.e. the projection of the full δ -range on β , also fit with a Gaussian the contribution of the respective systematic uncertainty to the total uncertainty is obtained.

The behaviour of a single uncertainty can be investigated in more detail by evaluating the effect of each systematic uncertainty on the split $t\bar{t}$ samples. As an example, the correlation of the jet energy scale δ -parameter with the β_i -parameters is shown in Fig. 10.11. One can see that the $t\bar{t}$ truth `lepton + 3 jets` template shows in contrast to the other $t\bar{t}$ templates an anti-correlated behaviour with the jet energy scale resulting in a reduced overall uncertainty on the fiducial cross section. Still, since the envelope of all jet energy scale uncertainties is used, which is expected to have the same effect on

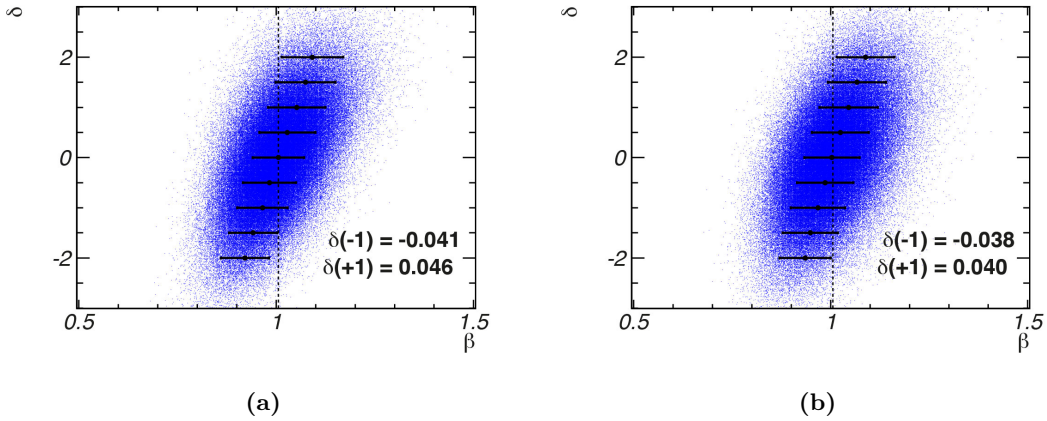


Figure 10.10.: Correlation of the $t\bar{t}$ fiducial cross section parameter β with the δ -value for (a) the jet energy scale, and (b) the b -tagging calibration uncertainty using 200,000 pseudo experiments. Additionally, mean value and uncertainty of fits of slices of the δ -projection on the β -axis are shown with black markers and the difference at $\delta = \pm 1$ with respect to the fit of the full projection are calculated.

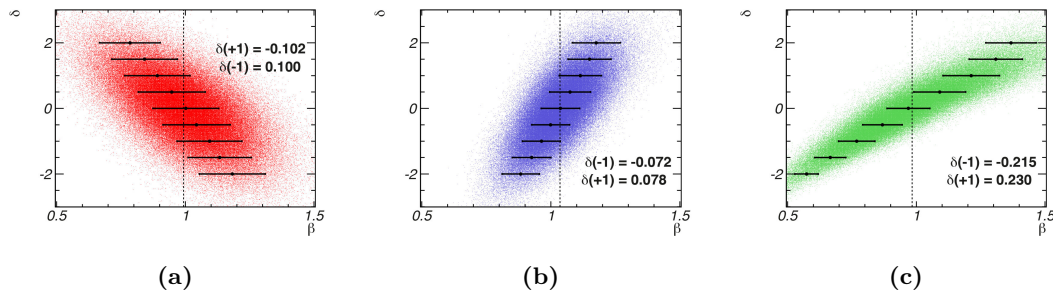


Figure 10.11.: Correlation of the $t\bar{t}$ fiducial cross section parameter β_i for the (a) $t\bar{t}$ truth lepton + 3 jets, (b) $t\bar{t}$ truth lepton + 4 jets, and the (c) $t\bar{t}$ truth lepton + 5 jets template with the δ -value for the jet energy scale using 200,000 pseudo experiments. Additionally, mean value and uncertainty of fits of slices of the δ -projection on the β -axis are shown with black markers and the difference at $\delta = \pm 1$ with respect to the fit of the full projection are calculated.

each of the $t\bar{t}$ subsets, the uncertainty is still among the largest ones.

The summary of the effect of all systematic uncertainties is given in Tab. 10.6. The dominant uncertainties are jet energy scale, b -tagging calibration, and the background normalisations. Shifts in the jet energy scale change the composition of the $t\bar{t}$ samples, which can only partly be compensated by the efficiency reweighting taking place in

10. Fiducial cross section measurement

the fit. In particular, the largest relative change observed is for templates for which the particle level selected jet bin is different to the reconstruction level selected one. Furthermore, migrations into and out of the fiducial volume occur only at reconstruction level and can therefore not be accounted for. Changes in the b -tagging calibration also affect the event yields, but do not cause jet bin migrations. The calibration uncertainty changes the shape of the individual templates and the efficiencies in each jet bin, but in a correlated way, which means that no compensation effects as for the jet energy scale can take place. The resulting background uncertainties on the non- $t\bar{t}$ processes could in principle be reduced by requiring two b -tagged jets and/or by allowing the individual background contributions to float in the fit. However, careful investigations show that the former causes an increase of the resulting b -tagging calibration uncertainty to the order of the total uncertainty of the measurement while the latter approach leads to compensation effects between the $t\bar{t}$ and the W + jets processes leading to an increase of the generator related uncertainties.

The theoretical/generator uncertainties are almost completely negligible for the fiducial measurement amounting to only 1.7%. This is discussed further below in Sec. 10.3.1.

10.2.2. Fit results

Applying the likelihood fit to data in all six analysis channels using the POWHEG+PYTHIA $t\bar{t}$ signal generator yields a fiducial $t\bar{t}$ production cross section of

$$\sigma_{t\bar{t}} = 24.41 \pm 0.09 \text{ pb}, \quad (10.1)$$

where the uncertainty quoted is the statistical uncertainty from the fit only. The fit result is shown in Fig. 10.12. In general, good agreement is observed. Some small discrepancies found at very low or very high values of the discriminant in some of the jet bins are well within the uncertainties evaluated in Sec. 10.2.1 above. One can furthermore infer that from Fig. 10.6 in the same section, which is not shown here again with rescaled values since the $t\bar{t}$ templates are only shifted by a few percent in the fit. The fit values of the individual processes are summarised in Appendix Sec. F.4.

The linear correlation coefficients of the fit parameters are shown in Fig. 10.13. One can observe that the neighbouring templates with respect to the jet multiplicity are anti-correlated. This is expected and desired since in this way the efficiency for the individual templates can be adjusted according to data. The `lepton + 3 jets` and the `lepton + 5 jets` template show no correlation because the overlap between them is very small.

10.3. Discussion of results

10.3.1. Lepton + jets fiducial cross section measurement

With the help of a likelihood method evaluating the uncertainties in pseudo experiments the fiducial $t\bar{t}$ production cross section based on a particle level selection described in Sec. 10.1 is measured in the lepton + jets channel using kinematic variables in a b -tagged

Table 10.6.: *Table of estimated uncertainties. The uncertainties are extracted as described in the text.*

Statistical error (%)	+0.5	-0.5
Object selection (%)		
Jet energy scale	+4.6	-4.1
Jet reconstruction efficiency	+0.5	-0.4
Jet energy resolution	+2.3	-2.0
Electron scale factors	+1.4	-1.4
Muon scale factors	+1.1	-0.9
Electron energy resolution	+0.2	-0.2
Muon momentum resolution	+0.5	-0.4
Electron energy scale	+0.2	-0.2
Muon energy scale	+0.2	-0.0
Missing E_T	+0.3	-0.1
Background modelling and normalisation (%)		
W + jets normalisation	+2.2	-2.5
single top normalisation	+1.1	-1.2
QCD multi-jet normalisation	+2.4	-2.2
Z + jets/diboson normalisation	+0.9	-0.8
W + jets heavy flavour content	+0.3	-0.4
W + jets shape	+0.2	-0.2
QCD shape	+0.1	-0.1
$t\bar{t}$ signal modelling (%)		
ISR/FSR ¹	+0.5	-0.5
NLO generator ¹	+0.1	-0.1
LO generator ¹	+0.5	-0.5
Hadronisation ¹	+0.4	-0.4
PDF	+1.1	-1.3
oops shape	+0.0	-0.1
oops normalisation	+1.0	-0.8
Others (%)		
b -tagging calibration	+4.1	-3.9
Jet vertex fraction scale factors	+1.8	-1.3
Luminosity	+2.1	-2.2
Total uncertainty (%)	+8.4	-7.8

¹ evaluated in addition to other uncertainties in pseudo experiments

10. Fiducial cross section measurement

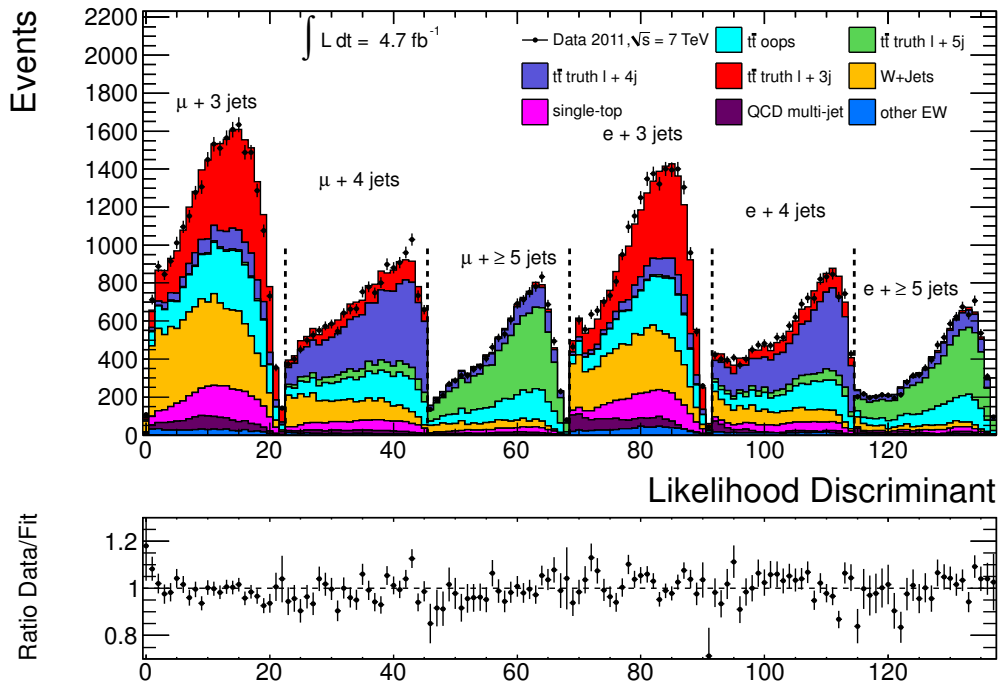


Figure 10.12.: Result of the combined likelihood fit in the six lepton + jets channels to data. Statistics tests of the compatibility of the fitted stack of templates with data are shown as well.

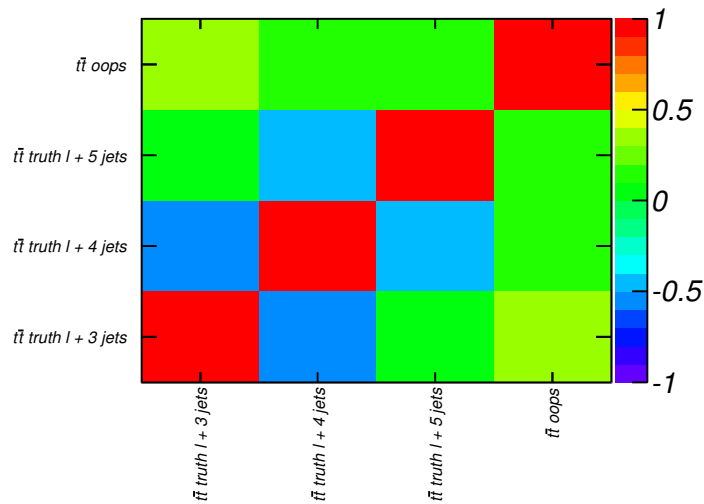


Figure 10.13.: Correlation matrix of the $t\bar{t}$ fit parameters as obtained from the fit in all six analysis channels. Shown are the linear correlation coefficients.

sample to

$$\sigma_{t\bar{t}} = 24.4_{-1.9}^{+2.0} \text{ pb}, \quad (10.2)$$

in a data set of $\mathcal{L} = 4.7 \text{ fb}^{-1}$ recorded with the ATLAS experiment in proton-proton collisions at a centre-of-mass energy of $\sqrt{s} = 7 \text{ TeV}$. The measurement is performed in events with 3, 4 and ≥ 5 jets assuming a top quark mass of $m_t = 172.5 \text{ GeV}$. The total uncertainty amounts to 8%. It is limited by the systematic uncertainties, where the dominant ones are found to be related to the jet energy scale and the b -tagging calibration. For sake of stability and validation of the method a simple binned likelihood fit is used instead of the profile likelihood method for the previous measurements. In general, as described in Sec. 7.2 most systematic variations are obtained in very different event topologies than top quark pair final states. Since they aim to be valid for a large number of event topologies they are conservatively estimated. As the understanding of experimental systematic uncertainties has only partly been improved with respect to the 2011 analysis (a) while the likelihood method used for the fiducial measurement is not able to adjust the size of uncertainties from data one cannot obtain more precise experimental uncertainties. However, the generator uncertainties are almost completely absorbed by the measurement in the fiducial volume showing the huge potential that resides within this measurement approach. Future measurements will be able to obtain significantly lower uncertainties than before when adapting the method of performing a fiducial cross section measurement. As a side-remark it should also be noted that due to the much larger data set the statistical uncertainty is now completely negligible.

To perform a cross-check of the measurement approach one can perform the fit to data using the other available $t\bar{t}$ samples. The fit results are shown in Fig. 10.14 and listed for the individual processes in Appendix Sec. F.4. One can see that not all cross section values are covered by the theory uncertainties within the 1σ -band shown. This is partly due to the choice that the uncertainties, which are evaluated separately, are symmetrised. Not symmetrising would increase the uncertainty bounds towards positive values and reduce them towards lower values so that all points were well inside two standard deviations. The large difference between POWHEG+PYTHIA and POWHEG+HERWIG is found to be related to the different response to b -tagging. The predictions drift apart the more b -tagged jets are required. This is covered by the b -tagging calibration uncertainty, but now shown here. Nevertheless, all points are clearly covered by the full 8% uncertainty.

Using the fit results of the individual $t\bar{t}$ signal generators one can observe significant improvement of the data-prediction ratio for a large number of kinematic distributions. This is shown in Fig. 10.15 for MC@NLO and ALPGEN+HERWIG, which show the largest deviations from data before fit in opposite directions for events with five and more jets. While MC@NLO predicts too few events with respect to data ALPGEN+HERWIG predicts about 10% too many. Even though the overall normalisation is improved significantly, the shape of the individual distributions changes only slightly. For an improved description of the discriminant shapes one would have to unfold object-wise rather than using the comparably simple approach of adjusting only the jet multiplicity efficiencies.

10. Fiducial cross section measurement

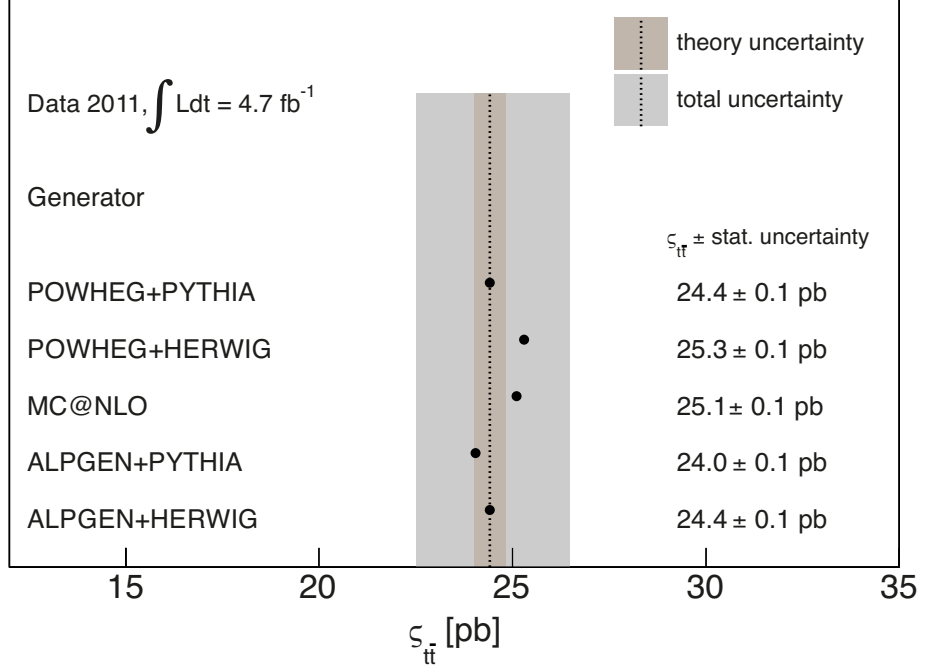


Figure 10.14.: Fiducial $t\bar{t}$ cross sections obtained using different $t\bar{t}$ signal generators fit to data in comparison to the value obtained using POWHEG+PYTHIA (error band). The theoretical uncertainties (brown) are added in quadrature to the total uncertainty (grey). Statistical uncertainties are negligible.

10.3.2. Interpretation in full phase space

For comparison to the full phase space cross sections obtained in the previous chapters one needs to extrapolate from the fiducial volume to the full phase space. This only depends on theoretical uncertainties, in particular the different generator acceptances and additionally also PDF uncertainties and ISR/FSR outside the fiducial volume. The acceptances of the different generators are given in Tab. 10.7. The POWHEG+PYTHIA prediction shows the lowest acceptance whereas ALPGEN+HERWIG has the highest one, the difference between them amounting to 8.3%. The effect of ISR/FSR amounts to (+2.5/−1.5)% while the PDF uncertainties add (+2.0/−1.5)% in quadrature.

The interpretation can now be made in several ways. The most conservative interpretation would be to take the envelope of uncertainties. Since the choice of the central $t\bar{t}$ generator has been made arbitrarily, the acceptance uncertainty is symmetrised. Using the acceptance for POWHEG+PYTHIA, the top quark-antiquark pair cross section in the full phase space is determined to

$$\sigma_{t\bar{t}} = 176 \pm 17 \text{ pb}, \quad (10.3)$$

with a total uncertainty of (+9.8/−9.6)%. A more realistic estimate is to only quote the acceptance uncertainty for the NLO generators, namely the parton shower uncertainty

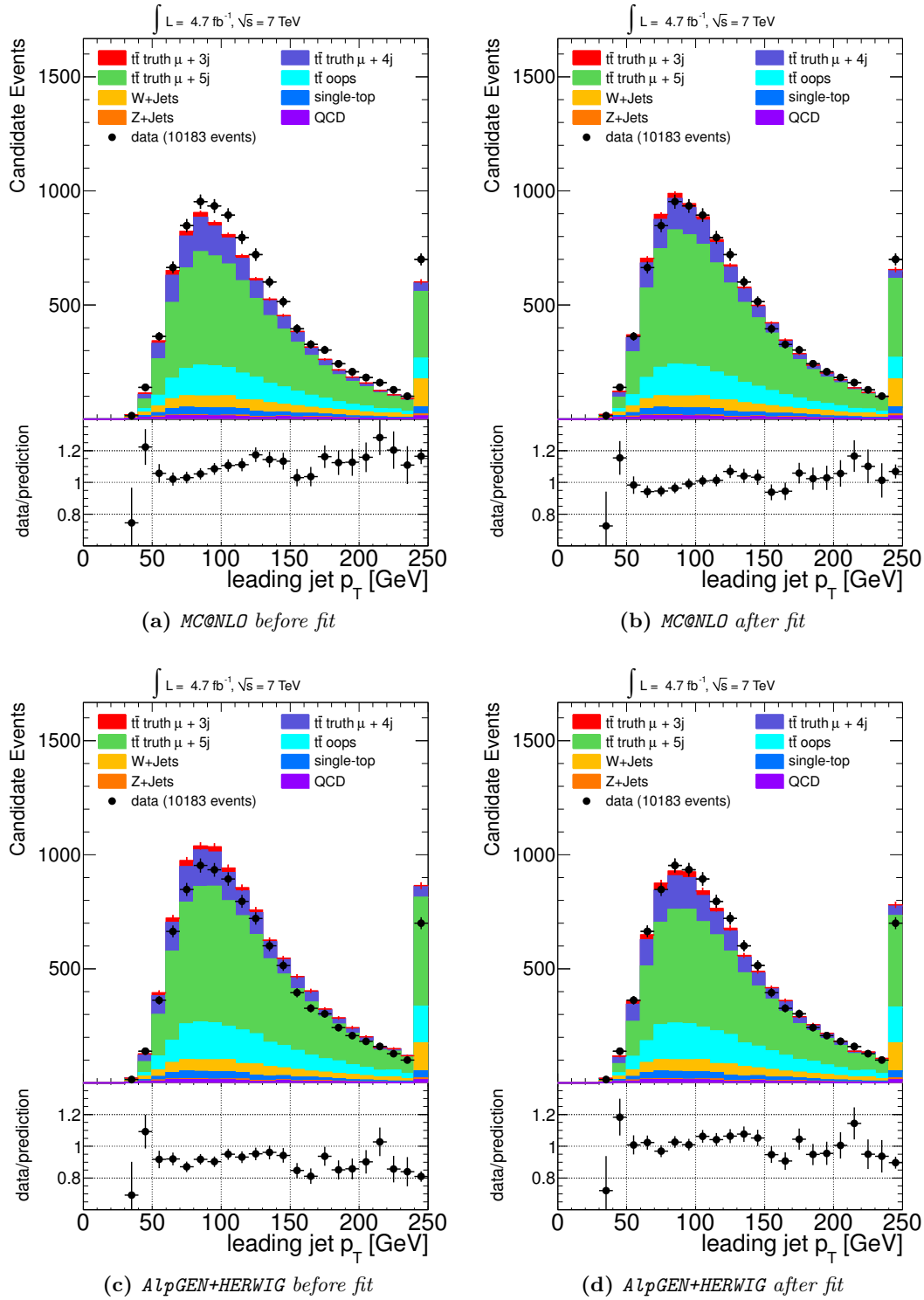


Figure 10.15.: Leading jet p_T for five and more jets for MC@NLO (top) and AlpGEN+HERWIG (bottom) before (left) and after fit (right).

Table 10.7.: *Fiducial cross sections, $\varsigma_{t\bar{t}}$, and particle level selection acceptance for the different $t\bar{t}$ signal generators and additionally for the ALPGEN+PYTHIA ISR/FSR variation samples.*

Generator	acceptance
POWHEG+PYTHIA	0.1390 ± 0.0002
POWHEG+HERWIG	0.1463 ± 0.0001
MC@NLO	0.1454 ± 0.0001
AlpGEN+PYTHIA	0.1453 ± 0.0002
AlpGEN+HERWIG	0.1506 ± 0.0002
AlpGEN+PYTHIA (ktfac = 0.5)	0.1489 ± 0.0002
AlpGEN+PYTHIA (ktfac = 2)	0.1431 ± 0.0001

between PYTHIA and HERWIG ($\pm 2.6\%$) and the difference between POWHEG+HERWIG and MC@NLO ($\pm 0.6\%$) instead of the envelope. Unfortunately, no ISR/FSR uncertainties for NLO generators were available, so that the larger LO generator ones have to be quoted. The uncertainty for the full phase space cross section is then found to be $(+9.4/-9.1)\%$.

Furthermore, instead of using the central fiducial cross section value obtained using POWHEG+PYTHIA one can use the values obtained employing the different $t\bar{t}$ signal generators shown in Sec. 10.3.1 and their individual acceptances. The results are shown in Fig. 10.16. For the AlpGEN predictions the parton shower uncertainty is taken from the intrinsic PYTHIA and HERWIG comparison, which amounts to $\pm 0.2\%$ and as generator uncertainty the difference between AlpGEN+PYTHIA and POWHEG+PYTHIA ($\pm 2.2\%$). All values are in agreement with theory. The LO cross sections are slightly lower than the NLO ones. However, with the experimental precision at hand there is now the need for the full NNLO calculation of the top quark-antiquark pair cross section (see Sec. 2.2.4) to allow further scrutiny of the Standard Model.

10.3.3. Comparison to previous measurements

In order to compare the different top quark-antiquark pair cross section measurements presented in this work on a reasonable basis one needs to evaluate the size of the individual uncertainty components. Herefore, the uncertainty is split into contributions from signal modelling, experimental, and statistical uncertainties. The experimental uncertainties are split further into uncertainties from the use of b -tagging (calibration and heavy flavour content in the $W + \text{jets}$ sample) and all other experimental uncertainties. This is shown in Fig. 10.17. It should, however, be noted that the analyses are not fully comparable since uncertainties are evaluated differently and also prescriptions changed over time. One can observe that the b -tagging calibration has a big impact on the total uncertainty, also for the 2011 analysis (b). While it is a powerful tool to suppress the dominant $W + \text{jets}$ background a measurement aiming for highest precision should most likely refrain from using b -tagging information as demonstrated in the 2011 analysis (a). One can also clearly see that the 2010 analysis being the first precision measurement of

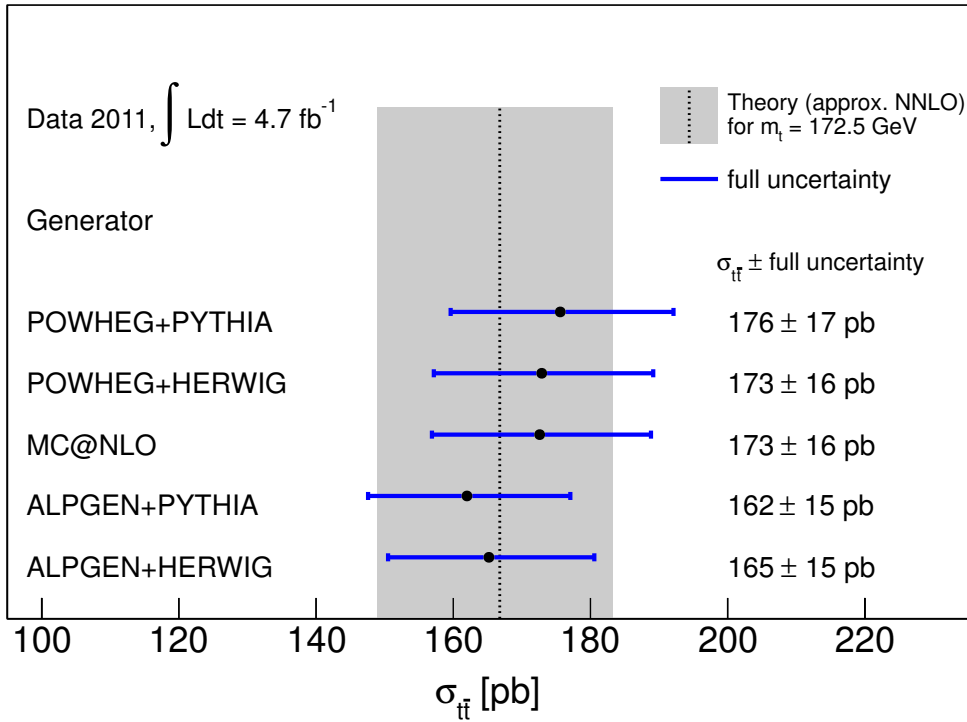


Figure 10.16.: Interpretation of the $t\bar{t}$ cross section in the full phase space obtained using different $t\bar{t}$ signal generators fit to data and their acceptances in comparison to theory calculated using *Hathor* [94]. Uncertainties are obtained as described in the text.

the $t\bar{t}$ cross section exploiting a comparably small data set is not competitive with the other two analyses with respect to the size of uncertainties. The uncertainty components for the 2011 analyses, however, nicely show the capabilities of both measurement approaches. For this purpose only the other uncertainties unrelated to b -tagging are compared. The 2011 analysis (a) unfortunately suffers from limited Monte Carlo statistics, making the statistical uncertainty comparably large, which would otherwise scale with the square root of the number of events. Nevertheless, the largest difference between the two methods lies in the experimental and signal modelling uncertainties. They roughly differ by factors of two between the two analyses: While the 2011 analysis (a) has very small experimental uncertainties of only 3.4% thanks to the profile likelihood method, the 2011 analysis (b) has an experimental uncertainty of 6.3% (7.6% including b -tagging) due to the evaluation of uncertainties in pseudo experiments only. Conversely, the size of the signal modelling uncertainties for the 2011 analysis (a) is even larger than the experimental ones (3.6%) whereas the 2011 analysis (b) is almost independent of the signal modelling uncertainties (1.7%). Even though the total uncertainty of the 2011 analysis (a) is smaller than the one of the 2011 analysis (b) it is questionable whether with the

10. Fiducial cross section measurement

knowledge and signal samples available for the 2011 analysis (b) the analysis would have been performed in the same way. As summarised in Tab. 10.8 no comparison to the leading order generators has been performed for the full phase space analyses, which would cause additional large uncertainties. Using the fiducial measurement approach, however, modelling uncertainties are almost completely negligible.

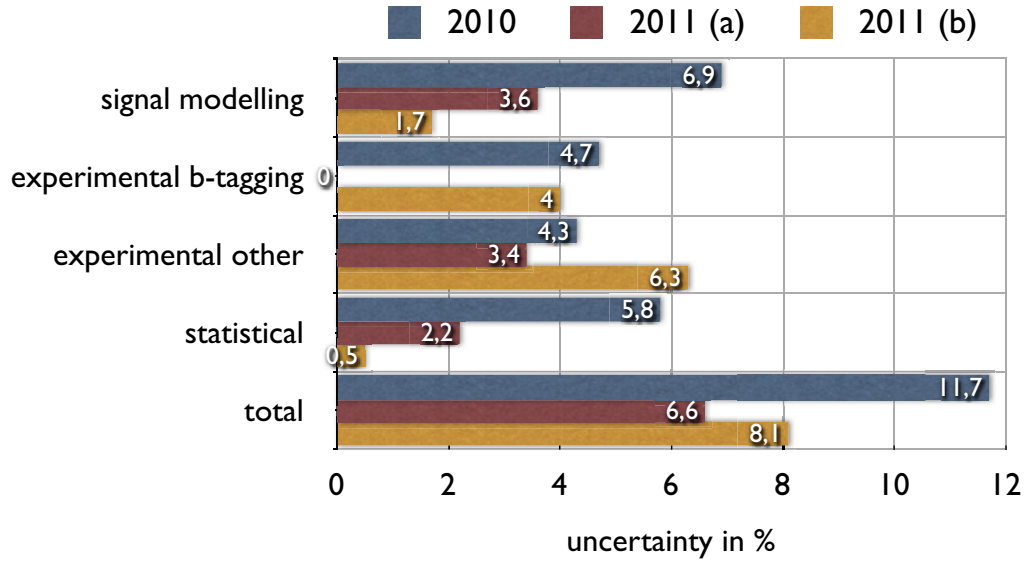


Figure 10.17.: Comparison of uncertainties for the different $t\bar{t}$ cross section measurements presented in this work. Luminosity uncertainty is not included in the experimental uncertainty. Mind that not all uncertainties are evaluated in the same way.

Table 10.8.: Significant differences in the evaluation of systematic uncertainties between the analyses presented in this work.

	2010 analysis	2011 analysis (a)	2011 analysis (b)
Use of profiling	✓	✓	-
Use of b -tagging	✓	-	✓
Treatment of background processes	fit	fit	fixed
<i>$t\bar{t}$ samples evaluated for modelling uncertainties:</i>			
POWHEG+PYTHIA	✓	✓	central
POWHEG+HERWIG	✓	✓	✓
MC@NLO	central	central	✓
AlpGEN+PYTHIA	-	-	✓
AlpGEN+HERWIG	-	-	✓

The only other top quark-antiquark measurement performed by ATLAS using the full

2011 data set in the lepton + jets channel is a measurement using semileptonic b decays [292]. This measurement has the advantage of being sensitive to substantially different sources of systematic uncertainties by relying on the identification of a lower momentum muon close to a jet. The dominant backgrounds are estimated from data and the signal cross section is extracted using a simple cut and count approach. The cross section yields:

$$\sigma_{t\bar{t}} = 165 \pm 2 \text{ (stat.)} \pm 17 \text{ (syst.)} \pm 3 \text{ (lumi.)pb,} \quad (10.4)$$

with a total uncertainty of 10.5%. However, the signal modelling uncertainties are also in this analysis significant amounting to 5.2%.

With the large 2011 data set the $t\bar{t}$ cross section measurements in the dilepton channels become more precise such as the latest CMS result [289] already briefly discussed in Sec. 9.4.2. It only has a total uncertainty of 4.2% of which the signal modelling uncertainties amount to less than 1%. Measurements in the dilepton channel have the advantage of being less sensitive to jet energy scale uncertainties due to the lower number of jets and are less prone to background processes.

10.3.4. Prospects of the measurement method

As discussed above in Sec. 10.3.3 all previous inclusive top quark cross section measurements are significantly affected by signal modelling uncertainties and acceptance corrections. The 2011 analysis (b) performing the first fiducial $t\bar{t}$ cross section measurement illustrates a new measurement approach for inclusive top quark cross section measurements with the big advantage of being almost independent of those uncertainties. Additional theoretical uncertainties e.g. for interpretation of the measurement in the full phase space are cleanly separated from the experimental ones. This measurement, however, can only be considered as pioneering work. Combining the fiducial cross section approach with a profile likelihood method as used for the previous two analyses presented in this work would significantly reduce systematic uncertainties. Furthermore, the unfolding approach could be refined by an object based unfolding approach. The latter, however, is easier in the dileptonic channel: The two leptons can easily be associated to the particle level by lepton flavour and charge, the jets from the top quark decays can be identified using b -tagging information and therefore additional radiation can also be pinned down. In principle, only E_T^{miss} is generator-dependent. Another advantage of the dilepton channel would be the smaller backgrounds as discussed before.

11. Conclusions

The Standard Model of Particle Physics (SM) summarises the current knowledge on the interactions of the basic building blocks of matter. The top quark, being the heaviest fundamental particle known today, is an important part of the Standard Model and plays a special role when searching for new phenomena beyond current knowledge. It may be that the top quark has unpredicted properties related to a role in electroweak symmetry breaking, or that undiscovered particles are contaminating the top quark sample, causing changes to the production rate of top quarks. At the same time, top quarks pose a major background to several new phenomena at large momentum transfer. Therefore, thorough understanding of its production mechanism is crucial.

At the end of the first Large Hadron Collider (LHC) run, current measurements of the top quark-antiquark pair production cross section reach a precision competitive to the Tevatron and theoretical predictions. In this thesis three of those measurements performed in proton-proton collisions at a centre-of-mass energy of $\sqrt{s} = 7$ TeV using the ATLAS detector are presented. They are based on the selection of decays of top quark-antiquark pairs in which one of the top quarks has a lepton (electron or muon) and a neutrino in the final state whereas the other top quark's final state consists of hadronic particles only. The events are classified by the flavour of the identified lepton and the number of jets in the event requiring three, four, or five and more jets. Using a small set of variables chosen to discriminate the $t\bar{t}$ signal from the dominant $W +$ jets background a projective likelihood discriminant is built for each of the six event classes. These distributions are employed to perform a negative log-likelihood fit to data to extract the signal cross section. The first two measurements incorporate a large number of systematic uncertainties as nuisance parameters in the fit. The behaviour of these parameters in the fit is studied in detail in this thesis.

The measurement performed using the data set recorded in 2010 with an integrated luminosity of $\mathcal{L} = 35 \text{ pb}^{-1}$ yields

$$\sigma_{t\bar{t}} = 187 \pm 11 \text{ (stat.) } {}^{+18}_{-17} \text{ (syst.) } \pm 6 \text{ (lumi.) pb} = 187 {}^{+21}_{-20} \text{ pb.} \quad (11.1)$$

With an uncertainty of 11% this constitutes the most precise measurement of the top quark-antiquark cross section in 2010 data. This analysis in contrast to the other two makes use of a transformed form of the b -tagging probability distribution for the two most b -like jets, which is a very good discriminant against $W +$ jets events. The measurement is limited by the experimental systematic uncertainties amounting to 8.5%, the dominant ones being the calibration of the b -tagging algorithms and the heavy flavour content in the $W +$ jets sample. The $t\bar{t}$ signal modelling uncertainties of 6.9% are also comparably large.

11. Conclusions

The first analysis using 2011 data and an integrated luminosity of $\mathcal{L} = 0.7 \text{ fb}^{-1}$ measures a $t\bar{t}$ production cross section of

$$\sigma_{t\bar{t}} = 179.0 \pm 4.1 \text{ (stat.)} \pm 8.8 \text{ (syst.)} \pm 6.6 \text{ (lumi.) pb} = 179.0_{-11.7}^{+11.8} \text{ pb}, \quad (11.2)$$

with a total uncertainty of only 6.6% thanks to the larger data set and an improved analysis approach. In the likelihood discriminant the b -tagging information used in the 2010 measurement is replaced by the transverse momentum of the jet with highest transverse momentum in the event. This allows to constrain better the jet energy scale uncertainty in the fit. Furthermore, the uncertainty due to the modelling of initial and final state radiation is reduced. For this analysis the signal modelling uncertainties of 3.6% are slightly larger than the experimental ones of 3.4%.

To overcome the large signal modelling uncertainties observed for the previous two measurements the cross section measurement exploiting the full 2011 data set with an integrated luminosity of 4.7 fb^{-1} restricts the phase space used for comparison with theory to the phase space accessible to the detector. This is usually referred to as fiducial measurement. By performing an additional selection at particle level and using a Bayesian data-driven efficiency reweighting to adjust simulation to data the signal modelling uncertainties are reduced to 1.7%. Since the experimental uncertainties are not included as nuisance parameters in the fit they cannot be constrained and are determined to 7.6%. In principle these could be included in the fit to reduce them to at least the same level as achieved for the first measurement in 2011 data. The total uncertainty amounts to 8%.

Both analyses performed using 2011 data exceed the precision of theoretical calculations performed at approx. NNLO. In combination they show how experimental and modelling uncertainties can be reduced to be competitive with the awaited top quark-antiquark pair production cross section calculation at full NNLO. With the large data set available from 2011 and 2012 proton-proton collisions at the LHC, however, measurements of the cross section in top quark pair final states with two leptons promise even higher precision due to lower backgrounds. Furthermore, precise measurements of the differential cross section as a function of several variables are desirable to improve the signal modelling.

With the measurements performed in this analysis the Standard Model has been scrutinised once again but no deviations have been found. However, with the accuracy reached more precise theoretical predictions are now needed for further investigation. Nevertheless, the excellent understanding of top quarks at the LHC now allows for further precision measurements and the use of top quark events as a laboratory for the development of novel analysis methods.

A. Monte Carlo samples used in the analyses

The detailed list of Monte Carlo simulation samples used in the analysis is given in Tab. A.1.

Table A.1.: Summary of Monte Carlo samples used for the analysis. The ID refers to the internal ATLAS MC sample ID.

physics process	generator	ID	comments
$t\bar{t}$ (no all-hadronic) $m_t = 172.5$ GeV	MC@NLO/HERWIG	105200	nominal NLO signal sample
$t\bar{t}$ (no all-hadronic)	POWHEG/HERWIG	105860	NLO generator uncertainty
$t\bar{t}$ (no all-hadronic)	POWHEG/PYTHIA	105861	parton shower uncertainty
$t\bar{t}$ dileptonic + 0 partons	AlpGEN/HERWIG	105890	LO signal sample ¹
$t\bar{t}$ dileptonic + 1 partons	AlpGEN/HERWIG	105891	LO signal sample ¹
$t\bar{t}$ dileptonic + 2 partons	AlpGEN/HERWIG	105892	LO signal sample ¹
$t\bar{t}$ dileptonic + 3 partons	AlpGEN/HERWIG	105897	LO signal sample ¹
$t\bar{t}$ dileptonic + 4 partons	AlpGEN/HERWIG	105898	LO signal sample ¹
$t\bar{t}$ dileptonic + ≥ 5 partons	AlpGEN/HERWIG	105899	LO signal sample ¹
$t\bar{t}$ l +jets + 0 partons	AlpGEN/HERWIG	105894	LO signal sample ¹
$t\bar{t}$ l +jets + 1 partons	AlpGEN/HERWIG	105895	LO signal sample ¹
$t\bar{t}$ l +jets + 2 partons	AlpGEN/HERWIG	105896	LO signal sample ¹
$t\bar{t}$ l +jets + 3 partons	AlpGEN/HERWIG	117887	LO signal sample ¹
$t\bar{t}$ l +jets + 4 partons	AlpGEN/HERWIG	117888	LO signal sample ¹
$t\bar{t}$ l +jets + ≥ 5 partons	AlpGEN/HERWIG	117889	LO signal sample ¹
$t\bar{t}$ dileptonic + 0 partons	AlpGEN/PYTHIA	117113	LO signal sample ¹
$t\bar{t}$ dileptonic + 1 partons	AlpGEN/PYTHIA	117114	LO signal sample ¹
$t\bar{t}$ dileptonic + 2 partons	AlpGEN/PYTHIA	117115	LO signal sample ¹
$t\bar{t}$ dileptonic + 3 partons	AlpGEN/PYTHIA	117116	LO signal sample ¹
$t\bar{t}$ dileptonic + 4 partons	AlpGEN/PYTHIA	117117	LO signal sample ¹
$t\bar{t}$ dileptonic + ≥ 5 partons	AlpGEN/PYTHIA	117118	LO signal sample ¹
$t\bar{t}$ l +jets + 0 partons	AlpGEN/PYTHIA	117083	LO signal sample ¹
$t\bar{t}$ l +jets + 1 partons	AlpGEN/PYTHIA	117084	LO signal sample ¹
$t\bar{t}$ l +jets + 2 partons	AlpGEN/PYTHIA	117085	LO signal sample ¹
$t\bar{t}$ l +jets + 3 partons	AlpGEN/PYTHIA	117086	LO signal sample ¹
$t\bar{t}$ l +jets + 4 partons	AlpGEN/PYTHIA	117087	LO signal sample ¹
$t\bar{t}$ l +jets + ≥ 5 partons	AlpGEN/PYTHIA	117088	LO signal sample ¹
$t\bar{t}$ (no all-had.)	AcerMC/PYTHIA	105205	ISR/FSR uncertainty
$t\bar{t}$ (no all-had.) min. ISR	AcerMC/PYTHIA	117255	ISR/FSR uncertainty ²
$t\bar{t}$ (no all-had.) max. ISR	AcerMC/PYTHIA	117256	ISR/FSR uncertainty ²
$t\bar{t}$ (no all-had.) min. FSR	AcerMC/PYTHIA	117257	ISR/FSR uncertainty ²

continued on next page

A. Monte Carlo samples used in the analyses

Table A.1.: Summary of Monte Carlo samples used for the analysis. The ID refers to the internal ATLAS MC sample ID.

physics process	generator	ID	comments
$t\bar{t}$ (no all-had.) max. FSR	AcerMC/PYTHIA	117258	ISR/FSR uncertainty ²
$t\bar{t}$ (no all-had.) ISR and FSR down	AcerMC/PYTHIA	117259	ISR/FSR uncertainty ²
$t\bar{t}$ (no all-had.) ISR and FSR up	AcerMC/PYTHIA	117260	ISR/FSR uncertainty ²
$t\bar{t}$ (no all-had.) more parton shower	AcerMC/PYTHIA	117209	ISR/FSR uncertainty ¹
$t\bar{t}$ (no all-had.) less parton shower	AcerMC/PYTHIA	117210	ISR/FSR uncertainty ¹
$t\bar{t}$ dileptonic + 0 partons	AlpGEN/PYTHIA	117093	ISR/FSR uncertainty $0.5 \cdot \alpha_s^1$
$t\bar{t}$ dileptonic + 1 partons	AlpGEN/PYTHIA	117094	ISR/FSR uncertainty $0.5 \cdot \alpha_s^1$
$t\bar{t}$ dileptonic + 2 partons	AlpGEN/PYTHIA	117095	ISR/FSR uncertainty $0.5 \cdot \alpha_s^1$
$t\bar{t}$ dileptonic + 3 partons	AlpGEN/PYTHIA	117096	ISR/FSR uncertainty $0.5 \cdot \alpha_s^1$
$t\bar{t}$ dileptonic + ≥ 4 partons	AlpGEN/PYTHIA	117099	ISR/FSR uncertainty $0.5 \cdot \alpha_s^1$
$t\bar{t}$ l +jets + 0 partons	AlpGEN/PYTHIA	117123	ISR/FSR uncertainty $0.5 \cdot \alpha_s^1$
$t\bar{t}$ l +jets + 1 partons	AlpGEN/PYTHIA	117124	ISR/FSR uncertainty $0.5 \cdot \alpha_s^1$
$t\bar{t}$ l +jets + 2 partons	AlpGEN/PYTHIA	117125	ISR/FSR uncertainty $0.5 \cdot \alpha_s^1$
$t\bar{t}$ l +jets + 3 partons	AlpGEN/PYTHIA	117126	ISR/FSR uncertainty $0.5 \cdot \alpha_s^1$
$t\bar{t}$ l +jets + ≥ 4 partons	AlpGEN/PYTHIA	117129	ISR/FSR uncertainty $0.5 \cdot \alpha_s^1$
$t\bar{t}$ dileptonic + 0 partons	AlpGEN/PYTHIA	117133	ISR/FSR uncertainty $2 \cdot \alpha_s^1$
$t\bar{t}$ dileptonic + 1 partons	AlpGEN/PYTHIA	117134	ISR/FSR uncertainty $2 \cdot \alpha_s^1$
$t\bar{t}$ dileptonic + 2 partons	AlpGEN/PYTHIA	117135	ISR/FSR uncertainty $2 \cdot \alpha_s^1$
$t\bar{t}$ dileptonic + 3 partons	AlpGEN/PYTHIA	117136	ISR/FSR uncertainty $2 \cdot \alpha_s^1$
$t\bar{t}$ dileptonic + ≥ 4 partons	AlpGEN/PYTHIA	117139	ISR/FSR uncertainty $2 \cdot \alpha_s^1$
$t\bar{t}$ l +jets + 0 partons	AlpGEN/PYTHIA	117183	ISR/FSR uncertainty $2 \cdot \alpha_s^1$
$t\bar{t}$ l +jets + 1 partons	AlpGEN/PYTHIA	117184	ISR/FSR uncertainty $2 \cdot \alpha_s^1$
$t\bar{t}$ l +jets + 2 partons	AlpGEN/PYTHIA	117185	ISR/FSR uncertainty $2 \cdot \alpha_s^1$
$t\bar{t}$ l +jets + 3 partons	AlpGEN/PYTHIA	117186	ISR/FSR uncertainty $2 \cdot \alpha_s^1$
$t\bar{t}$ l +jets + ≥ 4 partons	AlpGEN/PYTHIA	117189	ISR/FSR uncertainty $2 \cdot \alpha_s^1$
$t\bar{t}$ (no all-had.) $m_t = 140$ GeV	MC@NLO/HERWIG	117207	mass variation ²
$t\bar{t}$ (no all-had.) $m_t = 150$ GeV	MC@NLO/HERWIG	117208	mass variation ²
$t\bar{t}$ (no all-had.) $m_t = 160$ GeV	MC@NLO/HERWIG	116203	mass variation ²
$t\bar{t}$ (no all-had.) $m_t = 165$ GeV	MC@NLO/HERWIG	116208	mass variation ²
$t\bar{t}$ (no all-had.) $m_t = 167.5$ GeV	MC@NLO/HERWIG	116205	mass variation ²
$t\bar{t}$ (no all-had.) $m_t = 170$ GeV	MC@NLO/HERWIG	116201	mass variation ²
$t\bar{t}$ (no all-had.) $m_t = 175$ GeV	MC@NLO/HERWIG	116206	mass variation ²
$t\bar{t}$ (no all-had.) $m_t = 177.5$ GeV	MC@NLO/HERWIG	116207	mass variation ²
$t\bar{t}$ (no all-had.) $m_t = 180$ GeV	MC@NLO/HERWIG	116202	mass variation ²
$t\bar{t}$ (no all-had.) $m_t = 190$ GeV	MC@NLO/HERWIG	116204	mass variation ²
$t\bar{t}$ (no all-had.) $m_t = 200$ GeV	MC@NLO/HERWIG	117205	mass variation ²
$t\bar{t}$ (no all-had.) $m_t = 210$ GeV	MC@NLO/HERWIG	117206	mass variation ²
single top t -channel $W \rightarrow e\nu$	MC@NLO/HERWIG	108340	2
single top t -channel $W \rightarrow \mu\nu$	MC@NLO/HERWIG	108341	2
single top t -channel $W \rightarrow \tau\nu$	MC@NLO/HERWIG	108342	2
single top t -channel $W \rightarrow e\nu$	AcerMC/PYTHIA	117360	1
single top t -channel $W \rightarrow \mu\nu$	AcerMC/PYTHIA	117361	1
single top t -channel $W \rightarrow \tau\nu$	AcerMC/PYTHIA	117362	1

continued on next page

Table A.1.: Summary of Monte Carlo samples used for the analysis. The ID refers to the internal ATLAS MC sample ID.

physics process	generator	ID	comments
single top s -channel $W \rightarrow e\nu$	MC@NLO/HERWIG	108343	
single top s -channel $W \rightarrow \mu\nu$	MC@NLO/HERWIG	108344	
single top s -channel $W \rightarrow \tau\nu$	MC@NLO/HERWIG	108345	
single top tW production	MC@NLO/HERWIG	108346	
$W \rightarrow e\nu + 0$ partons	AlpGEN/HERWIG	107680	
$W \rightarrow e\nu + 1$ parton	AlpGEN/HERWIG	107681	
$W \rightarrow e\nu + 2$ partons	AlpGEN/HERWIG	107682	
$W \rightarrow e\nu + 3$ partons	AlpGEN/HERWIG	107683	
$W \rightarrow e\nu + 4$ partons	AlpGEN/HERWIG	107684	
$W \rightarrow e\nu + \geq 5$ partons	AlpGEN/HERWIG	107685	
$W \rightarrow \mu\nu + 0$ partons	AlpGEN/HERWIG	107690	
$W \rightarrow \mu\nu + 1$ parton	AlpGEN/HERWIG	107691	
$W \rightarrow \mu\nu + 2$ partons	AlpGEN/HERWIG	107692	
$W \rightarrow \mu\nu + 3$ partons	AlpGEN/HERWIG	107693	
$W \rightarrow \mu\nu + 4$ partons	AlpGEN/HERWIG	107694	
$W \rightarrow \mu\nu + \geq 5$ partons	AlpGEN/HERWIG	107695	
$W \rightarrow \tau\nu + 0$ partons	AlpGEN/HERWIG	107700	
$W \rightarrow \tau\nu + 1$ parton	AlpGEN/HERWIG	107701	
$W \rightarrow \tau\nu + 2$ partons	AlpGEN/HERWIG	107702	
$W \rightarrow \tau\nu + 3$ partons	AlpGEN/HERWIG	107703	
$W \rightarrow \tau\nu + 4$ partons	AlpGEN/HERWIG	107704	
$W \rightarrow \tau\nu + \geq 5$ partons	AlpGEN/HERWIG	107705	
$W(\rightarrow l\nu)bb + 0$ partons	AlpGEN/HERWIG	107280	
$W(\rightarrow l\nu)bb + 1$ parton	AlpGEN/HERWIG	107281	
$W(\rightarrow l\nu)bb + 2$ partons	AlpGEN/HERWIG	107282	
$W(\rightarrow l\nu)bb + \geq 3$ partons	AlpGEN/HERWIG	107283	
$W(\rightarrow l\nu)c\bar{c} + 0$ partons	AlpGEN/HERWIG	107284	
$W(\rightarrow l\nu)c\bar{c} + 1$ parton	AlpGEN/HERWIG	107285	
$W(\rightarrow l\nu)c\bar{c} + 2$ partons	AlpGEN/HERWIG	107286	
$W(\rightarrow l\nu)c\bar{c} + \geq 3$ partons	AlpGEN/HERWIG	107287	
$W(\rightarrow l\nu)c + 0$ partons	AlpGEN/HERWIG	107293	
$W(\rightarrow l\nu)c + 1$ parton	AlpGEN/HERWIG	107294	
$W(\rightarrow l\nu)c + 2$ partons	AlpGEN/HERWIG	107295	
$W(\rightarrow l\nu)c + 3$ partons	AlpGEN/HERWIG	107296	
$W(\rightarrow l\nu)c + \geq 4$ partons	AlpGEN/HERWIG	107297	
$Z \rightarrow ee + 0$ partons	AlpGEN/HERWIG	107650	
$Z \rightarrow ee + 1$ parton	AlpGEN/HERWIG	107651	
$Z \rightarrow ee + 2$ partons	AlpGEN/HERWIG	107652	
$Z \rightarrow ee + 3$ partons	AlpGEN/HERWIG	107653	
$Z \rightarrow ee + 4$ partons	AlpGEN/HERWIG	107654	
$Z \rightarrow ee + \geq 5$ partons	AlpGEN/HERWIG	107655	
$Z \rightarrow \mu\mu + 0$ partons	AlpGEN/HERWIG	107660	
$Z \rightarrow \mu\mu + 1$ parton	AlpGEN/HERWIG	107661	

continued on next page

A. Monte Carlo samples used in the analyses

Table A.1.: Summary of Monte Carlo samples used for the analysis. The ID refers to the internal ATLAS MC sample ID.

physics process	generator	ID	comments
$Z \rightarrow \mu\mu + 2$ partons	AlpGEN/HERWIG	107662	
$Z \rightarrow \mu\mu + 3$ partons	AlpGEN/HERWIG	107663	
$Z \rightarrow \mu\mu + 4$ partons	AlpGEN/HERWIG	107664	
$Z \rightarrow \mu\mu + \geq 5$ partons	AlpGEN/HERWIG	107665	
$Z \rightarrow \tau\tau + 0$ partons	AlpGEN/HERWIG	107670	
$Z \rightarrow \tau\tau + 1$ parton	AlpGEN/HERWIG	107671	
$Z \rightarrow \tau\tau + 2$ partons	AlpGEN/HERWIG	107672	
$Z \rightarrow \tau\tau + 3$ partons	AlpGEN/HERWIG	107673	
$Z \rightarrow \tau\tau + 4$ partons	AlpGEN/HERWIG	107674	
$Z \rightarrow \tau\tau + \geq 5$ partons	AlpGEN/HERWIG	107675	
$Z(\rightarrow ee)b\bar{b} + 0$ partons	AlpGEN/HERWIG	109300	¹
$Z(\rightarrow ee)b\bar{b} + 1$ parton	AlpGEN/HERWIG	109301	¹
$Z(\rightarrow ee)b\bar{b} + 2$ partons	AlpGEN/HERWIG	109302	¹
$Z(\rightarrow ee)b\bar{b} + \geq 3$ partons	AlpGEN/HERWIG	109303	¹
$Z(\rightarrow \mu\mu)b\bar{b} + 0$ partons	AlpGEN/HERWIG	109305	¹
$Z(\rightarrow \mu\mu)b\bar{b} + 1$ parton	AlpGEN/HERWIG	109306	¹
$Z(\rightarrow \mu\mu)b\bar{b} + 2$ partons	AlpGEN/HERWIG	109307	¹
$Z(\rightarrow \mu\mu)b\bar{b} + \geq 3$ partons	AlpGEN/HERWIG	109308	¹
$Z(\rightarrow \tau\tau)b\bar{b} + 0$ partons	AlpGEN/HERWIG	109310	¹
$Z(\rightarrow \tau\tau)b\bar{b} + 1$ parton	AlpGEN/HERWIG	109311	¹
$Z(\rightarrow \tau\tau)b\bar{b} + 2$ partons	AlpGEN/HERWIG	109312	¹
$Z(\rightarrow \tau\tau)b\bar{b} + \geq 3$ partons	AlpGEN/HERWIG	109313	¹
WW	HERWIG	105985	
ZZ	HERWIG	105986	
WZ	HERWIG	105987	

¹ used in 2011 analysis (b) only

² used in 2010 and 2011 analysis (a) only

B. QCD multi-jet background estimation using the anti-electron model

In this appendix a detailed discussion of the *anti-electron model* is conducted. Details on the fit procedure are given in Sec. B.1, the evaluation of systematic uncertainties is found in Sec. B.2 and further benchmark distributions in the signal region are shown in Sec. B.3.

B.1. Fit procedure

To estimate the number of expected multi-jet QCD events a binned likelihood fit is utilised of the form:

$$-\log \mathcal{L} = \sum_i^{\text{bins}} (\mu_i - N_i^{\text{data}} \log \mu_i) + \mathcal{G}, \quad (\text{B.1})$$

where

$$\mu_i = \sum_k^{\text{processes}} N_i^{\text{MC}} \cdot \beta_k, \quad (\text{B.2})$$

and the Gaussian constraint

$$\mathcal{G} = -\frac{1}{2} \sum_k^{\text{processes}} \left(\frac{\beta_k - 1}{\sigma_k} \right)^2. \quad (\text{B.3})$$

The variable β_k denotes the ratio of the number of fitted events over the number of expected events according to SM expectation:

$$\sum_k^{\text{processes}} \beta_k = \frac{N^{\text{fit}}}{N^{\text{expected}}}. \quad (\text{B.4})$$

The Gaussian constraints for each process are summarised in Tab. B.1. They are roughly oriented at their theoretical uncertainty. When performing the fit special care is taken that the fit parameters do not run into their limits.

B.2. Evaluation of systematic uncertainties

The statistical and systematic uncertainties are evaluated separately. If the QCD sample has very low statistics this uncertainty can become dominant but with the model chosen here sufficient statistics is ensured.

Table B.1.: *Gaussian constraints applied to MC samples in the fit.*

$t\bar{t}$	20%
single top	10%
W/Z + jets	30%
diboson	added to Z + jets

B.2.1. Statistical uncertainties

The statistical uncertainties of the fitting approach are twofold. The first contribution to the uncertainty is obtained from the fit. As the fit is performed in the sideband, but the estimation is then given in the signal region, one also has to take into account the extrapolation uncertainty. This is estimated by morphing the QCD template within its statistical uncertainty in the signal region. Both uncertainties are then added in quadrature. The statistical uncertainty is usually small compared to the systematic uncertainties (cf. next subsection).

B.2.2. Systematic uncertainties

There are several systematic uncertainties that one has take into account. The uncertainties that only have a very small effect such as the electron energy scale are not discussed here. Focus is put on evaluating potential biases of the method.

As usually done for likelihood methods the linearity of the method is investigated. Using the scale factors obtained from the fit pseudo-experiments are performed injecting QCD fractions from 0.5 to 1.5 the fitted value. The fitted fraction is compared to the injected fraction and fitted with a linear function. One can see that there is no bias of the method. The linearity tests are shown in Fig. B.1 for the different jet bins.

The anti-electron selection is very close to the signal selection. Therefore one has to make sure that contamination of the template with signal electrons is not too high. In order to investigate the effect the anti-electron selection is performed on the MC samples. The model is mainly obtained from `loose` electron and photon triggers, i.e. triggers that don't require good electron identification. These have been pre-scaled very early during data-taking due to the high rate they were producing so that the actual luminosity of the sample is a factor of 10 lower. The contamination of the anti-electron model is found to be at the permille level and therefore negligible.

In order to evaluate the shape uncertainty of the method intrinsically as required for instance for shape fits as used in this work different anti-electron selections have been investigated. The models that gives the largest shape difference has been selected to evaluate the QCD shape uncertainty and has the following requirements:

- require `loose`,
- fail `tight_WithTrackMatch`,

B.2. Evaluation of systematic uncertainties

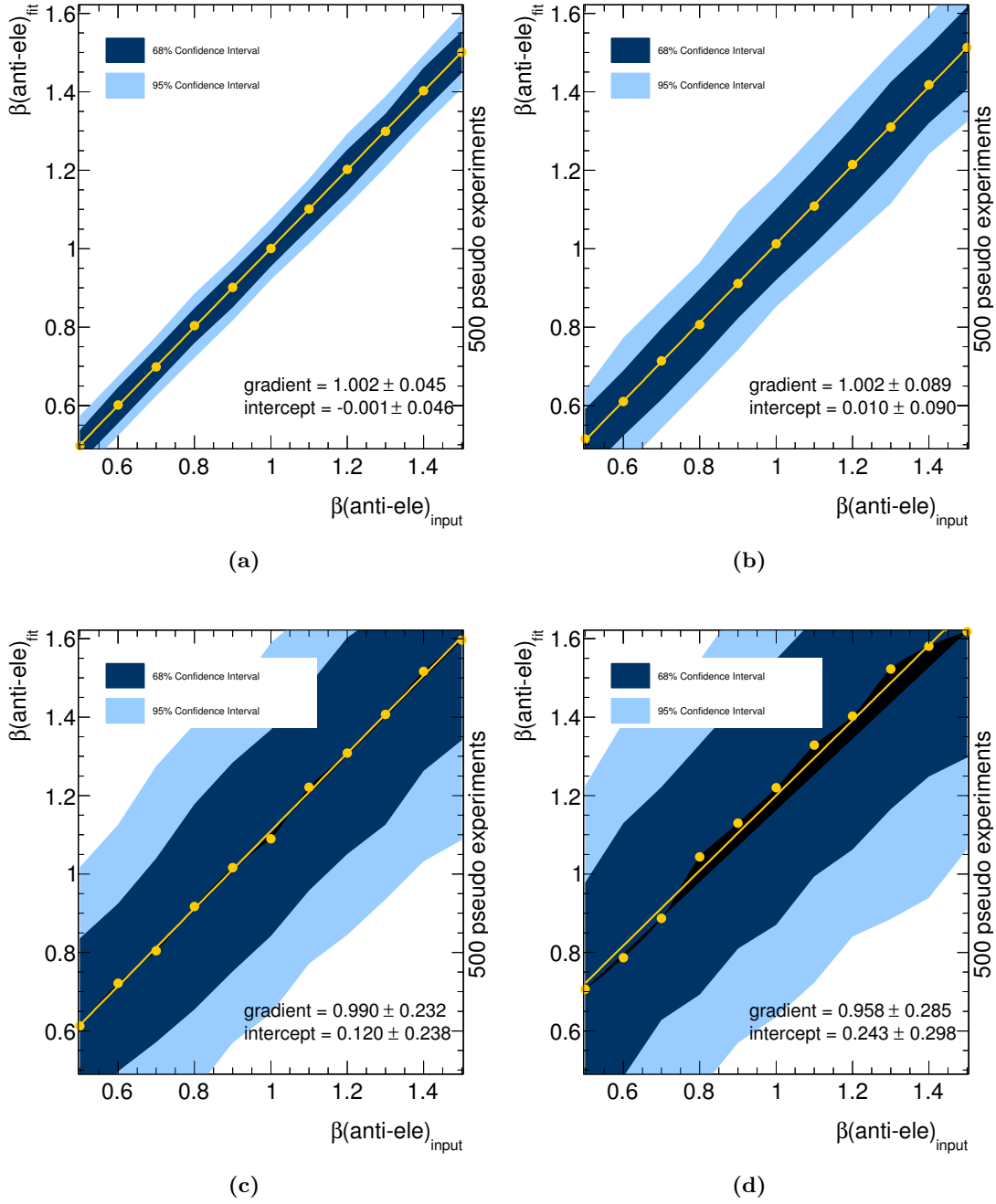


Figure B.1.: Linearity test using 500 pseudo experiments per point varying the QCD multi-jet contribution from 0.5 to 1.5: (a) 2 jet exclusive, (b) 3 jet exclusive, (c) 4 jet exclusive, and (d) 5 jet inclusive jet multiplicity bin. The dark and the light blue areas reflect the 68 and 90% confidence level bands, respectively. In the bottom right the fit result using a linear function is shown. All gradients are compatible with one and the intercepts with zero, though the high jet multiplicity bins are statistically limited.

B. QCD multi-jet background estimation using the anti-electron model

- require `TrackPixel_Electron`, `TrackSi_Electron`, and `TrackMatchEta_Electron`,
- fail `ClusterIsolation_Electron` or `TrackIsolation_Electron`.

A comparison of the nominal model and the alternative model is shown in Fig. B.2. Even though the model has very different shapes data-MC comparison still shows reasonable agreement and the fit results of the nominal and the alternative model agree within uncertainties.

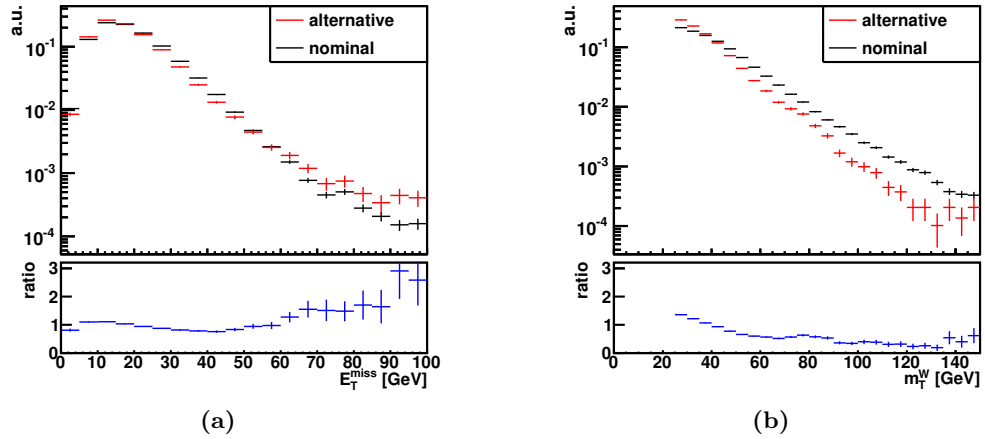


Figure B.2.: Comparison between the nominal (black) and the alternative (red) QCD multi-jet anti-electron model in the 2 jet bin: (a) E_T^{miss} , and (b) W boson transverse mass distribution before applying the E_T^{miss} cut scales to unity and displayed in logarithmic scale. In the bottom part the ratio between the two models is shown.

B.3. Further benchmark distributions

Performance of the method is evaluated using χ^2 and Kolmogorov-Smirnov (KS) statistical tests. From the fit in Sec. 6.2.1.3 one can already observe good agreement. However, to show the good performance of the *anti-electron method* further benchmark distributions in the signal region are considered. These are the transverse W mass (Fig. B.3) and $\Delta\phi$, the difference in ϕ , between E_T^{miss} (Fig. B.4) and the lepton as they show that combined modelling of lepton and E_T^{miss} works. In order to demonstrate that there is no bias when choosing an anti-electron or an electron the lepton kinematics, namely p_T (Fig. B.5), η (Fig. B.6), and ϕ (Fig. B.7) are also presented.

B.3. Further benchmark distributions

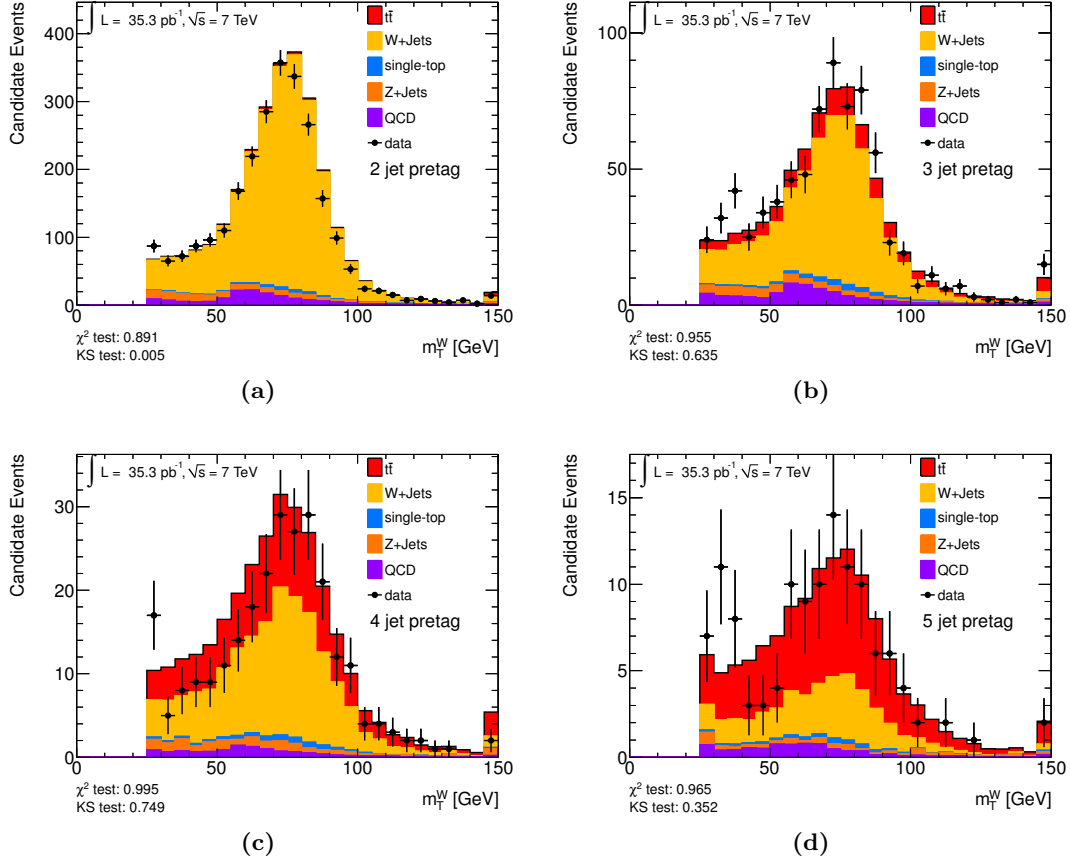


Figure B.3.: W boson transverse mass control plots for QCD multi-jet background evaluation using the anti-electron model after applying the E_T^{miss} cut: (a) 2 jet exclusive, (b) 3 jet exclusive, (c) 4 jet exclusive, and (d) 5 jet inclusive jet multiplicity bin. In the bottom left of each panel the χ^2 and KS test between data and the simulation stack plus QCD model are shown.

B. QCD multi-jet background estimation using the anti-electron model

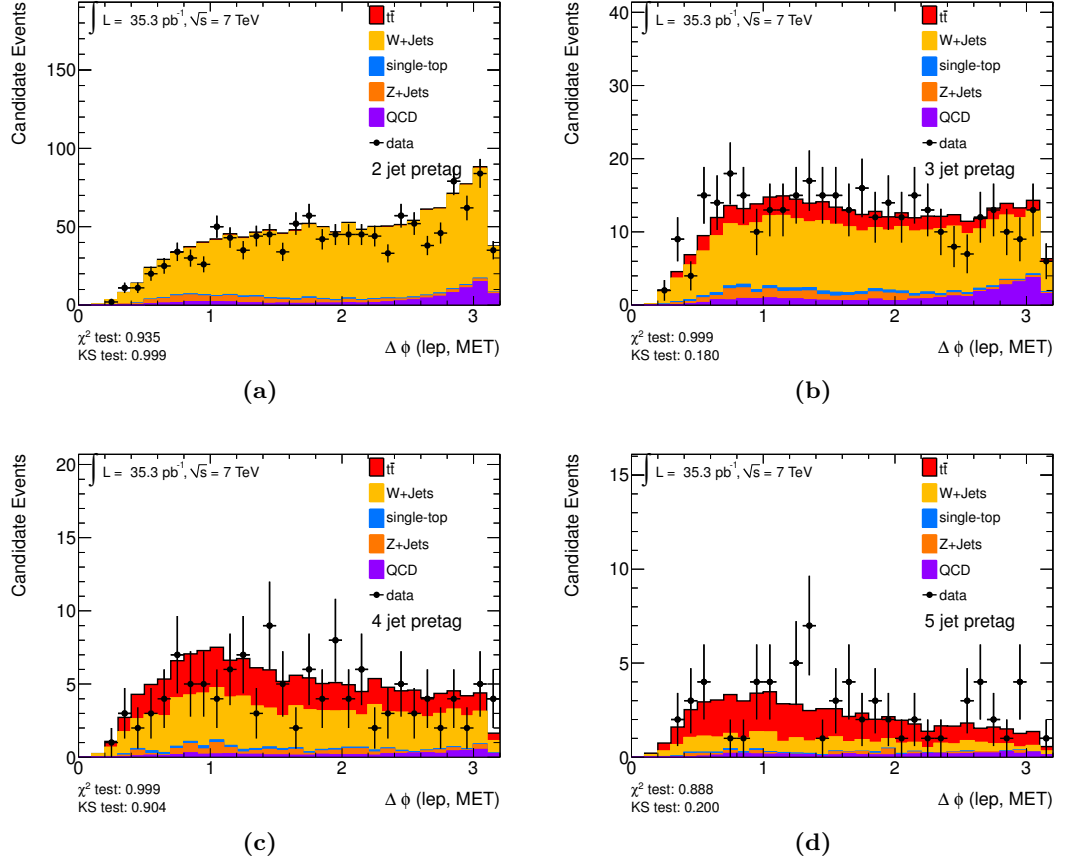


Figure B.4.: $\Delta\phi$ between the charged lepton and the E_T^{miss} vector control plots for QCD multi-jet background evaluation using the anti-electron model after applying the E_T^{miss} cut: (a) 2 jet exclusive, (b) 3 jet exclusive, (c) 4 jet exclusive, and (d) 5 jet inclusive jet multiplicity bin. In the bottom left of each panel the χ^2 and KS test between data and the simulation stack plus QCD model are shown.

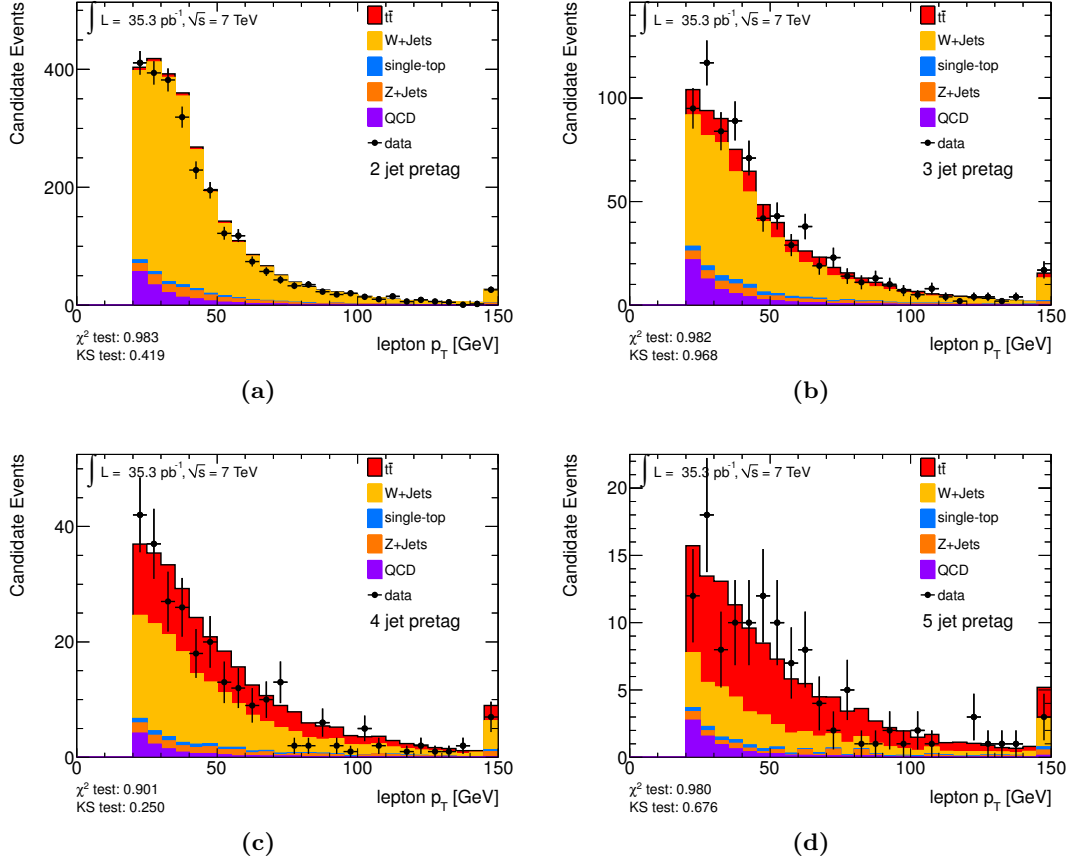


Figure B.5.: Lepton p_T control plots for QCD multi-jet background evaluation using the anti-electron model after applying the E_T^{miss} cut: (a) 2 jet exclusive, (b) 3 jet exclusive, (c) 4 jet exclusive, and (d) 5 jet inclusive jet multiplicity bin. In the bottom left of each panel the χ^2 and KS test between data and the simulation stack plus QCD model are shown.

B. QCD multi-jet background estimation using the anti-electron model

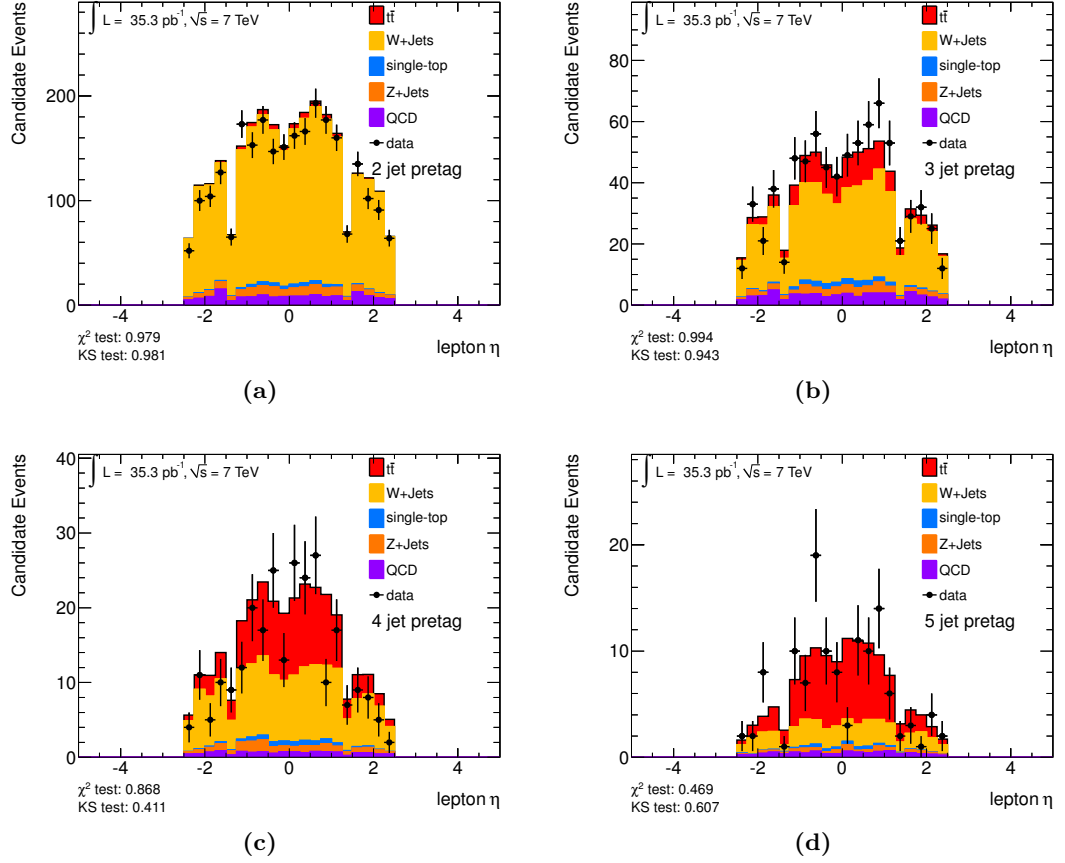


Figure B.6.: *Lepton η control plots for QCD multi-jet background evaluation using the anti-electron model after applying the E_T^{miss} cut: (a) 2 jet exclusive, (b) 3 jet exclusive, (c) 4 jet exclusive, and (d) 5 jet inclusive jet multiplicity bin. In the bottom left of each panel the χ^2 and KS test between data and the simulation stack plus QCD model are shown.*

B.3. Further benchmark distributions

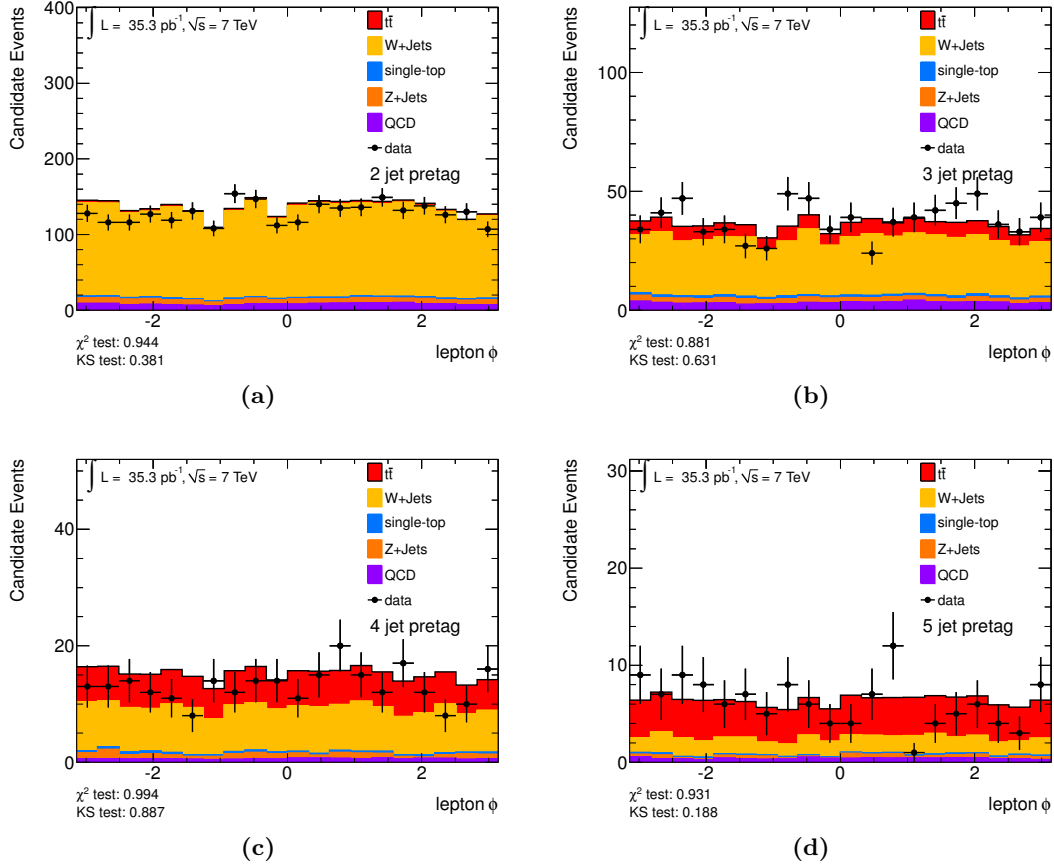


Figure B.7.: *Lepton ϕ control plots for QCD multi-jet background evaluation using the anti-electron model after applying the E_T^{miss} cut: (a) 2 jet exclusive, (b) 3 jet exclusive, (c) 4 jet exclusive, and (d) 5 jet inclusive jet multiplicity bin. In the bottom left of each panel the χ^2 and KS test between data and the simulation stack plus QCD model are shown.*

C. Investigation of the $W +$ heavy flavour contribution uncertainty

As described in Sec. 6.3.1 the $W +$ heavy flavour + jets contribution is estimated in the 1 and 2 jet bin. For the preliminary cross section measurement in the lepton + jets channel using b -tagging information [265] the uncertainty associated with this measurement was one of the dominant ones. Even though the measurement of the $W +$ heavy flavour content in the low jet bins itself shows large uncertainties, the scale factors for $Wb\bar{b}/Wc\bar{c}$ are determined to be 1.3 ± 0.65 and for Wc 1.0 ± 0.4 , the extrapolation to the signal jet bins increases the uncertainties further. Based on statistically and methodologically limited Monte Carlo studies a 20% uncertainty per jet bin is added linearly resulting in an uncertainty of 110% for the $Wb\bar{b}/Wc\bar{c}$ content in the 5 jet inclusive bin.

The idea of this investigation is to reduce this uncertainty. Hereby, the same setup for event generation is used as has been used for the samples analysed in this work. As described in Sec. 5.4.2 the $W +$ jets events are generated using `AlpGEN` [215] with `HERWIG/Jimmy` [218, 219] using the `CTEQ6L1` [73] PDF set. All lepton flavours are generated inclusively. Separate samples are generated for 0–5 partons for $W +$ jets, 0–3 partons for $Wb\bar{b} +$ jets and $Wc\bar{c} +$ jets, and 0–4 partons for $Wc +$ jets, where highest multiplicity sample is generated inclusively. Using the MLM algorithm [231] parton shower and the matrix element calculations are matched. The matching parameters for the parton-jet matching are a minimum transverse momentum of the jet, $p_T = 20$ GeV, and a matching cone of $\Delta R = 0.7$. Jets with transverse momentum or ΔR above these values are taken from a matrix element calculation, jets below this value come from a parton shower. This technique avoids double counting and the number of partons matched to the MLM algorithm defines the parton multiplicity of the sample.

For the systematic studies the following parameters are varied. There are three continuous choices for the parametrisation of the factorisation and normalisation scale denoted by μ in Chapter 2 but now called Q to follow the `AlpGEN` convention. A real parameter, `qfac`, is used to vary the nominal scale of Q , $Q = \text{qfac} \times Q_0$, while the functional form of Q_0 is chosen through the parameter `iqopt` as given in Tab. C.1.

The PDF set choice is steered by the parameter `ndns`. The α_s reweighting scale, which is a multiplicative factor to the appearance of branchings in the parton shower evolution referred to as nodes by the authors, is controlled by the `ktfac` variable. The minimum transverse momentum in GeV to meet the definition of a hard parton is defined by `ptjmin`. The parameter default values as well as the variations studied are summarised in Tab. C.2. The statistics generated for each of the variations is summarised in Tab. C.3. The number of events is only limited by the available computing power and the generator efficiency. The sample cross sections are taken from the generator output after showering

C. Investigation of the $W +$ heavy flavour contribution uncertainty

Table C.1.: Functional form choices of the factorisation and normalisation scale in *AlpGEN*, where m_T is the transverse mass defined as $m_T^2 = m^2 + p_T^2$, and the sum $\sum m_T^2$ extends to all final state partons (including the heavy quarks, excluding the W decay products). Default value is 1.

iqopt value:	0	1	2
Q_0^2 :	$m_W^2 + p_{TW}^2$	m_W^2	$m_W^2 + \sum m_T^2$

Table C.2.: *AlpGEN* default parameters and variations used for $W +$ heavy flavour studies as described in the text.

parameter	default value	variations
iqopt	1	2, 3
ndns	9	106 (MRST2002LO [293])
ktfac	1	2, 0.5
qfac	1	2, 0.5
ptjmin	15	10, 20

for each variation to ensure correct relative normalisation. These are shown in the table for the nominal parameters as well. The cross sections vary by up to 50% depending on the parameter variation but the statistical uncertainty is negligible.

To evaluate the extrapolation effect from the 2 jet bin to the $t\bar{t}$ signal jet bins, a top-like selection based on the electron channel selection in the 2010 analysis is applied at generator truth level. Jet finding is run after showering and hadronisation on the stable interacting particles excluding muons and electrons. The missing transverse energy, E_T^{miss} is calculated from the non-interacting stable particles in the event. Exactly one lepton (here electron, muon or τ lepton) is required with $p_T > 20$ GeV. Jets are taken into account if they have $p_T > 25$ GeV and $|\eta| < 2.5$. The E_T^{miss} has to be greater than 35 GeV and $m_T^W > 25$ GeV. This leads to a reduction of events but ensures that the effects from other phase space regions do not play a role. The same study is performed using the selection for the analysis presented in Reference [246], but is not detailed here.

As described in Sec. 5.4.2, the overlap of events in the $W +$ light jets and the $W +$ heavy flavour jets samples is removed using an angular distance scheme. This scheme is also applied here and divides the events into $W +$ light flavour, $Wb\bar{b}$, $Wc\bar{c}$, and $Wc +$ jets events. For each of these samples the effect of the systematic variations on the jet multiplicity distributions with respect to the nominal samples is evaluated. These are shown in Fig.C.1. One can observe that the higher the jet bin, the larger the effect of the systematic variations. Variations with the largest deviations are **ktfac** and depending on the process also **qfac** and **ptjmin**. Kinematic distributions, as an example the transverse momenta of all jets in the event are shown in Fig. C.3, show the same behaviour. However, the observable of interest is the relative heavy flavour content. Therefore, the relative fraction of each heavy flavour sample with respect to

Table C.3.: *Statistics generated for each parameter variation for a given sample and generator cross section values for the nominal parameter samples. The uncertainty is statistical only.*

sample	number of events	cross section in pb
$W \rightarrow l\nu + 0$ partons	1,000,000	20790 ± 60
$W \rightarrow l\nu + 1$ parton	1,000,000	3910 ± 30
$W \rightarrow l\nu + 2$ partons	1,000,000	1135 ± 11
$W \rightarrow l\nu + 3$ partons	375,000	301 ± 4
$W \rightarrow l\nu + 4$ partons	130,000	75.1 ± 1.9
$W \rightarrow l\nu + 5+$ partons	48,000	19.8 ± 0.5
$Wb\bar{b} \rightarrow l\nu + 0$ partons	1,000,000	47.3 ± 0.1
$Wb\bar{b} \rightarrow l\nu + 1$ parton	1,000,000	35.6 ± 0.2
$Wb\bar{b} \rightarrow l\nu + 2$ partons	200,000	16.97 ± 0.15
$Wb\bar{b} \rightarrow l\nu + 3+$ partons	36,000	6.52 ± 0.11
$Wc\bar{c} \rightarrow l\nu + 0$ partons	1,000,000	133.4 ± 0.2
$Wc\bar{c} \rightarrow l\nu + 1$ parton	1,000,000	105.4 ± 0.6
$Wc\bar{c} \rightarrow l\nu + 2$ partons	137,500	53.3 ± 0.7
$Wc\bar{c} \rightarrow l\nu + 3+$ partons	20,000	17.3 ± 0.18
$Wc \rightarrow l\nu + 0$ partons	1,000,000	438.2 ± 1.8
$Wc \rightarrow l\nu + 1$ parton	1,000,000	161.7 ± 1.3
$Wc \rightarrow l\nu + 2$ partons	1,000,000	42.9 ± 0.5
$Wc \rightarrow l\nu + 3$ partons	675,000	9.86 ± 0.14
$Wc \rightarrow l\nu + 4$ partons	200,000	2.388 ± 0.04

the light flavour sample is evaluated. This value is found to be constant for a given systematic variation over all jet bins as shown in Fig. C.2 and Tab. C.4. The variation with the largest deviation depends on the process. The largest deviations are in general at the 10% level. The extrapolation to the ≥ 5 jet bin suffers from limited statistics and deviations therefore increase to around 25% but with large statistical uncertainty.

In conclusion it is found that the extrapolation uncertainty is found to slightly increase when moving to higher jet bins. However, the previous recipe of linearly adding a 20% extrapolation uncertainty per jet bin to the measurement uncertainty in the 2 jet bin seems to be very conservative. The recommendation from this study is to assume an uncorrelated 25% extrapolation uncertainty independent of the jet bin, which should be added in quadrature since this study is independent of the measurement of the heavy flavour fraction in the 2 jet bin.

C. Investigation of the $W + \text{heavy flavour}$ contribution uncertainty

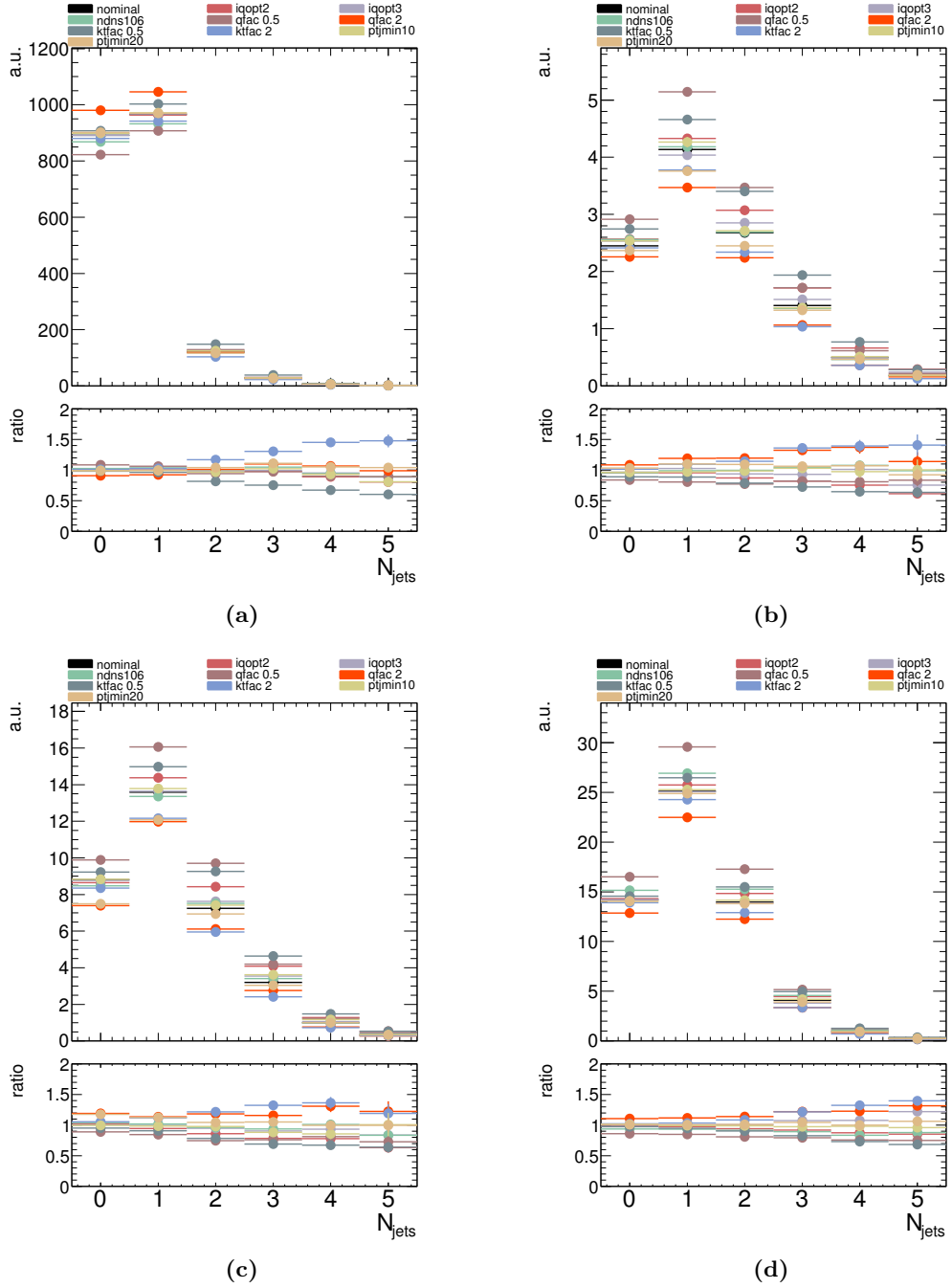


Figure C.1.: *Effect of the systematic variations of the generator parameters on the jet multiplicities in the (a) W light, (b) Wbb , (c) $Wc\bar{c}$, and (d) $Wc + \text{jets}$ sample normalised to 1 pb^{-1} . The 5 jet bin is inclusive. The bottom part of each plot shows the ratio of each variation with respect to the nominal settings. Uncertainties are statistical only.*

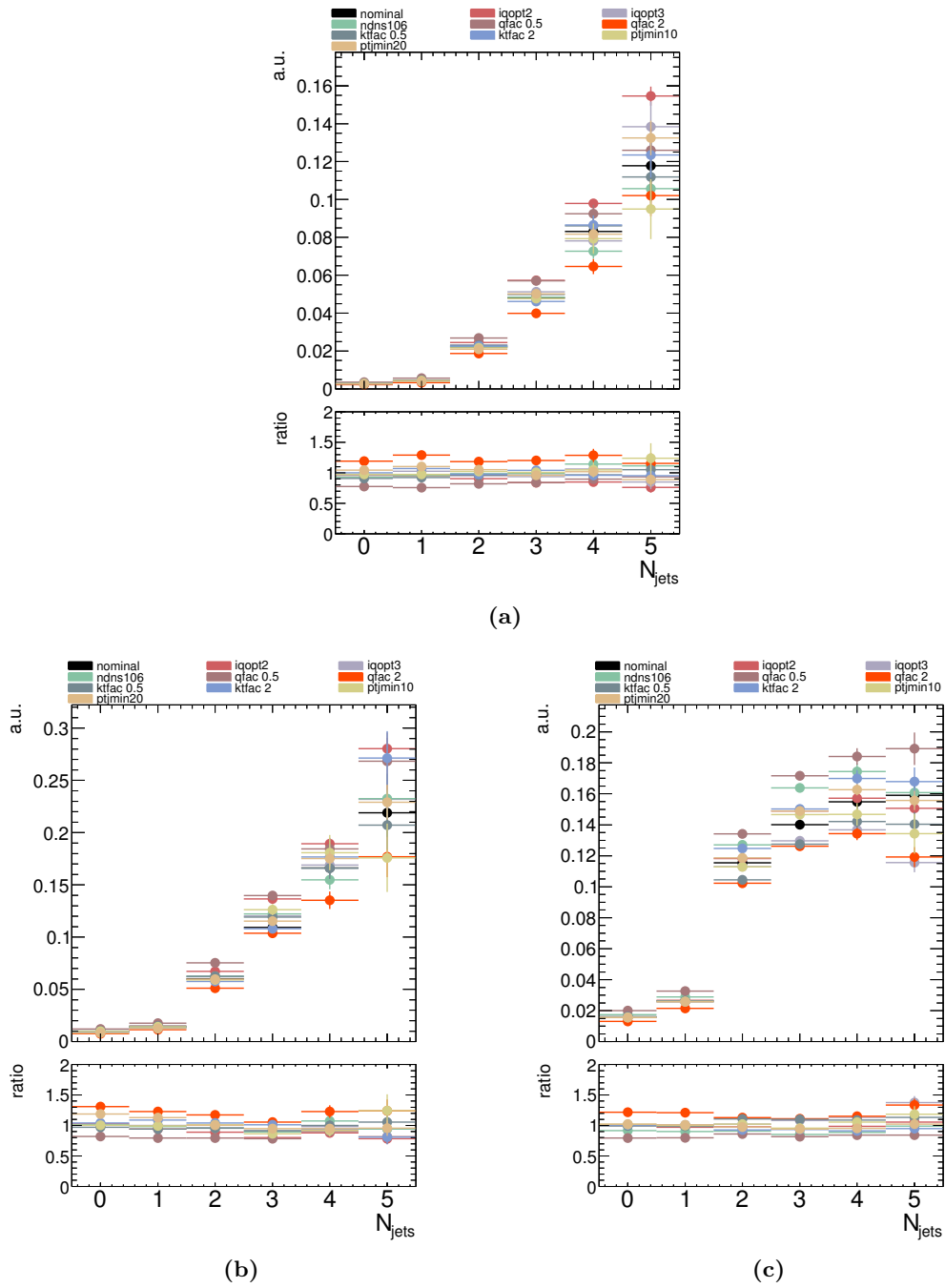


Figure C.2.: *Effect of the systematic variations of the generator parameters on the ratio of the jet multiplicities of the (a) $Wb\bar{b}$, (b) $Wc\bar{c}$, and (c) $Wc + \text{jets}$ sample to the $W + \text{light flavour jets}$ sample. The 5 jet bin is inclusive. The bottom part of each plot shows the ratio of each variation with respect to the nominal settings. Uncertainties are statistical only.*

C. Investigation of the $W +$ heavy flavour contribution uncertainty

Table C.4: Behaviour of $W +$ jets heavy flavour to light flavour fractions for $N/(N-1)$ jet bin ratios for given systematic variation. Deviation is quoted with respect to nominal. Uncertainties are statistical only.

variation	Wbb/W light	deviation	$Wc\bar{c}/W$ light	deviation	Wc/W light	deviation
nominal 3/2 jets	2.17 ± 0.08	$0.0 \pm 0.0\%$	1.83 ± 0.06	$0.0 \pm 0.0\%$	1.21 ± 0.02	$0.0 \pm 0.0\%$
iqopt2 3/2 jets	2.34 ± 0.04	$7.6 \pm 4.2\%$	2.03 ± 0.03	$11.3 \pm 3.7\%$	1.26 ± 0.01	$3.9 \pm 2.1\%$
iqopt3 3/2 jets	2.21 ± 0.08	$1.7 \pm 5.3\%$	1.94 ± 0.06	$6.0 \pm 4.8\%$	1.15 ± 0.02	$-5.4 \pm 2.6\%$
ndns106 3/2 jets	2.16 ± 0.08	$-0.6 \pm 5.3\%$	1.95 ± 0.07	$6.8 \pm 4.9\%$	1.29 ± 0.02	$6.3 \pm 2.7\%$
qfac 0.5 3/2 jets	2.12 ± 0.07	$-2.5 \pm 4.9\%$	1.85 ± 0.06	$1.3 \pm 4.5\%$	1.28 ± 0.02	$5.5 \pm 2.7\%$
qfac 2 3/2 jets	2.14 ± 0.09	$-1.7 \pm 5.6\%$	2.03 ± 0.07	$11.2 \pm 5.2\%$	1.23 ± 0.02	$1.7 \pm 2.7\%$
ktfac 0.5 3/2 jets	2.17 ± 0.09	$-0.0 \pm 5.5\%$	1.91 ± 0.07	$4.5 \pm 4.9\%$	1.22 ± 0.02	$0.6 \pm 2.6\%$
ktfac 2 3/2 jets	2.04 ± 0.08	$-6.1 \pm 5.1\%$	1.88 ± 0.06	$2.7 \pm 4.8\%$	1.20 ± 0.02	$-0.7 \pm 2.7\%$
ptjmin10 3/2 jets	2.21 ± 0.12	$1.4 \pm 6.7\%$	2.13 ± 0.10	$16.9 \pm 6.6\%$	1.30 ± 0.03	$7.1 \pm 3.3\%$
ptjmin20 3/2 jets	2.38 ± 0.07	$9.7 \pm 4.9\%$	1.93 ± 0.05	$5.8 \pm 4.3\%$	1.25 ± 0.02	$3.5 \pm 2.5\%$
RMS		4.7%		8.7%		4.5%
nominal 4/3 jets	1.73 ± 0.11	$0.0 \pm 0.0\%$	1.52 ± 0.10	$0.0 \pm 0.0\%$	1.10 ± 0.04	$0.0 \pm 0.0\%$
iqopt2 4/3 jets	1.71 ± 0.04	$-1.2 \pm 7.0\%$	1.39 ± 0.04	$-8.9 \pm 6.9\%$	1.05 ± 0.02	$-4.5 \pm 3.8\%$
iqopt3 4/3 jets	1.52 ± 0.09	$-11.9 \pm 8.5\%$	1.41 ± 0.09	$-7.5 \pm 8.7\%$	1.05 ± 0.04	$-4.5 \pm 4.8\%$
ndns106 4/3 jets	1.50 ± 0.10	$-13.1 \pm 8.5\%$	1.27 ± 0.08	$-16.6 \pm 8.5\%$	1.06 ± 0.04	$-3.7 \pm 4.7\%$
qfac 0.5 4/3 jets	1.62 ± 0.09	$-6.3 \pm 8.4\%$	1.32 ± 0.08	$-13.1 \pm 8.4\%$	1.07 ± 0.04	$-2.9 \pm 4.7\%$
qfac 2 4/3 jets	1.62 ± 0.11	$-6.4 \pm 9.2\%$	1.30 ± 0.09	$-14.2 \pm 8.8\%$	1.06 ± 0.04	$-3.7 \pm 4.8\%$
ktfac 0.5 4/3 jets	1.73 ± 0.12	$-0.1 \pm 9.7\%$	1.39 ± 0.09	$-8.5 \pm 8.9\%$	1.11 ± 0.04	$0.9 \pm 4.9\%$
ktfac 2 4/3 jets	1.87 ± 0.12	$8.3 \pm 9.5\%$	1.64 ± 0.10	$7.7 \pm 9.4\%$	1.13 ± 0.04	$2.3 \pm 5.1\%$
ptjmin10 4/3 jets	1.66 ± 0.18	$-3.9 \pm 12.5\%$	1.43 ± 0.15	$-5.9 \pm 11.6\%$	1.00 ± 0.05	$-9.4 \pm 6.0\%$
ptjmin20 4/3 jets	1.63 ± 0.08	$-5.8 \pm 7.9\%$	1.52 ± 0.07	$-0.1 \pm 7.9\%$	1.09 ± 0.03	$-1.1 \pm 4.3\%$
RMS		7.6%		10.3%		4.4%
nominal 5/4 jets	1.42 ± 0.17	$0.0 \pm 0.0\%$	1.32 ± 0.16	$0.0 \pm 0.0\%$	1.03 ± 0.07	$0.0 \pm 0.0\%$
iqopt2 5/4 jets	1.58 ± 0.06	$11.5 \pm 12.8\%$	1.48 ± 0.07	$12.4 \pm 13.2\%$	0.96 ± 0.03	$-6.7 \pm 6.8\%$
iqopt3 5/4 jets	1.77 ± 0.20	$25.0 \pm 18.5\%$	1.37 ± 0.16	$4.1 \pm 17.3\%$	0.84 ± 0.05	$-17.8 \pm 8.2\%$
ndns106 5/4 jets	1.45 ± 0.17	$2.6 \pm 17.0\%$	1.50 ± 0.18	$13.9 \pm 18.3\%$	0.92 ± 0.06	$-10.3 \pm 8.6\%$
qfac 0.5 5/4 jets	1.36 ± 0.14	$-3.9 \pm 15.6\%$	1.45 ± 0.17	$10.4 \pm 17.8\%$	1.03 ± 0.07	$-0.0 \pm 8.9\%$

Table C.4.: Behaviour of $W + \text{jets}$ heavy flavour to light flavour fractions for $N/(N-1)$ jet bin ratios for given systematic variation. Deviation is quoted with respect to nominal. Uncertainties are statistical only.

variation	Wbb/W light	deviation	$Wc\bar{c}/W$ light	deviation	Wc/W light	deviation
qfac 2 5/4 jets	1.58 ± 0.19	$11.5 \pm 18.3\%$	1.31 ± 0.17	$-0.8 \pm 17.5\%$	0.89 ± 0.06	$-13.6 \pm 8.4\%$
ktfac 0.5 5/4 jets	1.30 ± 0.17	$-8.3 \pm 17.0\%$	1.25 ± 0.16	$-5.2 \pm 17.2\%$	0.99 ± 0.06	$-3.9 \pm 8.9\%$
ktfac 2 5/4 jets	1.43 ± 0.16	$0.7 \pm 16.4\%$	1.53 ± 0.17	$16.4 \pm 17.9\%$	0.99 ± 0.06	$-3.8 \pm 8.8\%$
ptjmin10 5/4 jets	1.20 ± 0.23	$-15.6 \pm 20.4\%$	0.97 ± 0.20	$-26.2 \pm 19.8\%$	0.91 ± 0.10	$-11.0 \pm 11.5\%$
ptjmin20 5/4 jets	1.62 ± 0.13	$14.6 \pm 15.2\%$	1.31 ± 0.11	$-0.8 \pm 14.7\%$	0.96 ± 0.04	$-6.9 \pm 7.7\%$
RMS		12.6%		12.7%		9.7%

C. Investigation of the $W + \text{heavy flavour contribution}$ uncertainty

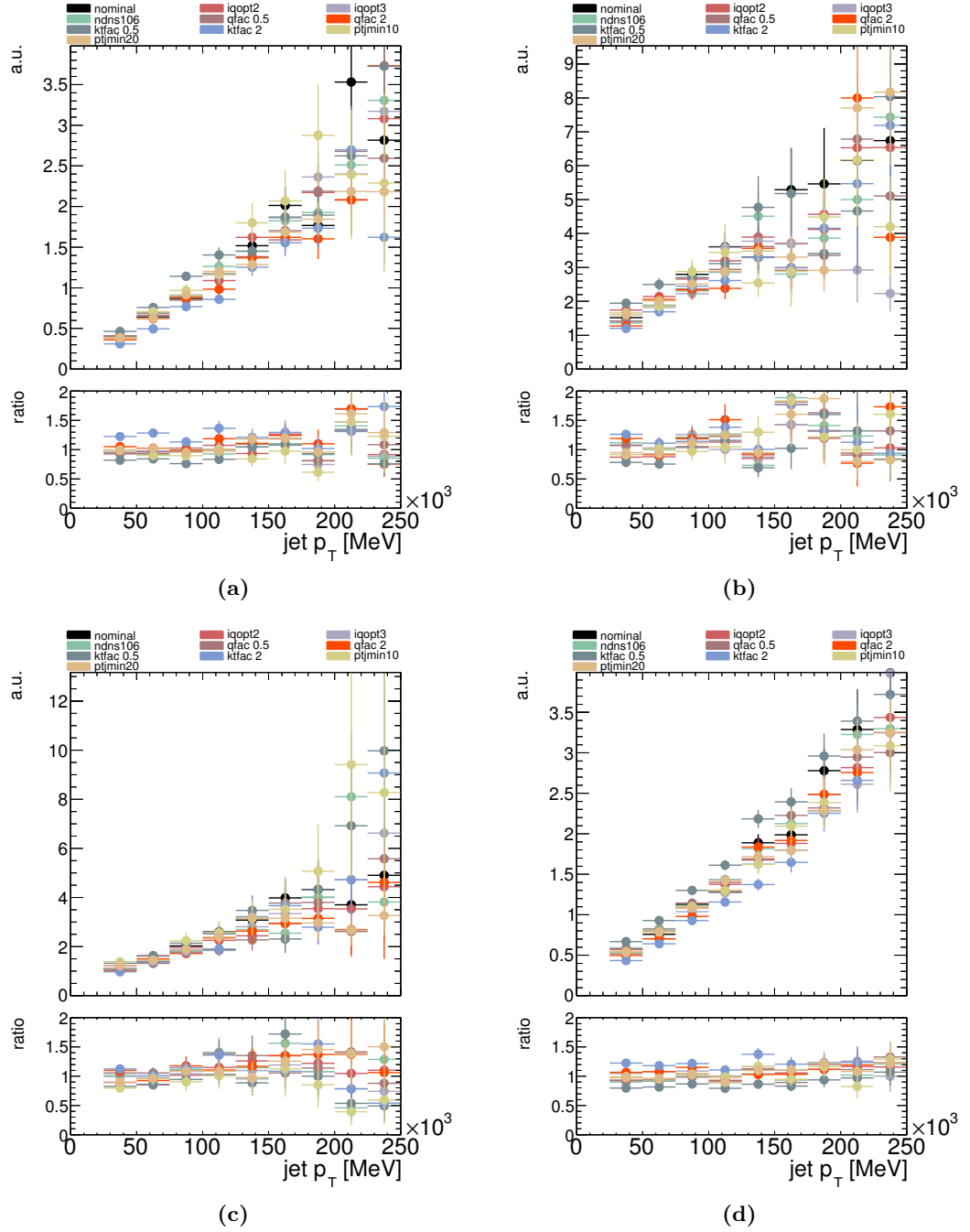


Figure C.3.: Ratio of the p_T distribution of all jets in the event in the 4 jet bin to the 2 jet bin for a given systematic variations of the generator parameters for the (a) W light, (b) $Wb\bar{b}$, (c) $Wc\bar{c}$, and (d) $Wc + \text{jets}$ sample. The bottom plot shows the ratio of each variation with respect to the nominal settings. Uncertainties are statistical only.

D. Additional details of the cross section measurement using b-tagging

D.1. Behaviour of the normalisation and nuisance parameters with respect to the value of β_0 in the profiling procedure

The behaviour of the normalisation and nuisance parameters, $\vec{\beta}$ and $\vec{\delta}$, is evaluated with respect to the value of β_0 to study the behaviour and stability of the fit. It is shown in Figs. D.1 to D.4. Any discontinuities observed occur far away from the minimum.

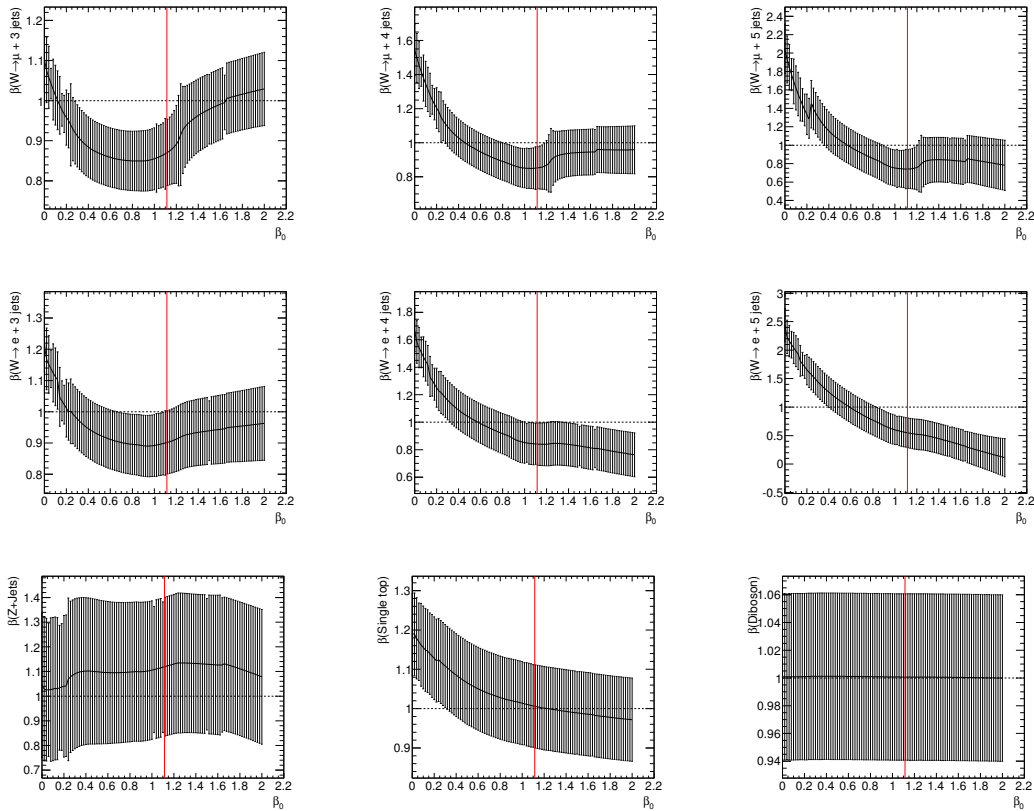


Figure D.1.: Behaviour of the normalisation parameters β_1 to β_9 as function of the parameter of interest β_0 in the fit during profiling procedure. The red line indicates the fitted value of $\beta_0 = 1.1142$.

D. Additional details of the cross section measurement using b -tagging

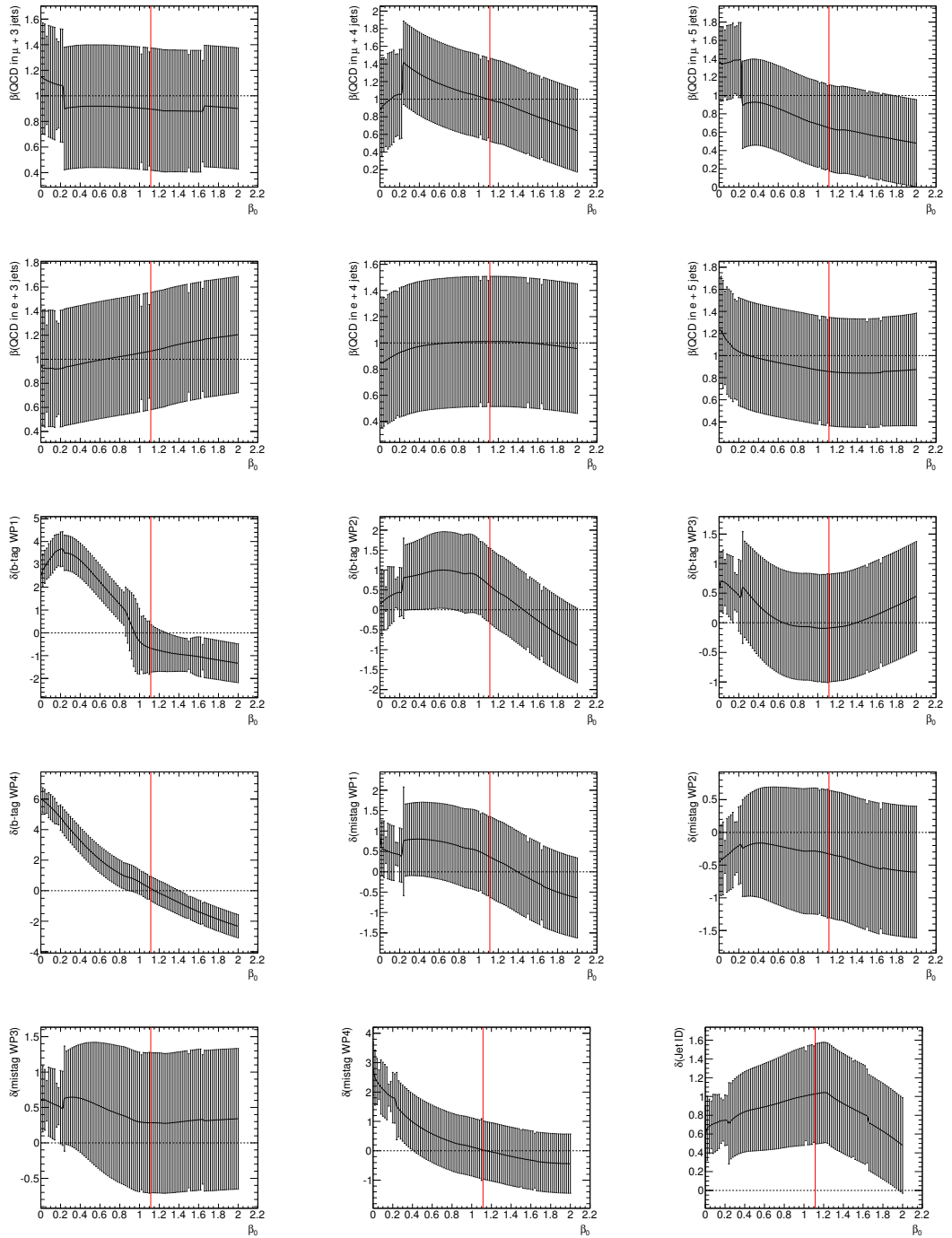


Figure D.2.: Behaviour of the normalisation parameters β_{10} to β_{15} and nuisance parameters δ_0 to δ_8 as function of the parameter of interest β_0 in the fit during profiling procedure. The red line indicates the fitted value of $\beta_0 = 1.1142$.

D.1. Behaviour of the normalisation and nuisance parameters in profiling procedure

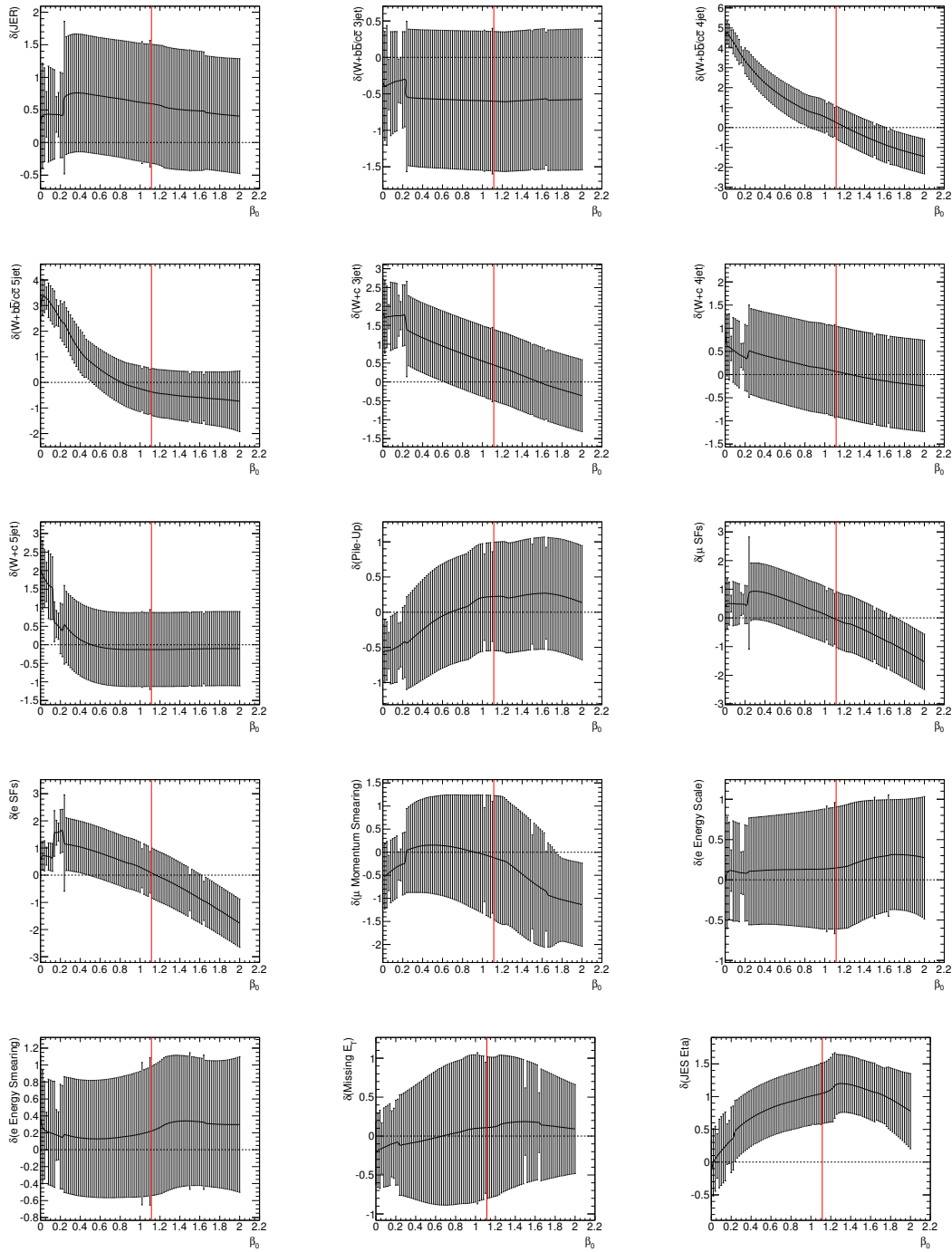


Figure D.3.: Behaviour of the nuisance parameters δ_9 to δ_{23} as function of the parameter of interest β_0 in the fit during profiling procedure. The red line indicates the fitted value of $\beta_0 = 1.1142$.

D. Additional details of the cross section measurement using b -tagging

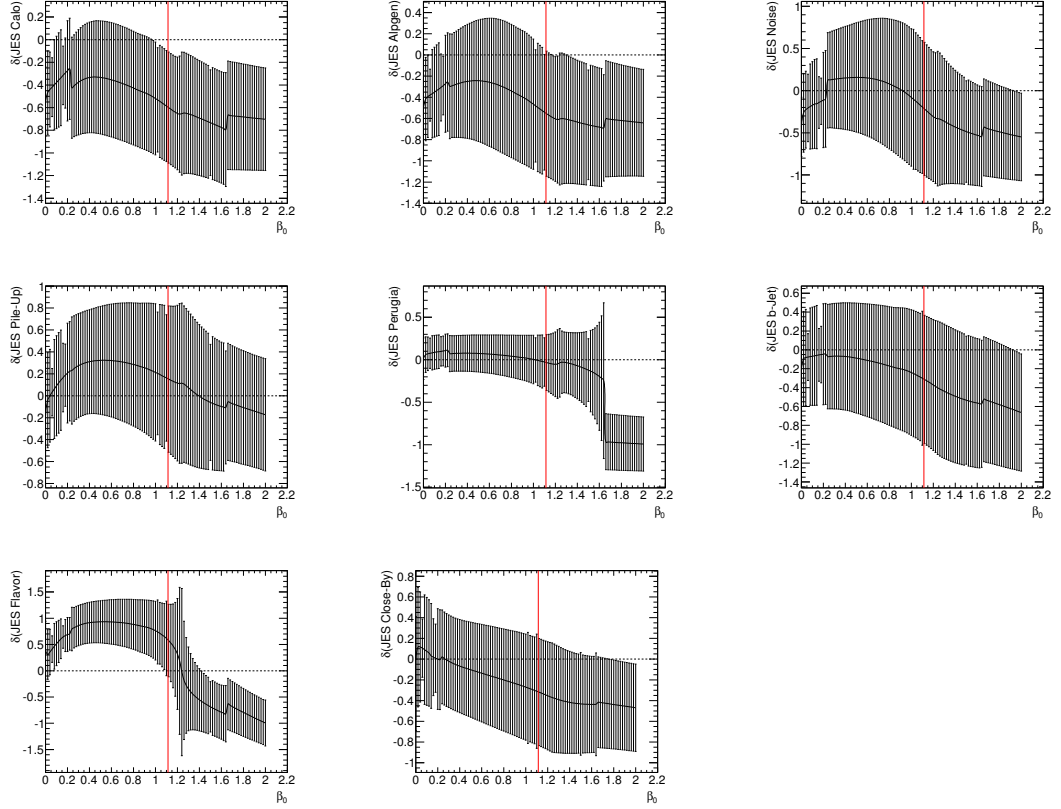


Figure D.4.: Behaviour of the nuisance parameters δ_{24} to δ_{31} as function of the parameter of interest β_0 in the fit during profiling procedure. The red line indicates the fitted value of $\beta_0 = 1.1142$.

E. Additional details of the cross section measurement using kinematic information only

E.1. Behaviour of the normalisation and nuisance parameters with respect to the value of β_0 in the profiling procedure

The behaviour of the normalisation and nuisance parameters, $\vec{\beta}$ and $\vec{\delta}$, is evaluated with respect to the value of β_0 to study the behaviour and stability of the fit. It is shown in Figs. E.1 to E.4. Any discontinuities observed occur far away from the minimum.

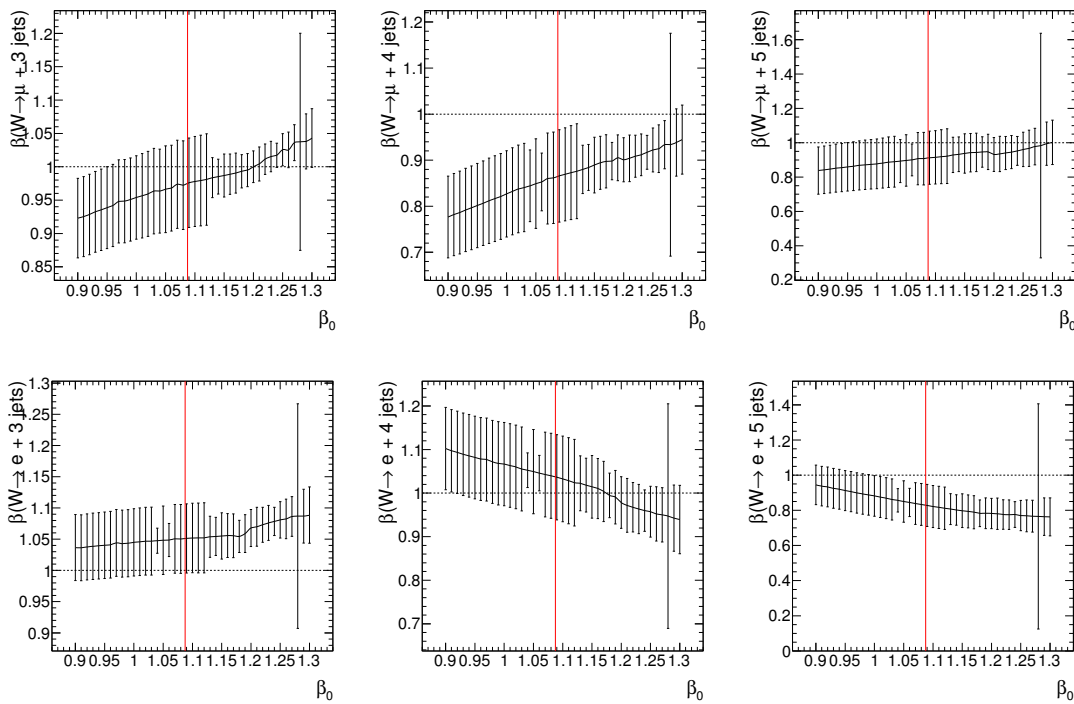


Figure E.1.: Behaviour of the normalisation parameters β_1 to β_6 as function of the parameter of interest β_0 in the fit during profiling procedure. The red line indicates the fitted value of $\beta_0 = 1.0875$.

E. Additional details of the cross section measurement using kinematic information only

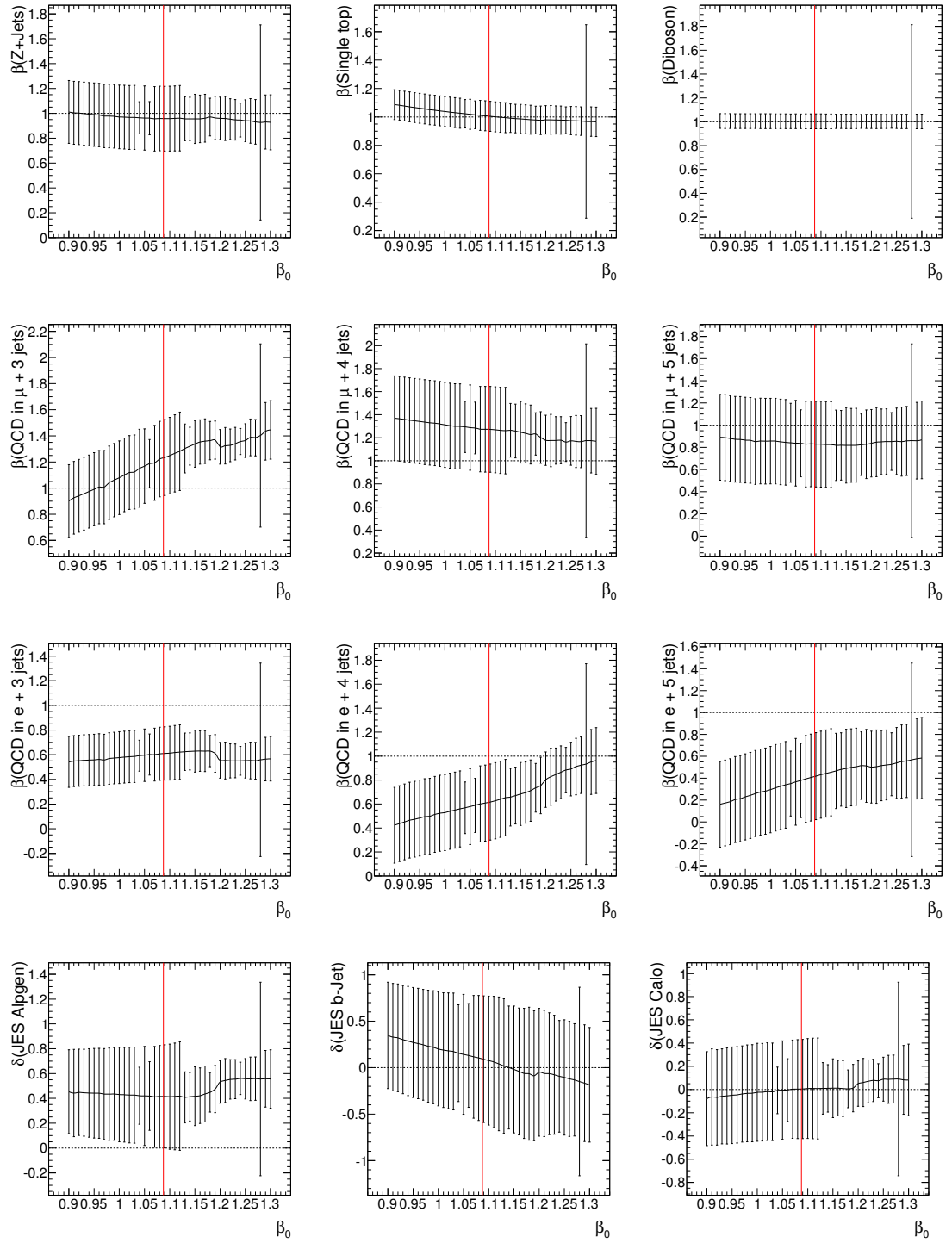


Figure E.2.: Behaviour of the normalisation parameters β_7 to β_{15} and nuisance parameters δ_0 to δ_2 as function of the parameter of interest β_0 in the fit during profiling procedure. The red line indicates the fitted value of $\beta_0 = 1.0875$.

E.1. Behaviour of the normalisation and nuisance parameters in profiling procedure

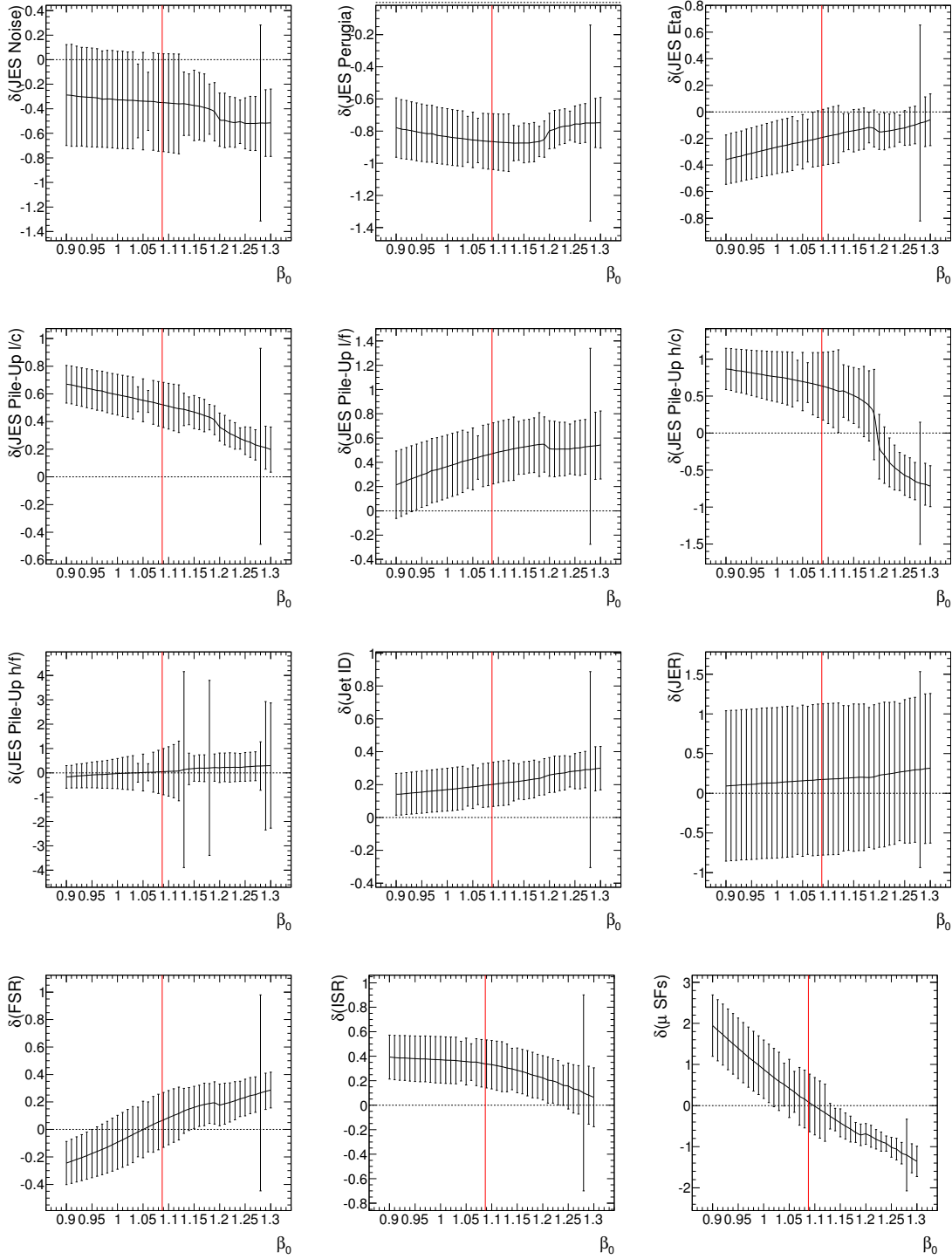


Figure E.3.: Behaviour of the nuisance parameters δ_3 to δ_{15} as function of the parameter of interest β_0 in the fit during profiling procedure. The red line indicates the fitted value of $\beta_0 = 1.0875$.

E. Additional details of the cross section measurement using kinematic information only

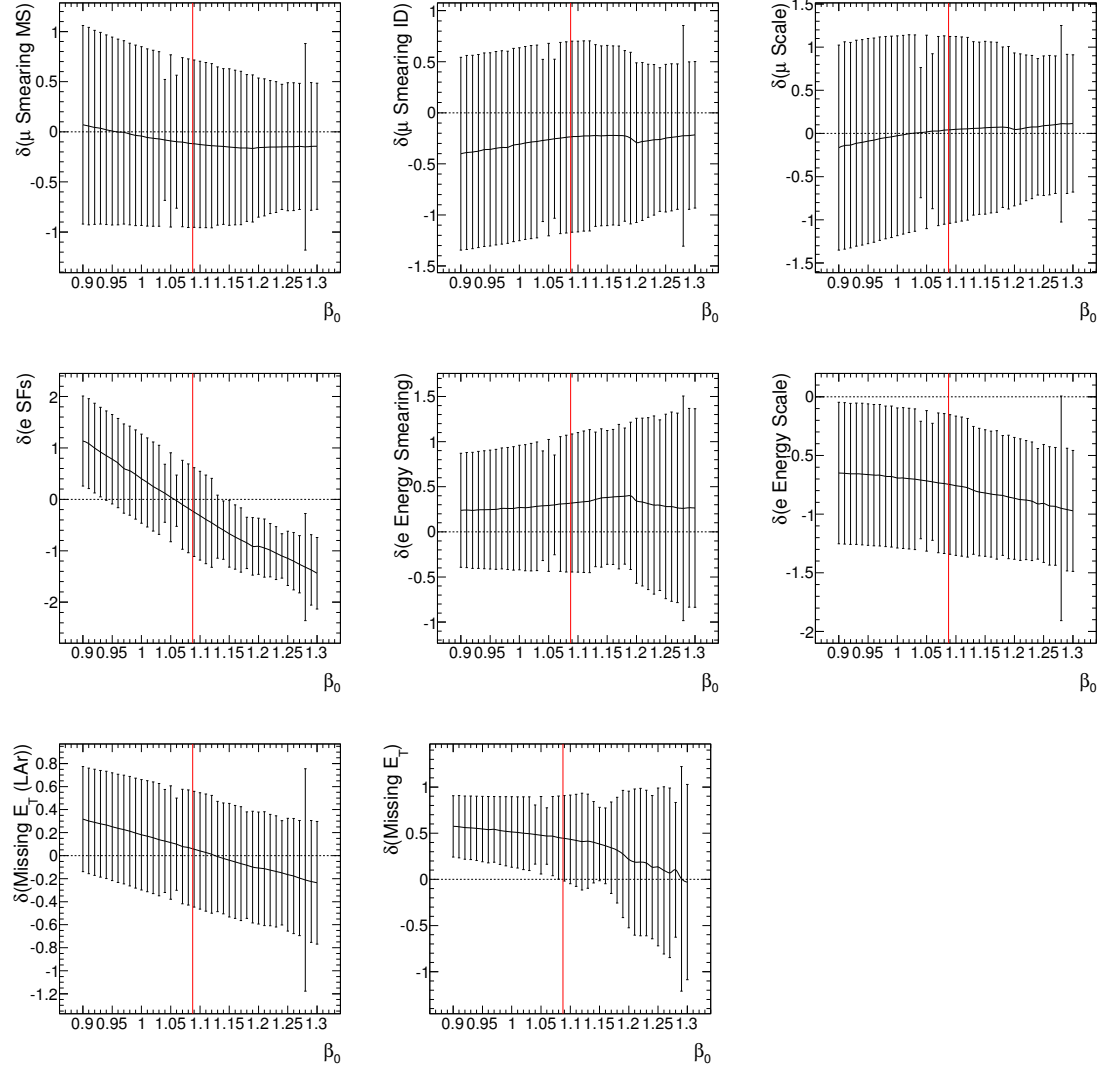


Figure E.4.: Behaviour of the nuisance parameters δ_{15} to δ_{22} as function of the parameter of interest β_0 in the fit during profiling procedure. The red line indicates the fitted value of $\beta_0 = 1.0875$.

E.2. Detailed listing of estimated systematic uncertainties

Table E.1.: Table of estimated systematic uncertainties. For each systematic uncertainty included in the fit the quadratic difference between the relative uncertainties of the full fit and the fit without the systematic in question is quoted. The remaining systematic uncertainties are added in quadrature afterwards.

Systematic	$\sigma(tt)$	up (pb)	down (pb)	up (%)	down (%)	$\sqrt{\Delta_{\text{up}}^2}$ (%)	$\sqrt{\Delta_{\text{down}}^2}$ (%)
Nominal	178.97	7.02	-6.92	3.92	-3.87		
No Systematics	187.51	4.11	-4.09	2.19	-2.18		
No alpgenJES	178.98	7.02	-6.93	3.92	-3.87	0.04	-0.2
No bJES	178.93	7.01	-6.85	3.92	-3.83	0.19	-0.54
No caloJES	179.1	6.88	-7.04	3.84	-3.93	0.79	-0.71
No noiseJES	178.97	7.02	-6.92	3.92	-3.87	0	0
No perugiaJES	178.9	7.08	-6.83	3.96	-3.82	0.53	-0.61
No pileupJES1	178.89	6.93	-6.65	3.87	-3.72	0.62	-1.06
No pileupJES2	178.9	6.97	-6.75	3.9	-3.77	0.45	-0.85
No pileupJES3	178.91	6.94	-6.69	3.88	-3.74	0.58	-0.98
No pileupJES4	179.0	6.89	-6.94	3.85	-3.88	0.75	-0.29
No etaJES	178.99	7.03	-7.03	3.93	-3.93	0.20	-0.69
No JEF	179.01	7.04	-7.04	3.93	-3.93	0.28	-0.72
No JER	179.14	6.85	-7.10	3.82	-3.96	0.87	-0.87
No FSR	179.00	6.52	-6.57	3.64	-3.67	1.46	-1.22
No ISR	179.04	6.86	-6.95	3.83	-3.88	0.84	-0.34
No Muon SF	178.9	6.23	-5.99	3.48	-3.35	1.81	-1.93
No Muon SmearMS	179.02	6.96	-6.96	3.89	-3.89	0.52	-0.41
No Muon SmearID	179.14	6.85	-7.09	3.82	-3.96	0.87	-0.84
No Muon Scale	179.14	6.84	-7.08	3.82	-3.95	0.9	-0.82
No ElectronSF	178.91	6.66	-6.47	3.72	-3.62	1.24	-1.37

continued on next page

Table E.1.1.: Table of estimated systematic uncertainties. For each systematic uncertainty included in the fit the quadratic difference between the relative uncertainties of the full fit and the fit without the systematic in question is quoted. The remaining systematic uncertainties are added in quadrature afterwards.

Systematic	$\sigma(tt)$	up (pb)	down (pb)	up (%)	down (%)	$\sqrt{\Delta_{\text{up}}^2}$ (%)	$\sqrt{\Delta_{\text{down}}^2}$ (%)
No ElectronSmear	178.91	7.06	-6.86	3.95	-3.83	0.43	-0.5
No ElectronScale	179.09	6.89	-7.07	3.85	-3.95	0.76	-0.8
No MET CellSoft	178.92	7.07	-6.82	3.95	-3.81	0.48	-0.65
No MET Lar	179.12	6.8	-7.03	3.8	-3.92	0.99	-0.67
Sum Fit						3.84	-4.05
QCD Shape ¹						0.37	-0.37
W ptmin ¹						0.48	-0.48
W iqopt ¹						0.07	-0.07
PDF ¹						1.01	-1.01
Generator ¹						3.06	-3.06
Hadronisation ¹						0.53	-0.53
Bin-by-bin ¹						1.80	-1.80
Sum additional				3.78	-3.78		
Syst. only		8.84	-8.77	4.99	-4.95		
Stat. & syst.		9.75	-9.68	5.45	-5.41		
Luminosity		6.62	-6.62	3.7	-3.7		
Total		11.78	-11.72	6.58	-6.55		

¹ evaluated outside the fit

F. Additional details of the fiducial cross section measurement in 2011 data

F.1. Signal Monte Carlo event normalisation

For the fiducial cross section measurement the normalisation of the signal simulation templates is performed with respect to the selection efficiency in the fiducial region, $C_{t\bar{t}} = N_{\text{selected}}/N_{\text{truth}}^{\text{fiducial}}$, where N_{selected} is the number of selected reconstruction level events and $N_{\text{truth}}^{\text{fiducial}}$ the number of selected particle level events in the fiducial volume for a given jet multiplicity at particle level, so that the cross section for this jet multiplicity yields:

$$\sigma_{\text{fiducial}} = \varsigma_{t\bar{t}} = \frac{N_{\text{selected}}}{C_{t\bar{t}} \cdot \text{BR}(t\bar{t} \rightarrow l + \text{jets}) \cdot \mathcal{L}}. \quad (\text{F.1})$$

The total fiducial cross section is then given by the linear sum of the fiducial cross sections of each of the six particle level channels. The extrapolation to the full cross section is then a pure theoretical uncertainty using the acceptance, $A_{t\bar{t}} = N_{\text{truth}}^{\text{fiducial}}/N_{\text{truth}}^{\text{total}}$, where $N_{\text{truth}}^{\text{total}}$ is the total number of generated events in the Monte Carlo sample. The full phase space cross section is therefore given by:

$$\sigma_{t\bar{t}} = \frac{N_{\text{selected}}}{A_{t\bar{t}} C_{t\bar{t}} \cdot \text{BR}(t\bar{t} \rightarrow l + \text{jets}) \cdot \mathcal{L}}. \quad (\text{F.2})$$

F.2. Cross section extraction and error propagation

The total fiducial cross section, ς , is extracted as linear sum of the $N_t = 3$ single fiducial $t\bar{t}$ cross sections, σ_i , obtained from the fit. The uncertainty is obtained using Gaussian error propagation:

$$\Delta\varsigma = \sqrt{\sum_{i=1}^{N_t} \left(\frac{\partial\varsigma}{\partial\sigma_i} \cdot \Delta\sigma_i \right)^2 + 2 \sum_{i=1}^{N_t-1} \sum_{k=i+1}^{N_t} \left(\frac{\partial\varsigma}{\partial\sigma_i} \right) \left(\frac{\partial\varsigma}{\partial\sigma_k} \right) \cdot \text{cov}(\sigma_i, \sigma_k)}, \quad (\text{F.3})$$

where $\text{cov}(\sigma_i, \sigma_k)$ is the covariance. Technically, this is implemented as

$$\Delta\varsigma = \sqrt{\sum_{i=1}^{N_t} (\Delta\sigma_i)^2 + 2 \sum_{i=1}^{N_t-1} \sum_{k=i+1}^{N_t} (\Delta\sigma_i) (\Delta\sigma_k) \cdot \varrho(\sigma_i, \sigma_k)}, \quad (\text{F.4})$$

where $\varrho(\sigma_i, \sigma_k) = \frac{\text{cov}(\sigma_i, \sigma_k)}{\Delta\sigma_i \cdot \Delta\sigma_k}$ is the correlation coefficient.

F.3. Additional control plots

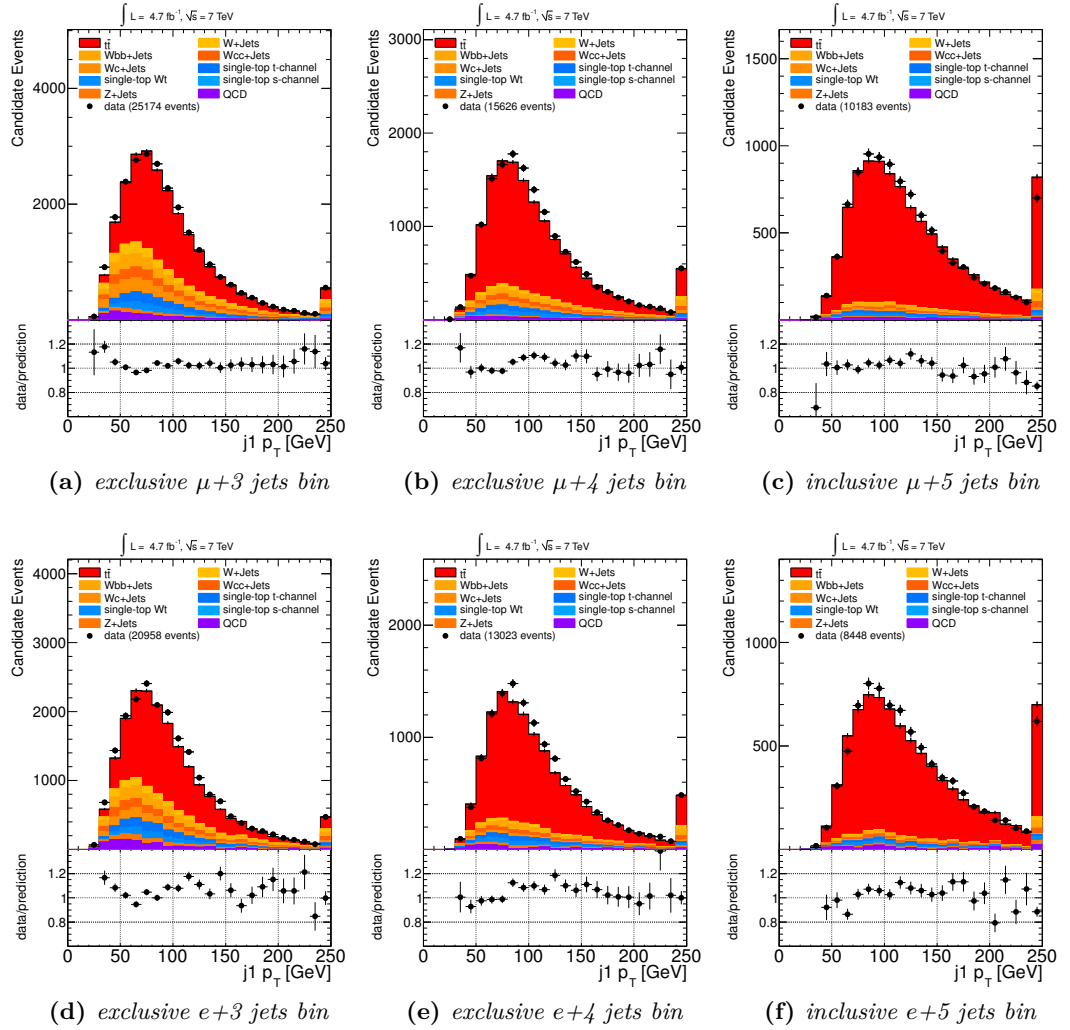


Figure F.1.: Leading jet transverse momentum in data and Monte Carlo simulated events in the signal region.

F.4. Results of the minimum log-likelihood fit to data

The individual fit results of the minimum log-likelihood fit to data using the different $t\bar{t}$ signal generators are shown in Tab. F.1.

F.4. Results of the minimum log-likelihood fit to data

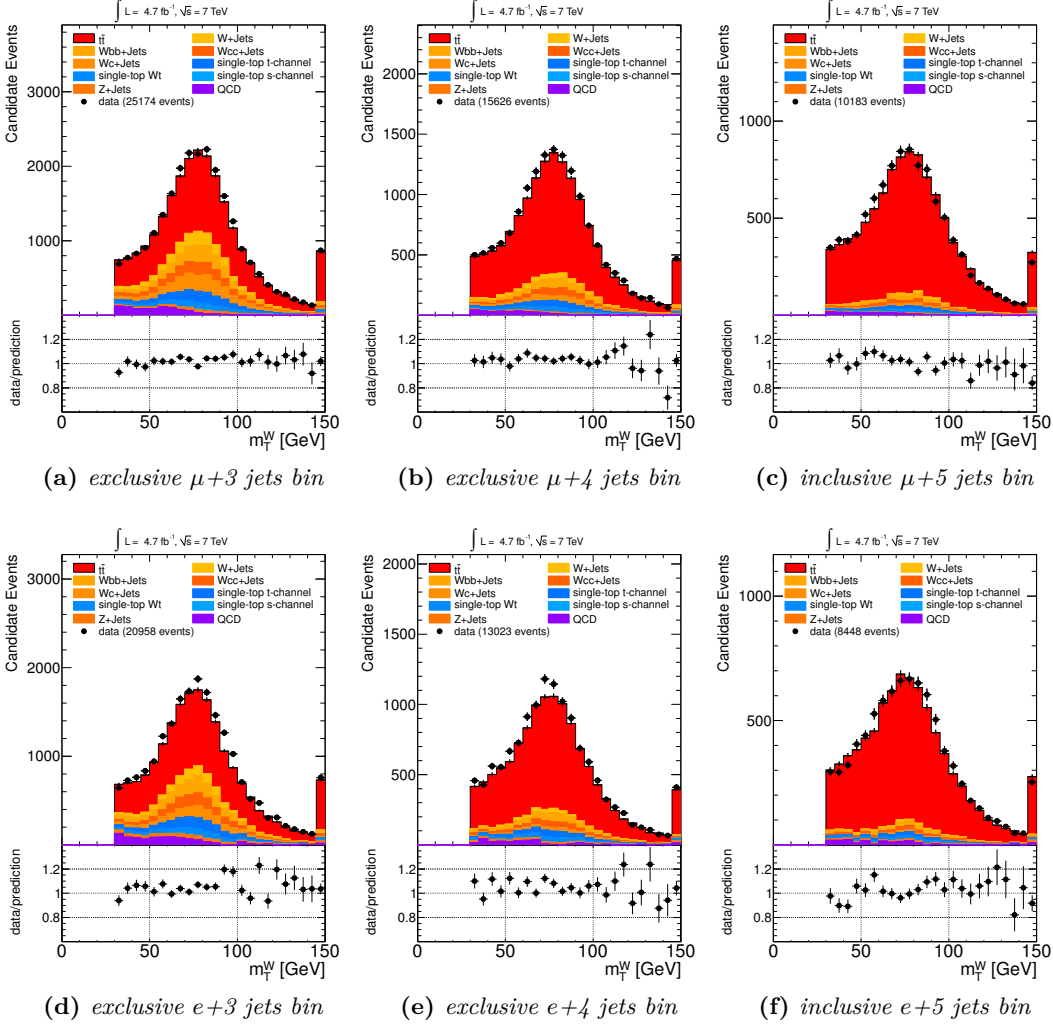


Figure F.2.: Transverse mass of leptonic W boson in data and Monte Carlo simulated events in the signal region.

Table F.1.: Fit results of the combined likelihood fit to data using the individual $t\bar{t}$ signal generators. Background processes are fixed and therefore not shown.

$t\bar{t}$ generator	truth $l+3$ jets	truth $l+4$ jets	truth $l+5$ jets	oops
POWHEG+PYTHIA	1.0729 ± 0.0159	1.0703 ± 0.0171	0.9964 ± 0.0148	1.0524 ± 0.0062
POWHEG+HERWIG	1.1456 ± 0.0170	1.0002 ± 0.0169	0.9352 ± 0.0135	1.0352 ± 0.0062
MC@NLO	1.0567 ± 0.0154	0.9149 ± 0.0154	1.1812 ± 0.0154	1.0380 ± 0.0063
AlpGEN+PYTHIA	1.1535 ± 0.0157	0.9396 ± 0.0157	0.8373 ± 0.0129	0.9942 ± 0.0060
AlpGEN+HERWIG	1.1281 ± 0.0158	0.9178 ± 0.0153	0.8398 ± 0.0124	0.9745 ± 0.0059

Bibliography

- [1] S. L. Glashow, “Partial Symmetries of Weak Interactions,” *Nucl. Phys.* **22** (1961) 579–588.
- [2] S. Weinberg, “A Model of Leptons,” *Phys.Rev.Lett.* **19** (1967) 1264–1266.
- [3] A. Salam, “Gauge Unification of Fundamental Forces,” *Rev. Mod. Phys.* **52** (1980) 525–538.
- [4] H. Fritzsch, M. Gell-Mann, and H. Leutwyler, “Advantages of the Color Octet Gluon Picture,” CALT-68-409, *Phys.Lett.* **B47** (1973) 365–368.
- [5] F. Englert and R. Brout, “Broken Symmetry and the Mass of Gauge Vector Mesons,” *Phys.Rev.Lett.* **13** (1964) 321–323.
- [6] G. Guralnik, C. Hagen, and T. Kibble, “Global Conservation Laws and Massless Particles,” *Phys.Rev.Lett.* **13** (1964) 585–587.
- [7] P. W. Higgs, “Broken symmetries, massless particles and gauge fields,” *Phys. Lett.* **12** (1964) 132–133.
- [8] P. W. Higgs, “Broken Symmetries And The Masses Of Gauge Bosons,” *Phys. Rev. Lett.* **13** (1964) 508–509.
- [9] P. W. Higgs, “Spontaneous Symmetry Breakdown Without Massless Bosons,” *Phys. Rev.* **145** (1966) 1156–1163.
- [10] **Particle Data Group**, J. Beringer *et al.*, “Review of Particle Physics (RPP),” *Phys.Rev.* **D86** (2012) 010001.
- [11] **Boomerang Collaboration**, P. de Bernardis *et al.*, “A flat universe from high resolution maps of the cosmic microwave background radiation,” *Nature* **404** (2000) 955–959, [arXiv:astro-ph/0004404](https://arxiv.org/abs/astro-ph/0004404) [astro-ph].
- [12] **WMAP Collaboration**, D. Spergel *et al.*, “First year Wilkinson Microwave Anisotropy Probe (WMAP) observations: Determination of cosmological parameters,” *Astrophys.J.Suppl.* **148** (2003) 175–194, [arXiv:astro-ph/0302209](https://arxiv.org/abs/astro-ph/0302209) [astro-ph].
- [13] **The SNLS Collaboration**, P. Astier *et al.*, “The Supernova legacy survey: Measurement of Ω_M , Ω_Λ and w from the first year data set,” *Astron.Astrophys.* **447** (2006) 31–48, [arXiv:astro-ph/0510447](https://arxiv.org/abs/astro-ph/0510447) [astro-ph].

Bibliography

- [14] **WMAP Collaboration**, D. Spergel *et al.*, “Wilkinson Microwave Anisotropy Probe (WMAP) three year results: implications for cosmology,” *Astrophys.J.Suppl.* **170** (2007) 377, [arXiv:astro-ph/0603449](#) [astro-ph].
- [15] W. Wagner, “Top quark physics in hadron collisions,” IEKP-KA-2005-8, *Rept.Prog.Phys.* **68** (2005) 2409–2494, [arXiv:hep-ph/0507207](#) [hep-ph].
- [16] M.-A. Pleier, “Review of Properties of the Top Quark from Measurements at the Tevatron,” FERMILAB-PUB-08-495-E, *Int.J.Mod.Phys.* **A24** (2009) 2899–3037, [arXiv:0810.5226](#) [hep-ex].
- [17] D. Wicke, “Properties of the Top Quark,” FERMILAB-HABIL-2009-01, *Eur.Phys.J.* **C71** (2011) 1627, [arXiv:1005.2460](#) [hep-ex].
- [18] A. Quadt, “Top quark physics at hadron colliders,” *Eur.Phys.J.* **C48** (2006) 835–1000.
- [19] W. Bernreuther, “Top quark physics at the LHC,” PITHA-08-09, *J.Phys.G* **G35** (2008) 083001, [arXiv:0805.1333](#) [hep-ph].
- [20] C. Lange, “Studies of Single Top Production in Proton-Proton Collisions with the ATLAS Experiment,” Diplom thesis, Humboldt-Universität zu Berlin, 2009.
- [21] F.-P. Schilling, “Top Quark Physics at the LHC: A Review of the First Two Years,” *Int.J.Mod.Phys.* **A27** (2012) 1230016, [arXiv:1206.4484](#) [hep-ex].
- [22] D. Ebert, *Eichtheorien. Grundlagen der Elementarteilchenphysik.* VCH-Verlag-Ges., 1989.
- [23] C. S. Wu, E. Ambler, R. W. Hayward, D. D. Hoppes, and R. P. Hudson, “Experimental Test Of Parity Conservation In Beta Decay,” *Phys. Rev.* **105** (1957) 1413–1414.
- [24] M. Goldhaber, L. Grodzins, and A. W. Sunyar, “Helicity Of Neutrinos,” *Phys. Rev.* **109** (1958) 1015–1017.
- [25] **Super-Kamiokande Collaboration**, Y. Fukuda *et al.*, “Evidence for oscillation of atmospheric neutrinos,” *Phys. Rev. Lett.* **81** (1998) 1562–1567, [arXiv:hep-ex/9807003](#).
- [26] **SNO Collaboration**, Q. R. Ahmad *et al.*, “Direct evidence for neutrino flavor transformation from neutral-current interactions in the Sudbury Neutrino Observatory,” *Phys. Rev. Lett.* **89** (2002) 011301, [arXiv:nucl-ex/0204008](#).
- [27] J. Goldstone, A. Salam, and S. Weinberg, “Broken Symmetries,” *Phys.Rev.* **127** (1962) 965–970.
- [28] H. Yukawa, “On the interaction of elementary particles,” *Proc. Phys. Math. Soc. Jap.* **17** (1935) 48–57.

- [29] M. Kobayashi and T. Maskawa, “CP Violation in the Renormalizable Theory of Weak Interaction,” *Prog. Theor. Phys.* **49** (1973) 652–657.
- [30] A. Höcker, H. Lacker, S. Laplace, and F. Le Diberder, “A new approach to a global fit of the CKM matrix,” LAL-01-06, *Eur.Phys.J.* **C21** (2001) 225–259, [arXiv:hep-ph/0104062](#) [hep-ph].
- [31] **CKMfitter Group**, J. Charles *et al.*, “CP violation and the CKM matrix: Assessing the impact of the asymmetric B factories,” *Eur. Phys. J.* **C41** (2005) 1–131, [arXiv:hep-ph/0406184](#).
- [32] B. Pontecorvo, “Superweak interactions and double beta decay,” *Phys.Lett.* **B26** (1968) 630–632.
- [33] Z. Maki, M. Nakagawa, and S. Sakata, “Remarks on the unified model of elementary particles,” *Prog.Theor.Phys.* **28** (1962) 870–880.
- [34] **ATLAS Collaboration**, G. Aad *et al.*, “Observation of a new particle in the search for the Standard Model Higgs boson with the ATLAS detector at the LHC,” CERN-PH-EP-2012-218, *Phys.Lett.B* no. 0370-2693, (2012) , [arXiv:1207.7214](#) [hep-ex].
- [35] **CMS Collaboration**, S. Chatrchyan *et al.*, “Observation of a new boson at a mass of 125 GeV with the CMS experiment at the LHC,” CMS-HIG-12-028, CERN-PH-EP-2012-220, *Phys.Lett.B* (2012) , [arXiv:1207.7235](#) [hep-ex].
- [36] M. E. Peskin and D. V. Schroeder, *An Introduction to Quantum Field Theory (Frontiers in Physics)*. Perseus Books, 2008.
- [37] F. Halzen and A. Martin, *Quarks & Leptons: An introductory course in modern particle physics*. John Wiley & Sons, New York, USA, 1984.
- [38] D. Gross and F. Wilczek, “Ultraviolet Behavior of Nonabelian Gauge Theories,” *Phys.Rev.Lett.* **30** (1973) 1343–1346.
- [39] H. D. Politzer, “Reliable Perturbative Results for Strong Interactions?,” *Phys.Rev.Lett.* **30** (1973) 1346–1349.
- [40] K. G. Wilson, “Confinement of Quarks,” *Phys. Rev.* **D10** (1974) 2445–2459.
- [41] M. Gell-Mann, “A Schematic Model of Baryons and Mesons,” *Phys.Lett.* **8** (1964) 214–215.
- [42] G. Zweig, “An SU(3) model for strong interaction symmetry and its breaking,” CERN-TH-412, NP-14146. Published in ‘Developments in the Quark Theory of Hadrons’. Volume 1. Edited by D. Lichtenberg and S. Rosen. Nonantum, Mass., Hadronic Press, 1980. pp. 22-101.

Bibliography

- [43] S. L. Glashow, J. Iliopoulos, and L. Maiani, “Weak Interactions with Lepton-Hadron Symmetry,” *Phys. Rev.* **D2** (1970) 1285–1292.
- [44] M. L. Perl *et al.*, “Evidence for anomalous lepton production in e^+e^- annihilation,” *Phys. Rev. Lett.* **35** (1975) 1489–1492.
- [45] S. W. Herb *et al.*, “Observation of a dimuon resonance at 9.5 GeV in 400-GeV proton-nucleus collisions,” *Phys. Rev. Lett.* **39** (1977) 252–255.
- [46] G. ’t Hooft, “Renormalization of Massless Yang-Mills Fields,” *Nucl. Phys.* **B33** (1971) 173–199.
- [47] G. ’t Hooft, “Renormalizable Lagrangians For Massive Yang-Mills Fields,” *Nucl. Phys.* **B35** (1971) 167–188.
- [48] E. Leader and E. Predazzi, “An Introduction To Gauge Theories And The ’New Physics’,” Cambridge University Press, Cambridge, UK (1982) 498p.
- [49] **Pluto Collaboration**, C. Berger *et al.*, “Observation of a Narrow Resonance Formed in e^+e^- Annihilation at 9.46 GeV,” *Phys. Lett.* **B76** (1978) 243–245.
- [50] J. K. Bienlein *et al.*, “Observation of a Narrow Resonance at 10.02 GeV in e^+e^- Annihilations,” *Phys. Lett.* **B78** (1978) 360–363.
- [51] C. W. Darden *et al.*, “Observation of a Narrow Resonance at 9.46 GeV in electron-positron Annihilations,” *Phys. Lett.* **B76** (1978) 246.
- [52] **ALEPH, DELPHI, L3, OPAL, SLD Collaborations, LEP Electroweak Working Group, SLD Electroweak Group, SLD Heavy Flavour Group**, “Precision electroweak measurements on the Z resonance,” SLAC-R-774, *Phys.Rept.* **427** (2006) 257–454, arXiv:hep-ex/0509008 [hep-ex].
- [53] **JADE Collaboration**, W. Bartel *et al.*, “A Measurement of the Electroweak Induced Charge Asymmetry in $e^+e^- \rightarrow B\bar{B}$,” *Phys. Lett.* **B146** (1984) 437.
- [54] W. A. Bardeen, A. J. Buras, D. W. Duke, and T. Muta, “Deep Inelastic Scattering Beyond the Leading Order in Asymptotically Free Gauge Theories,” *Phys. Rev.* **D18** (1978) 3998.
- [55] **ARGUS Collaboration**, H. Albrecht *et al.*, “Observation of $B^0\bar{B}^0$ Mixing,” *Phys. Lett.* **B192** (1987) 245.
- [56] P. Langacker, “Implications of Recent M_Z , m_W and Neutral Current Measurements for the Top Quark Mass,” *Phys. Rev. Lett.* **63** (1989) 1920.
- [57] W. F. L. Hollik, “Radiative Corrections in the Standard Model and their Role for Precision Tests of the Electroweak Theory,” *Fortschr. Phys.* **38** (1990) 165–260.
- [58] **CDF Collaboration**, F. Abe *et al.*, “Observation of top quark production in $\bar{p}p$ collisions,” *Phys. Rev. Lett.* **74** (1995) 2626–2631, arXiv:hep-ex/9503002.

- [59] **D0 Collaboration**, S. Abachi *et al.*, “Observation of the top quark,” *Phys. Rev. Lett.* **74** (1995) 2632–2637, [arXiv:hep-ex/9503003](#).
- [60] **ALEPH, DELPHI, L3, OPAL Collaborations, LEP Electroweak Working Group**, “Combined preliminary data on Z parameters from the LEP experiments and constraints on the Standard Model,” Contributed to the 27th International Conference on High- Energy Physics - ICHEP 94, Glasgow, Scotland, UK, 20 - 27 Jul 1994.
- [61] **ALEPH, CDF, D0, DELPHI, L3, OPAL, SLD Collaborations, LEP Electroweak Working Group, Tevatron Electroweak Working Group, SLD Electroweak and Heavy Flavour Groups**, “Precision Electroweak Measurements and Constraints on the Standard Model,” CERN-PH-EP-2010-095, FERMILAB-TM-2480-PPD, LEPEWWG-2010-01, TEVEWWG-2010-01, ALEPH-2010-001-PHYSICS-2010-001, CDF-NOTE-10338, D0-NOTE-6130, DELPHI-DELPHI-2010-001-PHYS-952, L3-NOTE-2837, OPAL-PR432, SLAC-PUB-14301, [arXiv:1012.2367 \[hep-ex\]](#).
- [62] **CDF, D0 Collaborations, Tevatron Electroweak Working Group**, “Combination of CDF and D0 results on the mass of the top quark using up to 5.8 fb^{-1} of data,” FERMILAB-TM-2504-E, CDF-NOTE-10549, D0-NOTE-6222, [arXiv:1107.5255 \[hep-ex\]](#).
- [63] C. Quigg, “Unanswered Questions in the Electroweak Theory,” FERMILAB-PUB-09-230-T, *Ann.Rev.Nucl.Part.Sci.* **59** (2009) 505–555, [arXiv:0905.3187 \[hep-ph\]](#).
- [64] **ALEPH, DELPHI, L3, OPAL, SLD Collaborations, LEP Electroweak Working Group, Tevatron Electroweak Working Group, SLD Electroweak and Heavy Flavour Groups**, “Precision Electroweak Measurements and Constraints on the Standard Model,” [arXiv:0811.4682 \[hep-ex\]](#). Updates from <http://lepewwg.web.cern.ch/LEPEWWG/plots/winter2012/>.
- [65] B. Povh, K. Rith, C. Scholz, and F. Zetsche, *Teilchen und Kerne. Eine Einführung in die physikalischen Konzepte*. Springer-Verlag GmbH, sixth ed., 2004.
- [66] J. C. Collins, D. E. Soper, and G. Sterman, “Heavy Particle Production in High-Energy Hadron Collisions,” *Nucl. Phys.* **B263** (1986) 37.
- [67] J. C. Collins and D. E. Soper, “The Theorems of Perturbative QCD,” *Ann. Rev. Nucl. Part. Sci.* **37** (1987) 383–409.
- [68] **ZEUS Collaboration**, “The ZEUS detector: Status report 1993,” ZEUS-STATUS-REPT-1993.

Bibliography

- [69] **H1 Collaboration**, I. Abt *et al.*, “The H1 detector at HERA,” *Nucl. Instrum. Meth.* **A386** (1997) 310–347.
- [70] Y. L. Dokshitzer, “Calculation of the Structure Functions for Deep Inelastic Scattering and e^+e^- Annihilation by Perturbation Theory in Quantum Chromodynamics. (In Russian),” *Sov. Phys. JETP* **46** (1977) 641–653.
- [71] G. Altarelli and G. Parisi, “Asymptotic Freedom in Parton Language,” *Nucl. Phys.* **B126** (1977) 298.
- [72] V. N. Gribov and L. N. Lipatov, “Deep inelastic ep scattering in perturbation theory,” *Sov. J. Nucl. Phys.* **15** (1972) 438–450.
- [73] J. Pumplin *et al.*, “New generation of parton distributions with uncertainties from global QCD analysis,” *JHEP* **07** (2002) 012, [arXiv:hep-ph/0201195](#).
- [74] H.-L. Lai, M. Guzzi, J. Huston, Z. Li, P. M. Nadolsky, *et al.*, “New parton distributions for collider physics,” MSUHEP-100707, SMU-HEP-10-10, *Phys.Rev.* **D82** (2010) 074024, [arXiv:1007.2241 \[hep-ph\]](#).
- [75] “Durham IPPP Online PDF plotting and calculation,” May, 2012. <http://hepdata.cedar.ac.uk/pdf/pdf3.html>.
- [76] N. Kidonakis, E. Laenen, S. Moch, and R. Vogt, “Sudakov resummation and finite order expansions of heavy quark hadroproduction cross sections,” *Phys. Rev.* **D64** (2001) 114001, [arXiv:hep-ph/0105041](#).
- [77] M. Glück, J. F. Owens, and E. Reya, “Gluon Contribution to Hadronic J/ψ Production,” *Phys. Rev.* **D17** (1978) 2324.
- [78] V. D. Barger and R. J. N. Phillips, *Collider Physics (Frontiers in Physics)*. Addison Wesley Publishing Company, 1987.
- [79] N. Kidonakis and B. D. Pecjak, “Top-quark production and QCD,” [arXiv:1108.6063 \[hep-ph\]](#).
- [80] P. Nason, S. Dawson, and R. K. Ellis, “The Total Cross-Section for the Production of Heavy Quarks in Hadronic Collisions,” *Nucl. Phys.* **B303** (1988) 607.
- [81] W. Beenakker, H. Kuijf, W. L. van Neerven, and J. Smith, “QCD Corrections to Heavy Quark Production in $p\bar{p}$ Collisions,” *Phys. Rev.* **D40** (1989) 54–82.
- [82] P. Bärnreuther, M. Czakon, and A. Mitov, “Percent level precision physics at the Tevatron: first genuine NNLO QCD corrections to $q\bar{q} \rightarrow t\bar{t} + X$,” [arXiv:1204.5201 \[hep-ph\]](#).
- [83] M. Czakon and A. Mitov, “NNLO corrections to top-pair production at hadron colliders: the all-fermionic scattering channels,” [arXiv:1207.0236 \[hep-ph\]](#).

- [84] A. Mitov, “Hot Topics in Top-Quark Physics,” Presented at Les Rencontres de Physique de la Vallée d’Aoste, Italy, Jan, 2013.
- [85] P. M. Nadolsky *et al.*, “Implications of CTEQ global analysis for collider observables,” *Phys. Rev.* **D78** (2008) 013004, [arXiv:0802.0007 \[hep-ph\]](#).
- [86] S. Moch and P. Uwer, “Theoretical status and prospects for top-quark pair production at hadron colliders,” *Phys. Rev.* **D78** (2008) 034003, [arXiv:0804.1476 \[hep-ph\]](#).
- [87] U. Langenfeld, S. Moch, and P. Uwer, “New results for $t\bar{t}$ production at hadron colliders,” DESY-09-104, SFB-CPP-09-61, HU-EP-09-31, [arXiv:0907.2527 \[hep-ph\]](#).
- [88] A. Martin, W. Stirling, R. Thorne, and G. Watt, “Parton distributions for the LHC,” IPPP-08-95, DCPT-08-190, CAVENDISH-HEP-08-16, *Eur.Phys.J.* **C63** (2009) 189–285, [arXiv:0901.0002 \[hep-ph\]](#).
- [89] N. Kidonakis, “Next-to-next-to-leading soft-gluon corrections for the top quark cross section and transverse momentum distribution,” *Phys.Rev.* **D82** (2010) 114030, [arXiv:1009.4935 \[hep-ph\]](#).
- [90] V. Ahrens, A. Ferroglia, M. Neubert, B. D. Pecjak, and L. L. Yang, “Precision predictions for the $t\bar{t}$ production cross section at hadron colliders,” MZ-TH-11-11, ZU-TH-10-11, *Phys.Lett.* **B703** (2011) 135–141, [arXiv:1105.5824 \[hep-ph\]](#).
- [91] M. Beneke, P. Falgari, S. Klein, and C. Schwinn, “Hadronic top-quark pair production with NNLL threshold resummation,” TTK-11-38, ITP-UU-11-26, SPIN-11-19, FR-PHENO-2011-015, SFB-CPP-11-49, *Nucl.Phys.* **B855** (2012) 695–741, [arXiv:1109.1536 \[hep-ph\]](#).
- [92] M. Cacciari, M. Czakon, M. L. Mangano, A. Mitov, and P. Nason, “Top-pair production at hadron colliders with next-to-next-to-leading logarithmic soft-gluon resummation,” CERN-PH-TH-2011-277, TTK-11-54, *Phys.Lett.* **B710** (2012) 612–622, [arXiv:1111.5869 \[hep-ph\]](#).
- [93] S. Moch, P. Uwer, and A. Vogt, “On top-pair hadro-production at next-to-next-to-leading order,” DESY-12-049, HU-EP-12-10, LTH-940, LPN-12-042, SFB-CPP-12-16, [arXiv:1203.6282 \[hep-ph\]](#).
- [94] M. Aliev, H. Lacker, U. Langenfeld, S. Moch, P. Uwer, *et al.*, “HATHOR: HAdronic Top and Heavy quarks crOss section calculatoR,” DESY-10-091, HU-EP-10-33, SFB-CPP-10-60, *Comput.Phys.Commun.* **182** (2011) 1034–1046, [arXiv:1007.1327 \[hep-ph\]](#).
- [95] M. Czakon and A. Mitov, “Top++: a program for the calculation of the top-pair cross-section at hadron colliders,” [arXiv:1112.5675 \[hep-ph\]](#).

Bibliography

- [96] A. Martin, W. Stirling, R. Thorne, and G. Watt, “Uncertainties on α_s in global PDF analyses and implications for predicted hadronic cross sections,” IPPP-09-33, DCPT-09-66, CAVENDISH-HEP-09-06, *Eur.Phys.J.* **C64** (2009) 653–680, [arXiv:0905.3531 \[hep-ph\]](#).
- [97] G. Watt, “Parton distribution function dependence of benchmark Standard Model total cross sections at the 7 TeV LHC,” CERN-PH-TH-2011-149, *JHEP* **1109** (2011) 069, [arXiv:1106.5788 \[hep-ph\]](#).
- [98] M. Beneke, M. Czakon, P. Falgari, A. Mitov, and C. Schwinn, “Threshold expansion of the $gg(q\bar{q}) \rightarrow Q\bar{Q} + X$ cross section at $\mathcal{O}(\alpha_s^4)$,” *Phys.Lett.* **B690** (2010) 483–490, [arXiv:0911.5166 \[hep-ph\]](#).
- [99] B. W. Harris, E. Laenen, L. Phaf, Z. Sullivan, and S. Weinzierl, “The fully differential single top quark cross section in next-to-leading order QCD,” *Phys. Rev.* **D66** (2002) 054024, [arXiv:hep-ph/0207055](#).
- [100] S. Zhu, “Next-to-leading order QCD corrections to $bg \rightarrow tW^-$ at the CERN Large Hadron Collider,” *Phys. Lett.* **B524** (2002) 283–288.
- [101] N. Kidonakis, “Next-to-next-to-leading-order collinear and soft gluon corrections for t-channel single top quark production,” *Phys.Rev.* **D83** (2011) 091503, [arXiv:1103.2792 \[hep-ph\]](#).
- [102] N. Kidonakis, “NNLL resummation for s-channel single top quark production,” *Phys.Rev.* **D81** (2010) 054028, [arXiv:1001.5034 \[hep-ph\]](#).
- [103] H. X. Zhu, C. S. Li, J. Wang, and J. J. Zhang, “Factorization and resummation of s-channel single top quark production,” *JHEP* **1102** (2011) 099, [arXiv:1006.0681 \[hep-ph\]](#).
- [104] N. Kidonakis, “Two-loop soft anomalous dimensions for single top quark associated production with a W^- or H^- ,” *Phys.Rev.* **D82** (2010) 054018, [arXiv:1005.4451 \[hep-ph\]](#).
- [105] A. P. Heinson, A. S. Belyaev, and E. E. Boos, “Single top quarks at the Fermilab Tevatron,” *Phys. Rev.* **D56** (1997) 3114–3128, [arXiv:hep-ph/9612424](#).
- [106] F. Anselmo, B. van Eijk, and G. Bordes, “Heavy flavor production at large transverse momentum through the boson - gluon fusion mechanism,” *Phys. Rev.* **D45** (1992) 2312–2322.
- [107] **CDF Collaboration**, D. Acosta *et al.*, “Measurement of $B(t \rightarrow Wb)/B(t \rightarrow Wq)$ at the Collider Detector at Fermilab,” FERMILAB-PUB-05-219-E, *Phys.Rev.Lett.* **95** (2005) 102002, [arXiv:hep-ex/0505091 \[hep-ex\]](#).

- [108] **D0 Collaboration**, V. Abazov *et al.*, “Precision measurement of the ratio $B(t \rightarrow Wb)/B(t \rightarrow Wq)$ and Extraction of V_{tb} ,” FERMILAB-PUB-11-300-E, *Phys.Rev.Lett.* **107** (2011) 121802, [arXiv:1106.5436 \[hep-ex\]](#).
- [109] **CMS Collaboration**, S. Chatrchyan *et al.*, “First measurement of $B(t \rightarrow Wb)/B(t \rightarrow Wq)$ in the dilepton channel in pp collisions at $\sqrt{s} = 7$ TeV,” CMS-PAS-TOP-11-029, CERN, Geneva, 2012.
- [110] **D0 Collaboration**, V. Abazov *et al.*, “Measurements of single top quark production cross sections and $|V_{tb}|$ in $p\bar{p}$ collisions at $\sqrt{s} = 1.96$ TeV,” FERMILAB-PUB-11-380-E, *Phys.Rev.* **D84** (2011) 112001, [arXiv:1108.3091 \[hep-ex\]](#).
- [111] **ATLAS Collaboration**, G. Aad *et al.*, “Measurement of the t-channel single top-quark production cross section in pp collisions at $\sqrt{s} = 7$ TeV with the ATLAS detector,” CERN-PH-EP-2012-082, [arXiv:1205.3130 \[hep-ex\]](#).
- [112] **D0 Collaboration**, V. Abazov *et al.*, “Observation of Single Top Quark Production,” [arXiv:0903.0850 \[hep-ex\]](#).
- [113] **CDF Collaboration**, T. Aaltonen *et al.*, “First Observation of Electroweak Single Top Quark Production,” FERMILAB-PUB-09-059-E, *Phys.Rev.Lett.* **103** (2009) 092002, [arXiv:0903.0885 \[hep-ex\]](#).
- [114] **CMS Collaboration**, S. Chatrchyan *et al.*, “Measurement of the t-channel single top quark production cross section in pp collisions at $\sqrt{s} = 7$ TeV,” FERMILAB-PUB-11-725-CMS, CMS-TOP-10-008, CERN-PH-EP-2011-066, *Phys.Rev.Lett.* **107** (2011) 091802, [arXiv:1106.3052 \[hep-ex\]](#).
- [115] A. J. Buras, W. Slominski, and H. Steger, “ $B^0\bar{B}^0$ Mixing, CP Violation and the B Meson Decay,” *Nucl. Phys.* **B245** (1984) 369.
- [116] J. Alwall *et al.*, “Is $V_{tb} = 1?$,” *Eur. Phys. J.* **C49** (2007) 791–801, [arXiv:hep-ph/0607115](#).
- [117] M. Jezabek and J. H. Kühn, “QCD Corrections to Semileptonic Decays of Heavy Quarks,” *Nucl. Phys.* **B314** (1989) 1.
- [118] J. H. Kühn, “Theory of top quark production and decay,” [arXiv:hep-ph/9707321](#).
- [119] J. H. Kühn, “Weak Interactions of Quarkonia,” *Acta Phys. Polon.* **B12** (1981) 347.
- [120] J. H. Kühn, “Weak Decays of Open and Hidden Top,” *Acta Phys. Austriaca Suppl.* **24** (1982) 203.

Bibliography

- [121] I. I. Y. Bigi, Y. L. Dokshitzer, V. A. Khoze, J. H. Kühn, and P. M. Zerwas, “Production and Decay Properties of Ultraheavy Quarks,” *Phys. Lett.* **B181** (1986) 157.
- [122] P. Skands and D. Wicke, “Non-perturbative QCD effects and the top mass at the Tevatron,” *Eur. Phys. J.* **C52** (2007) 133–140, [arXiv:hep-ph/0703081](#).
- [123] D. Wicke and P. Z. Skands, “Non-perturbative QCD Effects and the Top Mass at the Tevatron,” [arXiv:0807.3248 \[hep-ph\]](#).
- [124] G. L. Kane, G. A. Ladinsky, and C. P. Yuan, “Using the top quark for testing standard model polarization and CP predictions,” *Phys. Rev.* **D45** (1992) 124–141.
- [125] R. H. Dalitz and G. R. Goldstein, “The Decay and polarization properties of the top quark,” *Phys. Rev.* **D45** (1992) 1531–1543.
- [126] C. A. Nelson, B. T. Kress, M. Lopes, and T. P. McCauley, “General tests for $t \rightarrow W + b$ couplings at hadron colliders,” *Phys. Rev.* **D56** (1997) 5928–5944, [arXiv:hep-ph/9707211](#).
- [127] **CDF, D0 Collaborations**, “Combination of CDF and D0 measurements of the W boson helicity in top quark decays,” SLAC-PUB-14955, FERMILAB-PUB-12-043-E, [arXiv:1202.5272 \[hep-ex\]](#).
- [128] **ATLAS Collaboration**, G. Aad *et al.*, “Measurement of the W boson polarization in top quark decays with the ATLAS detector,” CERN-PH-EP-2012-112, *JHEP* **1206** (2012) 088, [arXiv:1205.2484 \[hep-ex\]](#).
- [129] **CMS Collaboration**, S. Chatrchyan *et al.*, “ W helicity in top pair events,” CMS-PAS-TOP-11-020, CERN, Geneva, 2012.
- [130] (ed.) Brüning *et al.*, “LHC design report. Vol. I: The LHC main ring,” CERN-2004-003-V-1.
- [131] (ed.) Evans and (ed.) Bryant, “LHC Machine,” *JINST* **3** (2008) S08001.
- [132] CERN, “LEP Design Report: Vol. 2. The LEP Main Ring,” CERN-LEP-84-01.
- [133] K. Schindl, “The PS booster as preinjector for LHC,” CERN-PS-97-011, CERN-PS-97-11, *Part.Accel.* **58** (1997) 63–78.
- [134] M. Benedikt, A. Blas, J. Borburgh, R. Cappi, M. Chanel, *et al.*, “The PS complex produces the nominal LHC beam,” CERN-PS-2000-039-OP.
- [135] P. Collier, B. Goddard, R. Jung, K. Kissler, T. Linnecar, *et al.*, “The SPS as injector for LHC: Conceptual design,” CERN-SL-97-007-DI, CERN-SL-97-07-DI, CERN-SL-97-7-DI.

- [136] “CERN Photolab,” 2006.
<http://cdsmedia.cern.ch/collection/CERNPhotoLab?ln=en>.
- [137] **ALICE Collaboration**, K. Aamodt *et al.*, “The ALICE experiment at the CERN LHC,” *JINST* **3** (2008) S08002.
- [138] **LHCb Collaboration**, A. A. Alves *et al.*, “The LHCb Detector at the LHC,” *JINST* **3** (2008) S08005.
- [139] **ATLAS Collaboration**, G. Aad *et al.*, “The ATLAS Experiment at the CERN Large Hadron Collider,” *JINST* **3** (2008) S08003.
- [140] **CMS Collaboration**, R. Adolphi *et al.*, “The CMS experiment at the CERN LHC,” *JINST* **3** (2008) S08004.
- [141] **ATLAS Collaboration**, “ATLAS magnet system: Technical design report,” CERN-LHCC-97-18.
- [142] C. Lange, “Operational Experience with the ATLAS Pixel Detector,” ATL-INDET-PROC-2011-036, CERN, Geneva, Nov, 2011.
- [143] **ATLAS Collaboration**, M. Alam *et al.*, “ATLAS pixel detector: Technical design report,” CERN-LHCC-98-13.
- [144] G. Aad, M. Ackers, F. Alberti, M. Aleppo, G. Alimonti, *et al.*, “ATLAS pixel detector electronics and sensors,” *JINST* **3** (2008) P07007.
- [145] I. Peric, L. Blanquart, G. Comes, P. Denes, K. Einsweiler, *et al.*, “The FEI3 readout chip for the ATLAS pixel detector,” *Nucl.Instrum.Meth.* **A565** (2006) 178–187.
- [146] K. Gan, W. Fernando, P. Jackson, M. Johnson, H. Kagan, *et al.*, “Optical link of the ATLAS pixel detector,” *Nucl.Instrum.Meth.* **A570** (2007) 292–294.
- [147] **ATLAS Collaboration**, G. Aad *et al.*, “Expected Performance of the ATLAS Experiment - Detector, Trigger and Physics,” [arXiv:0901.0512](https://arxiv.org/abs/0901.0512) [hep-ex].
- [148] **ATLAS Collaboration**, G. Aad *et al.*, “Readiness of the ATLAS Liquid Argon Calorimeter for LHC Collisions,” *Eur.Phys.J.* **C70** (2010) 723–753, [arXiv:0912.2642](https://arxiv.org/abs/0912.2642) [physics.ins-det].
- [149] **ATLAS Collaboration**, G. Aad *et al.*, “Commissioning of the ATLAS Muon Spectrometer with Cosmic Rays,” *Eur.Phys.J.* **C70** (2010) 875–916, [arXiv:1006.4384](https://arxiv.org/abs/1006.4384) [physics.ins-det].
- [150] P. Jenni *et al.*, *ATLAS Forward Detectors for Measurement of Elastic Scattering and Luminosity*. Technical Design Report. CERN, Geneva, 2008.
- [151] V. Cindro, D. Dobos, I. Dolenc, H. Fraiss-Kölbl, *et al.*, “The ATLAS beam conditions monitor,” *JINST* **3** (2008) P02004.

Bibliography

- [152] S. van der Meer, “Calibration of the effective beam height in the ISR,” CERN-ISR-PO-68-31.
- [153] **ATLAS Collaboration**, G. Aad *et al.*, “Updated Luminosity Determination in pp Collisions at $\sqrt{s} = 7$ TeV using the ATLAS Detector,” ATLAS-CONF-2011-011, CERN, Geneva, Mar, 2011.
- [154] **ATLAS Collaboration**, G. Aad *et al.*, “Luminosity Determination in pp Collisions at $\sqrt{s} = 7$ TeV Using the ATLAS Detector at the LHC,” *Eur.Phys.J. C* **71** (2011) 1630, arXiv:1101.2185 [hep-ex].
- [155] **ATLAS Collaboration**, G. Aad *et al.*, “Luminosity Determination in pp Collisions at $\sqrt{s} = 7$ TeV using the ATLAS Detector in 2011,” ATLAS-CONF-2011-116, CERN, Geneva, Aug, 2011.
- [156] **ATLAS Collaboration**, G. Aad *et al.*, “Improved Luminosity Determination in pp Collisions at $\sqrt{s} = 7$ TeV using the ATLAS Detector at the LHC,” ATLAS-CONF-2012-080, CERN, Geneva, Jul, 2012.
- [157] *ATLAS level-1 trigger: Technical Design Report*. Technical Design Report ATLAS. CERN, Geneva, 1998.
- [158] **ATLAS Collaboration**, “ATLAS high-level trigger, data acquisition and controls: Technical design report,” CERN-LHCC-2003-022, ATLAS-TRD-016.
- [159] A. Asner, Y. Baconnier, O. Barbalat, M. Bassetti, C. Benvenuti, *et al.*, “ECFA-CERN Workshop on large hadron collider in the LEP tunnel, Lausanne and CERN, Geneva, Switzerland, 21-27 Mar 1984: Proceedings. 1.,” CERN-84-10-V-1, ECFA-84-85, CERN-YELLOW-84-10-V-1.
- [160] *ATLAS: letter of intent for a general-purpose pp experiment at the large hadron collider at CERN*. Letter of Intent. CERN, Geneva, 1992.
- [161] *ATLAS: technical proposal for a general-purpose pp experiment at the Large Hadron Collider at CERN*. LHC Tech. Proposal. CERN, Geneva, 1994.
- [162] ATLAS Luminosity Working Group, July, 2012. <https://twiki.cern.ch/twiki/bin/view/AtlasPublic/LuminosityPublicResults>.
- [163] T. Cornelissen, M. Elsing, S. Fleischmann, W. Liebig, E. Moyse, and A. Salzburger, “Concepts, Design and Implementation of the ATLAS New Tracking (NEWT),” ATL-SOFT-PUB-2007-007, CERN, Geneva, Mar, 2007.
- [164] R. E. Kalman, “A new approach to linear filtering and prediction problems,” *Transactions of the ASME-Journal of Basic Engineering* **82** no. Series D, (1960) 35–45.

- [165] **ATLAS Collaboration**, G. Aad *et al.*, “Performance of the ATLAS Inner Detector Track and Vertex Reconstruction in the High Pile-Up LHC Environment,” ATLAS-CONF-2012-042, CERN, Geneva, Mar, 2012.
- [166] **ATLAS Collaboration**, G. Aad *et al.*, “Alignment of the ATLAS Inner Detector Tracking System with 2010 LHC proton-proton collisions at $\sqrt{s} = 7$ TeV,” ATLAS-CONF-2011-012, CERN, Geneva, Mar, 2011.
- [167] **ATLAS Collaboration**, G. Aad *et al.*, “Performance of primary vertex reconstruction in proton-proton collisions at $\sqrt{s} = 7$ TeV in the ATLAS experiment,” ATLAS-CONF-2010-069, CERN, Geneva, Jul, 2010.
- [168] R. Frühwirth, W. Waltenberger, and P. Vanlaer, “Adaptive vertex fitting,” CERN-CMS-NOTE-2007-008, *J.Phys.G* **G34** (2007) N343.
- [169] **ATLAS Collaboration**, G. Aad *et al.*, “Characterization of Interaction-Point Beam Parameters Using the pp Event-Vertex Distribution Reconstructed in the ATLAS Detector at the LHC,” ATLAS-CONF-2010-027, CERN, Geneva, May, 2010.
- [170] **ATLAS Collaboration**, G. Aad *et al.*, “Expected electron performance in the ATLAS experiment,” ATL-PHYS-PUB-2011-006, CERN, Geneva, Apr, 2011.
- [171] **ATLAS Collaboration**, G. Aad *et al.*, “Electron performance measurements with the ATLAS detector using the 2010 LHC proton-proton collision data,” CERN-PH-EP-2011-117, *Eur.Phys.J.* **C72** (2012) 1909, [arXiv:1110.3174](https://arxiv.org/abs/1110.3174) [hep-ex].
- [172] ATLAS Electron Gamma Performance Group, August, 2012.
<https://twiki.cern.ch/twiki/bin/view/AtlasPublic/ElectronGammaPublicCollisionResults>.
- [173] **ATLAS Collaboration**, G. Aad *et al.*, “Performance of the ATLAS Trigger System in 2010,” CERN-PH-EP-2011-078, *Eur.Phys.J.* **C72** (2012) 1849, [arXiv:1110.1530](https://arxiv.org/abs/1110.1530) [hep-ex].
- [174] **ATLAS Collaboration**, G. Aad *et al.*, “Performance of the Electron and Photon Trigger in pp Collisions at $\sqrt{s} = 7$ TeV,” ATLAS-CONF-2011-114, CERN, Geneva, Aug, 2011.
- [175] R. O. Duda and P. E. Hart, “Use of the Hough transformation to detect lines and curves in pictures,” *Commun. ACM* **15** no. 1, (Jan., 1972) 11–15.
<http://doi.acm.org/10.1145/361237.361242>.
- [176] T. Lagouri, D. Adams, K. Assamagan, M. Biglietti, G. Carlino, *et al.*, “A Muon Identification and Combined Reconstruction Procedure for the ATLAS Detector at the LHC at CERN,” ATL-CONF-2003-011, *IEEE Trans.Nucl.Sci.* **51** (2004) 3030–3033.

Bibliography

- [177] **ATLAS Collaboration**, G. Aad *et al.*, “Muon reconstruction efficiency in reprocessed 2010 LHC proton-proton collision data recorded with the ATLAS detector,” ATLAS-CONF-2011-063, CERN, Geneva, Apr, 2011.
- [178] **ATLAS Collaboration**, G. Aad *et al.*, “Muon Momentum Resolution in First Pass Reconstruction of pp Collision Data Recorded by ATLAS in 2010,” ATLAS-CONF-2011-046, CERN, Geneva, Mar, 2011.
- [179] ATLAS Muon Performance Group, August, 2012. <https://twiki.cern.ch/twiki/bin/view/AtlasPublic/MuonPerformancePublicPlots>.
- [180] **UA1 Collaboration**, G. Arnison *et al.*, “Hadronic Jet Production at the CERN Proton - anti-Proton Collider,” *Phys. Lett.* **B132** (1983) 214.
- [181] G. C. Blazey *et al.*, “Run II jet physics,” arXiv:hep-ex/0005012.
- [182] Y. L. Dokshitzer, G. D. Leder, S. Moretti, and B. R. Webber, “Better Jet Clustering Algorithms,” *JHEP* **08** (1997) 001, arXiv:hep-ph/9707323.
- [183] S. D. Ellis and D. E. Soper, “Successive combination jet algorithm for hadron collisions,” *Phys. Rev.* **D48** (1993) 3160–3166, arXiv:hep-ph/9305266.
- [184] M. Cacciari and G. P. Salam, “Dispelling the N^3 myth for the k_T jet-finder,” *Phys. Lett.* **B641** (2006) 57–61, arXiv:hep-ph/0512210.
- [185] S. Catani, Y. L. Dokshitzer, and B. Webber, “The K^- perpendicular clustering algorithm for jets in deep inelastic scattering and hadron collisions,” CERN-TH-6473-92, LU-TP-92-14, *Phys.Lett.* **B285** (1992) 291–299.
- [186] M. Cacciari, G. P. Salam, and G. Soyez, “The Anti-k(t) jet clustering algorithm,” LPTHE-07-03, *JHEP* **0804** (2008) 063, arXiv:0802.1189 [hep-ph].
- [187] A. T. Pierce and B. R. Webber, “Comparisons of new jet clustering algorithms for hadron hadron collisions,” *Phys. Rev.* **D59** (1999) 034014, arXiv:hep-ph/9807532.
- [188] M. H. Seymour, “Jets in hadron collisions,” arXiv:hep-ph/0007051.
- [189] J. M. Butterworth, B. E. Cox, and J. R. Forshaw, “ W - W scattering at the LHC,” *Phys. Rev.* **D65** (2002) 096014, arXiv:hep-ph/0201098.
- [190] M. Cacciari, G. P. Salam, and G. Soyez, “FastJet user manual,” CERN-PH-TH-2011-297, *Eur.Phys.J.* **C72** (2012) 1896, arXiv:1111.6097 [hep-ph].
- [191] W. Lampl, S. Laplace, D. Lelas, P. Loch, H. Ma, *et al.*, “Calorimeter clustering algorithms: Description and performance,” ATL-LARG-PUB-2008-002, ATL-COM-LARG-2008-003.

- [192] **ATLAS Collaboration**, G. Aad *et al.*, “Jet energy measurement with the ATLAS detector in proton-proton collisions at $\sqrt{s} = 7$ TeV,” CERN-PH-EP-2011-191, FERMILAB-PUB-11-802-E, arXiv:1112.6426 [hep-ex].
- [193] **ATLAS Collaboration**, G. Aad *et al.*, “Pile-up corrections for jets from proton-proton collisions at $\sqrt{s} = 7$ TeV in ATLAS in 2011,” ATLAS-CONF-2012-064, CERN, Geneva, Jul, 2012.
- [194] **ATLAS Collaboration**, G. Aad *et al.*, “Single hadron response measurement and calorimeter jet energy scale uncertainty with the ATLAS detector at the LHC,” CERN-PH-EP-2012-005, arXiv:1203.1302 [hep-ex].
- [195] **ATLAS Collaboration**, G. Aad *et al.*, “Determination of the ATLAS jet energy measurement uncertainty using photon-jet events in proton-proton collisions at $\sqrt{s} = 7$ TeV,” ATLAS-CONF-2011-031, CERN, Geneva, Mar, 2011.
- [196] **ATLAS Collaboration**, G. Aad *et al.*, “Probing the measurement of jet energies with the ATLAS detector using photon+jet events in proton-proton collisions at $\sqrt{s} = 7$ TeV,” ATLAS-CONF-2012-063, CERN, Geneva, Jul, 2012.
- [197] **ATLAS Collaboration**, G. Aad *et al.*, “Validating the measurement of jet energies with the ATLAS detector using $Z +$ jet events from proton-proton collisions at $\sqrt{s} = 7$ TeV,” ATLAS-CONF-2011-159, CERN, Geneva, Dec, 2011.
- [198] **ATLAS Collaboration**, G. Aad *et al.*, “Probing the measurement of jet energies with the ATLAS detector using $Z +$ jet events from proton-proton collisions at $\sqrt{s} = 7$ TeV,” ATLAS-CONF-2012-053, CERN, Geneva, May, 2012.
- [199] **ATLAS Collaboration**, G. Aad *et al.*, “ATLAS jet energy scale uncertainties using tracks in proton proton collisions at $\sqrt{s} = 7$ TeV,” ATLAS-CONF-2011-067, CERN, Geneva, May, 2011.
- [200] **ATLAS Collaboration**, G. Aad *et al.*, “Close-by Jet Effects on Jet Energy Scale Calibration in pp Collisions at $\sqrt{s} = 7$ TeV with the ATLAS Detector,” ATLAS-CONF-2011-062, CERN, Geneva, Apr, 2011.
- [201] **ATLAS Collaboration**, G. Aad *et al.*, “Jet energy resolution and selection efficiency relative to track jets from in-situ techniques with the ATLAS Detector Using Proton-Proton Collisions at a Center of Mass Energy $\sqrt{s} = 7$ TeV,” ATLAS-CONF-2010-054, CERN, Geneva, Jul, 2010.
- [202] **ATLAS Collaboration**, G. Aad *et al.*, “Data-Quality Requirements and Event Cleaning for Jets and Missing Transverse Energy Reconstruction with the ATLAS Detector in Proton-Proton Collisions at a Center-of-Mass Energy of $\sqrt{s} = 7$ TeV,” ATLAS-CONF-2010-038, CERN, Geneva, Jul, 2010.

Bibliography

- [203] **ATLAS Collaboration**, G. Aad *et al.*, “Performance of Impact Parameter-Based b -tagging Algorithms with the ATLAS Detector using Proton-Proton Collisions at $\sqrt{s} = 7$ TeV,” ATLAS-CONF-2010-091, CERN, Geneva, Oct, 2010.
- [204] **ATLAS Collaboration**, G. Aad *et al.*, “Calibrating the b -Tag Efficiency and Mistag Rate in 35 pb^{-1} of Data with the ATLAS Detector,” ATLAS-CONF-2011-089, CERN, Geneva, Jun, 2011.
- [205] **ATLAS Collaboration**, G. Aad *et al.*, “Commissioning of the ATLAS high-performance b -tagging algorithms in the 7 TeV collision data,” ATLAS-CONF-2011-102, CERN, Geneva, Jul, 2011.
- [206] G. Piacquadio and C. Weiser, “A new inclusive secondary vertex algorithm for b -jet tagging in ATLAS,” *J. Phys. Conf. Ser.* **119** (2008) 032032.
- [207] **ATLAS Collaboration**, G. Aad *et al.*, “Measurement of the b -tag Efficiency in a Sample of Jets Containing Muons with 5 fb^{-1} of Data from the ATLAS Detector,” ATLAS-CONF-2012-043, CERN, Geneva, Mar, 2012.
- [208] **ATLAS Collaboration**, G. Aad *et al.*, “Measurement of the Mistag Rate with 5 fb^{-1} of Data Collected by the ATLAS Detector,” ATLAS-CONF-2012-040, CERN, Geneva, Mar, 2012.
- [209] **ATLAS Collaboration**, G. Aad *et al.*, “ b -jet tagging calibration on c -jets containing D^{*+} mesons,” ATLAS-CONF-2012-039, CERN, Geneva, Mar, 2012.
- [210] **ATLAS Collaboration**, G. Aad *et al.*, “Measuring the b -tag efficiency in a top-pair sample with 4.7 fb^{-1} of data from the ATLAS detector,” ATLAS-CONF-2012-097, CERN, Geneva, Jul, 2012.
- [211] **ATLAS Collaboration**, G. Aad *et al.*, “Performance of Missing Transverse Momentum Reconstruction in Proton-Proton Collisions at 7 TeV with ATLAS,” CERN-PH-EP-2011-114, *Eur.Phys.J.* **C72** (2012) 1844, arXiv:1108.5602 [hep-ex].
- [212] **ATLAS Collaboration**, G. Aad *et al.*, “Performance of Missing Transverse Momentum Reconstruction in ATLAS with 2011 Proton-Proton Collisions at $\sqrt{s} = 7$ TeV,” ATLAS-CONF-2012-101, CERN, Geneva, Jul, 2012.
- [213] **ATLAS Collaboration**, G. Aad *et al.*, “Improved luminosity determination in pp collisions at $\sqrt{s} = 7$ TeV using the ATLAS detector at the LHC,” CERN-PH-EP-2013-026, arXiv:1302.4393 [hep-ex].
- [214] M. A. Dobbs *et al.*, “Les Houches guidebook to Monte Carlo generators for hadron collider physics,” arXiv:hep-ph/0403045.

- [215] M. L. Mangano, M. Moretti, F. Piccinini, R. Pittau, and A. D. Polosa, “ALPGEN, a generator for hard multiparton processes in hadronic collisions,” *JHEP* **07** (2003) 001, [arXiv:hep-ph/0206293](#).
- [216] A. Markov, “An example of statistical investigation of the text Eugene Onegin concerning the connection of samples in chains,” *Science in Context* **19** no. 4, (2006) 591–600.
- [217] T. Sjostrand, S. Mrenna, and P. Skands, “PYTHIA 6.4 physics and manual,” *JHEP* **05** (2006) 026, [arXiv:hep-ph/0603175](#).
- [218] G. Corcella *et al.*, “HERWIG 6.5: an event generator for Hadron Emission Reactions With Interfering Gluons (including supersymmetric processes),” *JHEP* **01** (2001) 010, [arXiv:hep-ph/0011363](#).
- [219] J. M. Butterworth, J. R. Forshaw, and M. H. Seymour, “Multiparton interactions in photoproduction at HERA,” *Z. Phys.* **C72** (1996) 637–646, [arXiv:hep-ph/9601371](#).
- [220] S. Frixione and B. R. Webber, “Matching NLO QCD computations and parton shower simulations,” *JHEP* **06** (2002) 029, [arXiv:hep-ph/0204244](#).
- [221] S. Frixione, P. Nason, and B. R. Webber, “Matching NLO QCD and parton showers in heavy flavour production,” *JHEP* **08** (2003) 007, [arXiv:hep-ph/0305252](#).
- [222] P. Nason, “A New method for combining NLO QCD with shower Monte Carlo algorithms,” BICOCCA-FT-04-11, *JHEP* **0411** (2004) 040, [arXiv:hep-ph/0409146](#) [[hep-ph](#)].
- [223] S. Frixione, P. Nason, and C. Oleari, “Matching NLO QCD computations with Parton Shower simulations: the POWHEG method,” BICOCCA-FT-07-9, GEF-TH-21-2007, *JHEP* **0711** (2007) 070, [arXiv:0709.2092](#) [[hep-ph](#)].
- [224] S. Frixione, P. Nason, and G. Ridolfi, “A Positive-weight next-to-leading-order Monte Carlo for heavy flavour hadroproduction,” BICOCCA-FT-07-12, GEF-TH-19-2007, *JHEP* **0709** (2007) 126, [arXiv:0707.3088](#) [[hep-ph](#)].
- [225] **ATLAS Collaboration**, (ed.) Duckeck, “ATLAS computing: Technical design report,” CERN-LHCC-2005-022.
- [226] **GEANT4 Collaboration**, S. Agostinelli *et al.*, “GEANT4: A simulation toolkit,” *Nucl. Instrum. Meth.* **A506** (2003) 250–303.
- [227] **ATLAS Collaboration**, G. Aad *et al.*, “First tuning of HERWIG/JIMMY to ATLAS data,” ATL-PHYS-PUB-2010-014, CERN, Geneva, Oct, 2010.
- [228] **ATLAS, CMS Collaborations**, “New ATLAS event generator tunes to 2010 data,” ATL-PHYS-PUB-2011-008, CERN, Geneva, Apr, 2011.

Bibliography

- [229] **ATLAS Collaboration**, G. Aad *et al.*, “ATLAS tunes of PYTHIA 6 and Pythia 8 for MC11,” ATL-PHYS-PUB-2011-009, CERN, Geneva, Jul, 2011.
- [230] C. Wasicki, “Monte-Carlo-Simulation von Top-Paaren in nächstführender Ordnung am ATLAS-Experiment,” Diplom thesis, Freie Universität Berlin, Berlin, 2010. Presented on 01 Jul 2010, CERN-THESIS-2010-169.
- [231] J. Alwall *et al.*, “Comparative study of various algorithms for the merging of parton showers and matrix elements in hadronic collisions,” *Eur. Phys. J.* **C53** (2008) 473–500, [arXiv:0706.2569 \[hep-ph\]](#).
- [232] **CTEQ Collaboration**, H. Lai *et al.*, “Global QCD analysis of parton structure of the nucleon: CTEQ5 parton distributions,” MSUHEP-903100, FERMILAB-PUB-00-266-E, *Eur.Phys.J.* **C12** (2000) 375–392, [arXiv:hep-ph/9903282 \[hep-ph\]](#).
- [233] P. Z. Skands, “Tuning Monte Carlo Generators: The Perugia Tunes,” MCNET-10-08, CERN-PH-TH-2010-113, *Phys.Rev.* **D82** (2010) 074018, [arXiv:1005.3457 \[hep-ph\]](#).
- [234] B. P. Kersevan and E. Richter-Was, “The Monte Carlo event generator AcerMC version 2.0 with interfaces to PYTHIA 6.2 and HERWIG 6.5,” [arXiv:hep-ph/0405247](#).
- [235] **ATLAS Collaboration**, G. Aad *et al.*, “Measurement of $t\bar{t}$ production with a veto on additional central jet activity in pp collisions at $\sqrt{s} = 7$ TeV using the ATLAS detector,” CERN-PH-EP-2012-062, *Eur.Phys.J.* **C72** (2012) 2043, [arXiv:1203.5015 \[hep-ex\]](#).
- [236] **ATLAS Collaboration**, G. Aad *et al.*, “Jet Shapes in ATLAS and MC modeling,” ATL-PHYS-PUB-2011-010, CERN, Geneva, Jul, 2011.
- [237] K. Melnikov and F. Petriello, “Electroweak gauge boson production at hadron colliders through $O(\alpha(s)^2)$,” *Phys. Rev.* **D74** (2006) 114017, [arXiv:hep-ph/0609070](#).
- [238] J. Campbell, R. K. Ellis, and D. L. Rainwater, “Next-to-leading order QCD predictions for $W + 2$ jet and $Z + 2$ jet production at the CERN LHC,” *Phys. Rev.* **D68** (2003) 094021, [arXiv:hep-ph/0308195](#).
- [239] A. Sherstnev and R. Thorne, “Parton Distributions for LO Generators,” CAVENDISH-HEP-2007-12, *Eur.Phys.J.* **C55** (2008) 553–575, [arXiv:0711.2473 \[hep-ph\]](#).
- [240] B. P. Kersevan and I. Hinchliffe, “A consistent prescription for the production involving massive quarks in hadron collisions,” *JHEP* **09** (2006) 033, [arXiv:hep-ph/0603068](#).

- [241] **ATLAS Collaboration**, G. Aad *et al.*, “Search for top pair candidate events in ATLAS at $\sqrt{s} = 7$ TeV,” ATLAS-CONF-2010-063, CERN, Geneva, Jul, 2010.
- [242] S. Catani, M. Dittmar, D. Soper, W. J. Stirling, S. Tapprogge, *et al.*, “QCD,” CERN-TH-2000-131, [arXiv:hep-ph/0005025](#) [hep-ph].
- [243] J. A. Adelman, “Measurement of the Top Quark Mass at CDF Using the Template Method in the Lepton + Jets Channel,” FERMILAB-THESIS-2008-67.
- [244] **ATLAS Collaboration**, G. Aad *et al.*, “Measurement of the top quark-pair production cross section with ATLAS in pp collisions at $\sqrt{s} = 7$ TeV,” *Eur. Phys. J. C* **71** (2011) 1577, [arXiv:1012.1792](#) [hep-ex].
- [245] I. Chakravarti, R. Laha, and J. Roy, *Handbook of Methods of Applied Statistics*, vol. I. John Wiley and Sons, 1967.
- [246] **ATLAS Collaboration**, G. Aad *et al.*, “Measurement of the cross section for the production of a W boson in association with b -jets in pp collisions at $\sqrt{s} = 7$ TeV with the ATLAS detector,” CERN-PH-EP-2011-132, *Phys.Lett. B* **707** (2012) 418–437, [arXiv:1109.1470](#) [hep-ex].
- [247] **ATLAS Collaboration**, G. Aad *et al.*, “A search for $t\bar{t}$ resonances with the ATLAS detector in 2.05 fb^{-1} of proton-proton collisions at $\sqrt{s} = 7$ TeV,” CERN-PH-EP-2012-122, *Eur.Phys.J. C* **72** (2012) 2083, [arXiv:1205.5371](#) [hep-ex].
- [248] A. Henrichs, *Precision Measurements of the Top Quark Pair Production Cross Section in the Single Lepton Channel with the ATLAS Experiment*. PhD thesis, Universität Göttingen, Mar, 2012. Presented 19 Apr 2012, CERN-THESIS-2012-043.
- [249] C.-H. Kom and W. J. Stirling, “Charge asymmetry in W + jets production at the LHC,” CAVENDISH-HEP-2010-06, *Eur.Phys.J. C* **69** (2010) 67–73, [arXiv:1004.3404](#) [hep-ph].
- [250] F. A. Berends, W. Giele, H. Kuijf, R. Kleiss, and W. J. Stirling, “Multi-jet production in W , Z events at $p\bar{p}$ colliders,” Print-89-0318 (LEIDEN), *Phys.Lett. B* **224** (1989) 237.
- [251] S. Ellis, R. Kleiss, and W. J. Stirling, “ W ’s, Z ’s and Jets,” CERN-TH 4096/85, *Phys.Lett. B* **154** (1985) 435.
- [252] A. Höcker, J. Stelzer, F. Tegenfeldt, H. Voss, K. Voss, *et al.*, “TMVA - Toolkit for Multivariate Data Analysis,” CERN-OPEN-2007-007, *PoS ACAT* (2007) 040, [arXiv:physics/0703039](#) [PHYSICS].
- [253] R. Brun and F. Rademakers, “ROOT: An object oriented data analysis framework,” *Nucl.Instrum.Meth. A* **389** (1997) 81–86. See also <http://root.cern.ch>.

Bibliography

- [254] **ATLAS Collaboration**, G. Aad *et al.*, “ATLAS Calorimeter Response to Single Isolated Hadrons and Estimation of the Calorimeter Jet Scale Uncertainty,” ATLAS-CONF-2011-028, CERN, Geneva, Mar, 2011.
- [255] **ATLAS Collaboration**, G. Aad *et al.*, “In situ jet pseudorapidity intercalibration of the ATLAS detector using dijet events in $\sqrt{s} = 7$ TeV proton-proton 2011 data,” ATLAS-CONF-2012-124, CERN, Geneva, Aug, 2012.
- [256] M. Bahr, S. Gieseke, M. Gigg, D. Grellscheid, K. Hamilton, *et al.*, “Herwig++ Physics and Manual,” CERN-PH-TH-2008-038, CAVENDISH-HEP-08-03, KA-TP-05-2008, DCPT-08-22, IPPP-08-11, CP3-08-05, *Eur.Phys.J.* **C58** (2008) 639–707, [arXiv:0803.0883 \[hep-ph\]](#).
- [257] **ATLAS Collaboration**, G. Aad *et al.*, “Light-quark and Gluon Jets in ATLAS,” ATLAS-CONF-2011-053, CERN, Geneva, Apr, 2011.
- [258] M. Botje, J. Butterworth, A. Cooper-Sarkar, A. de Roeck, J. Feltesse, *et al.*, “The PDF4LHC Working Group Interim Recommendations,” [arXiv:1101.0538 \[hep-ph\]](#).
- [259] R. D. Ball, V. Bertone, S. Carrazza, C. S. Deans, L. Del Debbio, *et al.*, “Parton distributions with LHC data,” EDINBURGH-2012-08, IFUM-FT-997, FR-PHENO-2012-014, RWTH-TTK-12-25, CERN-PH-TH-2012-037, SFB-CPP-12-47 *Nucl.Phys.* **B867** (2013) 244–289, [arXiv:1207.1303 \[hep-ph\]](#).
- [260] R. D. Ball, L. Del Debbio, S. Forte, A. Guffanti, J. I. Latorre, *et al.*, “A first unbiased global NLO determination of parton distributions and their uncertainties,” EDINBURGH-2010-05, IFUM-952-FT, FR-PHENO-2010-014, CP3-10-08, *Nucl.Phys.* **B838** (2010) 136–206, [arXiv:1002.4407 \[hep-ph\]](#).
- [261] F. James and M. Roos, “Minuit: A System for Function Minimization and Analysis of the Parameter Errors and Correlations,” CERN-DD-75-20, *Comput.Phys.Commun.* **10** (1975) 343–367.
- [262] **ATLAS, CMS Collaborations**, “Procedure for the LHC Higgs boson search combination in summer 2011,” ATL-PHYS-PUB-2011-011, CERN, Geneva, Aug, 2011.
- [263] W. C. Johnson, “Search for Pair Production of Supersymmetric Top Quarks in Dilepton Events at the Tevatron,” FERMILAB-THESIS-2010-16.
- [264] N. Reid, “Likelihood Inference in the Presence of Nuisance Parameters,” PHYSTAT-2003-THAT001, *eConf* **C030908** (2003) THAT001.
- [265] **ATLAS Collaboration**, G. Aad *et al.*, “Measurement of the top quark-pair cross-section with ATLAS in pp collisions at $\sqrt{s} = 7$ TeV in the single-lepton channel using b-tagging,” ATLAS-CONF-2011-035, CERN, Geneva, Mar, 2011.

- [266] **ATLAS Collaboration**, G. Aad *et al.*, “Measurement of the top quark pair production cross-section with ATLAS in the single lepton channel,” CERN-PH-EP-2011-201, *Phys.Lett.* **B711** (2012) 244–263, [arXiv:1201.1889 \[hep-ex\]](#).
- [267] **ATLAS Collaboration**, G. Aad *et al.*, “Measurement of the top quark pair production cross-section with ATLAS in pp collisions at $\sqrt{s} = 7$ TeV in dilepton final states,” ATLAS-CONF-2011-034, CERN, Geneva, Mar, 2011.
- [268] **CMS Collaboration**, S. Chatrchyan *et al.*, “Measurement of $t\bar{t}$ pair production cross section at $\sqrt{s} = 7$ tev using b -quark jet identification techniques in lepton + jet events,” CMS-PAS-TOP-11-003, CERN, Geneva, Oct, 2011.
- [269] **ATLAS Collaboration**, G. Aad *et al.*, “A combined measurement of the top quark pair production cross-section using dilepton and single-lepton final states,” ATLAS-CONF-2011-040, CERN, Geneva, Mar, 2011.
- [270] **ATLAS Collaboration**, G. Aad *et al.*, “Measurement of the top quark pair production cross section in pp collisions at $\sqrt{s} = 7$ TeV in dilepton final states with ATLAS,” ATLAS-CONF-2011-100, CERN, Geneva, Jul, 2011.
- [271] **ATLAS Collaboration**, G. Aad *et al.*, “Measurement of the top quark pair production cross-section based on a statistical combination of measurements of dilepton and single-lepton final states at $\sqrt{s} = 7$ TeV with the ATLAS detector,” ATLAS-CONF-2011-108, CERN, Geneva, Aug, 2011.
- [272] A. Buckley, J. Butterworth, S. Gieseke, D. Grellscheid, S. Hoche, *et al.*, “General-purpose event generators for LHC physics,” CAVENDISH-HEP-10-21, CERN-PH-TH-2010-298, DCPT-10-202, HD-THEP-10-24, IPPP-10-101, KA-TP-40-2010, LU-TP-10-28, MAN-HEP-2010-23, MCNET-11-01, SLAC-PUB-14333, *Phys.Rept.* **504** (2011) 145–233, [arXiv:1101.2599 \[hep-ph\]](#).
- [273] **ATLAS Collaboration**, G. Aad *et al.*, “Determination of the top-quark mass from the $t\bar{t}$ cross section measurement in pp collisions at $\sqrt{s} = 7$ tev with the atlas detector,” ATLAS-CONF-2011-054, CERN, Geneva, Apr, 2011.
- [274] **D0 Collaboration**, S. Abachi *et al.*, “Combination of t anti- t cross section measurements and constraints on the mass of the top quark and its decays into charged Higgs bosons,” FERMILAB-PUB-09-092-E, *Phys.Rev.* **D80** (2009) 071102, [arXiv:0903.5525 \[hep-ex\]](#).
- [275] **CMS Collaboration**, S. Chatrchyan *et al.*, “Determination of the Top Quark Mass from the $t\bar{t}$ Cross Section at $\sqrt{s} = 7$ TeV,” CMS-PAS-TOP-11-008, Dec, 2011.
- [276] **ATLAS, CMS Collaborations**, “Combination of ATLAS and CMS results on the mass of the top quark using up to 4.9 fb^{-1} of data,” ATLAS-CONF-2012-095, CERN, Geneva, Jul, 2012.

Bibliography

- [277] V. Ferrara, *Extraction of the Top Quark Mass from the Total Top Quark Pair Production Cross Section in the Single Lepton Channel*. PhD thesis, Humboldt-Universität zu Berlin, 2012. Presented 19 Dec 2012, to be published.
- [278] **ATLAS Collaboration**, G. Aad *et al.*, “Measurement of the $t\bar{t}$ production cross-section in pp collisions at $\sqrt{s} = 7$ TeV using kinematic information of lepton+jets events,” ATLAS-CONF-2011-121, CERN, Geneva, Aug, 2011.
- [279] **ATLAS Collaboration**, G. Aad *et al.*, “Measurements of top quark pair relative differential cross-sections with ATLAS in pp collisions at $\sqrt{s} = 7$ TeV,” CERN-PH-EP-2012-165, *submitted to European Physical Journal C* (2012) , [arXiv:1207.5644](https://arxiv.org/abs/1207.5644) [hep-ex].
- [280] **ATLAS Collaboration**, G. Aad *et al.*, “Measurement of the jet multiplicity in top anti-top final states produced in 7 TeV proton-proton collisions with the ATLAS detector,” ATLAS-CONF-2012-155, CERN, Geneva, Nov, 2012.
- [281] **ATLAS Collaboration**, G. Aad *et al.*, “Measurement of $t\bar{t}$ production in the all-hadronic channel in 1.02 fb^{-1} of pp collisions at $\sqrt{s} = 7$ TeV with the ATLAS detector,” ATLAS-CONF-2011-140, CERN, Geneva, Sep, 2011.
- [282] **ATLAS Collaboration**, G. Aad *et al.*, “Statistical combination of top quark pair production cross-section measurements using dilepton, single-lepton, and all-hadronic final states at $\sqrt{s} = 7$ TeV with the ATLAS detector,” ATLAS-CONF-2012-024, CERN, Geneva, Mar, 2012.
- [283] L. Lyons, D. Gibaut, and P. Clifford, “How to combine correlated estimates of a single physical quantity,” PRINT-88-0048 (OXFORD), OXFORD-NP-5-88, *Nucl.Instrum.Meth.* **A270** (1988) 110.
- [284] A. Valassi, “Combining correlated measurements of several different physical quantities,” *Nucl.Instrum.Meth.* **A500** (2003) 391–405.
- [285] **CMS Collaboration**, S. Chatrchyan *et al.*, “Top pair cross section in dileptons,” CMS-PAS-TOP-11-005, CERN, Geneva, Aug, 2011.
- [286] **CMS Collaboration**, S. Chatrchyan *et al.*, “First measurement of the top quark pair production cross section in the dilepton channel with tau leptons in the final state in pp collisions at $\sqrt{s} = 7$ TeV,” CMS-PAS-TOP-11-006, CERN, Geneva, Jul, 2011.
- [287] **CMS Collaboration**, S. Chatrchyan *et al.*, “Measurement of the $t\bar{t}$ production cross section in the fully hadronic decay channel in pp collisions at 7 TeV,” CMS-PAS-TOP-11-007, CERN, Geneva, Jul, 2011.
- [288] **ATLAS, CMS Collaborations**, “Combination of atlas and cms top-quark pair cross section measurements using up to 1.1 fb^{-1} of data at 7 tev,” ATLAS-CONF-2012-134, CERN, Geneva, Sep, 2012.

- [289] **CMS Collaboration**, S. Chatrchyan *et al.*, “Measurement of the $t\bar{t}$ production cross section in the dilepton channel in pp collisions at $\sqrt{s} = 7$ TeV,” CMS-TOP-11-005, CERN-PH-EP-2012-224, *JHEP* **1211** (2012) 067, [arXiv:1208.2671](#) [[hep-ex](#)].
- [290] G. D’Agostini, “A Multidimensional unfolding method based on Bayes’ theorem,” DESY-94-099, *Nucl.Instrum.Meth.* **A362** (1995) 487–498.
- [291] G. D’Agostini, “Improved iterative Bayesian unfolding,” *ArXiv e-prints* (Oct., 2010) , [arXiv:1010.0632](#) [[physics.data-an](#)].
- [292] **ATLAS Collaboration**, G. Aad *et al.*, “Measurement of the top quark pair production cross-section with atlas in pp collisions at $\sqrt{s} = 7$ tev in the single-lepton channel using semileptonic b decays,” ATLAS-CONF-2012-131, CERN, Geneva, Sep, 2012.
- [293] A. Martin, R. Roberts, W. Stirling, and R. Thorne, “NNLO global parton analysis,” IPPP-02-01, DCPT-02-02, CERN-TH-2001-362, CAVENDISH-HEP-2001-15, *Phys.Lett.* **B531** (2002) 216–224, [arXiv:hep-ph/0201127](#) [[hep-ph](#)].

List of Figures

2.1.	Observed and expected local p-values as a function of the Higgs boson mass	9
2.2.	Radiative corrections to the W and Z propagator with top quark contribution	12
2.3.	Radiative corrections to the W and Z propagator with Higgs boson contribution	12
2.4.	Indirect and direct top mass measurements	13
2.5.	CTEQ6M parton distribution functions	17
2.6.	Feynman diagrams of the leading order processes for $t\bar{t}$ production . . .	18
2.7.	Example Feynman diagrams of the leading order processes for single top production	23
2.8.	Top quark pair decay	27
2.9.	Top pair branching fractions	27
3.1.	The CERN accelerator complex.	30
3.2.	Cut-away view of the ATLAS detector.	32
3.3.	Cut-away view of the ATLAS Inner Detector.	34
3.4.	Barrel region of the ATLAS Inner Detector.	35
3.5.	The ATLAS Pixel Detector module.	36
3.6.	Layout of pixel readout system.	37
3.7.	Cut-away view of the ATLAS calorimeter system.	38
3.8.	Sketch of a barrel module of the electromagnetic calorimeter.	39
3.9.	Cut-away view of the ATLAS muon system.	40
3.10.	Block diagram of the ATLAS trigger and data acquisition systems. . . .	44
3.11.	Luminosity in 2010 and 2011	46
4.1.	Mean number of interactions per bunch crossing.	49
4.2.	Electron reconstruction efficiencies	53
4.3.	Electron energy calibration	54
4.4.	Muon reconstruction efficiencies	57
4.5.	Muon momentum calibration	58
4.6.	Jet energy scale correction and response.	63
4.7.	Jet energy resolution and reconstruction efficiency.	65
4.8.	b -tagging probability distribution comparison of MC with 2010 data. . .	66
4.9.	b -tagging efficiencies for the JetProb algorithm.	67
4.10.	Mistag rates for the MV1 algorithm.	69
4.11.	Measured b -tagging efficiencies for the MV1 algorithm.	71

List of Figures

4.12.	Missing transverse energy performance.	74
5.1.	Steps of Monte Carlo event generation	76
5.2.	Feynman diagrams for $W + \text{jets}$ production production	82
5.3.	Feynman diagrams for diboson production production	84
6.1.	Event display of a $t\bar{t}$ candidate in the electron + jets channel.	88
6.2.	Feynman diagrams for QCD multi-jet production	90
6.3.	QCD multi-jet background fit results using the anti-electron model.	93
6.4.	Control plots for QCD multi-jet background evaluation using the anti-electron model.	94
7.1.	Expected fraction and number of selected events as a function of the number of selected jets.	103
7.2.	Lepton η distribution for $t\bar{t}$ production and the $W + \text{jets}$ background process.	105
7.3.	Transformed form of aplanarity, $\exp(-8 \times \mathcal{A})$, distribution for $t\bar{t}$ production and the $W + \text{jets}$ background process.	106
7.4.	$\exp(-4 \times H_{T,3p})$ distribution for $t\bar{t}$ production and the $W + \text{jets}$ background process.	106
7.5.	Leading jet p_T distribution for $t\bar{t}$ production and the $W + \text{jets}$ background process.	107
7.6.	Quadratic sum of all sources of systematic uncertainties for the sum of predicted events for the 2010 analysis,	110
7.7.	Fractional jet energy scale systematic uncertainty as a function of p_T	111
7.8.	Additional fractional b -jet JES uncertainty as a function of the truth jet transverse momentum.	115
7.9.	Effect of the systematic variations of the generator parameters on the ratio of the different samples.	119
8.1.	Observed and expected event yields for the 2010 analysis.	128
8.2.	Average <code>JetProb</code> weight of the two selected jets with highest b -tagging probability distribution for $t\bar{t}$ production and the $W + \text{jets}$ background process.	130
8.3.	Input variable \bar{w}_{JP} for the $\mu + \text{jets}$ and the $e + \text{jets}$ channel in the signal regions.	131
8.4.	Input variable η^ℓ for the $\mu + \text{jets}$ and the $e + \text{jets}$ channel in the signal regions.	132
8.5.	Input variable $\exp[-8 \times A]$ for the $\mu + \text{jets}$ and the $e + \text{jets}$ channel in the signal regions.	133
8.6.	Input variable $\exp[-4 \times H_{T,3p}]$ for the $\mu + \text{jets}$ and the $e + \text{jets}$ channel in the signal regions.	134
8.7.	Likelihood discriminant for the $\mu + \text{jets}$ and the $e + \text{jets}$ channel in the signal regions.	135

8.8.	Distribution of fitted $t\bar{t}$ cross section parameter and its pull using pseudo experiments.	135
8.9.	Linearity test and pull distribution as a function of input $t\bar{t}$ cross section	136
8.10.	Error bands for the distributions of \mathcal{D} of the sum of predicted signal and background events overlaid on the discriminant distributions in data for the six different analysis channels.	137
8.12.	Correlation matrix of fit parameters.	140
8.13.	Negative log-likelihood value as function of β_0	141
8.14.	Single channel results for the cross section fit with all nuisance parameters included.	142
8.15.	Illustration of shape variations inside a given systematic variation template.	145
8.16.	Results of 1,000 pseudo experiments with b -tagging shape at working point 1 shifted to -1σ	146
8.17.	Top quark mass extraction from top quark pair cross section	153
9.1.	Observed and expected event yields for the 2011 analysis (a).	156
9.2.	Transverse momentum of the leading jet in data and Monte Carlo simulated events in the signal regions.	160
9.3.	Lepton pseudorapidity in data and Monte Carlo simulated events in the signal regions.	161
9.4.	Transformed version of event aplanarity for data and Monte Carlo simulated in the signal regions.	162
9.5.	Variable $H_{T,3p}$ in its transformed form for data and Monte Carlo simulated events in the signal regions.	163
9.6.	Comparison of the likelihood discriminant \mathcal{D} in data and Monte Carlo simulated events for all fit channels.	165
9.7.	Distribution of fitted $t\bar{t}$ cross section parameter and its pull using pseudo experiments.	165
9.8.	Linearity test and pull distribution as a function of input $t\bar{t}$ cross section	166
9.9.	Result of the profile likelihood fit to data.	166
9.10.	Correlation matrix of fit parameters.	168
9.11.	Negative log-likelihood value as function of β_0	169
9.12.	Single channel results for the cross section fit with all nuisance parameters included.	170
9.13.	Top quark pair cross section measurements at ATLAS and CMS and their combination	174
9.14.	$\sigma_{t\bar{t}}$ as a function of top quark mass	175
10.1.	Observed and expected event yields for the 2011 analysis (b).	182
10.2.	Observed and expected event yields for the 2011 analysis (b) for POWHEG + PYTHIA.	183
10.3.	Lepton pseudorapidity in data and Monte Carlo simulated events in the signal region.	188

List of Figures

10.4.	Transformed version of $H_{T,3p}$ in data and Monte Carlo simulated events in the signal region.	189
10.5.	Transformed version of aplanarity in data and Monte Carlo simulated events in the signal region.	190
10.6.	Projective likelihood discriminant in data and Monte Carlo simulated events in the signal region.	191
10.7.	Lepton pseudorapidity in data and Monte Carlo simulated events in the signal region split according to particle level selection.	192
10.8.	Projective likelihood discriminant in data and Monte Carlo simulated events in the signal region split according to particle level selection.. . . .	193
10.9.	Distribution of fitted $t\bar{t}$ fiducial cross section parameter using pseudo experiments.	194
10.10.	Correlation of the $t\bar{t}$ fiducial cross section parameter with selected uncertainties.	195
10.11.	Correlation of the $t\bar{t}$ fiducial cross section parameters with the JES uncertainty.	195
10.12.	Result of the likelihood fit to data.	198
10.13.	Correlation matrix of fit parameters.	198
10.14.	Comparison of fiducial $t\bar{t}$ cross sections.	200
10.15.	Leading jet p_T for five and more jets before and after fit.	201
10.16.	$t\bar{t}$ cross sections in full phase space.	203
10.17.	Comparison of uncertainties for the different measurements.	204
B.1.	Linearity test for QCD multi-jet background evaluation using the anti-electron model.	215
B.2.	Comparison between the nominal and the alternative QCD multi-jet anti-electron model.	216
B.3.	W boson transverse mass control plots for QCD multi-jet background evaluation using the anti-electron model.	217
B.4.	$\Delta\phi$ control plots for QCD multi-jet background evaluation using the anti-electron model.	218
B.5.	Lepton p_T control plots for QCD multi-jet background evaluation using the anti-electron model.	219
B.6.	Lepton η control plots for QCD multi-jet background evaluation using the anti-electron model.	220
B.7.	Lepton ϕ control plots for QCD multi-jet background evaluation using the anti-electron model.	221
C.1.	Effect of the systematic variations of the generator parameters on the different samples.	226
C.2.	Effect of the systematic variations of the generator parameters on the ratio of the different samples.	227

C.3.	Ratio of the p_T distribution of all jets in the event in the 4 jet bin to the 2 jet bin for a given systematic variations of the generator parameters for the different samples.	230
D.1.	Behaviour of the normalisation parameters during profiling procedure .	231
D.2.	Behaviour of the normalisation parameters during profiling procedure .	232
D.3.	Behaviour of the normalisation parameters during profiling procedure .	233
D.4.	Behaviour of the normalisation parameters during profiling procedure .	234
E.1.	Behaviour of the normalisation parameters during profiling procedure .	235
E.2.	Behaviour of the normalisation parameters during profiling procedure .	236
E.3.	Behaviour of the normalisation parameters during profiling procedure .	237
E.4.	Behaviour of the normalisation parameters during profiling procedure .	238
F.1.	Leading jet transverse momentum in data and Monte Carlo simulated events in the signal region.	242
F.2.	Transverse mass of leptonic W boson in data and Monte Carlo simulated events in the signal region.	243

List of Tables

2.1.	The fields of the Standard Model and their gauge quantum numbers . . .	4
2.2.	Cross sections for $t\bar{t}$ production at the LHC ($\sqrt{s} = 7$ TeV).	20
2.3.	Cross sections for single top production at the LHC ($\sqrt{s} = 7$ TeV). . . .	24
4.1.	Definition of variables used for loose , medium and tight electron identification.	51
4.2.	Electron trigger chains used for analyses	55
4.3.	Muon trigger chains used for analyses	59
5.1.	Summary of Monte Carlo samples.	84
5.1.	Summary of Monte Carlo samples.	85
6.1.	Offline event selection cuts.	88
6.2.	Fitted fraction of QCQ events in 2010 data.	93
6.3.	Summary of the use of the different QCD multi-jet background estimation methods.	98
6.4.	W + jets scale factors for the 2011 analysis (a).	99
6.5.	W + jets scale factors for the 2011 analysis (b).	100
6.6.	Scale factors for the heavy flavour fractions in the W + jets background for the 2011 analysis (b)	100
7.1.	Discriminating variables used for the analyses.	109
7.2.	Sources of systematic uncertainties and their treatment in the cross section extraction.	126
8.1.	Selected events in the μ + jets channel for the 2010 analysis.	129
8.2.	Selected events in the e + jets channel for the 2010 analysis.	129
8.3.	Result of the profile likelihood fit to data for the 2010 analysis.	137
8.4.	Cross section results for the single channel fits for the 2010 analysis. . .	143
8.5.	Table of estimated systematic uncertainties for the 2010 analysis.	144
8.6.	Top quark pair cross section dependence on m_t for the 2010 analysis. . .	152
9.1.	Selected events in the μ + jets channel for the 2011 analysis (a).	157
9.2.	Selected events in the e + jets channel for the 2011 analysis (a).	158
9.3.	Resulting fit parameters and uncertainties from the fit in all six analysis channels to data for the 2011 analysis (a).	163
9.4.	Cross section results for the single channel fits for the 2011 analysis (a). .	168
9.5.	Table of estimated systematic uncertainties for the 2011 analysis (a). . .	171

List of Tables

10.1.	Selected events in the μ + jets channel	180
10.2.	Selected events in the e + jets channel	181
10.3.	Particle level vs. reconstruction level event selection cuts for the 2011 analysis (b).	181
10.4.	Selected $t\bar{t}$ events in the μ + jets channel.	184
10.5.	Selected $t\bar{t}$ events in the e + jets channel.	185
10.6.	Table of estimated uncertainties for the 2011 analysis (b)	197
10.7.	Fiducial cross sections and particle level selection acceptance.	202
10.8.	Differences in the evaluation of systematic uncertainties between the analyses presented in this work.	204
A.1.	Summary of Monte Carlo samples.	209
B.1.	Gaussian constraints applied to MC samples in the fit.	214
C.1.	Functional form choices of the factorisation and normalisation scale in AlpGEN.	224
C.2.	AlpGEN default parameters and variations used for W + heavy flavour studies.	224
C.3.	Statistics generated for each parameter variation for a given sample for W + heavy flavour studies.	225
C.4.	Behaviour of W + jets heavy flavour to light flavour fractions for $N/(N-1)$ jet bin ratios for given systematic variation.	228
E.1.	Detailed table of estimated systematic uncertainties for the 2011 analysis (a).	239
F.1.	Fit results of the combined likelihood fit to data for the 2011 analysis (b).	243

Selbständigkeitserklärung

Ich erkläre, dass ich die vorliegende Arbeit selbständig und nur unter Verwendung der angegebenen Literatur und Hilfsmittel angefertigt habe.

Berlin, den 25.03.2013

Clemens Gregor Lange

Acknowledgements

This work would not have been possible without the support of a large number of people—be it with regards to physics or not. All of them I owe a big thank you!

First of all I would like to thank my supervisor Ulrich Husemann for giving me the opportunity to continue in particle physics after my Diplom and for continuous advice and support. Even though he decided to live with the "Gelbfüßler" almost two years ago he always had an open ear for my numerous complaints and ideas.

Having said that, I am indebted to Thorsten Kuhl for taking over the largest part of supervision once Ulrich had left. He had the idea of a fiducial measurement that I eventually turned into the last analysis chapter. His grumpiness in combination with availability for discussion almost 24/7 helped a lot. Also thanks to Michael Kobel for being second adviser and for a critical view on my work, and Lucia Masetti and Heiko Lacker for refereeing this work.

I am grateful for having been able to work at DESY in Zeuthen in general and to all the people in the ATLAS group and the DV department. In particular, I would like to thank Sascha Mehlhase and Marcello Barisonzi for the good times in my early years in Zeuthen, Hermann Kolanoski for an always open office door, and the Experimente Support team for giving me the opportunity to join several outreach activities, which gave my life in particle physics an extra twist. Furthermore, thanks go out to Christoph Wasicki and Conrad Friedrich and the guys from the physics department of the Humboldt-Uni in Adlershof for the nice evenings at the GK block courses and one or the other Feierabendbier.

I especially would like to mention my closest collaborators when I was at CERN and later on, Anna Henrichs and Philipp Sturm, who have both become good friends making work so much more enjoyable. My ICQ chat history with them is most likely longer than this thesis and is still growing. Not to forget Yvonne Peters and Dominic Hirschbühl with whom I enjoyed working and gossiping very much.

The GoDESY team with which I published the first two cross sections, in particular Lisa Shabalina for trusting in my work, and several good discussions. The ATLAS pixel detector community under the leadership of Beniamino di Girolamo for creating such a friendly atmosphere, especially the DCS team and the run coordinators.

The university choir, of course primarily my fellow tenors, who made every Wednesday a good one and each concert tour a Klassenfahrt. The Hochschulsport without their large variety of offers I would never had started fencing and hip-hop classes, which were such great fun I would not want to have missed. The Backstreet Boys and 'N Sync for their music that just makes me happy (and everyone else think I am very "special" when realising what I am listening to).

Last but surely not least, I would like to thank my friends and family in Berlin and in other places and a special thanks to Steffi for who she is to me. Without them I would not be where I am now. Even though almost everyone had a hard time understanding what I was actually doing, they were always there for me and supported me no matter what. Thank you!